RESPONSE OF UNDERGROUND POWER TRANSMISSION CABLES SUBJECTED TO EARTHQUAKE INDUCED PERMANENT GROUND DEFORMATIONS

by

Alireza Ahmadnia

B.Sc., Amirkabir University of Technology, Tehran, Iran, 1999

M.Sc. Sharif University of Technology, Tehran, Iran, 2001

A THESIS SUBMITTED IN PARTIAL FULFILLMENT OF

THE REQUIREMENTS FOR THE DEGREE OF

DOCTOR OF PHILOSOPHY

in

THE FACULTY OF GRADUATE STUDIES

(Civil Engineering)

THE UNIVERSITY OF BRITISH COLUMBIA

(Vancouver)

December 2011

Abstract

The aim of this study is to evaluate the response of underground power transmission cables subjected to earthquake induced permanent longitudinal and lateral ground movements. The experimental work related to this research involved full-scale physical modeling. The testing facility used for this project comprises a 2.5 m x 3.8 m soil chamber, with the capacity to subject buried transmission cables to large relative displacements. The buried cables were subjected to axial and transverse soil movements, and the corresponding longitudinal and horizontal transverse soil loads were measured. A total of 15 axial pullout tests and 10 lateral pullout tests were conducted for the cable with different burial depths. In the absence of guidelines available for buried underground cables, the results of the full-scale experimental studies, which provide first-hand information on the cable-soil interaction behaviour, were compared with the response predicted from previous research work and also those based on current pipeline design guidelines such as ASCE (1984) to assess the applicability of those guidelines for buried power transmission cables.

To better understand the cable-soil interaction behaviour, 3D numerical models were created to simulate the longitudinal and transverse experimental test set-ups. Numerical models, with the help of parameters derived from the laboratory element testing, were calibrated and validated based on the experimental testing. A parametric study was conducted to study the effect of the cable/soil relative stiffness, the material model parameters, burial depths and cable/soil interface friction on the response of buried cables. Furthermore, numerical models were developed to study the effect of out-of-straightness in the cable on the longitudinal soil loads. An analytical procedure, verified with numerical simulation, was developed to calculate the additional axial soil loads on the buried cable with out-of-straightness.

Based on the results of experimental and numerical simulation, nonlinear longitudinal and horizontal transverse soil spring models were developed. Then, the response of buried cable subjected to the longitudinal and transverse permanent ground deformation was assessed as a

function of different ground deformation parameters. Finally, analytical procedures were also developed for the quick assessment of the response of the buried cable subjected to PGD.

Table of Contents

List of Tables

List of Figures

Acknowledgements

I would like to express my sincere appreciation to those without their support and assistance, the completion of this research would have not been possible.

Above all, I would like to thank my supervisor, Dr. Carlos Ventura, for his unconditional support. He provided me the opportunity to freely choose my path, while sharing his invaluable experience and knowledge as well as his precious time. Without his patience and positive attitude, this project could have not been completed.

I would like to thank my co-supervisor, Dr. Dharma Wijewickreme, for his sharing his experience in pipeline engineering. His endless efforts and precious feedback was a great help through the research program. His penetrating questions taught me to question more deeply.

I owe particular thanks to Dr. Janos Toth from BC-Hydro for providing the necessary cable materials and technical details promptly. His valuable comments and support was a significant help towards the completion of this thesis and in publishing technical papers on this area. Financial support provided by BC-Hydro is also gratefully acknowledged.

I offer my enduring gratitude to the faculty, staff and my fellow students at the UBC, who have inspired me to continue my work in this field. These include Mr. Harald Shrempp, Doug Smith, Bill Leung, Doug Hudniuk, Max Nazar, Scott Jackson, and John Wong. During the research program, I was grateful to get assistance from some of my fellow graduate students and undergraduate students. I would like to thank Lalinda Weerasekara, Roozbeh Chehrehpardaz, Devin Sauer, and Nazli Azimikor.

Chapter 1: Introduction

1.1 Background

With increased use of underground cables for transmission of electrical power, the performance of buried power transmission cables in areas prone to ground deformations is an important engineering consideration for the utility owners since the failure of such systems could cause property damage and business disruptions. Permanent ground deformation (PGD) might result from creeping ground, landslides, slope instability, and earthquake-induced ground movement including lateral spreading or fault movements. A large differential ground movements are able to create detrimental strains in underground cables, joints, and terminations that disrupt the operation of buried power transmission cables.

The performance of buried power transmission cables is affected by the magnitude and pattern of ground deformation, the orientation of cable with respect to ground deformation, and more importantly the cable-soil interaction behaviour. Therefore, a thorough understanding of the cable-soil interaction will form a key step in the evaluation of the response of buried power transmission cable to the ground movements.

Current knowledge on the response of buried power cables subjected to ground movement is scarce although there may be some findings from investigations performed by private entities for specific uses that are either not published and documented or cannot be generalized to other conditions. Guidelines such as ASCE (1984), PRCI (1994) and ALA(2001) provide provisions that are mainly intended for steel pipeline or polyethylene gas pipeline and their applicability to buried power cables is in enquiry for different reasons. First, the cable structure has different mechanical properties from the lifeline structure studied previously. Second, the power cables are buried in a thermal backfill material that also has different characteristics from the surrounding soil of studied lifeline so far.

1.2 Scope and Objective of the Thesis

With this background, the main objective of this research is to understand the response of buried power transmission cable subjected to ground movements. To accomplish this objective, three-phase research program was conducted to gain improved understanding of the cable-soil interaction problem.

1.2.1 Phase 1: Experimental Studies

The main goal of this phase is to provide all necessary information to evaluate the response of buried power transmission cables subjected to permanent longitudinal and transverse ground movement. In order to achieve this goal, experimental studies have been conducted with the following objectives:

- to simulate and capture the longitudinal and horizontal transverse soil loads on the buried cable;
- to identify the key parameters influencing longitudinal and transverse soil loads on buried power transmission cables;
- to compare the previously published analytical and experimental studies with the measured results and to review the applicability of the current approaches for pipeline design to the cable-soil interaction problems;
- to characterize the soil loads on the buried cable in terms of simple mathematical model.

1.2.2 Phase 2: Numerical Simulation of Cable-Soil Interaction

The controlled experimental studies in phase-1 not only will contribute to a better understanding of cable-soil interaction but also they can be used to validate and calibrate numerical models. Developing the numerical models is one of the important aspects of cable-soil characterization since the experimental studies cannot cover the full range of cases that might be encountered in practice and consequently are limited with respect to the cable diameter, length, stiffness and soil properties.

The validated numerical model with the controlled experimental studies can be employed to investigate the effects of different soils and geometric parameters affecting cable-soil interaction. In addition, the numerical simulation will allow understanding and capturing the soil-cable interaction behaviour in a fundamental manner. Therefore, the goal of numerical simulation can be summarized into the following sections:

- to investigate the nonlinear, stress-level dependent, and dilation of soil behaviour;
- to calibrate the numerical model with controlled experimental studies;
- to perform parametric studies for different cable-soil interaction scenario.

1.2.3 Phase 3: Application of Results

Although modeling the cable-soil interaction by using continuum finite elements is a better approach to analyze the cable response subjected to the ground deformation, modeling the cable-soil interaction by representing the soil as nonlinear soil springs 1) provide less computational analysis time for a buried cable subjected to hundred meters of ground deformation and 2) and are more appealing in the engineering practice. The results from 3-D finite element analyses coupled with experimental studies are used to calibrate the non-linear

springs in the longitudinal and transverse direction. The results are, then, used to assess the response of the cable network to the permanent ground deformation. The finite element program ABAQUS is employed to model the buried power transmission cables subjected to the transverse and longitudinal PGD. The goals of this phase of study can be summarized into the following sections:

- to investigate the response of buried power transmission cables subjected to transverse and longitudinal PGD and to perform parametric studies ;
- to identify the effect of ground deformation parameters on the buried cable response;
- to present closed form analytical formulations and to propose design flowcharts for assessing the behaviour of the cable subjected to longitudinal and transverse PGD.

1.3 Thesis Organization

This thesis is organized into 6 chapters and 2 appendices as follow:

Chapter 1:

In this chapter, which is this chapter, the introduction, background, scope and motivation, and organization of the thesis are discussed.

Chapter 2:

This chapter describes a review of literature on the topics that can be related to the buried cable-soil interaction such as pipe-soil interaction or anchor-soil interaction from experimental, analytical and numerical perspectives.

Chapter 3:

This chapter presents the full-scale experiment of the buried cable-soil interaction which has included the transverse and longitudinal loading of buried cables. The experimental test set-

up, test preparation, measurements, testing method, and the limitation of the experimental testing are discussed in this chapter. The results of experimental testing are compared with the previous studies and with commonly used approach in practices. The results of laboratory element testing on the thermal backfill material for numerical simulation are also presented.

Chapter 4:

In this chapter, a numerical model using the finite element code ABAQUS is developed based on the large scale test results in the axial and lateral pullout tests. A parametric study using finite element method is presented to investigate the effect of different parameters on the longitudinal and transverse soil loads on buried cable.

Chapter 5:

In this chapter, the response of the buried cable subjected to the permanent ground deformation is investigated through a numerical simulation. The effect of the ground deformation parameter on the response of buried cable is investigated. Closed-form analytical formulation is presented and validated to calculate the response for the longitudinal and transverse permanent ground deformation. Also, the methodology to calculate the response of the buried cable for the longitudinal and transverse permanent ground deformation is presented.

Chapter 6:

This chapter presents a conclusion of this research. It also describes the methodology to assess the performance of the buried power transmission cable subjected to earthquake induced permanent ground deformation. Recommendations for the future work are also provided.

Appendix A:

The detail results of axial and lateral pullout tests are presented in this chapter. The results of laboratory direct shear tests are presented here.

Appendix B:

In this section, the theory of the element type, material model, contact element, and analysis type which were used in Chapter 4 are fully presented. Most of the focus of this appendix is on the plasticity theory of Mohr-Coulomb and Drucker-Prager material models for the calibration of the soil model.

Chapter 2: Literature Review

Since limited studies on the cable-soil interaction exist the literature reviews are focused on the relevant topics such as pipe-soil interaction or the behaviour of vertical anchor. These studies are mainly divided in two categories: experimental studies and numerical/analytical studies. In each category the longitudinal and horizontal transverse soil loads are examined. Also a brief review of current guidelines for buried pipelines is included in this section.

2.1 Review of Analytical and Numerical Studies

In this section, the early approach to obtain the response of the pipeline to the horizontal transverse movements, adapted from the analytical results of the vertical anchors, piles, retaining walls, and foundations was first reviewed. Studies on the lateral response of the pipeline buried in the medium to dense material showed that that the behaviour of pipeline can be broadly categorized into the shallow and deep failure mechanisms. In shallow failure mechanisms, a passive wedge developed in the front the pipeline extends to the surface while in deep failure mechanisms the passive wedge confines in the soil (Audibert (1977)).

Rankine theory as described by Terzaghi (1946) can be used to calculate the ultimate horizontal transverse of a shallow vertical anchor plate by assuming a complete development of passive and active regions in the front and back of anchor plate respectively. Furthermore, in order to provide the vertical equilibrium due to side shear on the vertical anchor plate, Terzaghi assumed the passive wedge formed a parallel shape to the tie rod as shown in Figure 2-1. Thus ultimate resistance of anchor plate can be obtained:

$$T_u = P_p + P_s - P_a \qquad \text{Eqn. 2-1}$$

Where P_p and P_a are the Rankine passive pressure and active pressure and P_s is the side shear resistance.

Hansen (1961) developed two different models for the ultimate lateral resistance estimation of deep and shallow rigid piles. The shallow rigid piles were assumed to behaves as a retaining wall and the deep rigid piles was modeled as a strip footing at the corresponding depth. At the intermediate depth, the ultimate lateral resistance was measured by an empirical interpolation function. Furthermore, the analytical model for piles was assumed to be vertically restrained and only horizontal equilibrium was satisfied. This assumption results in overestimation of calculation of ultimate lateral resistance in case that buried structure tend to rise upward. Hansen used a composite rupture zone in front of anchor plate consisting of a straight line starting from the base of the anchor in combination with a Rankine and logarithmic spiral Prandtl zone as shown in Figure 2-2. Hansen analytical model was adopted by Audibert (1977) to predict transverse soil restraints on buried pipeline.

Ovesen (1964) adopted a failure rupture plane for a vertical anchor plate as proposed by Hansen. Unlike Hanson analytical model, his formulation accounted for both vertical and horizontal force equilibrium. The results of this analysis were summarized as earth pressure coefficients on design charts. Later Trautmann and O'Rourke (1983) adapted a model developed by Ovsen to buried pipeline problems.

Rowe and Davis (1982) investigated the behaviour of thin and rigid anchor plates with horizontal and vertical axis in cohesion less soil. Their investigations were based on the numerical simulation of elasto-plastic finite element analysis. The soil behaviour was assumed to have a Mohr-Coulomb failure criterion and either an associated flow rule or non-associated flow rules were considered. The effects of friction angle (ϕ), the dilation angle (ψ), anchor embedment, and the initial stress state were considered. They proposed an expression that anchor plate capacity can be derived from a basic anchor capacity with a number of modification factors as expressed by Eqn.2-2.

$$F' \approx F.R_k.R_\psi.R_R \qquad \text{Eqn. 2-2}$$

The basic anchor capacity (F) was defined for the case of smooth anchor in nondilatant soil ($\psi=0$) and with coefficient of earth pressure at rest $k_0=1$. The basic anchor capacity can then

be corrected by R_k, R_φ, R_R for the effects of initial stress state, soil dilatancy (ψ) , and anchor roughness respectively. They observed that the dilation angle had a significant effect on the ultimate capacity while the effect of the coefficient of the soil at rest for typical value of $.4 < K_0 < 1$ on the anchor capacity is less than 10%. Furthermore, the effect of roughness on the collapse capacity of anchor plate with vertical axis is negligible. However, its effect on the anchor with horizontal axis in shallow depth is significantly influenced. Finally, their studies included graphs and tables of the anchor capacity in different conditions.

Hsu et al. (1996) estimated the transverse soil restraint on the pipeline buried in loose sand by adopting the approach for vertical anchor plate. They replaced the pipeline with the virtual vertical anchor plate placed at the pipeline centerline with the height equal to pipeline diameter. They assumed a planar sliding surface at the front of the pipeline and they used an implicit limiting equilibrium to calculate the lateral soil restraint on the pipeline. Trial sliding surfaces with different angle were examined. Horizontal and vertical equilibrium of forces on the soil wedge were formulated along with the constraint that the minimum soil restraint must be achieved as shown in Figure 2-3. The forces in soil wedge are as follows; R_1 is the resultant of active earth pressure on the soil wedge, W is the weight of soil wedge, R_2 is the resultant of shear and normal force on the trial sliding surface with angle of θ, and P_u is the lateral soil restraint.

Popescu et al. (2002) carried out a number of full scale experiments of pipe-soil interaction at Center for Cold Oceans Resources Engineering (C-CORE). The tests consisted of 24 full-scale tests of axial and lateral loading tests using rigid pipeline and 3 tests of moment bending using a flexible pipe. The outer diameter and the length of the pipe for lateral loading was 0.328 m and 3 m respectively, and the outer diameter, the wall thickness and the length of the pipe for moment bending test was 0.203 m, 3.175 mm and 5.8 m respectively. Lateral and axial soil-pipeline interaction tests were conducted on pipeline buried in the dense/loose sand with the minimum void ratio of 0.47 and maximum void ratio of 0.84, and in kaolin clay with 37 kPa and 19 kPa at compacted water content of 37% and 33% respectively. The average shear wave velocity was measured to be 199 m/s in firm clay and

167 m/s in the soft clay. Based on their experimental tests, they observed that the failure mechanism in loose sand was local punching failure and the failure mechanism in the dense sand was a general shear failure. Numerical model using ABAQUS/Standard was validated and calibrated based on the experimental studies. In their numerical models, the modified Cam-Clay (MCC) model and non-associated Mohr-Coulomb (NAMC) model were used for clay and for sand respectively. The details of the parameter calibration for MCC model can be found in Popescu et al. (1999). The details of the parameter calibration for NAMC model can be found in Nobahar et al. (2001) and Popescu et al. (2001). Based on their numerical analysis, they concluded that their model can satisfactory simulate their experimental tests.

Popescu and Nobahar (2003) conducted 3D finite element analysis of pipe-soil interaction to see the effect of ground water effects. To calibrate and verify their numerical model, they used the results of lateral tests performed by Hurley and Phillips (1999). Hurley and Philips (1999) used dry dense material with a relative density of 95% and the density of 1984 kg/m^3 and submerged sand with the relative density of 66% and the density of 1864 kg/m^3. Hurley and Phillips observed that 60 % reduction in the peak forces occurred due to saturation. Popescu and Nobahar (2003) used the finite element code ABAQUS in their numerical study. Sand materials were modelled using an extended Mohr-Coulomb model with the apparent friction angle and cohesion. The friction angle for the dense sand was reported 53 degrees. Since they believe that the larger friction angle is often attributed to apparent cohesion and interlocking, they limited the friction angle to 44 degrees with an equivalent cohesion to compensate the larger friction angle using expressions developed by Craig (1987) in the *p*-*q* plane as

$$\tan(\alpha) = \sin(\phi)$$

$$c = \frac{a}{\cos\phi} \qquad \text{Eqn. 2-3}$$

in which ϕ and c are the friction angle and cohesion , α and a are the modified shear strength parameters. For their numerical studies, α=34.8˚ and a=7.23 kPa were calculated. The

dilation angle,ψ, was estimated using Rowe (1962) expression as a function of constant volume friction angle (ϕ_{cv})

$$\sin\psi = \frac{\sin\phi - \sin\phi_{cv}}{1 - \sin\phi\sin\phi_{cv}} \qquad \text{Eqn. 2-4}$$

The elastic modulus and soil poison's ratio were selected as 9000 kPa and 0.33 (Popescu 2001). The friction coefficient at soil/pipe interface was $\mu=tan(0.6\varphi)=0.5$ was used. For the saturated sand with relative density of 65 %, the peak friction angle was reduced to 41 degrees and due to the presence of water the smaller cohesion c=2.5 kPa were used in the analysis. The soil elastic modulus was reduced based on the effective stress at the pipeline level according to Lambe and Whitman (1969)

$$E \propto (\sigma')^{0.5} = 6650kPa \qquad \text{Eqn. 2-5}$$

Although the results of their numerical simulation agree well with experimental data, the introduction of the apparent cohesion to compensate the large dilation angle is unjustified. Since dilation occurs in the dense material, the large friction angle can be better compensated by definition a dilation angle (ψ).

Guo and Stolle (2005) used a two-dimensional plane strain finite element to investigate the lateral pipe-soil interaction in sand. They used ABAQUS finite element program for the numerical simulation. In their finite element analyses, the effects of pipe diameter (size effect), model scale, stress level, and soil properties were studied through a parametric study. Two types of constitutive models are used for soil: a classical elasto-perfectly plasticity model with constant dilation angle and an elasto-plastic hardening model. Their results showed that the pipe responses are not sensitive to the hardening model. Their study on the soil dilatancy shows that it increases the horizontal bearing capacity factor (N_h). Their analysis showed that the effect of dilatancy on N_h can be described by

$$N_h(\psi) = R_\psi . N_h(\psi = 0) \qquad \text{Eqn. 2-6}$$

in which $N_h(\psi)$ is the horizontal bearing capacity for the soil with dilation angle (ψ) and R_ψ is the dilation factor described as

$$R_\psi = 1 + 0.23(1 + 0.24\frac{H}{D})\sin\psi \qquad \text{Eqn. 2-7}$$

By proportionally varying H and D, the scale effects were investigated to study the validity of the small scale model test to full-scale in situ pipeline. Based on a parametric study, the variation of horizontal force factor N_h with respect to reference horizontal force factor N_{h0}, defined for the pipe with diameter of D_0=0.33 m and H_0/D_0=2.85, was established as

$$\frac{N_h}{N_{h0}} = 0.91(1 + \frac{1}{10s_m}), \quad s_m = \frac{D}{D_0} = \frac{H}{H_0} \qquad \text{Eqn. 2-8-a,b}$$

2.2 Review of Experimental Research Studies

The early experimental study on pipeline dates back to the research by Audibert and Nyman (1977). Audibert and Nyman studied the performance of conduits buried in both loose and dense air-dried Carver sand. Three sizes of conduits with diameter of 25, 60, and 111 (mm) were selected. Each pipe was buried at different embedment ratios to study the effect of burial depth. The limited size of testing apparatus just allowed the burial depth of up to 50 cm. The embedment ratios considered in their tests were 1, 3, 6, 12, and 24 for small diameter conduits and 1 and 2 for large diameter conduits. These testing arrangements helped them to 1) quantify the influence of embedment depth, pipe diameter, and soil density 2) find an analytical expression for pipe-soil interaction behaviour. Based on their experimental results, the rectangular hyperbolic curves were presented to simulate the pipe soil interaction (p-y curve). The p-y curves were expressed as non-dimensional parameters relating the normalized force ($\bar{P}$) with normalized displacement ($\bar{y}$) as depicted by Eqn.2-9.

$$\bar{p} = \frac{\bar{y}}{0.145 + 0.855\bar{y}} \qquad \text{Eqn. 2-9}$$

in which $\bar{P}$ and $\bar{y}$ are the normalized parameters defined as

$$\bar{p} = \frac{p}{p_u} \quad \text{and} \quad \bar{y} = \frac{y}{y_u} \qquad \text{Eqn. 2-10}$$

y_u is the displacement where the maximum soil restraint (p_u) is mobilized. Their experimental results showed a similar failure mechanism to those observed by Brinch Hansen (1961) model footing tests. In addition, the ultimate soil resistances of buried pipes were shown that they were in a good agreement with the Hanson studies. Hanson ultimate load bearing capacity is expressed by:

$$q_u = \gamma Z N_q \qquad \text{Eqn. 2-11}$$

Where γ is the unit weight of soil , Z is the depth to the center of pipe and N_q is the bearing capacity factor. The bearing capacity factor was expressed as a function of internal friction angle (ϕ) and the normalized depth to pipe diameter ratio. Figure 2-4 showed the variation of *Nq* versus *Z/D* as adapted by Audibert.

Trautmann and O'Rourke (1985) studied the response of buried pipes to lateral ground movements through experimental investigations. Two pipe sizes with diameter of 102-mm and 324-mm were tested in buried Cornell filter sands at five burial depth ratios of 1.5, 3.5, 5.5, 8, and 11. To observe the effect of the soil density, three different densities of 14.8, 16.4, and 17.7 kN/m^3 were prepared to simulate the condition of compact, medium, and loose sands. The effect of several parameters including pipe burial depth, soil density, pipe roughness, and pipe diameter were evaluated. The test data were presented as a non-dimensional force (N_h) versus a non-dimensional displacement (*Y/D*). The test results were compared by other experimental and analytical studies which were mainly on the vertical anchor or pile due to lateral movements. They observed that the Hansen (1961) theoretical results overestimate the maximum restraint force by 150- 200% while Ovesen (1964) and Rowe and Davis (1982) agree closely with their experimental test results. They argue that the discrepancy between the results obtained by Hansen and their results is due to the assumption regarding full vertical restraint. Hanson theoretical model was based on vertical restraint and

horizontal mobilization while the Ovsen model was accounted for vertical equilibrium. The force-displacement relationships were modeled by a two constant rectangle hyperbola as expressed by Eqn. 2-6.

$$F'' = \frac{Y''}{0.17 + 0.83Y''} \qquad \text{Eqn. 2-12}$$

in which $F'' = (F / \gamma HDL) / N_h ; Y'' = (Y / D) / (Y_f / D)$; Y= the displacement measurement; and F= the force measurement at each Y. They suggested that force-displacement curve for any combination of pipe burial depth and soil friction angle can be obtained by properly estimating the N_h value and Y_f / D ratio. For application purposes, they presented a plot for calculating the N_h value as a function of embedment ratio (H/D) and friction angle (ϕ) as shown in Figure 2-5.

Hsu (1994) conducted 120 tests on pipes buried in local sand from the Da-Du riverbed in Taiwan. The large-scale drag box of 1.83 × 1.83× 1.22 m^3 was utilized to investigate the effect of soil densities, burial depths, pipe diameter and relative velocity of pullout force on the pipe lateral soil restraints. He used pipes with outside diameters of 38 mm up to 229 mm. The results of dimensionless lateral soil restraints for different burial depth and pipe diameter positioned between the experimental studies by Audibert et al (1977) and Trautmann (1985). In addition, he observed that increasing the pullout rate leads to increase in the maximum lateral soil restraint. However, he concluded that this increase is not significant, for instance increasing the pullout rate 10 times leads to increase in maximum soil restraints less than 5%. Also, he presented a power law relationship to correlate the pullout rate with the maximum soil restraint. In his continuation of his study, Hsu (1996) studied the soil restraint on the oblique pipeline in loose sand with internal friction angle of 33 and average density of 15.20 kN/m^3 in the same chamber as described above. Pipe diameters of 38.1, 76.2, 152.4, and 228.6 mm with normalized burial depth of 1.5 and 3.5 were tested with inclination angle between 0 to 90 degrees with angular increment of 10 degrees. He observed that maximum lateral soil restraints and corresponding displacements increase as the oblique angle increases. The maximum soil restraints show a power law relationship with the pullout

velocity rate. He also presented a force-displacement relationship as two constant hyperbolic as described by Eqn.2-13. The constant value *a* and *b* are given as the function of oblique angle. Based on his observation, the constant value *a* increases while the constant *b* decreases with oblique angle respectively.

$$F'' = \frac{Y''}{a + bY''} \qquad \text{Eqn. 2-13}$$

Hsu et al (2006) studied the soil restraints on the oblique movement of 0.61 (m) long steel pipes with diameters of 152.4, 228.6, and 304.8 buried in dense sand. They showed that the longitudinal and transverse soil restraint of the oblique pipes can be obtained by measuring the longitudinal soil restraint of axial pipeline and transverse soil restraint of lateral pipeline and calculating their corresponding values in the direction of pipes by multiplying the cosine and sine value of oblique angle respectively. Furthermore, they also observed that the dimensionless longitudinal and transverse ultimate forces are independent of the pipe diameters up to 304.8 mm. Figure 2-6 shows the longitudinal and transverse soil restraints for oblique pipe with the angle of α as described by Hsu.

Pauline et al (1997) performed large-scale testing on buried pipelines performed at the Center for Cold Oceans Resources Engineering (C-CORE) at the Memorial University of Newfoundland, St. John's, Newfoundland, Canada in the mid-1990's on steel pipe with outside diameter of 324 (mm). They used the experimental results to calibrate their numerical simulation. Popescu et al (1999) and Popesue et al (2002) used the same facility at C-CORE to study the pipe-soil interaction behaviour.

Anderson (2004) studied the Polyethylene (PE) gas pipelines at the University of British Columbia research facilities. He investigated a longitudinal soil restraints on the straight and branch PE pipes with diameter of 60 mm and 114 mm buried in loose and dense Fraser River Sand. He observed that the longitudinal soil restraints on PE pipes buried in loose sand were over predicted by ASCE (1985), ALA (2001) and PRCI (2004) while the results in dense sand showed that they were over predicted by those guidelines. However, the author made a

limited comment about the effect of normal stress on pipe, or coefficient of lateral earth pressure (K).

Turner (2004) investigated the effect of moisture content on the lateral soil restraints on buried steel pipes with external diameter of 119 mm. He used the same facility at Cornell University and used Cornell sand as a testing material with burial depth ranging from 6 to 20 diameters. He observed that the maximum lateral soil restraint in moist sand is approximately twice the value generated under dry sand condition. He argued that the failure pattern in dry sand conditions show the distinct regions of heave and subsidence while the soil deformation pattern in moist sand conditions show a mass movement of soil which is pushed forward and up. Based on his research, a series of new curves were presented compatible with the work by Trautmann and O' Rourke (1985) as shown in Figure 2-7. Furthermore, the tests results on sand with 4 % and 8 % moisture contents show load displacement curve, that the maximum soil restraint and their corresponding displacement are almost identical.

Karimian (2006) performed a series of experimental studies at the University of British Columbia Facilities on relatively large steel pipe to assess the longitudinal and transverse soil restraints. The steel pipes with outside diameter 18-in buried in the Fraser River Sand were tested. The axial pullout tests were conducted in loose and dense sand with the average density of 1430 kg/m^3 to 1600 kg/m^3 respectively with less than 1 % moisture content. The lateral pullout tests were performed on dense sand with 1% up to 10 % moisture content. He observed that the longitudinal soil restraint in the case of loose sand were comparable with the results of ASCE (1984) guidelines. However, the longitudinal soil restraints in the case of dense sand were much higher, approximately three times greater, than recommended value by ASCE guideline. By monitoring the normal soil stresses on the pipe surface during axial pullout test, numerical simulations were calibrated to investigate the effect of different parameters on the coefficient of earth pressure at rest (K). In his numerical studies the effect of soil dilation at the interface with parameters such as burial depth, pipe diameter and soil parameters were investigated. His studies showed that, first, the effect of soil dilation is higher for small diameter pipes. Second, the effect of soil dilation is higher for shallow burial

depth. Furthermore, he showed that the use of two-layers of geotextile wrapping provides an effective means of reducing axial loads on pipelines.

Weerasekara (2007) studied the performance of buried MDPE (medium-density polyethylene) natural gas pipeline subjected to ground displacements. The large scale facility test at University of British Columbia was used to investigate the longitudinal and transverse soil restraints on PE pipes of diameter 60 mm and 114 mm buried in Fraser River Sand with burial depth equal to 60 cm. He observed that that the axial pullout of PE pipes were significantly affected by the flexibility of PE pipes. The analytical closed-form formulations were provided for the longitudinal response of PE pipes that can adequately capture the experimental response. The developed frictional force resistance along per unit length of the pipe was expressed by:

$$T = \pi D H \gamma \psi \qquad \text{Eqn. 2-14}$$

in which D, H , and γ are the pipe diameter, the burial depth, and the soil density. Parameter ψ was defined as a function of the relative displacement between pipe and surrounding soil. Basically, the parameter ψ replaced the expression $0.5(1+k)\tan\delta$, which is used in guideline such as ASCE (1984), ALA (2001), or Honegger and Nyman (2004), to include the effect of normal stresses and the interface friction angle. Three-stage interaction model was proposed for the parameter ψ. In obtaining the parameter ψ, the results from a number of direct shear tests which were conducted by O'Rourke et al. (1990) on the mobilized interface friction angle (δ) and also the experimental results which were conducted by Karimian (2006) on the K value were used. The value for the interface friction angle is assumed to be 20˚. The K value of 2.4 and K value of 1.4 were selected for a pipe with the diameter of 60 and 114 mm pipe when the displacement was about 500 mm (region I and II) and they were degraded to the value of 1.9 and 0.9 for the diameter of 60 and 114 mm pipe (region III). It should be mentioned that K value for the P.E. Pipes were selected smaller than the steel pipe due to the smoother surface leading to a lesser amount of dilation. The more detail of his studies can be found in Weerasekara and Wijewickreme (2008).

Wijewickreme and Karimian (2009) studied the response of buried steel pipelines subjected to relative axial soil movement. Their study was based on the results of axial full-scale testing conducted by Karimain (2006). They reported that measured axial soil loads on the pipeline buried in loose material are comparable to those obtained by commonly used guideline (ASCE 1984). However, they observed that the axial soil loads on the pipeline buried in the dense material are almost two times higher than those predicted by commonly used guideline. With the help of pressure transducers mounted around the buried pipeline, they monitor the variation of the soil pressure on the pipeline during the axial pullout tests. They observed that the soil pressure undertaken during axial pullout testing of the pipeline buried in the dense material was higher than the initial values due to the constrained dilation during shear deformation. The plane strain numerical models were developed in the FLAC 2D program to study the effect of the dilation on the axial soil loads on the pipeline. In order to analytically model the dilation around the pipeline, they expanded the pipeline radially by the same thickness of a shear zone during axial pullout test as depicted in Figure 2-8 . The thickness of shear zone was measured by monitoring the movement of colored sand placed in the vicinity of the pipe. Observation showed that a annular zone with thickness of 1.2 to 2.8 mm was affected during axial pullout testing. The validated numerical models were used to obtain the equivalent lateral earth pressure (k) for different soil dilation levels, pipe diameter and burial depth, which can be used to determine the soil loads on the pipeline.

2.3 Summary of Literature Review

The review of literature shows that significant amount of studies have been conducted on the pipe-soil interaction either from numerical simulation or experimental testing perspectives. However, to the author's knowledge, most of studies were undertaken on the steel and polyethylene gas or water pipeline system, and current understanding on the response of the buried power transmission cable to the ground movement is incomplete and the applicability of the current guideline such as ASCE (1984) is in question since the cable structure has a different mechanical properties from the lifelines structure studied previously. Secondly, the

power cables are buried in a thermal backfill material that also has different characteristics from the surrounding soil of studied lifeline so far. In recognition of those needs, a three-phase study was conducted. The next following chapters describe in details the methodology and the results of this study.

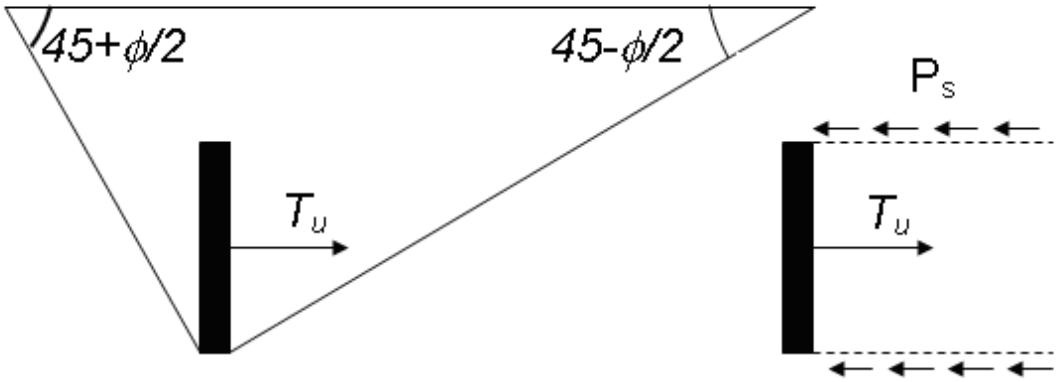

Figure 2-1 : Failure pattern in vertical anchor plate as assumed by Terzaghi.

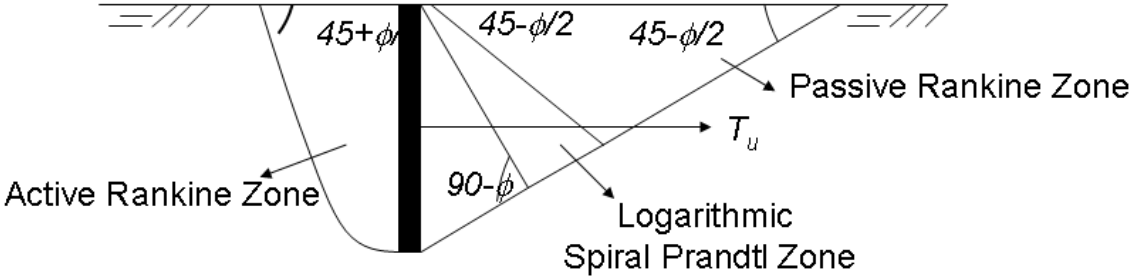

Figure 2-2: The failure pattern as described by Hansen(1961)

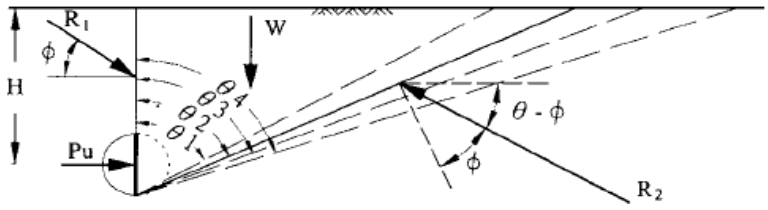

Figure 2-3: The approach by Hus for estimation of the horizontal transverse soil restraint

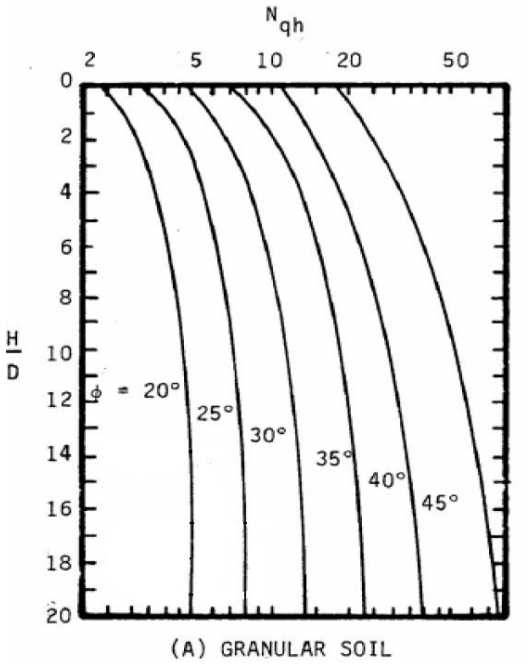

Figure 2-4: Variation of bearing capacity factor (*Nq*) as a function of (H/D) developed by Hansen (1961) and adopted by Audibert (1971)

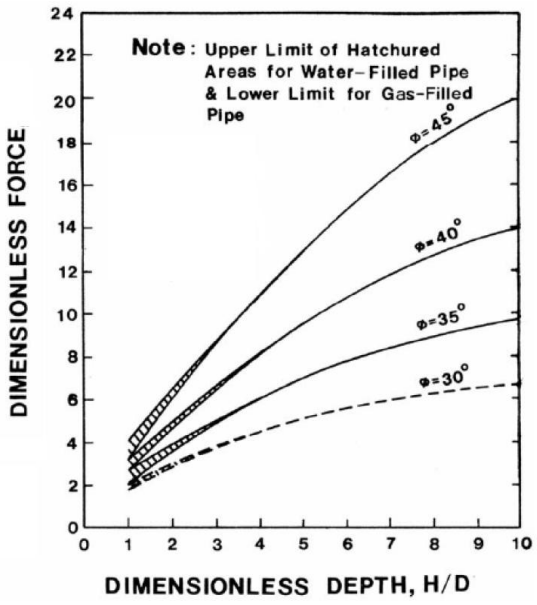

Figure 2-5: Horizontal bearing capacity as a function of friction angle and embedment depth ratio developed by Ovesen(1961) and adopted by Trautmann (1983)

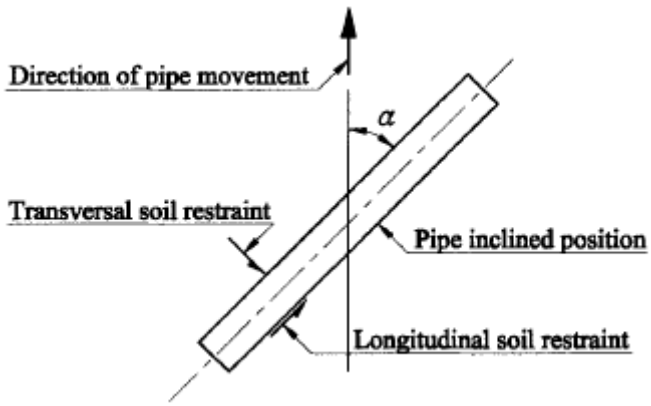

Figure 2-6: Schematic view of pipeline with oblique angle α

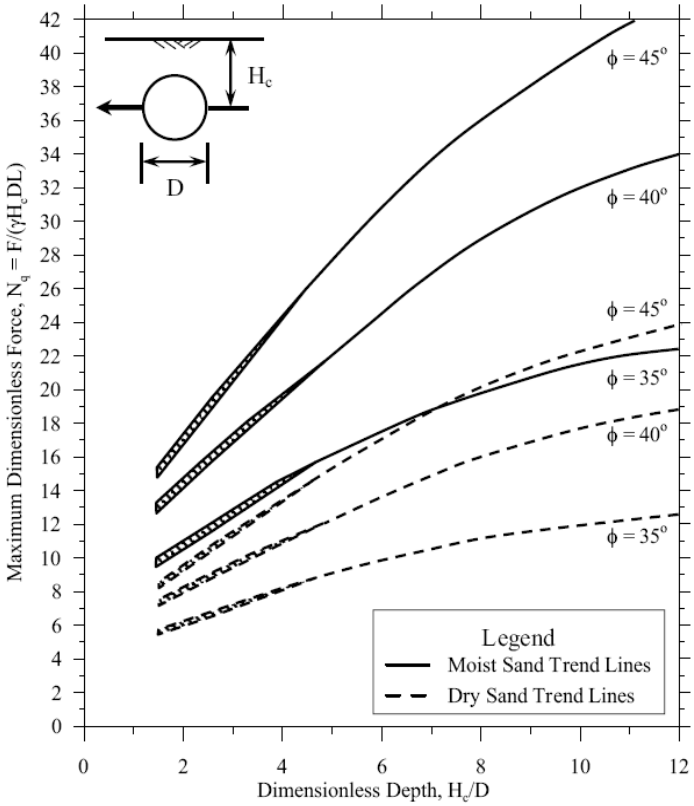

Figure 2-7: Horizontal bearing capacity of buried pipes for dry and moist sands as a function of embedment ratio and friction angle developed by Turner (2004)

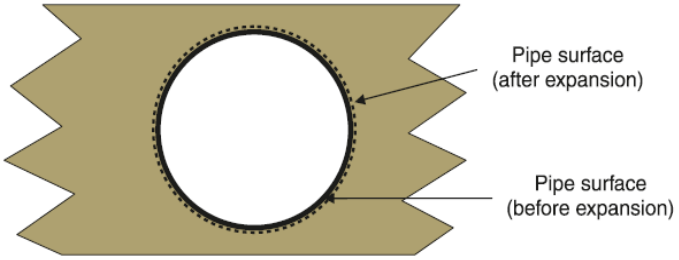

Figure 2-8: The analytical modeling of dilation effect, after Wijewickreme et al. (2009).

Chapter 3: Experimental Study

In this chapter, experimental studies on the buried power transmission cables subjected to ground movements will be described. The first part of this chapter consists of experimental modeling aspects which include the experimental setup, methodology, measurements, and limitations. The second part of chapter describes the results of experimental studies and discussions.

3.1 Physical Modeling Aspects

Depending on the direction of the relative movement between buried cable and soil, four modes of soil loads on the buried cable can be distinguished as shown in

Figure 3-1: 1) longitudinal, 2) horizontal transverse, 3) vertical bearing, and 4) vertical uplift (ASCE 1984). In this experimental research, the differential ground movements are imposed independently in the longitudinal and horizontal transverse directions to the cable alignment to characterize the cable-soil interaction. A total of 15 axial pullout tests and 10 lateral pullout tests were conducted to simulate the longitudinal and horizontal transverse soil loads on cables respectively with different burial depths using the experimental facility at the University of British Columbia. The results from controlled experimental studies contribute to developing a reliable database for developing and validating numerical models to capture the response of buried cables under general field loading conditions.

This chapter presents the full-scale experimental studies to characterize the longitudinal and horizontal transverse soil loads on the cable. The experimental test set-up, test preparation, measurements, testing method, and the limitation of the experimental testing are discussed in this chapter. The results of experimental testing are compared with the previous studies and with commonly used approach in practices.

3.1.1 Review of Materials Tested

3.1.1.1 Thermal Backfill Material

The cables for pullout testing were buried in a specially prepared backfill soil (called "thermal backfill"). The backfill material is identical to that commonly used in the field installations by BC-Hydro. The material was supplied by Lafarge from Pitt-River Quarries in Pitt, Meadows, B.C.. The results of trace metal analysis on this material, conducted by SOILCON Laboratories Ltd, Richmond, B.C. is given in Table 3-1, and the units are in micrograms per gram.

Grain size distributions obtained from particle size analysis of the thermal backfill are shown in Figure 3-2. The envelope (limits) of grain size distribution as specified by BCTC for their field applications is overlain in Figure 3-2 for comparison; as may be noted, the grain size distribution of thermal backfill material used for testing is well within the allowable limits specified by BCTC. The particle sizes D_{10}, D_{30}, D_{50}, and D_{60} are 0.09, 0.5, 1.51 and 2.2 mm respectively. The coefficient of uniformity (C_u) and the coefficient of curvature (C_c) are 24 and 1.3 respectively; the thermal backfill material can be classified as well-graded coarse material with little fines.

The compaction characteristics of thermal backfill were assessed by means of a Modified Proctor test. Figure 3-3 shows the dry density-water content relationship. The optimum water content (w_{opt}) at which the maximum dry density of γ_{dry} =21.7 kN/m^3 (2.17 g/cm^3) can be achieved is 6.7%.

3.1.1.2 Power Transmission Cable

The power transmission cables for testing were provided by BCTC. The cables can be described as smooth aluminum-sheath oil-filled type. The cable consists of a jacket, aluminum sheath, insulation, and conductor. A typical cross section of the power

transmission cable is shown in Figure 3-4. The jacket protects the cable from environmental effects and external loads. An aluminum sheath is placed between the jacket and insulation. It is understood that the purpose of this sheath is to reduce the electromagnetic effect arising from the conductors during power transmission and also to keep the internal configuration of the cable intact. A layer of insulation paper is present between the inner conductors and aluminum sheath. The inner core of the cable is comprised of inner conductors, which are standard helically-bundled copper wires. The transmission cable is designed to operate at 230 kV.

3.1.2 Characterization of Key Properties of Tested Material

3.1.2.1 Characterization of Shear Response of Thermal Backfill Material

Since the thermal backfill is a specially prepared crushed rock material, it was considered important to have material-specific strength parameters (friction angles) for the interpretation of the results from buried cable-soil interaction pullout testing and numerical simulations. Considering the particle size and high angularity, it was judged reasonable to use the direct shear apparatus to obtain the shear strength parameters.

A series of conventional direct shear tests, as described in more detail in Lamb (1991), were conducted. The tests were performed on both the dry and moist thermal backfill with water content (*w)* of about 4 % (Note: this moisture content is comparable to the water content of the thermal backfill used in full scale testing).

The dry thermal backfill were prepared at three different density levels: dense (with specimen density of 17.9 kN/m^3), medium dense (density of 16 kN/m^3), and the loose (density of 13.9 kN/m^3). It should be mentioned that the limited size of the direct shear test apparatus and the high angularity of thermal backfill material prevents preparing a high density specimen due to the possibility of crushing thermal backfill material. After performing sieve test to measure the crushability of specimen after each direct shear test, it was concluded to prepare the specimen at three levels of densities. The dense specimens

were prepared by placing thermal backfill in lifts of 20 mm in the shear box and compacting each layer with a square-shaped wooden tamper. During preparing specimen, it was noticed that although same preparing methods used two levels of densities, which were called dense and medium, were created. The small size of direct shear test and the large particle size of thermal backfill material causes the variation in the density. Since density affects the friction angle, the higher density corresponds to dense specimen and a level lower than the dense material refers to medium density. The loose thermal backfill material was prepared by pouring it evenly through a funnel and from a drop height of about 15 to 20 mm. The vertical loads were selected in such a way that they could cover the range of anticipated stress levels (6 kPa to 50 kPa) in the soil adjacent to the cables under typical burial depths. The dense specimen under moist conditions was also prepared following essentially the same approach as that used for the preparation of the dry material. After placement, the moist specimen was kept undisturbed for 24 hours in the direct shear box prior to being sheared to simulate the condition of the experimental studies.

Figure 3-5 and Figure 3-6 present typical plots of normalized shear stress versus horizontal shear displacement, and vertical normal displacement versus horizontal shear displacement observed during direct shear testing of dry thermal backfill. As can be seen, dense and medium dense thermal backfill specimens exhibit a peak shear resistance followed by a progressive reduction in shear resistance as interlocking is overcome up to the point of shear failure. The measured peak shear force vs. normal forces from the test on dry thermal backfill is shown in Figure 3-7. The estimated average peak friction angles (ϕ'_{max}) for the three soil density conditions (dense, medium dense, and loose) are about 59°, 53°, and 44°, respectively. The observed relatively high value of peak friction is attributable to the excess energy required to overcome (dilation) the interlocking between particles and rearrangement of particles in this very angular material made of crushed rock. The shear stress versus normal stress observed at large shear strains for these tests is depicted in Figure 3-8. The large–strain friction angle at ultimate state (ϕ'_{cv}) appears to be about 42°, which is close to the peak friction angle obtained for the loose material as expected.

The results from direct shear tests conducted on dense thermal backfill under moist conditions (w = 4%) are shown in Figure 3-9 and Figure 3-10 for two levels of vertical stress (19.3 kPa and 32.7 kPa). The results obtained from the testing of the dry thermal backfill are also overlain in the same graph for comparison. Although the moist thermal backfill seems to offer a slightly higher resistance in the test conducted under a low stress level, generally speaking, the shear strength characteristics of the moist thermal backfill seems to be similar to those derived from tests conducted under dry conditions.

3.1.2.2 Characterization of Shear Response of Thermal Backfill-Cable Interface

Direct shear testing was also undertaken to determine the interface frictional characteristics between the thermal backfill material and buried cable. A square coupon of the cable's outer layer was cut out and prepared for this purpose. The coupon was trimmed so that it would exactly fit the bottom part of the direct shear box (76 mm by 76 mm). The coupon was positioned in the shear box so that its surface was flush with the bottom edges of the direct shear box. The crushed stone was placed on top of the coupon using the same sample preparation as described in the direct shear test on crushed stone. The tests were performed in two density levels, medium dense and dense thermal backfill material with 16 kN/m^3 and 17.9 kN/m^3, respectively.

The measured peak shear stress vs. vertical stress obtained for medium and dense thermal backfill during interface testing is shown in Figure 3-11. Also shown in this figure are the data for these tests at large displacement levels. As may be noted, the average peak interface friction angle for dense and medium thermal backfill are about 38° and 33°, respectively. The average interface friction angle at large strain levels was taken as 29°. Based on this, the interface friction factor ($f = \delta/\phi$) would be about 0.64.

3.1.2.3 Characterization of Cable Mechanical Properties

Two cable types as shown in Figure 3-4, namely type C1 and type C2 were used in the experimental studies. The Type C1 cable has 900 kcmil copper conductors with an overall diameter of 89 mm (3.5 inches), and the Type C2 cable is 1500 kcmil copper conductors with an overall diameter of 100 mm (4 inches). The cable Type C1 was used throughout axial pullout tests, and Type C2 was used for lateral pullout testing.

In order to obtain the mechanical characteristics of the power transmission cable, two sets of the tests were conducted. An axial compression test was carried out to determine the axial elastic properties and axial yield strength of the composite cable. The axial compression test was conducted by using Baldwin 60,000 lb Universal Testing Machine at the UBC structural laboratory. The tested cable sample was prepared by trimming to provide a length to diameter ratio of 2.5. This ratio was considered suitable in order to mobilize compressive strength with minimal effect from end platens, while minimizing the opportunity for buckling failure of the specimen. The test set up is shown in Figure 3-12. The force-displacement curve for a power transmission cable is shown in Figure 3-13.

The flexural properties of buried cable were obtained by performing standard three-point-bending test. Figure 3-14 shows the three point bending test set up. Power transmission cable was cut to fit between the two supports of the apparatus. The clear distance between the two supports were 780 mm, and they restrain vertical and out of plane movements. A displacement-controlled movement was applied at the midpoint of the cable. The required force and corresponding displacement were measured. Figure 3-15 shows the force-displacement curve of the buried transmission cable.

3.1.3 Experimental Apparatus

The physical full-scale model pullout testing to study the subject buried cable-soil interaction was undertaken at the large soil chamber at the University of British Columbia. The device has been already utilized to study the pipe-soil interaction effects in buried steel and polyethylene pipelines (Wijewickreme et al. 2009; Wijewickreme and Weerasekara 2007). The testing apparatus was modified to enable buried cable-soil interaction studies. The details of testing chamber, loading apparatus, sample preparation, and instrumentation are briefly described in the following sections. Additional details of the testing apparatus can be found in Anderson (2004) and Karimian (2006).

3.1.3.1 Testing Chamber

As noted by Anderson (2004), the dimensions of the soil testing chamber were selected to satisfy the following criteria:

- the width and the length of the soil chamber must be adequate enough to allow the full development of the active and passive soil wedges during lateral pullout testing;
- the chamber must have reasonable dimensions so that the effects of side and end walls on the soil deformation during axial pullout test would be minimized, and
- the chamber height must be selected in relationship to its length, since a deeper burial depth would require a longer chamber dimension during lateral pullout testing.

Based on the numerical simulations and classical soil wedge considerations, the final dimensions of the testing chamber were chosen as 3.8 m (length), 2.5 m (width) , and 2.5 m (height).

Figure 3-16 shows a photograph depicting the overall dimensions of the testing chamber. As may be noted, the walls of the testing chamber are made of plywood (with thickness of 19 mm) and restrained/stiffened by timber beams (90×140 mm), placed at every 300 mm. The wall system is supported by modular steel frames consisting of W150×37 sections, placed at every 1.2 m dimension intervals along the four sides of the chamber. In the upright part of the modular, steel frames are buttressed by a diagonal HSS 89×89×3.8 element welded to the base plate, which are then bolted to the concrete strong-floor of the structures laboratory. Furthermore, the interior of the plywood walls are lined with smooth stainless steel sheets to minimize potential side friction between the wall and the soil backfill.

3.1.3.2 Loading Mechanism

3.1.3.2.1 Loading apparatus

The loading apparatus consists of two hydraulic actuators which can apply loads in a displacement-controlled manner. The system has two double-acting hydraulic actuators, each having a capacity of 418 kN (93 kips), with a digital hydraulic control system. The actuator has a flexibility of applying different displacement rates. The displacement capacity of actuator is limited to 600 mm. The hydraulic power is provided by an in-house hydraulic system with the maximum oil flow capacity of 75 lit/min. The actuators are trunnion-mounted to the pedestal which is bolted to the strong floor. This arrangement positions the height of the actuator axis at 700 mm above the strong floor level.

- The control system of the hydraulic cylinders consists of the following components:
- Delta RMC controller, model RMC100-S2-ENET;
- Synchronous serial interface (SSI) module and Temposonic position sensor, and
- PQ Servo-Proportional Valve Controller.

RMCWIN, a powerful motion controller software, is used to drive the RMC controller. It allows the user to setup, configure, and control the motion of several axes. Command values such as displacement or displacement rates are given in the RMC software. The signal is then sent to servo valve via RMC controller to adjust the valve opening to control the amount of oil flow. The SSI module with Temposonic position transducer probes the actual position of the actuator and sends feedback to the controller until the actual position and target position are equal. Furthermore, SSI unit enables the synchronization of more than one axis when they are operated at the same time, which is an important consideration in lateral pullout tests. Figure 3-17 shows the schematic figure of the control system.

3.1.3.2.2 Coupling system

The main clamping mechanism connecting the load cell to buried cable in axial pullout test consists of two split-metal-collar pieces. When bolted together these split-collars form a hollow cylinder with the diameter smaller than buried cables (89 mm) and with the length of 25 cm. The two halves were bolted around the buried cable with three equally spaced clamping bolts at each side as shown in Figure 3-18. The inner parts of the coupling were thread-marked to increase the friction and essentially prevent any possibility of the buried cable sliding out from the coupling during testing.

The coupling system for lateral pullout tests consists of four parts: the end clamps at each end of the buried cables, connecting steel cables, shackles, and the couplings at each end of the actuators. The end clamps have a very similar structure to the coupling system in the axial pullout test. They comprise of two-split-metal collar pieces that in combination forms a hollow cylinder with the diameter smaller than the buried cable (100 mm) and with a length of 10 cm. The split-collars are tightly secured around the buried cable (at each end) with two equally spaced high strength bolts at each side. A given end clamp is connected through a loose shackle to a 29 mm (1-1/8-inch) diameter steel cable. The steel cables are passed through the vertical slots provided in the soil chamber wall so that connection can be made through another coupling to a load cell connected to the actuator shaft. Figure 3-19 shows the

coupling system for a lateral pullout test. The vertical slots are sealed with MLC, close cell foam material, to prevent any "flowing out" of the backfill material during lateral pullout testing.

3.1.3.3 Instrumentation

All measurements during testing were primarily focused on the buried cable. The instrumentation used included devices for measuring pullout force, displacements at various cable segments, and strains. The following sections provide details related to some of the key instrumentation.

3.1.3.3.1 Pullout force measurement

The axial pullout force and lateral pullout force were measured using load cells connecting the actuator shaft to cable via couplings described in Section 3.3.2.2 above. Baldwin-Lima-Hamilton Corp**.** SR-4 load cells with a maximum load capacity of 90 kN (20,000 lbs) were used. The load cell was operated at an excitation voltage of 10 volts. All load cells were calibrated over the range of expected axial and lateral loads, up to 50 kN.

3.1.3.3.2 Displacement measurement

Displacement of the actuator during testing was monitored using a Temposonic linear position sensor type RP. Point displacements were also measured at various locations along the buried cables using Celesco-PT101 cable extension position transducers, also called string potentiometers (SP). The SPs had a capacity of measuring displacements up to 2.0m with very high resolution. The displacement transducers were subjected to an excitation voltage of 5 volts. The SPs were connected to the buried cables with very thin extension cables, so that the displacements would be communicated to the transducer with minimal drag forces arising from the backfill soil.

3.1.3.3.3 Strain measurement

Point strains along the buried cables were measured using KFEL-5-1-120-C1 high elongation stain gauge manufactured by Kyowa, Japan, (up to 15 % strain). The Loctite 414 cyanoacrylate adhesives were used to place the strain gauges on the cables. Further detail on strain gauge selection, and specialized procedure for surface preparation and mounting procedures for bonding has been reported by Anderson (2004).

3.1.3.3.4 Data acquisition system

All measurement from load cells, string potentiometers, and strain gauges were collected using a National Instruments NI SCXI-1001 signal conditioning board, Texas, Austin, with Daisylab software (Data Acquisition System Library). Data were recorded at a relatively high frequency of 1 Hz (1 samples per second) in order to capture any potential sudden rapid changes that might result during the tests. However, after review, data were later post-processed to obtain manageable file sizes.

3.1.4 Preparation of Specimens and Cable-Soil Interaction Testing

3.1.4.1 Material Handling and Cable Placement

The procedure used for the placement of soil backfill is similar to that previously used for sand backfill at UBC by Anderson (2004), Karimian (2006), and Weerasekara (2007). The same procedure was maintained throughout all tests in axial and lateral pullout tests.

The amount of thermal backfill required to achieve the specific burial depth varied approximately between 10 to 20 m^3 depending on the type of the test. The backfill material was stored in large bulk-storage bags (with a capacity of 0.9 m^3) in an enclosed area in a structural laboratory. The bags were moved to the location of the chamber by the overhead

crane. Once a bag is positioned at a specific location, the backfill material is released from the bag under gravity into the chamber through a chute as depicted in Figure 3-20. The lower end of the chute was held to allow a fall height of about 20 cm for the material. (Note: a "pull-string" system allows opening the chute at the bottom of the bags). Once the soil flow out of the bag has commenced, the opened chute was traversed over the footprint of the box using the overhand crane to spread the material.

The material was placed in lifts of ~12 cm thickness and levelled with a rake. Each lift was compacted by using a ½-ton smooth roller with three passes in north-south and east-west directions. Following placement of each layer, soil density measurements were taken using density pans.

3.1.4.2 Testing Procedure

Typical cable layout configurations for lateral and axial pullout tests on transmission cables are shown in Figure 3-21. In axial and lateral pullout testing, the transmission cables are aligned parallel to larger and shorter chamber dimensions, respectively. The tests were conducted with cables pulled out in a displacement-controlled manner with a servo-hydraulic actuator as described in the Loading Mechanism section. The rates of displacement were set at 3.6 cm/hr for both axial and lateral pullout tests.

Fifteen (15) longitudinal and ten (10) transverse soil deformations were simulated in the pullout tests. The test program is summarized in Table 3-2 and Table 3-3. As may be noted, several tests were repeated to increase the statistical robustness of collected data. To distinguish between tests, each test is designated with a number as an identification code. The identification code carries information on: the cable type, burial depth, and a digit showing the number of replication in a particular set. For example the Test No. *C1-B2-03* would suggest that a test was performed on the cable *C1* with burial depth *B2,* and this is the third test in this set. A similar labelling approach was utilized to name the lateral pullout tests.

3.1.5 Experimental Limitation and Implementation of the Axial and Lateral Pullout Test

A controlled environment to investigate the cable-soil interaction is a key consideration in the experimental program. As with any experimental study, limitations exist in the interpretation of the test results and the applicability of test results to the field condition. Indeed, the limitations, shortcoming, and possible errors during experimental studies should be identified for test result interpretations and the applicability of test results to real-scenario field condition. The two important shortcomings associated with the current cable-soil interaction experimental studies are the effect of boundary conditions and the effects arising from the pulling system mechanism.

3.1.5.1 Effect of Boundary Conditions

It is most preferable if the real field condition can be simulated by the physical modeling tests. However, the limitation on the scale of the experimental studies forces the size of the chamber to the manageable size by introducing artificial boundary conditions. When selecting the chamber size several key parameters are considered to minimize the effect of the boundary condition. The box size should be large enough to allow the free formation of the active and passive soil wedge in the lateral pullout test, and also allow the free development of the displacement zones during axial pullout test.

3.1.5.1.1 Effect of sidewalls

The observation of sand particle movement during axial pullout test by Karimian (2006) indicated that the only small annular zone in the vicinity of the pipe is influenced during axial pullout (1.2 to 2.8 mm).This observation implied that the sidewalls, located 1.25 m away from the buried cable, would not influence the response of the buried cable during axial

pullout test. In the lateral pullout test; however, the sidewalls create different mobilized friction force. In the previous studies on the pipe-soil interaction, the problem of the sidewall friction was reduced by introducing material for sidewall with reduced interface friction angle. For instance, Trautmann and O'Rourke (1983) used a glass material, Paulin (1998) used steel material, and Karimian (2006) used stainless steel sheets attached to the plywood panel to reduce the sidewall friction force. In the current study, the same procedure as described by Karimian (2006) was used. The 20 Ga 304 stainless steel sheets were used to cover the plywood panel. The frictional force at the side wall can be roughly estimated by considering a failure wedge as shown in Figure 3-22. As shown, the passive wedge can be simplified as a triangular shape with the failure surface of $45^\circ - \phi/2 = 24^\circ$ with the horizon. In calculating the angle of the failure wedge, the friction angle assumed to be $\phi_{cv}=42^\circ$. The magnitude of the mobilized frictional force according to this assumption can be calculated as

$$F_f = \frac{1}{6} k_0 f \gamma H^3 \cot\theta \qquad \text{Eqn. 3-1}$$

In which, γ is the density of the thermal backfill material, H is the buried depth, k_0 is the coefficient of the lateral earth pressure, and f is the coefficient of friction angle between the thermal backfill material and steel panel. If k_0 and f assumed to be 0.5 and $tan(.6\varphi)$,respectively, the mobilized friction force (F_f) for different burial depth ranging from 0.3 m to 1.2 m can be estimated as .04 to 2.81 *kN* respectively. The maximum computed sidewall friction force is an order of 4% of the total soil loads on the buried cable during lateral pullout test.

3.1.5.1.2 Effect of front/rear walls

The direct measurement of stresses on the chamber wall by Karimian (2006) indicated that no noticeable stress changes during axial pullout test were observed. With the knowledge that current tests were conducted on the buried cable with much smaller diameter (89 mm) in comparison to Karimian's tests, which was on pipelines having a diameter of 457 mm, it can

be concluded that the effects of sidewall and front/rear wall would not influence the results of the current axial pullout tests. In the lateral pullout tests, the front and rear walls should allow the formation of the active and passive wedge freely as shown in Figure 3-22. Observations of the surface deformation of the thermal backfill material during lateral pullout tests showed that the active and passive wedge freely formed well within the chamber. The size and the shape of the failure surface can also be evaluated either by the aid of the numerical simulation or the limit equilibrium analysis. In the limit equilibrium analysis, depending on the upper bound or lower bound equilibrium analysis, the failure surface can follow either the velocity characteristics or the stress characteristics. If the planar failure surfaces as suggested by Rankine is assumed, passive wedges would be inclined to the horizontal angle of $45°-\varphi/2\approx24°$ and $45°-\psi/2\approx36°$ for the stress characteristics and velocity characteristics respectively, in which the friction angle (φ) and dilation angle (ψ) were assumed to be 42˚ and 18˚. The buried cable axis during lateral pullout test was positioned 2.5 m from the front wall which is more than the necessary length to form a passive wedge based on the above simplified procedure.

Under the field condition, the power transmission cable is buried in the trench of thermal backfill material which is surrounded by a native soil in contrast to the experimental studies in which the cable is surrounded only by thermal backfill material. Since only a small region immediately around the buried cable is influenced during axial pullout tests, the condition in the test simulates the axial soil loads on the cable. However, the passive wedge for a cable with a larger burial depth during lateral pullout test can be extended to as much as 2.7 m. That means in the field condition the failure surface crosses not only the thermal backfill material zone but may also cross the local soil surrounding the trench. Since the buried power transmission cable traverses a large area with variable soil properties, it is difficult to perform a test with the exact field condition. If the local soil condition is sandy material, the results of experimental tests can be conservative since the thermal backfill material has a higher friction angle and density than a sandy material.

3.1.5.2 Effect of Pulling System Mechanism

As mentioned before, the coupling system for the lateral pullout tests consisted of the end clamps which were connected by the 5/8 inch (16 mm) steel rope sling to the actuators. The modulus of elasticity of the steel rope sling was 120000 N/mm^2 (±5000 N/mm^2). Based on the mechanical and geometric properties of the steel rope sling, its axial stiffness (*AE/L*) for a length of 3 m is 5.7 MN/m, which shows that the rope sling elongates .011 (m) at the peak force of 65 kN when the cable end moves .3 m. As such it is reasonable to assume that the rope sling is inextensible.

The steel cable and thermal backfill material were passed through ducts in order to reduce the friction force between them. Those ducts only extended 2 m from the front wall so they didn't interfere with the buried cable movement during lateral pullout test. Thus, only a half meter of the rope sling was in contact with just the thermal backfill material, and this length was also decreasing during the lateral pull test. The measured axial pullout force of the buried cable can be used to calculate the amount of the axial pullout force of the rope sling. Based on the conventional formula, the axial soil load is proportional to the diameter and the length of the buried cable. Thus, the soil loads on the rope sling was an order of 2% of the soil loads on the buried cable which can be negligible.

The rope sling was connected through the shackle to the buried cable. This type of the connection creates a flexible hinge, which permits the buried cable deforms easily and it also keeps the direction of applied load the same during lateral pullout test. The other benefit of using a flexible hinge is to allow the possible vertical uplift of the buried cable during lateral pullout tests.

3.1.5.3 Other Possible Associated Errors

The other possible associated error can be related to the variation of the density in each test and throughout all the axial and lateral pullout tests. Achieving a uniform density is an

important consideration in the experimental tests since the change in the density would affect the friction angle, dilatancy, the stresses around the buried cable, and finally the pattern of the failure during the axial and lateral pullout test. In order to achieve specimen with uniform density, a systematic and consistent approach was developed to prepare the specimen for all tests. The reader is referred to the specimen preparation for more detail. The pan test, using bowls placed during thermal backfill compaction, was used to measure the local density and moisture content of thermal backfill material at four random points at different layers. In this test, a pan with the known volume was placed in the soil and then the thermal backfill material was poured into the box and compacted. The pan was removed and the local soil density and moisture content were measured. Table 3-2 and Table 3-3 show the mean density and corresponding standard variation of density in the axial pullout and lateral pullout tests respectively. The average soil density ranges from 19.2 to 20 kN/m^3 in the axial pullout test and from 19.2 to 20.1 kN/m^3 in the lateral pullout test. The effect of density changes in the results of the axial and lateral pullout tests will be investigated by the numerical simulation in the later phase of this study.

3.2 Experimental Testing on the Buried Cable Subjected to Longitudinal and Transverse Ground Movements

This section describes the results from axial and lateral pullout tests on buried cables as well as comparison between other studies and the current study. As mentioned previously, two types of test are conducted: 1) the axial pullout tests simulate the longitudinal soil loads on the buried cable and 2) lateral pullout tests simulate the transverse soil loads on the buried cable.

3.2.1 Axial Pullout Testing

Axial pullout tests were performed on the cable type *C1* with diameter of 89 mm buried in dense thermal backfill as in procedures in the earlier sections of this report. Tests were conducted at four different burial depths (*H*) equal to 30, 60, 100, and 120 cm to investigate the effects of burial depth on longitudinal soil restraint - the burial depth (*H*) is the depth of the centreline t the surface. The axial pullout loads, the corresponding leading and tailing displacement were measured for each test. The test results are typically reported herein in terms of axial load vs. axial displacement responses under different burial depth levels, the axial displacement corresponds to the leading part of the cable or front displacement.

3.2.1.1 Results of Axial Pullout Testing

Detailed results of all axial pullout tests are reported in Appendix A. Figure 3-23 depicts the average axial pullout response observed for burial depths of 30, 60, 100, and 120 cm; the plotted displacement represents the displacement of the leading end of the cable. As shown, the characteristic force-deformation curve for all tests shows a peak in axial pullout force at relatively low pullout displacement (5 to 7 mm), followed by a drop of axial force.

After experiencing the initial drop, the pullout resistances on cables increase with further increase in axial displacement. In connection with this observation, it is worthwhile noting that most of the transmission cables had a slight initial curvature at the time of installation in the soil chamber for testing, which is likely an artifact from being placed curved for a long time in a reel as supplied by the cable manufacturer. In spite of concerted efforts expended, it was not possible to remove this curvature and straighten the cable prior to installation for pullout testing. It appears that, at larger axial displacements, the presence of the inherent curvature (out-of-straightness) of the cable would likely have promoted the development of some passive soil restraint in addition to the “shaft friction” - in turn, contributing to the increase in the observed axial soil resistance at larger cable movements. The out-of-

straightness can be purely horizontal, purely vertical, or a combination of the two. The level of the ascent of the axial pullout force (with increasing relative axial displacement) can be argued to be dependent on the degree of the out-of-straightness. As may be noted from the axial force-displacement curves in Appendix A, some tests exhibit an increased amount of increase in axial pullout force with further increasing in axial displacement; this may be indicative of the total randomness of the amount of the out of straightness. This hypothesis requires further investigation prior to confirmation.

Figure 3-24 shows the trailing end versus leading end displacement of the buried cables during test C1-B1-05. The observed, almost 1:1 slope of the relationship indicates that the trailing end of the cable moved in harmony with the front end during axial pullout process. In essence, the observation confirms that the overall axial stiffness of the cable is sufficiently large to allow the cable to behave as a rigid body for the tested length. This figure and similar tailing-end and leading-end displacement measurement in other tests, as depicted in Appendix A, confirms that the failure occurs simultaneously along the interface of the buried cables and surrounding soil over the tested length.

In order to facilitate the comparison of test results with other studies and guidelines such as ASCE (1984), the axial pullout force and displacement are expressed as a non dimensional quantity. The displacement is normalized with respect to the buried cable diameter. The axial force is normalized to the average soil density, buried cable diameter, length of the cable buried in the box, and burial depth as depicted by following equation:

$$N_a = \frac{F_a}{\gamma HDL} \qquad \text{Eqn. 3-2}$$

In which F_a= axial pullout force; γ= the average crushed stone density; L= the cable length; D= cable diameter and H=burial depth

A quick examination of the above equation with ASCE (1984) equation for longitudinal soil restraints would suggest that the dimensionless quantity ($F/\gamma HDL$) is a reflection of the soil normal stress and soil frictional components (i.e., k and $\tan \delta$), and such representation also

provides an opportunity to effectively compare results from tests conducted at different burial depths. As per ASCE(1984) longitudinal soil restraint can be expressed as a function of N_a as:

$$F_{axial} = N_a(\frac{1+k}{2})\pi \tan\delta \qquad \text{Eqn. 3-3}$$

in which δ= interface friction angle and $k = \sigma_h^{'} / \sigma_v^{'}$ (coefficient of lateral earth pressure) is defined as the ratio of horizontal stress to the vertical stress. $\sigma_h^{'}$ and $\sigma_v^{'}$ are the horizontal and vertical effective stresses. The coefficient of lateral earth pressure strongly depends on soil properties and the stress history of the soil (Northcutt (2010)). Jacky (1948) proposed a formula for a coefficient of lateral pressure at rest (k_0) for sand as a function of internal friction angle (ϕ) as follows:

$$k_0 = 1 - \sin\phi \qquad \text{Eqn. 3-4}$$

The non-dimensional axial pullout force versus non-dimensional displacement is shown in Figure 3-25 for different burial depths of 30, 60,100, 120 cm, and ASCE formula. The k_0 value in ASCE is derived from Jacky's equation with the friction angle of 53° and interface friction angle of 38° as obtained from laboratory direct shear test. This interpreted information in the figure clearly suggests that the average normal stresses on the cable during axial pullout are much larger than those typically estimated for coefficient of lateral earth pressure at rest using conventional approaches. It is of interest to note that these observations are similar to those observed by Karimian (2006) for steel pipes buried in dense sand, where the peak axial soil resistance observed on buried steel pipes were noted to be several-fold (in excess of 2 times) higher than the predictions from guidelines. As can be seen in Figure 3-25, the predicted value for axial pullout force is very sensitive to the variation of the assumed value for k.

With direct measurement of soil stresses on pipes during full-scale testing combined with numerical modeling, Wijewickreme et al. (2009) have demonstrated that this increase is

primarily due to significant increase of overall normal soil stresses on the pipelines as a result of constrained dilation of dense soil during interface shear deformations. It appears that the limitations in the current approaches for the estimation of axial soil loads on steel pipes in dense soils may also exist for the cables buried in dense soils.

Using the angle of interface friction (δ) obtained from direct shear testing and the first peak axial force from pullout testing, it is possible to back-calculate values for the coefficient of lateral earth pressure (*k*) as depicted in Figure 3-26 as a function of burial depth ratio (*H*/*D*). The figure shows the k value gradually decays with increasing *H*/*D* ratio. This observation is similar to findings by Karimian (2006) during numerical modeling of constrained-dilation during axial pullout testing of steel pipes in dense sand.

3.2.2 Lateral Pullout Testing

Lateral pullout tests were performed on the cable Type *C2* (having a diameter of 100 mm) buried in dense thermal backfill material. Tests were conducted at four burial depths equal to 30, 60, 90, and 120 cm. Measurements included lateral pullout forces, the horizontal displacement at both ends of cable, and displacement at selected locations along the cable. The displacement were measured using string potentiometers (i.e., string potentiometer locations are shown as points A, B, C and D in Figure 3-21(b); in this, thin steel wires were attached to the transmission cable at the desired locations, and they were passed through the soil to the outside of the box and then attached to the string potentiometers. In some lateral pullout tests, strain gauges were also mounted on the cable (at the same locations as those used for the string potentiometers) to measure axial strains in the back and front sides of the transmission cable. The primary results include lateral pullout force and displacement at both cable ends.

3.2.2.1 Results of Lateral Pullout Testing

The results from lateral pullout testing are given in Appendix A. The lateral pullout forces are reported as the sum of the forces measured from each load cell connected to each end of the cable during pulling. Force-displacement data for lateral loading are summarized in Figure 3-27 for burial depth ratios (H/D) of 3, 6, 9, and 12. Clearly, the lateral pullout forces increase by an increase in burial depth ratio. In order to facilitate the comparison of test results with other studies and guidelines such as ASCE (1984), the lateral pullout force and displacement are expressed as a non-dimensional quantity. The lateral force is normalized to the average soil density, buried cable diameter, length of the cable buried in the box, and burial depth as depicted by following equation:

$$N_h = \frac{F_L}{\gamma HDL} \qquad \text{Eqn. 3-5}$$

in which F_L=the measured lateral force; and H, D, and L are as previously defined. Displacement is expressed as the non dimensionless quantity Y/D, the ratio of displacement cable ends to the diameter of the cable. Figure 3-28 depicts the non-dimensional force-displacement curve for lateral pullout test for different burial depth ratios (3, 6, 9, and 12). Arrows on the curve represents the maximum dimensionless force. The maximum dimensionless force, which will be called the horizontal transverse force factor thereafter, is depicted in Figure 3-29 as a function of burial depth. The current test results are compared with experimental studies by Trautmann and O'Rourke (1985), Audibert and Nyman (1977) and Karimian (2006) in Figure 3-30. The many differences in their experimental studies such as material density, friction angle, and pipe diameter cause the disparity among the individual results. The main cause of differences between our test results and reported studies by O'Rourke and Karimian is the higher friction angle and dilation angle associated with the thermal backfill material.

Two analytical models were proposed by Audibert and Nyman (1977) and Trautman and O'Rourke (1983) to calculate the horizontal force factor (N_h) for buried pipeline. Audibert

and Nyman used Hansen (1961) model developed for vertical piles and Trautman and O'Rourke (1983) used Ovesen (1964) model developed for vertical plate anchors. The results of their analysis are reported in ASCE (1984). Figure 3-31 shows the variation of the horizontal force factor as a function of *H*/D for soil with different friction angle based on the model of Hansen (1961) and Figure 3-32 shows the variation of the horizontal force factor as a function of *H*/D for soil with different friction angle based on the model by Ovesen (1964). The horizontal transverse force factor of the current study is also compared with the analytical work of Ovesen (1964) and Hansen (1961) for φ=45˚ as shown in Figure 3-31 and Figure 3-32. The comparison shows that Ovesen model under predict the test results by 20 %, while Hansen model over predict the tests results as much as 100 %. The assumption in the Hansen analytical model regarding the vertical restraints causes the exaggerated overprediction of test data while satisfying vertical equilibrium as the Ovesn model causes a more reasonable prediction. It is important to note that the disparity in the test results with Ovesen model arises from two reasons. The Ovesen prediction considers a 2-dimensional plane-strain movement whereas the lateral pullout test simulated in the chamber in fact is a three dimensional cable-soil interaction problem. In addition, the friction angles for thermal backfill are much higher; as such, it is not surprising to see an observed lateral resistance to be larger than Ovesen analytical model. As can be seen, the suggested design values for N_h fall below those of current test results.

3.2.3 Summary of Experimental Testing Results

The main objective of the current research was to study the contributing factors and key parameters influencing the response of the buried power transmission cables subject to permanent ground deformation. A systematic full-scale laboratory testing program was undertaken using a large soil chamber to examine this topic. The research findings are intended to provide a database for development of guidelines and criteria to assess the performance of the buried power transmission cables, and validation of numerical models. The research work has generated several key findings related to the characterization of

longitudinal and horizontal transverse soil restraints, the applicability of the current guidelines, and the methods that have been developed for pipelines to buried power transmission cables. A series of tests were conducted where buried cables were subjected to longitudinal and transverse pullout. The test results have been compared with the predictions from the ASCE (1984) guidelines and other similar studies for assessing the performance of buried pipelines under relative ground movements.

Some of the key findings are summarized below

- Under relative axial movements, power transmission cables buried in dense sand exhibited a load-displacement response involving a relatively nonlinear increase to a peak point followed by strain-softening behaviour, and increase in pullout resistance.

- The peak soil loads under relative axial soil movements on cables buried in dense soil were noted to be under-predicted by the current approaches used for buried pipeline design; this is likely due to the increased soil normal stresses on the cable due to constrained soil dilation not accounted by the current approaches. It appears that the limitations in the current approaches for the estimation of axial soil loads on steel pipes in dense soils may also exist for the cables buried in dense soils. In using the ASCE (1984) approach, the determination of the lateral earth pressure coefficient (k) that adequately represents the normal soil pressure on the cable seems to present a challenge.

- The maximum axial pullout force depends on the cable diameter, the interface friction angle, soil density, burial depth, and the coefficient of earth pressure (k). Studies show that the correct estimation of the normal earth pressures on the structural element is crucial in determining the axial soil resistance against pullout. Based on the test results, the variation of the coefficient of the earth pressure as a function of burial depth was developed.

- "Out-of-straightness" of cables seems to be another important consideration that affects the development of axial soil loads on cable at relatively large soil

movements. Depending on the degree of "out-of-straightness", the axial soil resistance can increase the apparent initial peak axial soil restraints. Therefore, it is prudent to account for alignment curvatures when assessing the buried power transmission cables subjected to relative axial soil ground movements.

- The load-displacement curves for the buried power transmission cables subjected to the horizontal transverse movement were developed using tests conducted at varying embedment ratios (3, 6, 9, and 12) were developed. The load response curves show a rectangular hyperbola shape, i.e., the load increases nonlinearly and gets to the asymptotic value. The test results show that the horizontal force factor (N_h) varies as a function of friction angle and embedment ratio (H/D ratio). The new database provides an opportunity to characterize the transverse horizontal soil restraint for buried power transmission cables.

- The lateral pullout test results were compared with other experimental, analytical studies, and ASCE 1984 guidelines. The comparison between the current test results and Trautmann and O'Rourke (1983) result shows that their method under-predict the maximum transverse soil loads on the buried cable. The comparison between the current test results and Audibert and Nyman shows that their method over-predicts the maximum transverse soil loads on the cable as much as 100%.

- In an overall sense, the test results contribute to developing a reliable database for validating numerical models to capture the response of underground power transmission systems subjected to permanent ground deformation.

Table 3-1: Results of chemical soil analysis (Test results were provided by Soilcon Laboratory Ltd.)

Strong Acid Soluble Metals	ug/g	Strong Acid Soluble Metals	ug/g
Antimony Sb	< 10	Tin Sn	< 5
Arsenic As	< 10	Vanadium V	52
Barium Ba	142	Zinc Zn	42
Beryllium Be	< 1	Aluminum Al	15700
Cadmium Cd	< 0.5	Boron B	< 1
Chromium Cr	5	Calcium Ca	9130
Cobalt Co	9	Iron Fe	19700
Copper Cu	48	Magnesium Mg	8710
Lead Pb	6	Manganese Mn	387
Mercury Hg	< 0.01	Phosphorus PO4	429
Molybdenum Mo	< 4	Potassium K	2410
Nickel Ni	4	Sodium Na	638
Selenium Se	< 0.2	Strontium Sr	74
Silver Ag	< 2	Titanium Ti	773
		Zirconium Zr	< 1

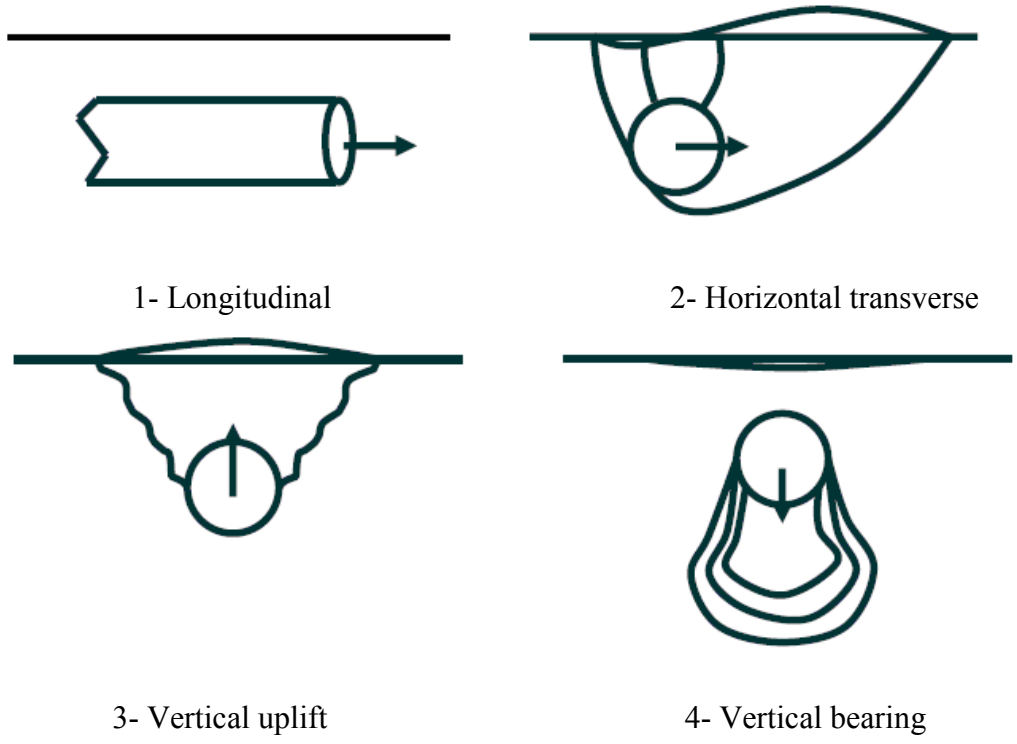

Figure 3-1: Modes of soil loads on the buried cable

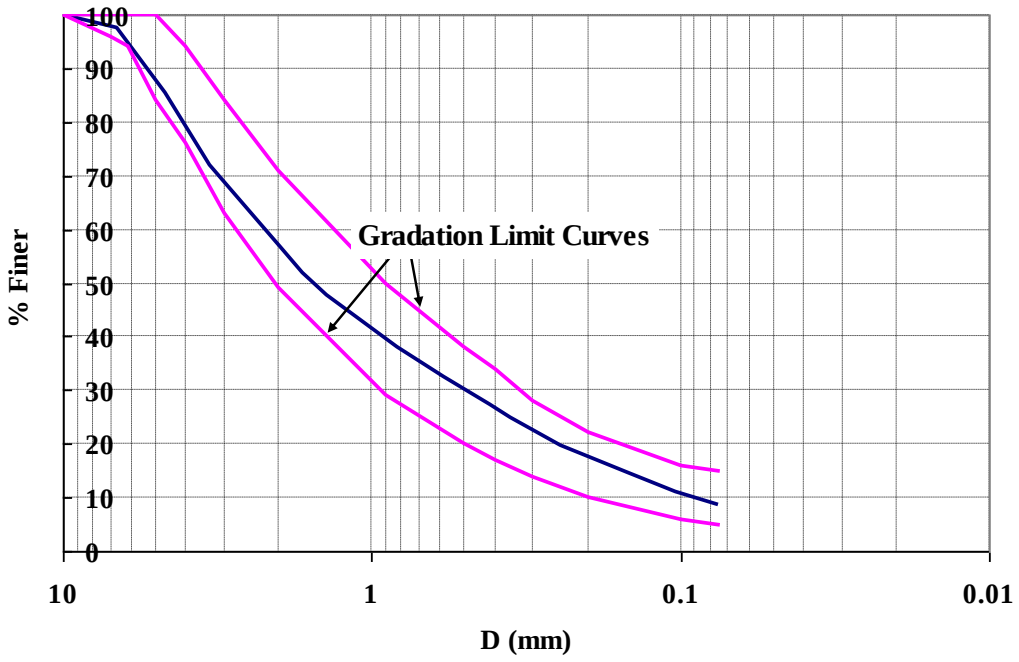

Figure 3-2: Grain size distribution of the thermal back fill material and grading limits as specified by British Columbia Transmission Corporation (BCTC).

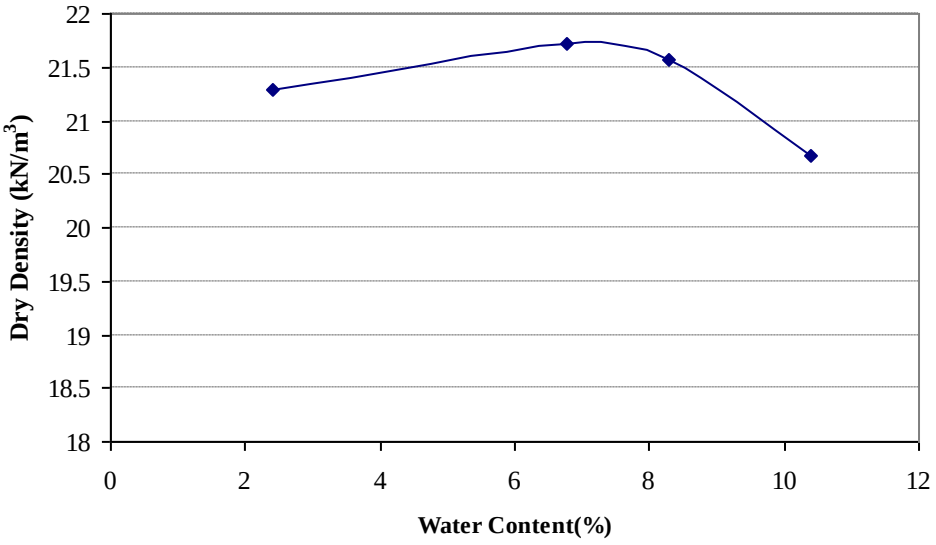

Figure 3-3: The results from Modified Proctor testing of thermal backfill material.

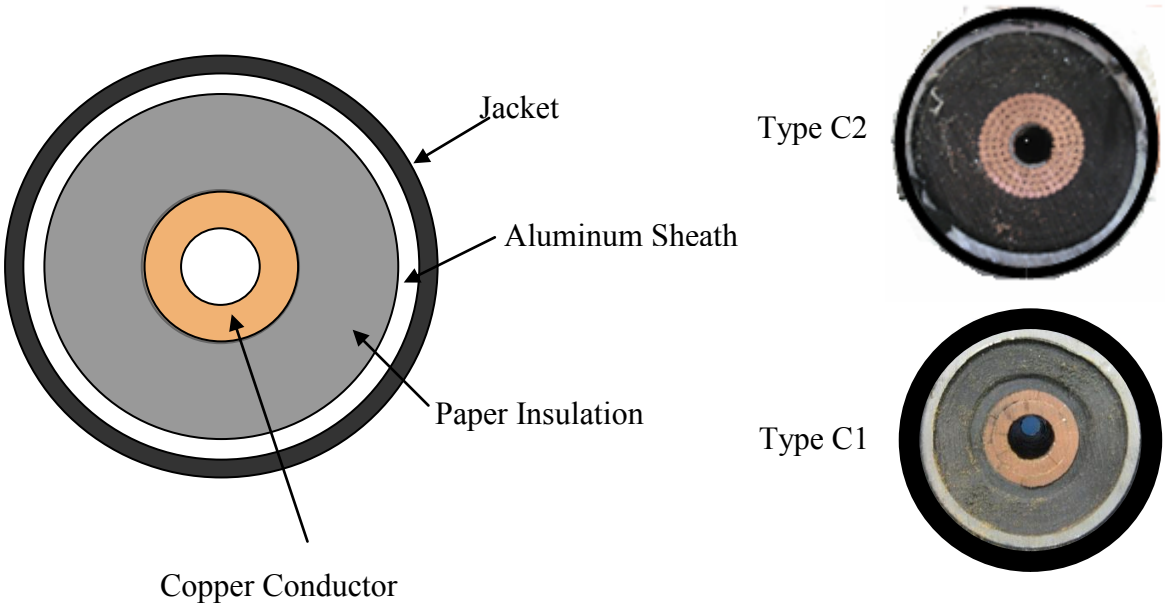

Figure 3-4: Cross section of tested power transmission cable (Left: schematic drawing, Right: photograph of Type C1 and Type C2 cable)

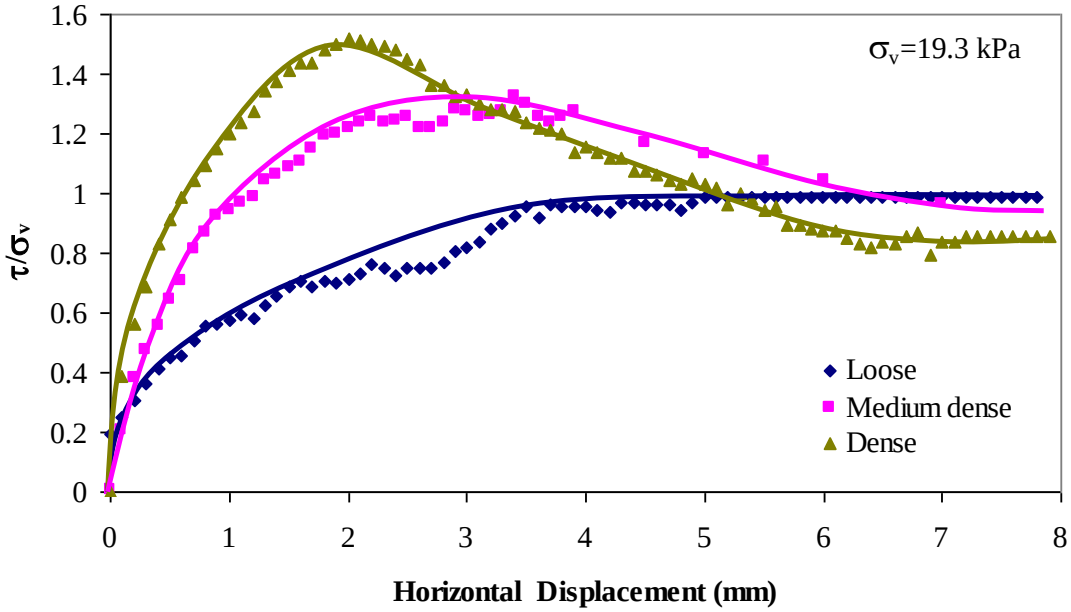

Figure 3-5: Variation of normalized shear stress during direct shear loading of a loose (13.90 kN/m^3), medium dense (16 kN/m^3), and dense (17.90 kN/m^3) thermal backfill material .

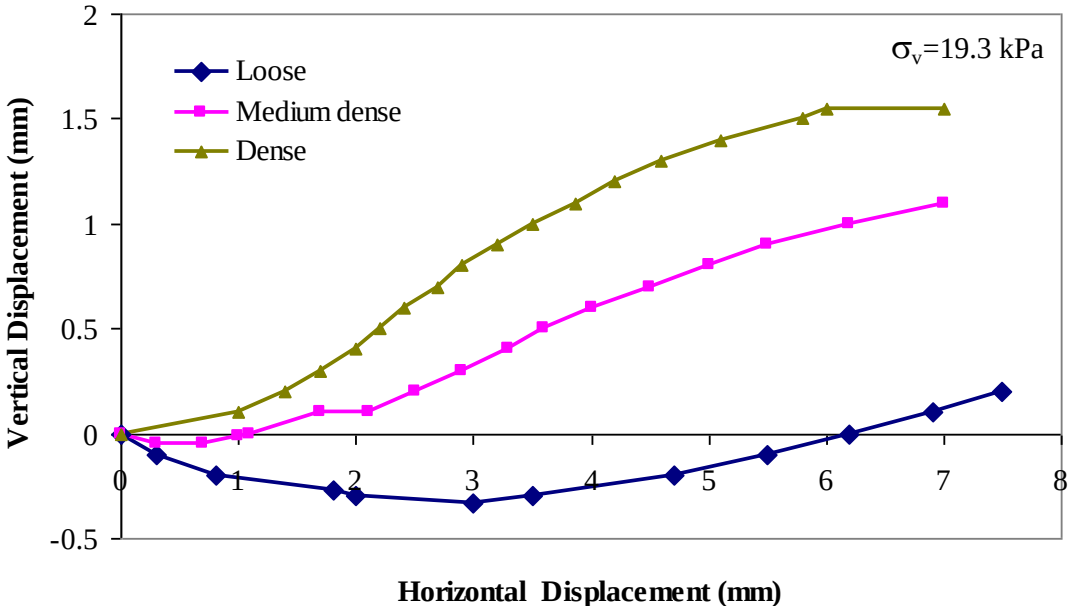

Figure 3-6: Vertical displacement of top cap during direct shear loading of a loose (13.9 kN/m^3), medium dense (16 kN/m^3), and dense (17.90 kN/m^3) thermal backfill material.

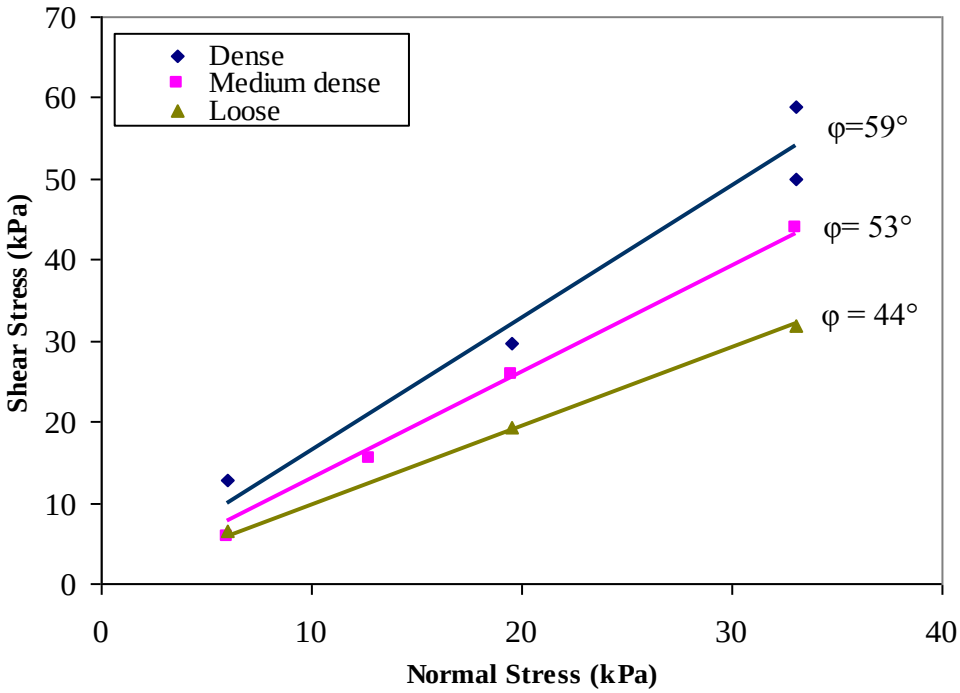

Figure 3-7: Peak shear stress versus normal stress from direct shear testing of a loose (13.9 kN/m^3), medium dense (16 kN/m^3), and dense (17.9 kN/m^3) thermal backfill material

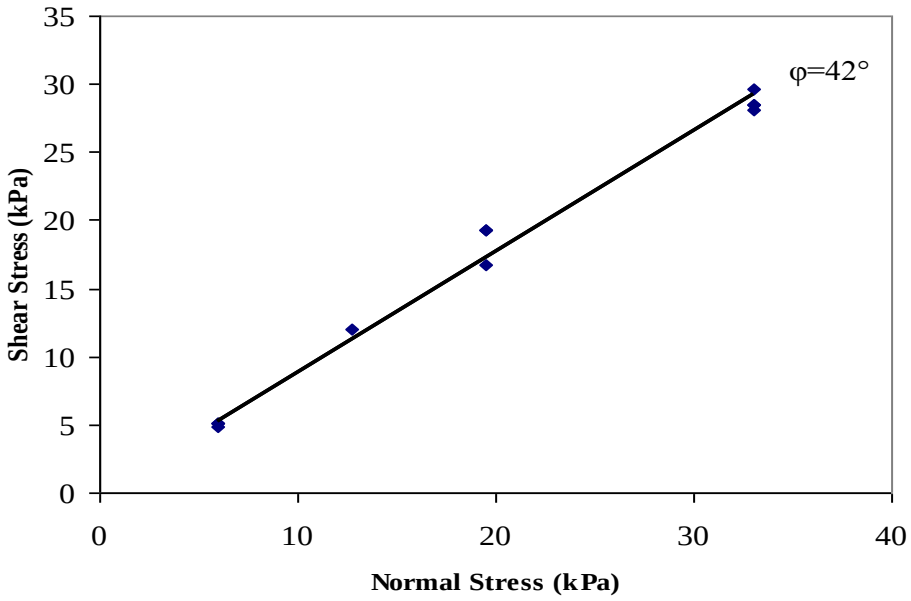

Figure 3-8: Peak shear stress versus normal stress from direct shear testing of a loose (13.9 kN/m^3), medium dense (16 kN/m^3), and dense (17.9 kN/m^3) thermal backfill material

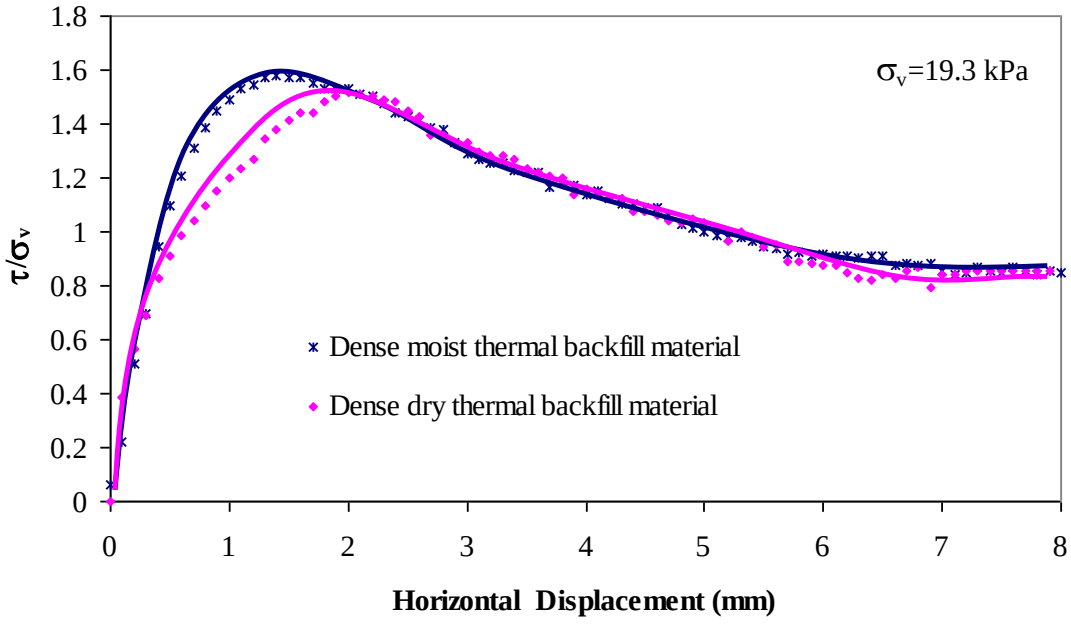

Figure 3-9: Variation of normalized shear stress during direct shear loading of a moist and dry thermal backfill material for vertical stress level of 19.3 kPa

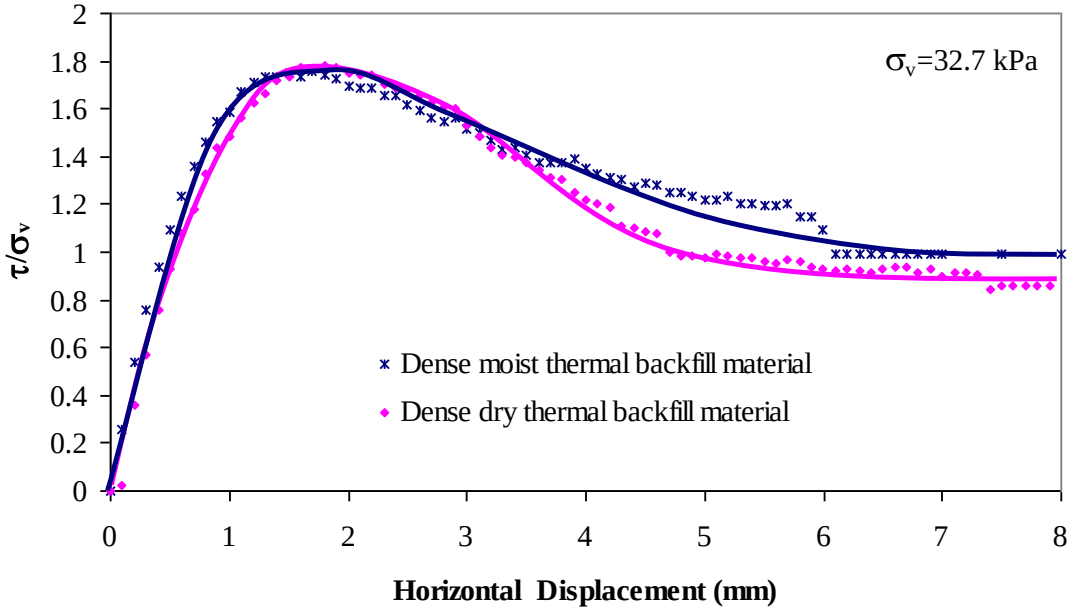

Figure 3-10: Variation of normalized shear stress during direct shear loading of a moist and dry thermal backfill material for vertical stress level of 32.7 kPa

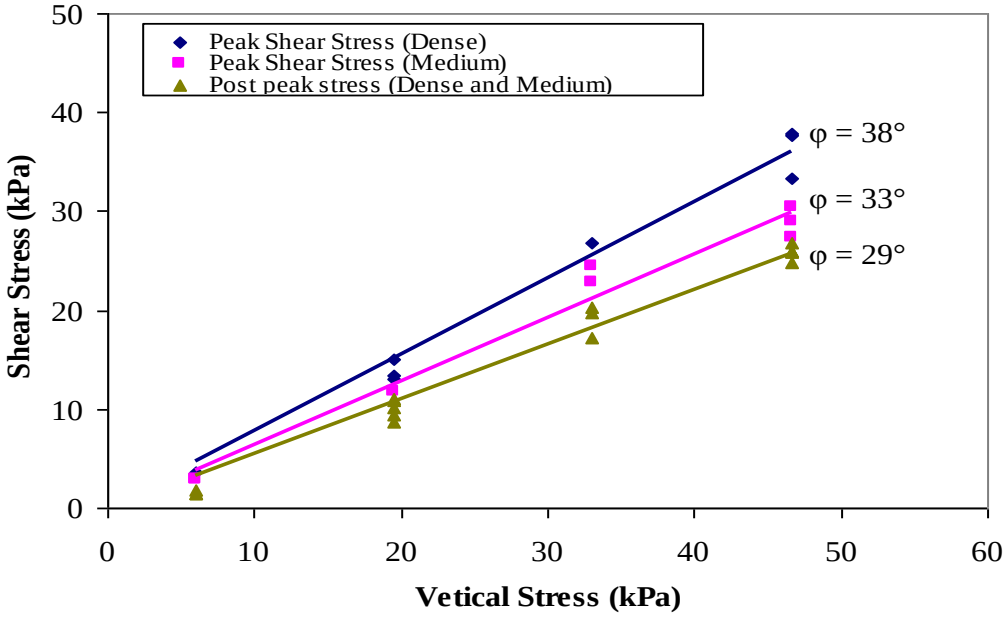

Figure 3-11: Results of Direct shear test on the interface friction angle between thermal backfill material and buried cable.

Figure 3-12: Compression test set up of power transmission cable

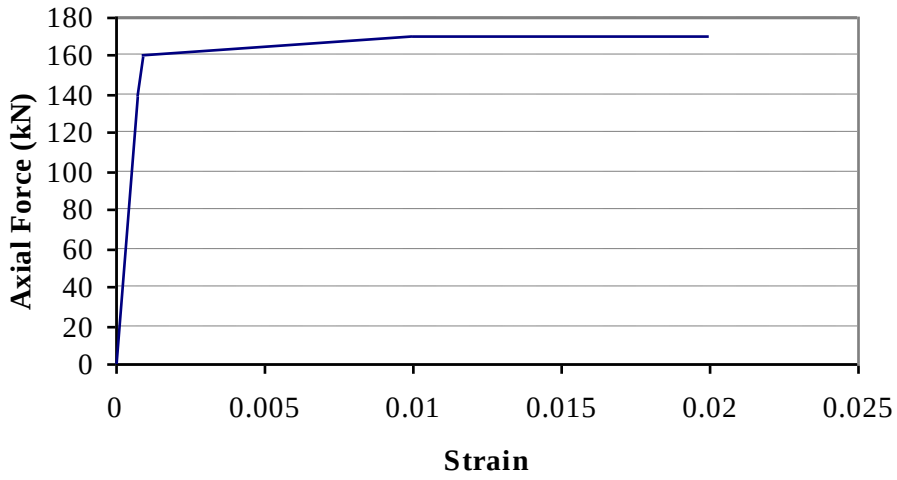

Figure 3-13: Force-displacement results of compression test on power transmission cable

Figure 3-14: Three-point-bending test setup of power transmission cable

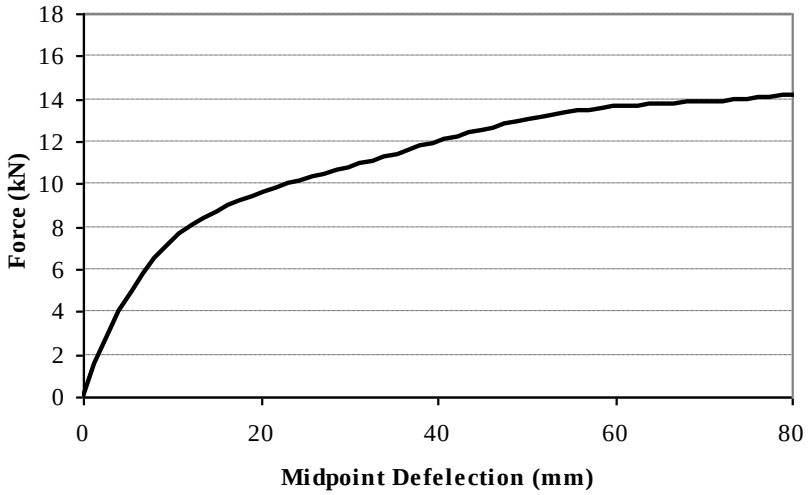

Figure 3-15: Force-displacement result of three-point bending test of power transmission cable

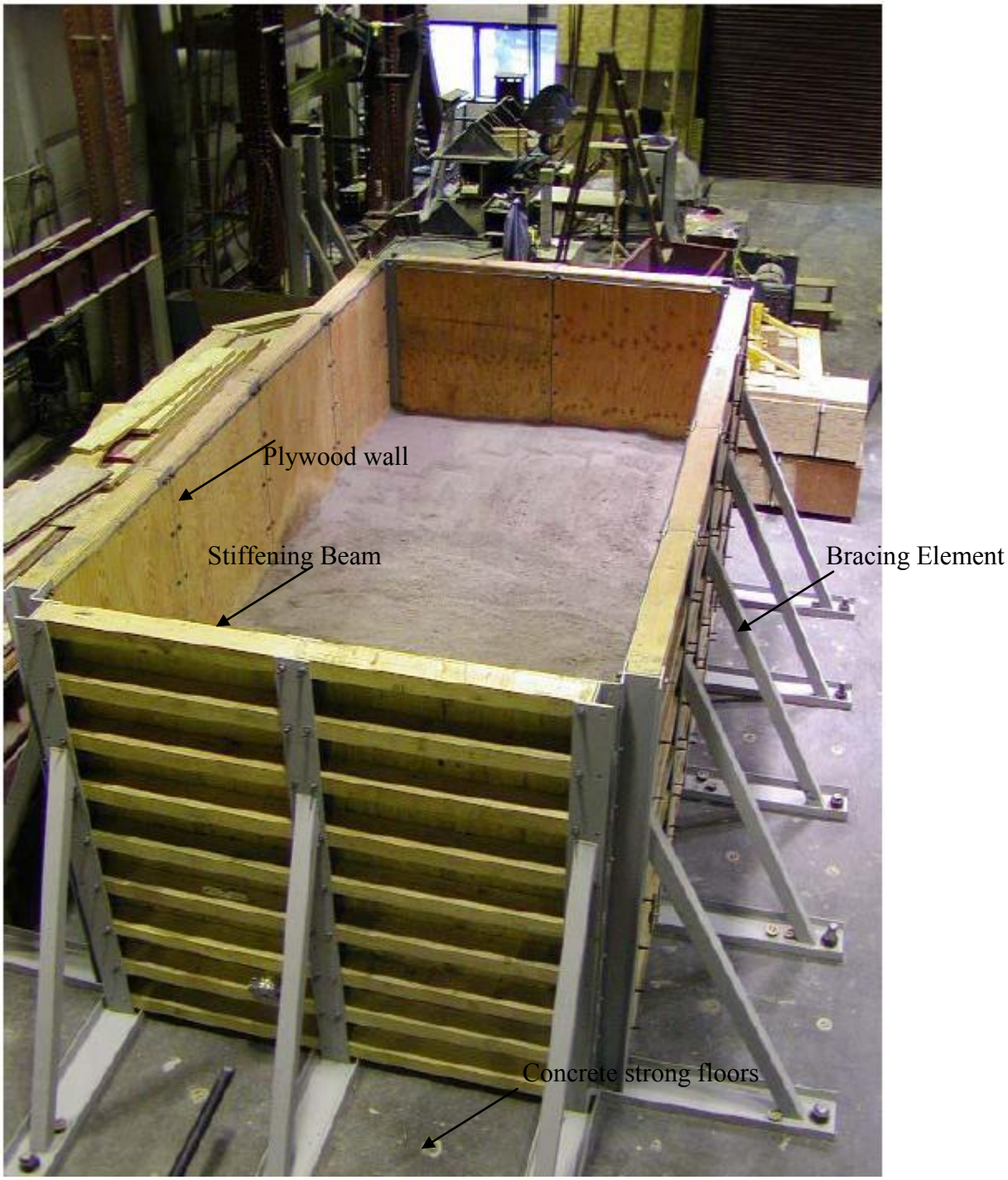

Figure 3-16: Configuration of soil-cable interaction testing chamber

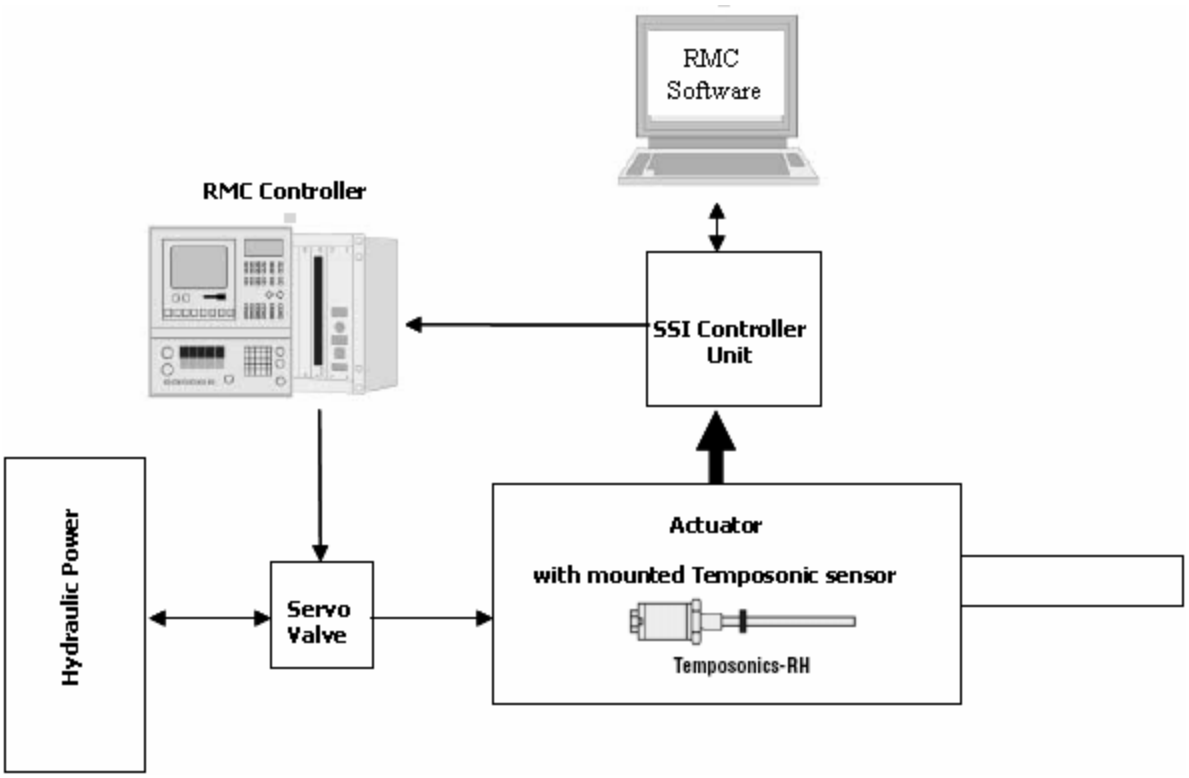

Figure 3-17: Schematic configuration of the actuator controlling system.

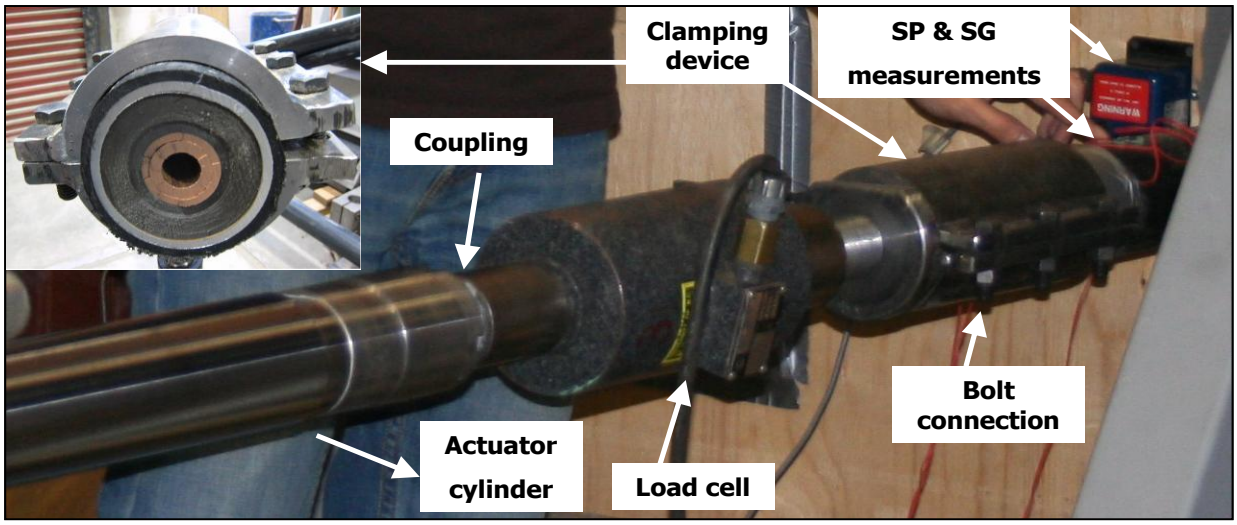

Figure 3-18: Clamping mechanism in axial pullout test

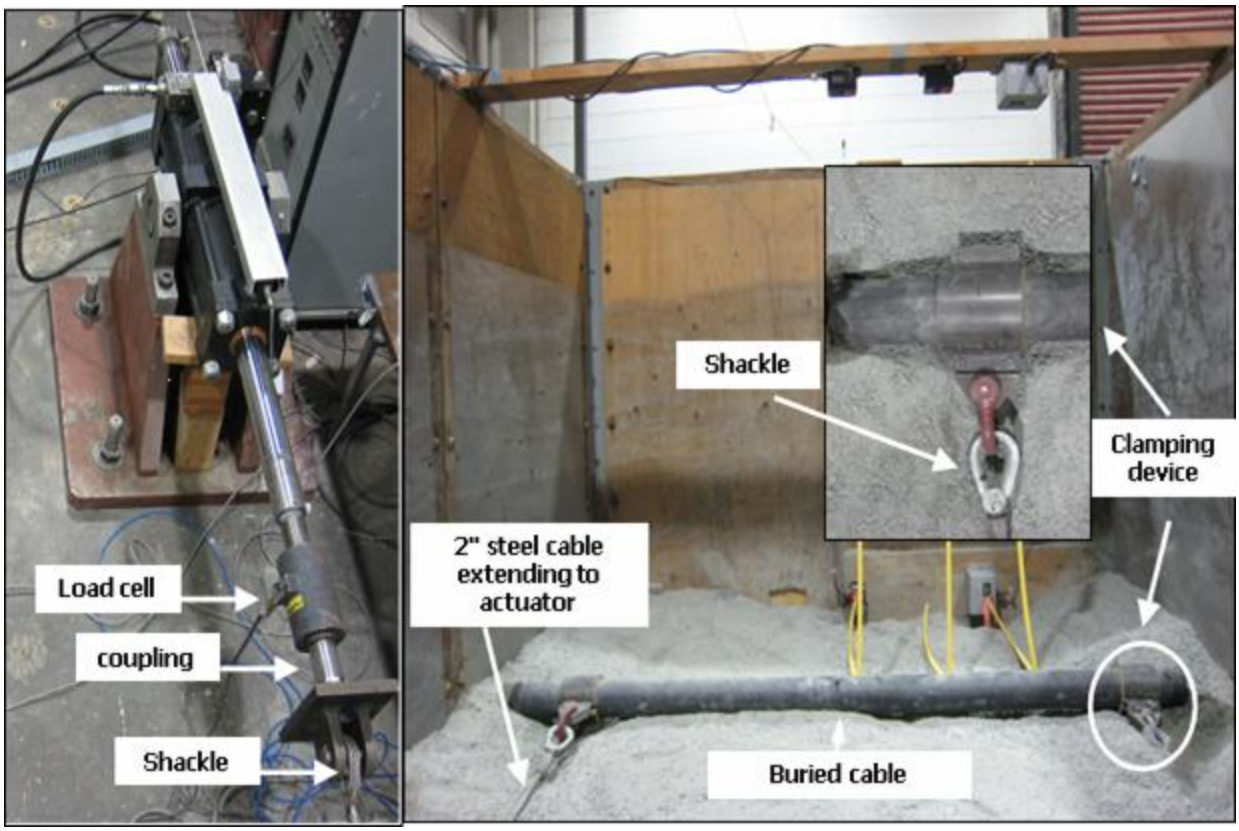

Figure 3-19: Clamping mechanism in lateral pullout test

Figure 3-20: Loading preparation phase, bulk bag suspended by overhand crane.

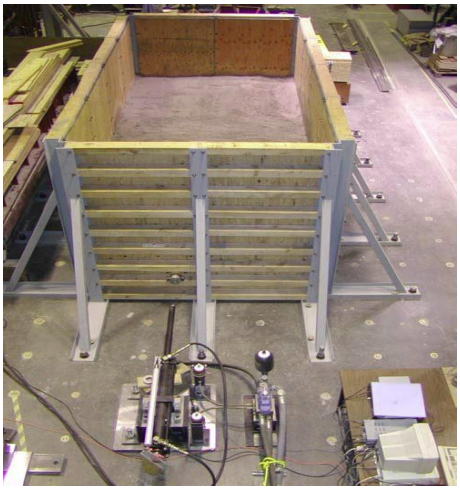

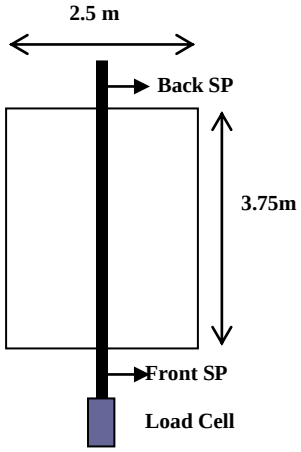

(1-a)

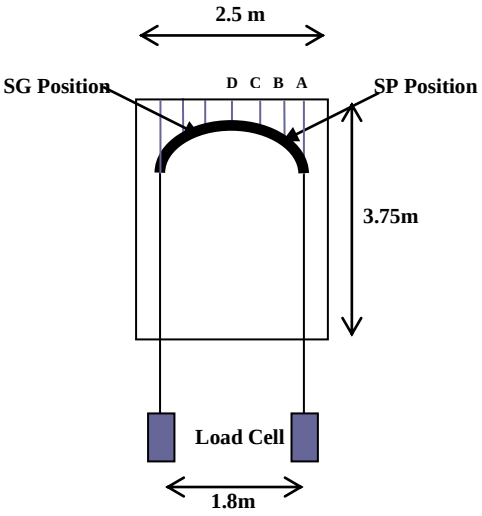

(1-b)

Figure 3-21: Photograph and schematic diagram showing typical test set up for: (a) axial pullout testing; and (b) lateral pullout testing (SP= String Potentiometer, SG=Strain Gauge).

Table 3-2: Axial pullout testing program

Test No.	Test ID	Burial Depth (cm)	Cable Size (mm/in)	Average Soil Density (kN/m^3)	Standard Deviation of Density	H/D	Data
1	C1-B1-D01	60	89 mm (3.5")	19.2	0.25	6.75	N.R
2	C1-B1-D02	60	89 mm (3.5")	19.2	0.36	6.75	N.R
3	C1-B1-D03	60	89 mm (3.5")	19.8	0.18	6.75	R
4	C1-B1-D04	60	89 mm (3.5")	19.7	0.22	6.75	R
5	C1-B1-D05	60	89 mm (3.5")	19.6	0.24	6.75	R
6	C1-B1-D06	60	89 mm (3.5")	19.7	0.18	6.75	R
7	C1-B2-D01	100	89 mm (3.5")	20.0	0.30	11.25	R
8	C1-B2-D02	100	89 mm (3.5")	19.7	0.14	11.25	R
9	C1-B2-D03	100	89 mm (3.5")	19.9	0.20	11.25	R
10	C1-B2-D04	100	89 mm (3.5")	19.2	0.35	11.25	R
11	C1-B2-D05	100	89 mm (3.5")	19.6	0.28	11.25	R
12	C1-B3-D01	120	89 mm (3.5")	19.4	0.43	13.5	R
13	C1-B3-D02	120	89 mm (3.5")	19.2	0.34	13.5	R
14	C1-B4-D01	30	89 mm (3.5")	19.9	0.28	3.4	R
15	C1-B4-D02	30	89 mm (3.5")	19.6	0.13	3.4	R
16	C1-B4-L01	30	89 mm (3.5")	19.9	0.25	3.4	N.R

N.R: Not Reported , R: Reported

Table 3-3: Lateral pullout testing program

Test No.	Test ID.	Burial depth (cm)	Cable size (mm/in)	Average density (kN/m^3)	Standard deviation of density	H/D
1	C2-B1-D01	30	100 mm (4")	20.0	0.32	3
2	C2-B1-D02	30	100 mm (4")	19.7	0.18	3
3	C2-B1-D03	30	100 mm (4")	19.8	0.21	3
4	C2-B2-D01	60	100 mm (4")	19.9	0.28	6
5	C2-B2-D02	60	100 mm (4")	20.1	025	6
6	C2-B2-D03	60	100 mm (4")	19.8	0.38	6
7	C2-B3-D01	90	100 mm (4")	19.3	0.32	9
8	C2-B3-D02	90	100 mm (4")	19.2	0.34	9
9	C2-B3-D03	90	100 mm (4")	19.3	0.27	9
10	C2-B4-D01	120	100 mm (4")	19.8	0.21	12

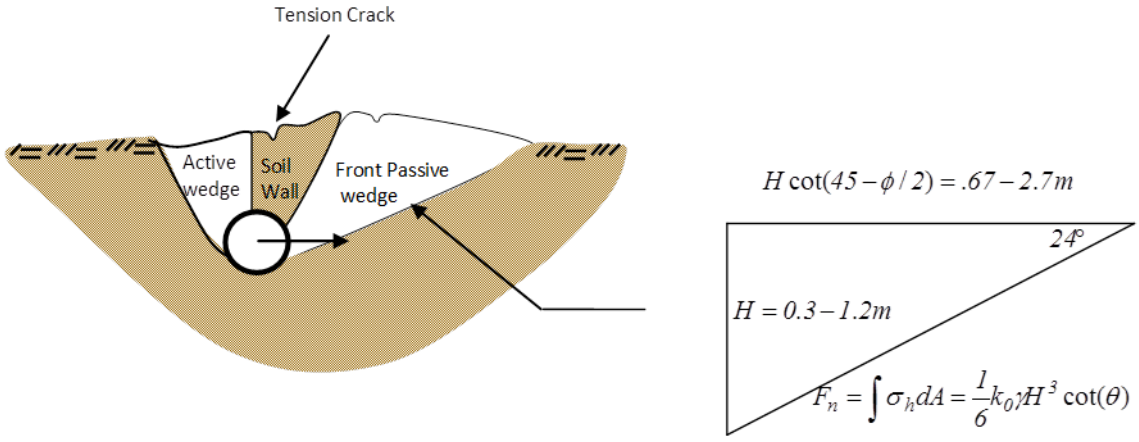

Figure 3-22: A simplified assumption to calculate the side friction force in the soil-cable interaction chamber.

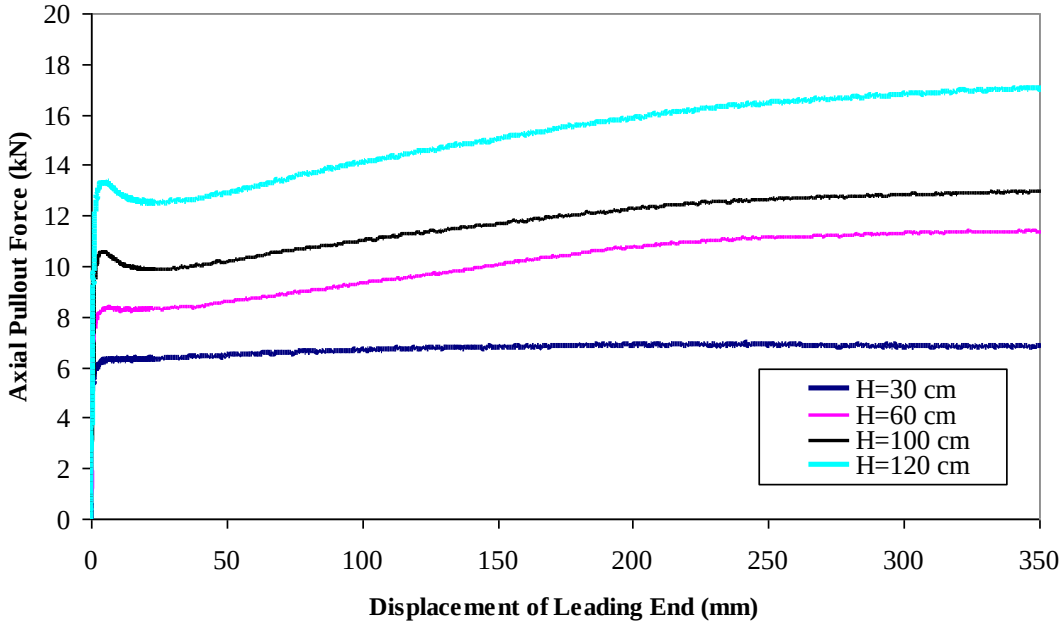

Figure 3-23: Average axial pullout force versus cable leading displacement for burial depth 30,60,100, and 120 cm.

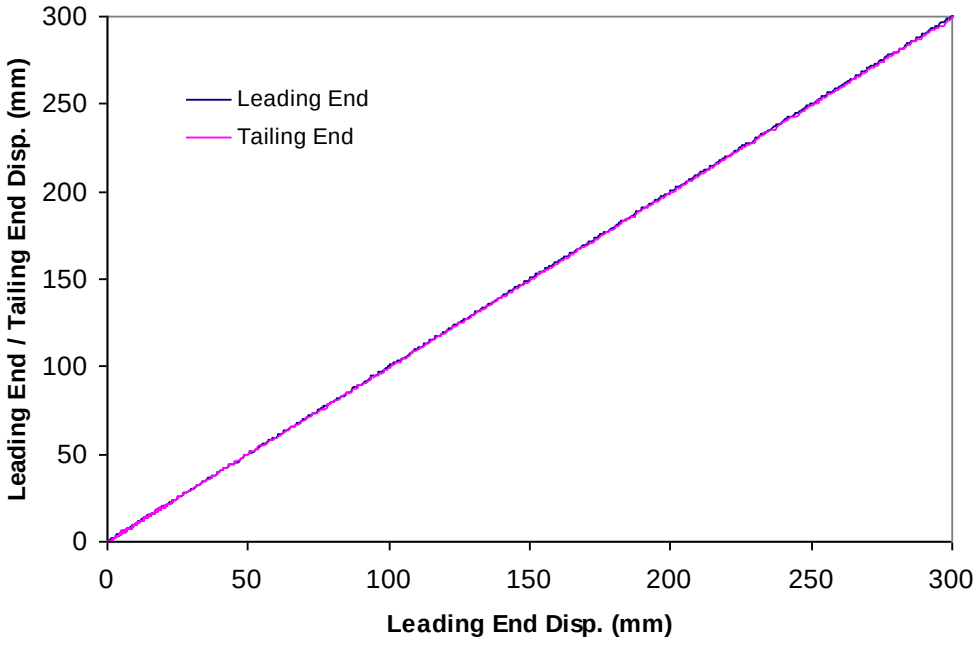

Figure 3-24: Observed axial displacement of cable at the front and back ends in Test C1-B1-03

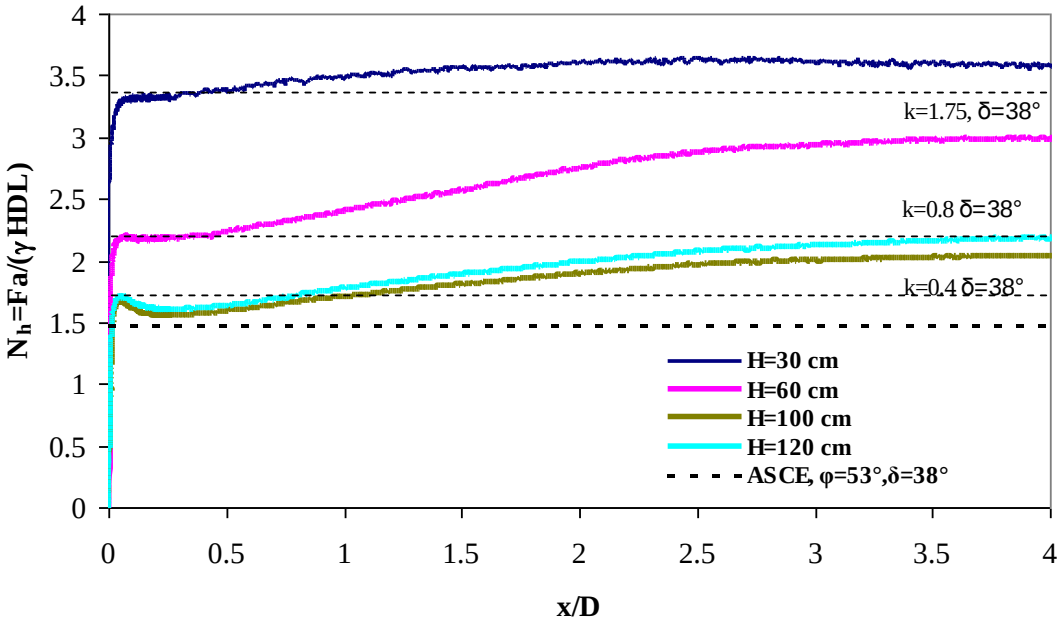

Figure 3-25: Comparison of test results with predictions using ASCE (1984) formula

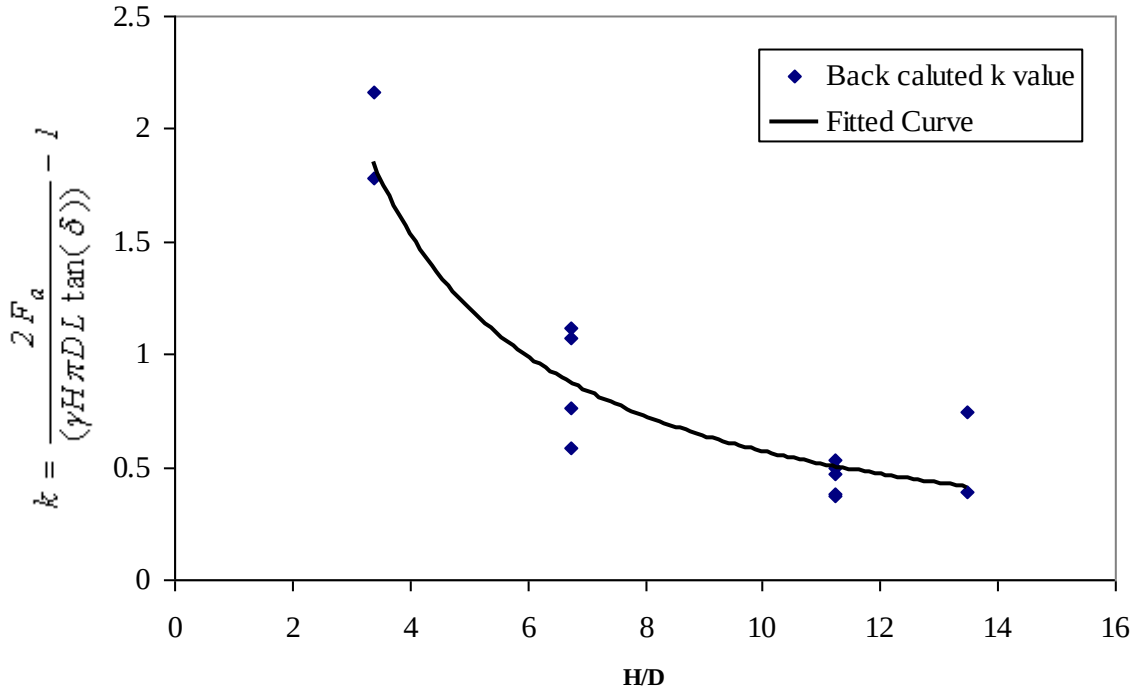

Figure 3-26: Variation of the back calculated value of *k* with burial depth ratio

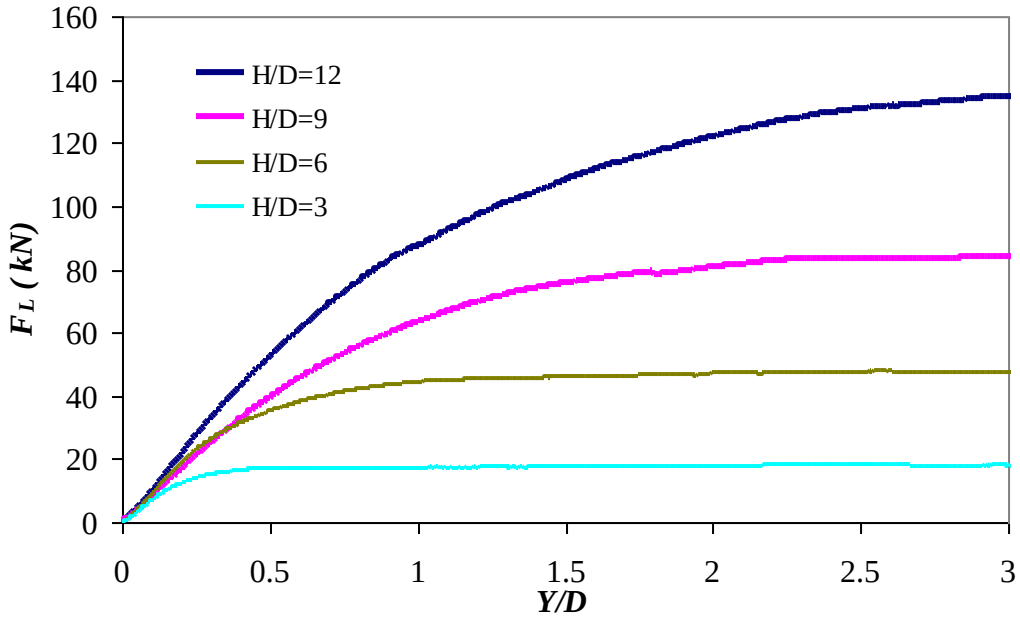

Figure 3-27: Response of the buried cable in lateral pullout tests for burial depth of 3,6, 9, and 12.

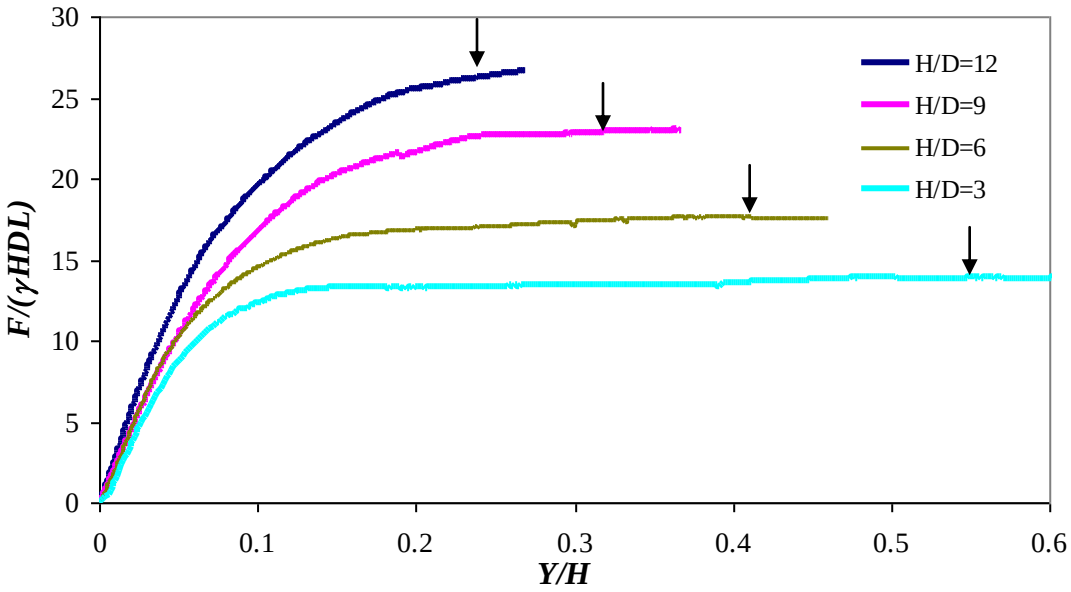

Figure 3-28: Non-dimensional force-displacement data for embedment ratio of 3, 6, 9, and 12.

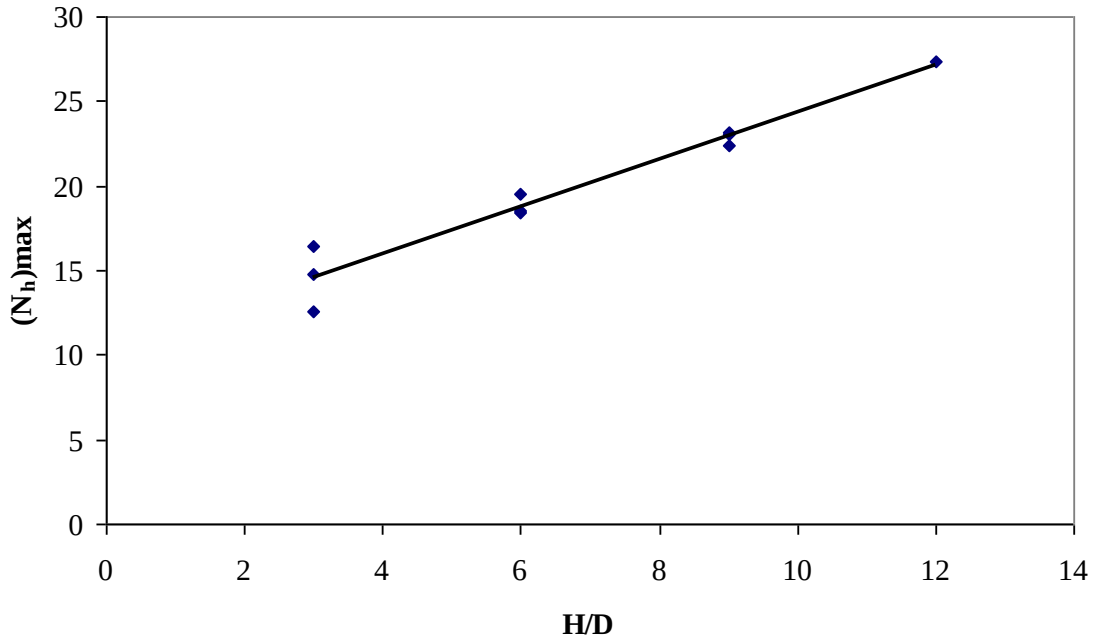

Figure 3-29: Plot of horizontal transverse force factor (N_h) versus burial depth ratio (H/D) for all tests

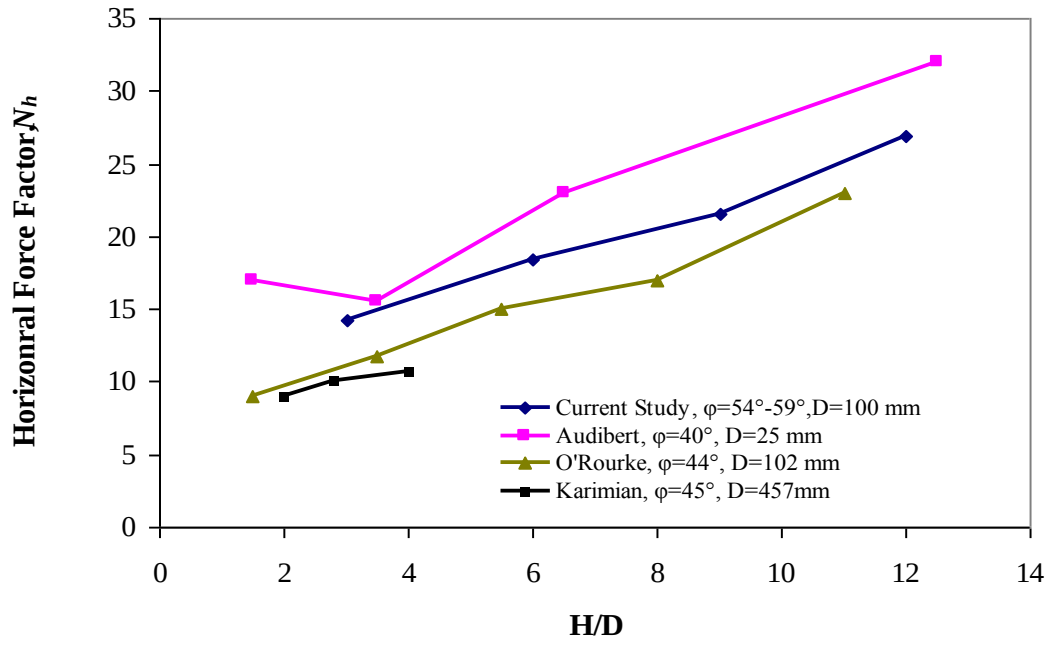

Figure 3-30: Comparison of the current lateral pullout tests with experimental studies by Trautmann and O'Rourke (1985), Audibert and Nyman (1977), Karimian (2006).

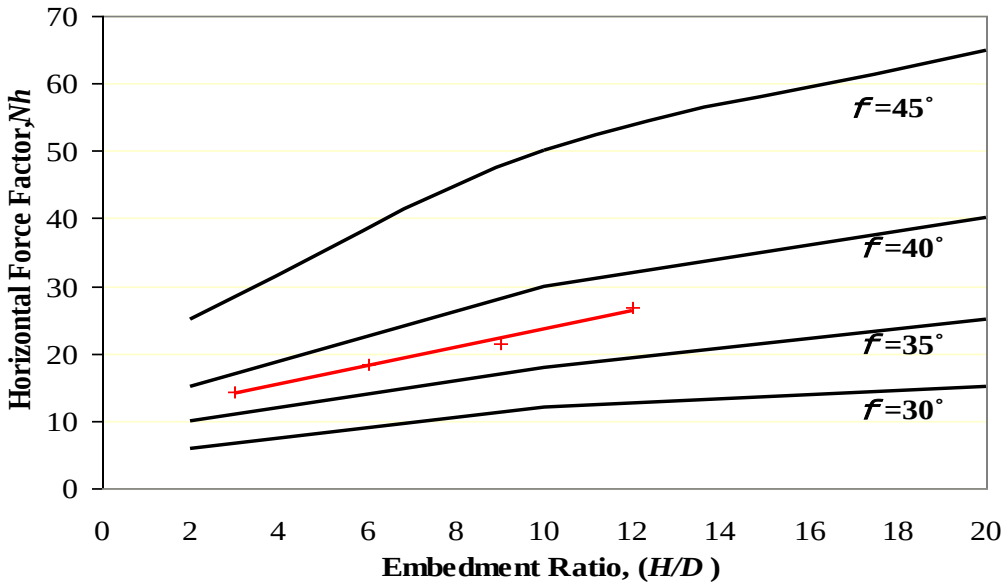

Figure 3-31: Comparison of current studies (red line) with analytical models based on the Hansen (1961), adapted from ASCE (1984)

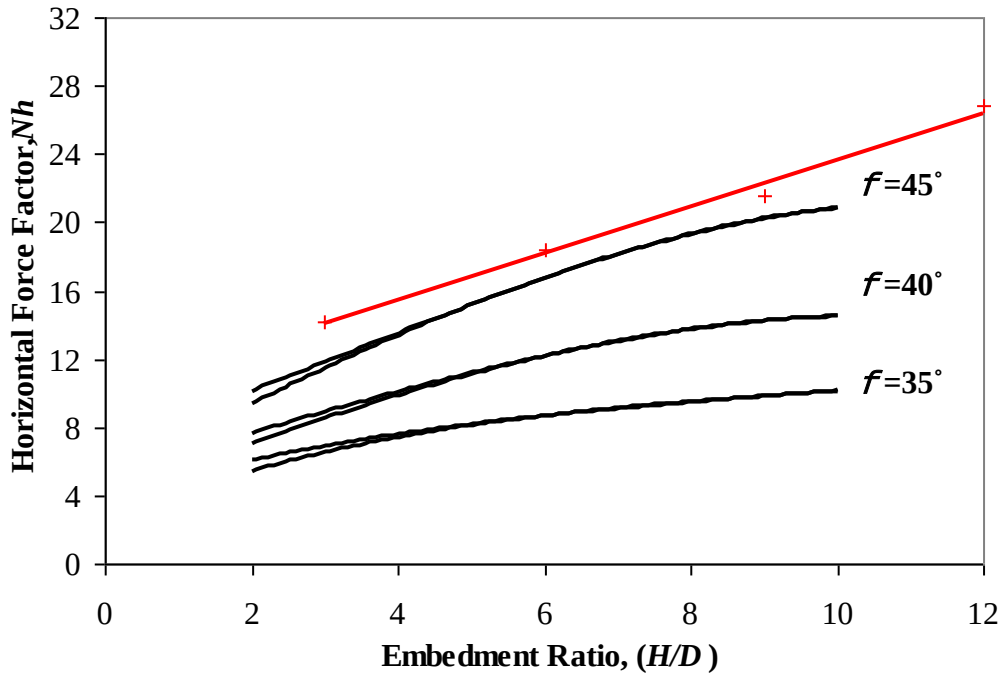

Figure 3-32: Comparison of current studies (red line) with analytical models based on the Ovesen (1964), after Trautmann and O'Rourke (1983), adapted from ASCE (1984)

Chapter 4: Numerical Simulation of Cable-Soil Interaction

Numerical models are critically important in analysis of the cable-soil interaction problem. Experimental studies conducted with selected cable diameter, length, stiffness and soil properties provide a good opportunity to validate numerical model. Once validated and calibrated, the numerical models can be employed to investigate the effects of different soils and geometric properties affecting cable-soil interaction. The numerical simulation will allow capturing the complexities in the soil behaviour in a fundamental manner. With this background, a numerical model was developed and the goals of this numerical simulation can be summarized as follows:

- Investigate the effects of nonlinear, stress-level dependent, and dilative soil behaviour on cable-soil interaction;
- Calibrate the numerical model with controlled experimental studies;
- Perform parametric studies for different cable-soil interaction scenario.

The cable-soil interaction is numerically modeled using nonlinear finite element program ABAQUS Ver. 6.7-1. (Hibbitt et al., 2007). ABAQUS is a software package that enables engineering problems with nonlinearity in material and geometry to be simulated. Extensive rich element libraries as well as the implicit and explicit methods of analysis make this software a good option for our numerical simulation. The reader is referred to Appendix B for a thorough descriptions on the element, material, contact types, and the method of analysis used in this section, and they are not described here.

This chapter consists of two main parts. In the first part, the numerical analysis of the lateral pull test is undertaken, and in the second part, the numerical analysis of the axial pullout test is conducted.

4.1 Numerical Simulation of Lateral Cable Pullout Testing

4.1.1 Elastic Analysis of Soil-Cable Interaction

The aim of this section is to present an examination of the initial part of the load-deformation curve (initial tangent stiffness) of the buried cable response with the help of controlled experimental and numerical simulation results. Initially, an analytical formula derived for a beam resting on linearly deformable elastic media will be reviewed with particular attention on the response of the beam resting on the elastic half space subjected to concentrated load at both ends. The analytical formula is revised to capture the initial tangent stiffness of the buried cable during lateral pullout test, and subsequently verified with the numerical simulation. The study of the initial tangent stiffness will help to effectively calibrate the numerical models with experimental studies.

Various soil response idealizations are discussed in detail by Selvadurai (1979). The soil idealizations include the Winkler model, elastic continuum, and two parameter models. In this part, our attention is focused on widely used model in practices, the Winkler model. The Winkler model is the simplest idealization of the soil medium. This model assumes that the contact pressure (p) at the soil structure interface is directly proportional to the soil deformation, i.e.

$$p(x) = k.y(x) \qquad \text{Eqn. 4-1}$$

where k is usually termed as a coefficient of subgrade reaction. In essence, the soil medium in Winkler model is virtually replaced by infinite set of uncoupled springs with the stiffness (k). The important feature of this model is that only the loaded region deforms and the displacement outside the loaded region is zero. It is apparent that this model cannot be a good representation of the soil medium. However, studies have shown that many engineering problems can be adequately idealized by Winkler model if the correct estimation of the coefficient of subgrade reaction can be achieved (Selvadurai).

Biot (1937) derived a solution for an infinite beam on an isotropic elastic medium subjected to a concentrated load by using elastic theory. Based on a comparison between the maximum moments by rigorous classic elasticity theory and formulation by Winkler model, the coefficient of subgrade reaction was suggested as a function of soil elastic parameters (E_s, v_s) and beam flexural stiffness (E_bI_b).

$$k = \frac{1.23E_s}{(1-\upsilon_s^2)}\left[\frac{E_s b^4}{16C(1-\upsilon_s^2)E_b I_b}\right]^{0.11} \qquad \text{Eqn. 4-2}$$

Vesic (1961) investigated the validity of the Winkler's hypothesis for a finite beam and examined the amount of error imparted by the Winkler's theory. He suggested a similar expression to the Biot's expression for the coefficient of subgrade reaction as

$$k = \frac{0.65E_s}{(1-v_s^2)}\sqrt[12]{\frac{E_s D^4}{E_b I_b}} \qquad \text{Eqn. 4-3}$$

and

$$k = \frac{0.65E_s}{(1-v_s^2)} \qquad \text{Eqn.4-4}$$

for a relatively long beams *(*L/D *>10*).

Results by Vesic indicate that the long beam analysis based on the Winkler's model gives accurate results, but the Winkler's hypothesis does not account the results for short beams. Vesic used the characteristic length (*λL)* to determine the limit that Winkler's hypothesis remains correct, where λ is a defined as

$$\lambda^4 = \frac{k}{4E_b I_b} \qquad \text{Eqn. 4-5}$$

According to the characteristic length (*λL*), beams were classified into four categories:

Class I. Short beams $\lambda L<0.8$

Class II. Beams with medium length $0.8<\lambda L<2.25$

Class III. Moderately long beams $2.25<\lambda L<5.00$

Class IV . Long beams $\lambda L>5.00$

Results by Vesic (1961) indicate that an analysis based on the Winkler's model gives reasonable results for class II, III, and IV.

4.1.1.1 The Static Stiffness of Rigid Beam in Elastic Half Space

The vertical and horizontal static stiffness (k_h and k_v) of embedded rigid cylindrical foundation in the elastic homogeneous half-space are taken from Pais and Kausel (1988) as follows:

$$K_h = \frac{8Ga}{2-\upsilon}(1+\frac{h}{a}) \text{ and } K_v = \frac{4Ga}{1-\upsilon}(1+0.54\frac{h}{a}) \quad \text{Eqn. 4-6}$$

where G is the soil shear modulus; h is the burial depth; and a is the foundation radius. The static stiffness for a buried cable can be approximated by defining the equivalent foundation radius ($\bar{a}$). It can be defined by equating the projected area of buried cable in the horizontal or vertical directions to the area of the circle with the equivalent radius as follows:

$$\bar{a} = \sqrt{\frac{LD}{\pi}} \quad \text{Eqn. 4-7}$$

where L and D is the buried cable length and its diameter.

4.1.1.2 The Static Stiffness of Flexible Beam on Elastic Half Space

The bending of a beam of finite element length on an elastic foundation as shown in Figure 4-1 was obtained by Timoshenko (1960). The flexibility of the beam causes non uniform deformation along the beam length. For instance, the deflections at the ends and mid point can be obtained as a function of characteristics length and applied load by the following expression:

$$y_{end} = \frac{2p\lambda}{k}\frac{\cosh\lambda L + \cos\lambda L}{\sinh\lambda L + \sin\lambda L} \qquad \text{Eqn. 4-8}$$

$$y_{mid} = \frac{4p\lambda}{k}\frac{\cosh\frac{\lambda L}{2}\cos\frac{\lambda L}{2}}{\sinh\lambda L + \sin\lambda L} \qquad \text{Eqn. 4-9}$$

with the damping factor

$$\lambda = \sqrt[4]{\frac{k}{4E_b I_b}} \qquad \text{Eqn. 4-10}$$

where k denotes the coefficient of subgrade reaction. The above expressions can be arranged to derive $k_t=p/y$, where y is the end displacement. The stiffness (k_t) for the beam ends can be rewritten as:

$$k_t = \frac{\sin\lambda L + \sinh\lambda L}{\cos\lambda L + \cosh\lambda L}.\frac{k}{2\lambda} \qquad \textbf{Eqn. 4-11}$$

The variation of k_t with regard to characteristic length (λL) is shown in Figure 4-2. In this graph the k_t is normalized to $kL/2$. As can be seen in this graph, the normalized k_t decreases by increasing characteristic length. The normalized k_t stiffness approaches unity for a small characteristic length ($\lambda L \to 0$) and approaches zero for a large characteristic length $\lambda L \to \infty$. An important feature of this graph is that for ($\lambda L < 1.35$), the normalized k_t stiffness can be assumed unity with less than 10 % error, for characteristic length ($1.35 < \lambda L < 2$) it drops

rapidly in a linear fashion, and for characteristic length $\lambda L > 8$ monotonically decreases to zero. By substituting the corresponding value for *k*, the k_t for a limiting case of a rigid beam ($\lambda L < 1.35$) can be obtained as

$$k_t = \frac{2}{\sqrt{\pi}} \frac{E\sqrt{DL}}{(2-\upsilon)(1-\nu)} (1 + \frac{\sqrt{\pi} h}{\sqrt{DL}}) \qquad \text{Eqn. 4-12}$$

For the characteristic length greater than 1.35, the k_t can be adopted by analogy with Vesic's expression for a beam on elastic half space. The complete description of this analogy can be found in next chapter. Therefore, the k_t stiffness can be derived as:

$$k_t = \frac{\sin \lambda L + \sinh \lambda L}{\cos \lambda L + \cosh \lambda L} \cdot \frac{1}{\lambda} \cdot \frac{1.3E_s}{(1+\nu_s)(2-\nu_s)} \sqrt[12]{\frac{E_s D^4}{E_b I_b}} (1 + \frac{1}{1 + \frac{1}{\frac{16}{\pi(2-\nu_s)} \cdot \frac{\sqrt{\pi} h}{\sqrt{DL}}}}) \qquad \text{Eqn. 4-13}$$

Figure 4-3 and Figure 4-4 illustrate the variation of the k_t versus the ratio of the soil elastic modulus to the cable elastic modulus $(Es/Ec)^{.089}$, and also versus the characteristic length (λL) respectively. This ratio between elastic modulus $(Es/Ec)^{.089}$ is selected to resemble the analytical formulation for k_t. In both figures, the cut off line, corresponding to the rigid beam behaviour (small λL), is also depicted to show that the using Vesic's formula is justified for sufficiently long beams.

In order to investigate the suitability of the analytical formula to predict k_t stiffness, numerical simulations were conducted. Furthermore, this model will serve later as a prototype for a calibration of numerical simulation with the experimental studies. A numerical model of the beam-soil interaction model with the burial depth of 0.9 m was built. The beam is assumed to be an elastic hollow cylinder with the diameter of 0.1 m, thickness of 0.01 m, and 2.15 m long. This dimension resembles the lateral cable pullout testing. The soil is an isotropic elastic media with ν_s=0.3. The numerical model is depicted in Figure 4-5. The pullout forces (*P*) are applied at both cable ends, and the corresponding force-displacement curve is obtained for various model parameters. The main model parameter

selected in this study is the beam elastic modulus (E_c or E_b) and the soil elastic modulus (E_s). Since beam with different flexibility can be simulated by assigning different value for E_c , the soil modulus of elasticity is set to the conventional values of 1,10, and 100 MPa, and the beam elastic modulus is varied to cover the beam with rigid behaviour and the beam with cable like behaviour. Figure 4-6 shows the variation of k_t stiffness as a function of $(Es/Ec)^{.089}$ for the soil with the elastic modulus of 1,10, and 100 MPa. The horizontal axis is selected as $(Es/Ec)^{.089}$ since the analytical formula for initial k_t suggests this relation. The analytical formula is also depicted with solid line in the same figure to verify the analytical formula prediction for the k_t stiffness. As can be seen, the analytical formula gives satisfactorily prediction for k_t stiffness. The application of the proposed analytical formula will be discussed in the next chapter in the effect of the out-of-straightness on the axial soil force on the cable.

4.1.2 Nonlinear Analysis of Cable-Soil Interaction

The previous section deals with the elastic analysis of the soil cable interaction. In this section, the nonlinear response of cable-soil interaction will be investigated. The cable and soil are modeled independently in ABAQUS program, and they interact with each other via the contact element. The detail of this modeling is as follows.

The numerical modeling of the cable is preferably performed by an equivalent cable. This modeling method is preferred to the detail modeling of the whole cable since the aim of finite element modeling is to simulate the load-deformation curve of the cable response as observed during the experimental studies. Secondly, the equivalent cable adequately captures the flexural and axial stiffness of the cable providing the necessary information to simulate the cable-soil interaction.

The interface between soil and cable is an important consideration in modeling the interaction between the buried cable and surrounding soil. As such, the buried cable cannot be modeled using the one dimensional elements such as beam, or truss elements. The best

approach to develop the equivalent cable idea is to assess the mechanical properties of cable compartment individually contributing to the flexural and axial stiffness of the cable. The real cable section consists of: polyethylene jacket, aluminum sheath, paper insulation, and copper core. The oil impregnated paper insulation has a protective purpose and has no significant mechanical properties. However, it can create a confinement around the copper core to provide stability for the core while in compression. The polyethylene jacket and aluminum sheath, located at the outer surface of the cable, are components contributing to the flexural stiffness and axial stiffness of the cable. The copper core, located at the center of the cable, is mainly responsible for the axial stiffness of the cable. Observation during experimental testing and evidence from three-point-bending tests indicate that the cable flexural stiffness is not substantial in compare to axial stiffness of the cable. Indications of this statement are the ability to coil the cable around the reel and low maximum point force in the three-point bending test. Therefore, the effect of the flexural behaviour of buried cable can be ignored for a long cable.

Based on the above, the equivalent cable was represented by creating a hollow section with the same diameter as the cable so that the interacting surface is retained. The thickness of the hollow section was assumed to be the total thickness of the polyethylene jacket and aluminum sheath. The material properties of the hollow cross section were estimated by calibrating with experimental results. The equivalent elastic modulus (E_{eq}), which will be used as E_c, is assumed to be the parameter required to create a match between numerical simulation and experimental data. Then a beam element is coupled coaxially to the hollow section structure. The beam has the same mechanical properties as the copper core, i.e., the area and moment of inertia. Consequently the buried cable finite element modeling resulted in a hollow section with the diameter of 100 mm and thickness of 10 mm. A uniform mesh of fully integrated 8-node continuum C3D8 element was used. Figure 4-7 shows the mesh configuration of the hollow section. Core is modeled with the beam element B31, 2-node element with linear interpolation function. Kinematics coupling is applied to constrain the degree of freedom of nodes on the hollow section to that of the beam so that the translation

movements of nodes on the hollow section occur together with inside core nodes as shown Figure 4-8.

Soil was modeled as a continuum three dimensional medium using C3D8 element. The dimension and boundary conditions of the model were defined similar to the condition of full-scale tests. As described in Chapter 3, length and width of soil model were selected as 3.75 m and 2.15 m respectively, and the height of soil model varies depending on burial depth. Soil nodes on the boundary are restrained against lateral movement, but are allowed to move vertically. The mesh configuration for the soil was selected so that the numerical results were not mesh-sensitive. Some key criteria considered in selecting an appropriate mesh configuration are: the convergence, the analysis time and accuracy. After examining several mesh configurations for convergence and minimum analyses time, those mesh configurations as shown in Figure 4-9 were selected. Two constitutive material models were selected to represent the soil behaviour: the Mohr-Coulomb and Drucker-Prager material models. The description of these two material models is presented in details in Appendix B. The results of analysis by those two material models are presented separately in the next sections.

4.1.2.1 Numerical Simulation Using Mohr-Coulomb Material Model

The Mohr-Coulomb material model in ABAQUS shows an elastic behaviour in the small strain range when the stress state is within the yield surface, and exhibits the plastic behaviour when the stress state is on the yield surface. The elastic part of the Mohr-Coulomb plasticity model uses linear isotropic elasticity based on the Cauchy stress model. The model requires the elastic modulus (E), Poisson's ratio (ν), friction angle (ϕ), dilation angle (ψ), meridional eccentricity, and deviatoric eccentricity to describe the elastic and plastic behaviour of the material. The summary of Mohr-Coulomb model parameters is presented in Table 4-1. The table shows that some parameters are set to their conventional values and others are set to a range.

In general, the soil Young's modulus for different types of soils is a function of confining pressure, initial stress state, stress history, long term and short term loading, and relative density (D_r), (Das 1979). Modulus of elasticity is often obtained from deviator stress versus axial strain curve from a tri-axial laboratory test. Two types of modulus can be defined for such a curve: the tangent or secant modulus. Those two modulus types are not constant for a soil and they must be defined based on the stress level. Since the Mohr-Coulomb material model in ABAQUS is elastic until the stress state reaches to the yield surface, a secant elastic modulus should be selected to represent the soil elastic behaviour (Karimian 2005). For instance, Byrne et al. (1987) and Karimian (2005) used one third of tangent modulus in their numerical works as a secant elastic modulus. Since no triaxial testing data is available for the thermal backfill material the typical range of the soil elastic modulus and Poisson's ratio for loose and dense sandy and gravelly material, as indicated by Das (1979), are used as a guideline for performing the parametric study in this research. The representative value of the soil tangent elastic modulus varies in the range of 20,000 to 200,000 kN/m^2 for loose and dense sandy and gravelly material respectively and the representative values for Poisson's ratio vary in the range of 0.1 to 0.4. It should be mentioned those typical values vary depending on the stress history, stress level, density, and etc. Byrne et al. (1987) showed that Poisson's ratio varies between 0.1 to 0.5 for small strain levels and strains at failure for a sand mass. In this research, the constant Poisson's ratio of 0.3 is assumed. Two different soil elastic moduli E_s=6,000 and E_s=60,000 kN/m^2 are selected in the parametric study. The variations in the friction angle and dilation values are discussed in part 4.1.2.1.2 of this section.

4.1.2.1.1 The effect of cable/soil relative stiffness

The aim of this part is to study the effect of cable/soil relative stiffness on the force-displacement curve during lateral pullout tests. Most of the previous numerical studies were performed on the plane strain condition such as the problem of the rigid pipeline system where the pipeline remains straight during pullout; however, cases exist which the plane

strain assumption is invalid such as the current study of the buried cable response. The three dimensional numerical simulation in this section gives this opportunity to investigate further the effect of the three dimensional analysis of the lifeline system. Studies on the response of the cable buried in the elastic medium shows that the relative flexural stiffness of the cable to the soil stiffness plays an important key parameter to define the response of buried cable during lateral movement. As mentioned by Selvadurai (1971), characteristic length (λL) is the best parameter to characterize the relative stiffness of the cable-soil system. The characteristic length (λL), used here in this study to account for the relative cable-soil stiffness parameter, is defined as

$$\lambda L = \sqrt[4]{\frac{kL^4}{4E_C I_C}} \qquad \text{Eqn. 4-14}$$

in which

$$k = \frac{2.6E_s}{(1+\nu_s)(2-\nu_s)}\sqrt[12]{\frac{E_s D^4}{E_b I_b}}\left(1+\frac{1}{1+\frac{1}{\frac{16}{\pi(2-\nu_s)}\cdot\frac{\sqrt{\pi}h}{\sqrt{DL}}}}\right) \qquad \text{Eqn. 4-15}$$

Different values of the characteristics length are the representative of different relative cable-soil stiffness. In order to investigate the effect of the relative cable-soil stiffness together with the effect of soil plasticity on the horizontal transverse response of the buried cable, numerical analyses were performed which results were summarized in four graphs(Figure 4-10 to Figure 4-13). Two graphs are plotted for the soil with the elastic modules of 6 MPa ,the friction angle of 41° and two different dilation angles. Figure 4-10 shows the force-displacement response of cable with the burial depth of 0.9 m with characteristic lengths ranging from 6 to 40, the soil material model has the friction angle of $\varphi=41°$ with associated flow rule (ψ=38°). It should be noted that Mohr-Coulomb material model implemented in ABAQUS program does not allow $\psi=\varphi$ for associated flow rule. Figure 4-11 shows the force-displacement response for the same parameter but with the non-associated flow rule ($\psi = 21^\circ$). Two other graphs were also prepared for the soil with the elastic modulus of 60

MPa, different characteristic lengths ranging from 11 to 74 and the other remaining parameters remained the same as before. Figure 4-12 shows the force-displacement curve when the flow rule is associated and Figure 4-13 shows the force-displacement curve when the flow rule is non-associated ($\psi = 21^{\circ}$). As can be seen from those graphs, the following observation can be concluded: the load-displacement curves follows a hyperbolic shape, and its shape is influenced by the cable/soil relative stiffness, curves with small λL approaches to the asymptotic value at lower displacement. However, the asymptotic values are less affected by changes in the λL parameter, and smaller λL tends to have a higher asymptotic value than a larger λL.

4.1.2.1.2 The effect of friction angle and dilation parameters

As discussed in appendix B, Mohr-Coulomb material model requires many variables to define both the yield surface and potential surface. The most important variables, which significantly influences the yield and potential functions, are friction angle (φ) and dilation angle (ψ). These two parameters can be directly related to the results of the laboratory element testing such as direct shear tests or triaxial tests. A numerical model as described in the previous section was used in this section. The aim of numerical studies in this part is to assess the effect of the material model parameters on the load-deformation curve. In order to assess the effect of individual model parameters on the response of the buried cables, systematic numerical finite element analyses were performed as follows: based on the laboratory element testing on the thermal backfill material, an estimation of Mohr-Coulomb material parameter can be established. Successively, the sensitivity studies were performed around those estimated parameters. The (φ) parameter was varied from 33° to 47 °, and in order to assess the effect of the flow rule, both the non-associated and associated flow rule were considered. When the non-associated flow rule is selected the representative parameter (ψ) was changed to different values provided that ($\psi < \varphi$). It should be noted that the numerical stabilities in the ABAQUS program does not allow ψ close to φ; consequently, the maximum limit for ψ without any numerical instabilities was achieved if ($\psi \leq \varphi - 3°$).

The load-deformation relationships given by the finite element analyses for embedment depth ratio H/D=9 is shown in Figure 4-14 and Figure 4-15. Figure 4-14 shows this relationship for different friction angle and the associated flow rule, and Figure 4-15 shows the same relationship for different friction angle non-associated flow rule with $\psi=20°$. The load-deformation curve in each plot follows a hyperbolic curve with the horizontal asymptote. Larger value of friction angle and dilation angle parameters cause the load-deformation curve ending up at a higher plateau, and they also tend to increase the curvature of load-deformation curve. In order to clearly assess the effect of these two parameters on the peak value of the load-displacement curve, graphs were prepared showing the variation of the horizontal force factor (N_h) as a function of the dilation angle and as a function of a friction angle for a specific case of cable with burial depth of 0.9 *m* and λL=21. Figure 4-16 shows the variation of the horizontal force factor with friction angle (Nh-φ), the graphs are shown for different dilation angle. As depicted, the horizontal force factor for the specific dilation angle is an ascending function of friction angle. Figure 4-17 shows the variation of the horizontal force factor with the dilation angle. The same relationship as observed for (N_h-φ) also exists between the horizontal force factor and dilation angle (N_h-ψ); however, the amount of increase in the N_h factor due to increase in the dilation angle is much less than the amount of increase in the N_h factor due to increase in the friction angle. This observation can be realized by fitting a line through the points in each graph. The fitted line in the N_h-φ curve with constant dilation angle has five times greater slope angle than that in the N_h-ψ curve with constant friction angle.

4.1.2.1.3 Calibration and verification of numerical models

The results of sensitivity analyses and the results of the targeted laboratory element testing on the thermal backfill material were used to calibrate the numerical models with the experimental tests. First, the numerical results are calibrated with the experimental results of cables with burial depth of 0.9 m, and then they are validated by means of comparing the

results of finite element analysis with the experimental results of lateral pullout tests with burial depths of 0.3, 0.6 and 1.2 m.

The results of targeted laboratory element testing indicates that the thermal backfill material has the constant volume friction angle of 41° and the dilation angle can reach up to 20°, depending of the amount of compaction, according to Bolton equation as described in Appendix B. Numerical calibrations were started off with the help of laboratory element testing and other soil parameter models. The comparisons of different numerical simulation models reveal that the numerical model with the friction angle φ=39º, dilation angle ψ=18º, λL=37, and E_s=10 MPa can adequately represent the load-deformation curve of experimental results for embedment ratio of 9 as depicted in Figure 4-18. The square root of sum of square was used to define the best possible match between different numerical simulation and experimental study results. The small friction angle for the numerical model might be attributed to the fact that the rigid boundary conditions in the direct shear tests create an over constraint for the soil; therefore, the soil behaves stronger than the real condition when the soil has the softer boundary condition. Typical displacement contours, obtained at the end of geostatic analysis and after 30 cm pulling of the buried cable, are shown Figure 4-19. The displacement contours of the soil after 30 cm pulling of cable shows that the active and passive wedges are not interfered by the presence of fixed boundaries. This observation implies that the back and front wall allow the complete formation of the active and passive wedges.

The test results of experimental studies of different burial depths give this opportunity to verify the numerical models. Numerical models with different burial depths were constructed and the same material parameter model as obtained in the model calibration was used for the material model properties. Figure 4-20 shows the comparison of the load-displacement curve of experimental tests and that of numerical simulation. As the comparison reveals, the numerical model can adequately predict the load-displacement curve for other burial depths.

One of the drawbacks of the experimental tests is the limited size of the soil chamber to obtain the response of the buried cable for the large burial depth. After the verification of

numerical models with experimental test results, the numerical model was extended fur to cover the cable with the different burial depths that load-deformation curve are not available. Numerical simulations were conducted for the cable with the embedment ratio of 15 and 18. Figure 4-21 shows the load-deformation curve for the cable with different burial depth ranging from 3 to 15. The horizontal force factors (N_h) for the cable with different burial depth were calculated, and they were presented as a function of burial depth as shown in Figure 4-22. Also, the horizontal force factors as obtained by experimental test were depicted in the same figure.

4.1.2.2 Numerical Simulation Using Drucker-Prager Material Model

The other material model which extensively used in the geotechnical engineering is the Drucker-Prager model. In this part, the numerical simulations with the Drucker-Prager material model are conducted to investigate the response of buried cable. The mesh configuration and model dimension are selected the same as the one selected for numerical simulation with Mohr-Coulomb material model. To achieve this goal, parametric studies were performed to study the effect of the cable/soil relative stiffness, the effect of Drucker-Prager material model, and the effect of the flow rule on the load-displacement curve. Table 4-2 summarizes model parameters used in the numerical simulation, and the details of this investigation are described in the following section.

4.1.2.2.1 The effect of soil/ cable relative stiffness

Similar to the numerical simulation with Mohr-Coulomb material model, at first the effect of soil/cable relative stiffness is evaluated. The parameter λL presents the soil/cable relative stiffness, and it varies to cover the very flexible cable behaviour to the rigid cable behaviour. Two types of the soil model are assumed, the non-dilatant soil model with associated flow rule and dilatant soil model with the non-associated flow rule. In order to reduce the number of the parameters, the friction angle (β parameter in the Drucker-Prager model) is set to be

47°, the soil elastic modulus (*E*s) is set to 6 MPa and 60 MPa, and the burial depth is 0.9 m. Those values are set to be representative of the conventional values for thermal backfill material.

The load-deformation curves for the cable with different characteristic lengths (λL) are shown in Figure 4-23 to Figure 4-26. Figure 4-23 and Figure 4-24 show the load-displacement curve for soil with elastic modulus of 6 MPa and the soil model with non-dilatant flow and dilatant flow respectively. The next two graphs, Figure 4-25 and Figure 4-26, are prepared for the soil with the elastic modulus of 60 Mpa, and the soil model with non-dilatant flow and dilatant flow respectively. Those graphs can be compared with respect to their maximum asymptote value and corresponding displacement at which the load-deformation curves get to their maximum value. As can be observed, the buried cable with lower λL value reaches to its asymptote value at lower displacement, and the corresponding asymptote value is larger than its counterpart with higher λL value. Also, the maximum asymptote value occurs at a lower displacement for higher E_s even the value of λL is the same. The flow rule affects the shape of the load-displacement curve. The load-deformation for material model with dilatant flow has a higher plateau value. In the following section, the effect of material model parameters will be investigated further.

4.1.2.2.2 The effect of friction angle and dilation parameters

The effects of friction angle (β parameter) and dilation angle (ψ parameter) on the load-deformation curve were investigated by setting the other parameters to their conventional value and varying β and ψ parameters. The elastic soil modulus is set to 6 MPa, λL value is set to 0.8, friction angle (β) varies from 35° to 50°, and different flow rules are studied. Figure 4-27 shows load-displacement curves of non-dilatant soil for different friction angles (β), and Figure 4-28 shows the load-displacement curve of dilatant soil (ψ=25°) for different friction angles (β). To show the effect of dilation angle on the load-displacement curve, Figure 4-29 is prepared for the friction angle of (β=47°). As presented in those graphs, the

load-deformation curve is significantly affected by the changes in the friction angle (β) value, especially the asymptote value. However, the dilation angle does not change the asymptote value significantly as the friction angle does, and it tends to change the load-deformation shape, i.e., the path that load-displacement curve gets to its asymptote value.

4.1.2.2.3 Calibration and verification of numerical models

Numerical simulation with Mohr-Coulomb material model indicated that the experimental test results can be adequately achieved by using φ=39° and ψ=18°. This information is used to facilitate the calibration of the numerical simulation based on the Drucker-Prager material model. As mentioned in Appendix B, many relations can be found relating the Mohr-Coulomb material model parameters to the Drucker-Prager material model parameters. The most recognized expressions are those which matched under plane strain conditions or under the triaxial stress conditions. Those expressions express the relationship between φ and c of the Mohr-Coulomb material model to β and d of Drucker-Prager model. For instance, under the plane strain condition the Mohr-Coulomb parameters can be converted to Drucker-Prager parameters for associated flow (those relationships were described in more details in Appendix B)

$$\tan(\beta) = \frac{3\sqrt{3}\tan(\varphi)}{\sqrt{9+12\tan^2\varphi}} \quad \text{and} \quad d = \frac{3\sqrt{3}c}{\sqrt{9+12\tan^2\varphi}} \qquad \text{Eqn. 4-16}$$

Using the relationships under the plain strain condition, the Drucker-Prager parameters can be obtain as β=45.7° and d≈0 for the associated flow rule and β=47.5° and d≈0 for non-associated flow rule. However, few relationship exists that can directly relate the dilation angle of Mohr-Coulomb model to that of Drucker-Prager model. One of this few relationship for obtaining the Mohr-Coulomb dilation angle ($\psi_{Mohr-Coulomb}$) based on the Drucker-Prager dilation angle ($\psi_{Drucker-Prager}$) under the plain strain conditions and the associated flow rule in the Drucker-Prager material model ($(\psi)_{Drucker-Prager} = \beta$) is :

$$(\tan\psi)_{Mohr-Coulomb} = \frac{3-\sin\varphi}{6\cos\varphi}(\tan\psi)_{Drucker-Prager} \quad \text{Eqn. 4-17}$$

This equation can be used to approximately back calculate the Drucker-Prager dilation angle based on the $\psi_{Mohr-Coulomb}$. This formula gives $(\psi)_{Drukcer-Prager} = 32.6^{\circ}$.These estimations of the Drucker-Prager model parameter facilitates the calibration of the numerical model to the experimental test results. The comparisons of different numerical simulation models reveal that the numerical model with the friction angle of (β=49˚), dilation angle of (ψ=33˚), λL=37.0, and *Es=10* MPa can adequately represent the load-deformation curve of experimental results for embedment ratio of 9 as depicted in Figure 4-30. Figure 4-31 shows the comparison of the load-displacement curve of experimental tests and that of numerical simulation for burial depth of 30, 60, and 120 cm. As can be seen, a close match between the numerical simulation and experimental tests for different burial depth can be achieved. However, comparison between the validation by Mohr-Coulomb and Drucker-Prager models (Figure 4-31 and Figure 4-20) shows that Mohr-Coulomb material model provides the closer match to experimental test results.

4.2 Numerical Simulation of the Longitudinal Behaviour of the Cable-Soil Interaction

Numerical modeling was undertaken to capture the overall response of the longitudinal behaviour of the buried cables. It also helps to determine some important characteristics of the cable-soil behaviour in more fundamental manner.

4.2.1 Issues Relating the Longitudinal Behaviour of the Buried Cable

As mentioned in the experimental study of the cable-soil interaction, three important behaviours of the cable-soil interaction observed in the axial pullout tests are: 1) the cable's front and tailing ends move together in harmony, 2) the axial pullout force experiences the peak and follows a drop at low displacement, and 3) the axial pullout force increases by

further increase in the axial pullout displacement. The first observation can be inferred as the simultaneous frictional force mobilization along the cable shaft, and can be attributed to the large axial stiffness of the cable. The second observation is due to the shear-induced volumetric strains in region around the cable affecting the normal stress distribution around the cable. The third observation is attributed to the out-of-straightness of the cable. A full discussion about dilation around the pipeline in dense material can be found in Wijewickreme et al (2009). The aim of this section is to develop a numerical model that can assess the effect of out-of-straightness on the longitudinal behaviour of the buried cable.

4.2.2 Developing of Numerical Model

The longitudinal behaviour of the buried cable with the out-of-straightness can be investigated by analyzing the axial pullout response of the cable with different layout patterns. The aim of this numerical simulation is to quantify how the cable's out-of-straightness can affect the longitudinal behaviour of the buried power transmission cable in compared to the response of the straight cable.

As indicated earlier, the cable out-of-straightness can naturally occur during cable installation. In order to investigate the effect of the cable's out-of-straightness, two models were analyzed: the straight cable and various cables with different layout shapes. The response of the straight cable was selected as the bench mark analysis to explain any disparity in the response of the curved cable. The selection of the curved shape of the buried cable was challenging since: 1) the shape of the cable is irregular and no definite shape can be assigned to it, 2) the amount of curvature is unknown, and 3) the cable is curved arbitrarily in the three-dimensional space. In considering these issues, the cable with horizontal out-of-straightness with the maximum offset at midpoint as shown in Figure 4-32 was assumed. The cable was curved with the maximum offset in the middle and was straightened out at two ends. The mathematical formula assigned to the cable shape was

$$\delta(x) = \delta_{\max} \cos^2(\frac{\pi.x}{L})$$ Eqn. 4-18

in which δ_{max} is the maximum offset in the middle of the cable and L is the cable length. The cable with the offset was produced by connecting the points by a spline curve generator, available in the ABAQUS 6.7.1 drawing tools. The spline curve generator produces a continuous cubic function between points. The amount of the offset (δ_{max}) in the center of the cable was varied from 0 (cm) to 5 (cm). The length of the cable (L) is assumed to be the same as the length of the chamber box in the experimental study (L=3.75 m).

The same modelling approach as described previously in the numerical simulation of the lateral pullout test was used herein to model the cable structure. The cable was replaced by the equivalent cable. The equivalent cable consists of the hollow cylindrical section to model its flexural behaviour with the coaxial rod element to model its axial behaviour. The soil model was created by cutting through the cable shape so that the perfect fit between the soil and the buried cable was formed. Figure 4-33 depicts the mesh configuration for the cable with the burial depth of 30 cm and horizontal offset of 5 cm. The model was divided into two segments at the cable centerline to show the layout of the cable. The samples of the mesh configuration for the cable-soil interaction model for the cable with burial depth of 30, 60, 90, and 120 cm are depicted in Figure 4-34. Eight-node quadrilateral continuum element (C3D8) was used to model both the cable and the soil. As can be seen, the finer mesh was used in the zone around the buried cable. The interface between the buried cable and the soil was modelled by a contact element. The Coulomb friction model with the constant friction coefficient of f was used to model the tangential behaviour. The normal behaviour of the contact element was defined as a "hard contact". A detailed description of the contact models are presented in Appendix B. For the nonlinear analysis, the Mohr-Coulomb material with the non-associated flow rule as obtained in the lateral pullout simulation part (φ=39° and ψ=18°) was selected for the soil.

Analysis is performed into two steps. In the first step, geostatic analysis was performed to obtain the initial stress in all soil elements and on the cable interface. In the second step, the

cable was pulled out from the chamber. Implicit static analysis was performed to measure the deformation and corresponding load required for the cable pullout. In the next part, numerical simulations are conducted to investigate the effect of different parameters on the longitudinal behaviour of the buried cable.

4.2.2.1 The Effect of the Cable Out-of-Straightness on the Longitudinal Soil Loads on the Cable

The effect of out-of-straightness on the longitudinal behaviour of cable/soil interaction is investigated by creating three numerical models. The first model is the buried straight cable (δ/L=0%), the second model is the buried curved cable with the maximum horizontal offset of 2 cm (δ/L=0.53%), and the third model is the buried curved cable with the maximum horizontal offset of 5 cm (δ/L=1.33%). The maximum limit of δ/L=1.33% is selected since larger horizontal offset activates horizontal lateral soil restraint, and it obscures the interpretation of results. Figure 4-35 shows the longitudinal response of the cable for burial depths of 30, 60, 90, and 120 cm when the cable has an offset ratio of δ/L=0%, δ/L=0.53%, and δ/L=1.33%. This graphs are prepared when the interface soil/cable friction angle (f) is 0.7, the soil elastic modulus is E_s=10 Mpa, and the relative soil/cable stiffness (λ) is 4.7/m. As can be seen, the axial pullout force in the cable increases with the burial depth. Also, the cable without horizontal offset has no stiffness hardening, i.e., after yielding occurs the axial pullout force remains the same. However, the cable with larger horizontal offset shows a greater stiffness hardening ratio after yielding. Figure 4-36 shows the normal contact stresses at the cable/soil interface after geostatic analysis and after 30 cm pulling of the cable. Those figures clearly show an increase in the normal stress after pulling out the cable by 30 cm, and consequently increase the axial pullout force.

4.2.2.2 The Effect of the Cable Flexibility

As demonstrated in the previous section, offset ratio tends to increase the stiffness hardening in axial load-deformation curve for the cable with different burial depths. Two extreme cases can be assumed for the cable rigidity: a very flexible cable and the rigid cable. The rigid cable does not deform and it creates more stress to the surrounding soil. However, a very flexible cable easily deforms and it less stress normal stresses imposed on the interacting soil. In order to understand this effect, two soil models with elastic modulus of E_s=10 and E_s=20 MPa are considered. The same nonlinear parameters were assumed for the soil Mohr-Coulomb model (φ=39˚ and ψ=18˚). Three configurations are assumed for the cable (δ/L=0%, δ/L=0.53%, and δ/L=1.33%). Figure 4-37 shows the longitudinal load-deformation curve for the soil with E_s =10 MPa and the cable with the flexibility factor of λ=4.7, 3.0, and 2.5 /m.

Figure 4-38 shows the longitudinal load-deformation curve for the soil with E_s =20 MPa and the cable with the flexibility factor of λ=5.6, 3.7, and 3.0 /m. The flexibility factors (λ) for two soil models are different since λ is a function of the E_c/E_s ratio. Changing in the soil elastic modulus affects the E_c/E_s ratio and consequently changes the flexibility factor. As apparent in those graphs, the cable with offset ratio has a larger increase in the axial pullout force. Furthermore, the cable with smaller flexibility factor, i.e. rigid cables, has more stiffness hardening since smaller flexibility factors represent more rigid cable. Comparing the results of the axial pullout force for the soil with elastic modulus of 10 and 20 MPa shows that the soil with higher elastic modulus creates more axial pullout force. In order to conceive the importance of the soil elastic modulus, two numerical analyses are conducted. In this analysis, two soil models are selected with elastic modulus of 10 and 20 MPa. However, the cable elastic properties are changed so that the same flexibility factor λ obtained. Figure 4-39 compares the axial pullout force for the same flexibility factor (i.e. E_c/E_s=constant) but for the soil with different elastic modulus to demonstrate the importance of elastic soil modulus.

As can be seen, the soil with higher soil elastic modulus creates more stiffness hardening in the load-deformation curve.

4.2.2.3 The Effect of the Cable/Soil Interface Friction Angle

All the previous results were performed when the interface cable/soil friction angle(f) is 0.7. In order to study the effect of interface cable/soil friction angle on the longitudinal load-deformation curve, analyses were performed for the cable with offset ratios (δ/L=0%, δ/L=0.53%, and δ/L=1.33%), burial depth of 60 cm (H/D=6.7), and the soil elastic modulus (E_s=10 MPa). The results of these analyses are shown in Figure 4-40. As predicted, increasing the interface cable/soil interface friction angle causes an increase in the axial pullout force. The increase in the axial pullout force can be linearly interpolated between different interface cable/soil friction angles. The numerical simulation results and experimental results are compared in Figure 4-41 for burial depth of 30 and 60 cm. In the numerical simulation, the interface soil/cable friction (f) is 0.7, and the offset ratio is 1.33 %. It should be mentioned the amount of offset in the experimental studies is unknown, and it is difficult to compare the results of experimental and numerical simulation. However, the results of numerical simulation with 1.33% offset ratio matches the mean of the experimental studies.

4.2.3 Summary of the Chapter

This chapter investigates the response of the buried power transmission cables in the horizontal transverse and longitudinal directions through numerical simulations. The aim of the numerical model was mainly to study the ability of numerical simulation to predict the response of the buried cable and to gain an understanding on the effect of different parameters on soil loads on buried cables. Two separate numerical models were developed for the horizontal transverse and the longitudinal directions to simulate the experimental results of lateral pullout and axial pullout tests.

In the numerical simulation of lateral pullout tests, numerical models were developed according to the lateral pullout test setup. The effects of different factors such as soil model types (Mohr-Coulomb and Drucker-Prager models), soil parameter models (soil elastic modulus, friction angle (φ ,β), dilation angle (ψ)), relative soil/cable stiffness, and burial depth (H)) on the response of the buried power transmission cables were investigated. With the help of laboratory element testing on the thermal backfill material, the numerical model was calibrated to the burial depth of 90 cm. Then, the numerical simulation was validated for other buried depths of 30, 60, and 120 cm. Some of the key findings and observations from numerical simulations are summarized herein:

- Although Drucker-Prager material model provides a smooth yield surface offering best numerical convergence in compared to the Mohr-Coulomb material model, the Drucker-Prager model parameters cannot directly be related to the physical terms. In contrast, the Mohr-Coulomb model parameters can be directly related to the results of laboratory element testing such as direct shear tests causing the calibration of numerical models simpler. Besides that, the validation results show that both material models are capable to predict the result of the experimental studies.

- Parametric studies were performed to investigate the effect of different parameters on the response (load-deformation) of the buried cable. It was found that the representative parameter for the friction angle (β or φ) in both Drucker-Prager and Mohr-Coulomb models is the most influential parameters affecting the response of the buried cables, especially the horizontal force factor (N_h).

- The horizontal force factor (N_h) for Mohr-Coulomb and Drucker-Prager models with dilatant behaviour are greater than their counterparts with non-dilatant behaviour. However, the effect of the dilation parameter in both models is much less than the effect of the friction angle parameter. This finding is similar to those observed by Guo and Stolle (2005).

- Flexibility factor parameter (λ) is defined to characterize the relative cable/soil stiffness. The effect of this parameter on the load-deformation curve of the buried cable was investigated to compare the response of the flexible and rigid pipeline. Studies show that the horizontal force factor for the rigid cable (small λL) has a slightly higher than the horizontal force for the flexible cable (large λL). However, the effect of the cable flexibility on the load-deformation curve is on the displacement in which the response curve gets to its plateau. The response curve for a rigid cable reaches to its plateau at smaller displacement than the response curve for a flexible cable.

- Studies showed that a successful calibrated model requires the best selection of the dilation angle, friction angle, and modulus of elasticity in order to achieve the best match to the experimental results.

- Using the validated model, a family of load-deformation curves is developed for the soil with different friction angle, dilation angle, burial depths, and flexibility factors. In lieu of experimental test results, the numerical simulation results provide a reliable database to estimate the soil loads on the buried cable in the horizontal transverse direction. The next chapter will examine in further details the use of this database in the evaluation of the response of the buried cable to the transverse permanent ground deformation.

In the numerical simulation of axial pullout tests, numerical models were developed according to the axial pullout test setup. The main aim of the numerical studies was to characterize the effect of out-of-straightness on the longitudinal response of buried power transmission cable. The effect of out-of-straightness was studied by creating a numerical model for the cable with different offset ratios (δ/L), and its longitudinal response was compared to the benchmark longitudinal response of straight cables. Furthermore, the effects of out-of-straightness with the effects of other parameters such as burial depths, interface cable/soil friction, and the relative stiffness of the cable/ soil on the longitudinal response of

buried cable were studied. Some of the key findings and observations from these numerical simulations are summarized herein.

- Cable with out-of-straightness creates more soil loads on the buried cable. The amount of soil loads increases by an increase in the relative cable/soil movement. Furthermore, it was found that as offset ratio values increase the longitudinal soil loads on the buried cable increase.

- Non-straight cables with smaller flexibility factor (λ) creates more longitudinal soil restraints. Studies show that cables with the same flexibility factors but with larger soil elastic modulus (E_s) creates more longitudinal soil restraints.

- Interface soil/cable friction (f) was found to be a key parameter in determining the soil loads on the buried cable in both the yielding and hardening phase in the load-deformation curve.

- Parametric studies on the effect of the burial depth on the longitudinal soil loads on the buried cable show that the burial depth has a pronounced effect on the yielding; however, its effect on the hardening part of load-deformation is insignificant.

- The result of the numerical simulation provides a database to develop a method to estimate the amount of soil loads on the buried cable with different flexibility factors. The next chapter will discuss in further details the use of the database in the evaluation of the response of the buried cable to the longitudinal permanent ground deformation.

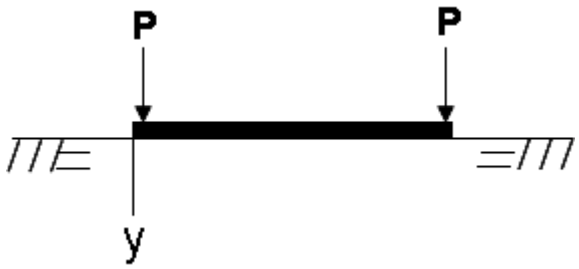

Figure 4-1: Beam on elastic foundation subjected to concentrated loads at both ends

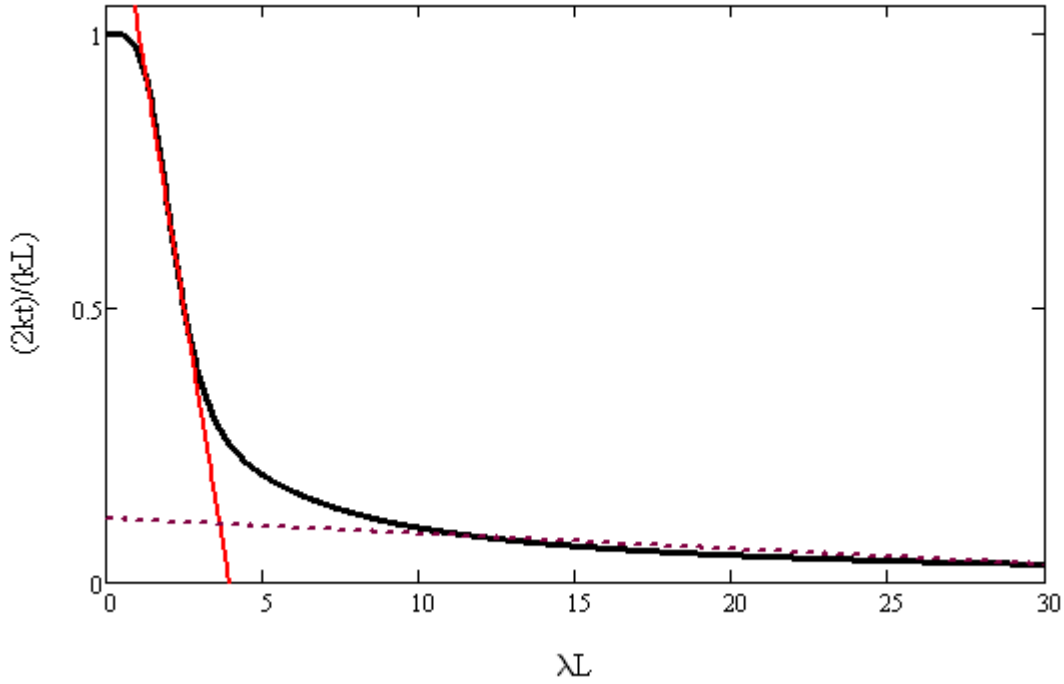

Figure 4-2: The variation of the k_t stiffness with respect to the characteristic length (λL), assuming a constant k.

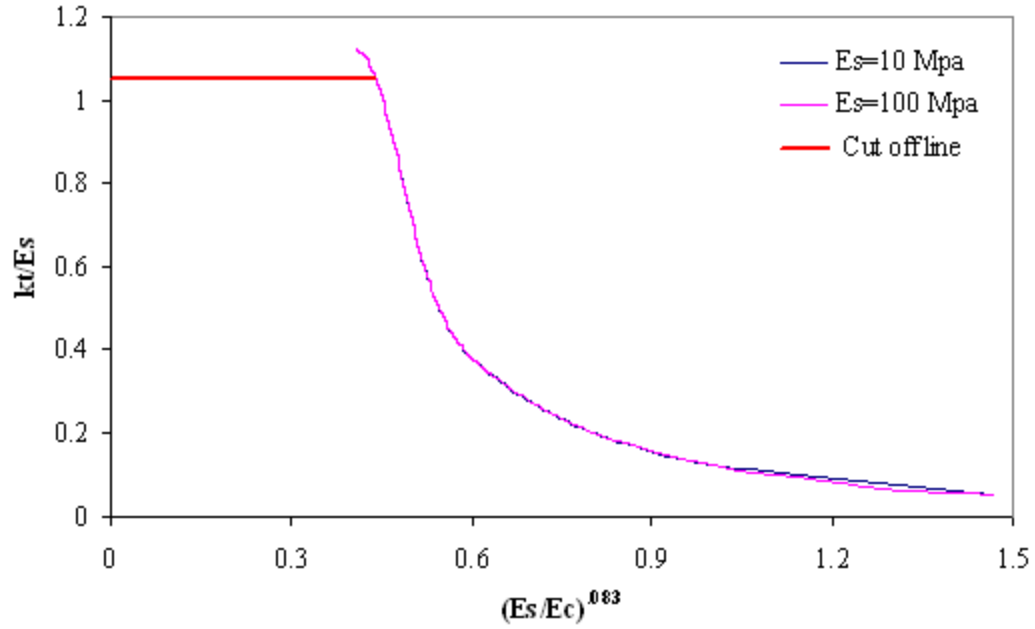

Figure 4-3: The k_t stiffness variation of a beam with the diameter of 0.1 m and the length of 2.15 m buried in the homogenous elastic soil (ν_s=0.3) with the burial depth of 0.9 m.

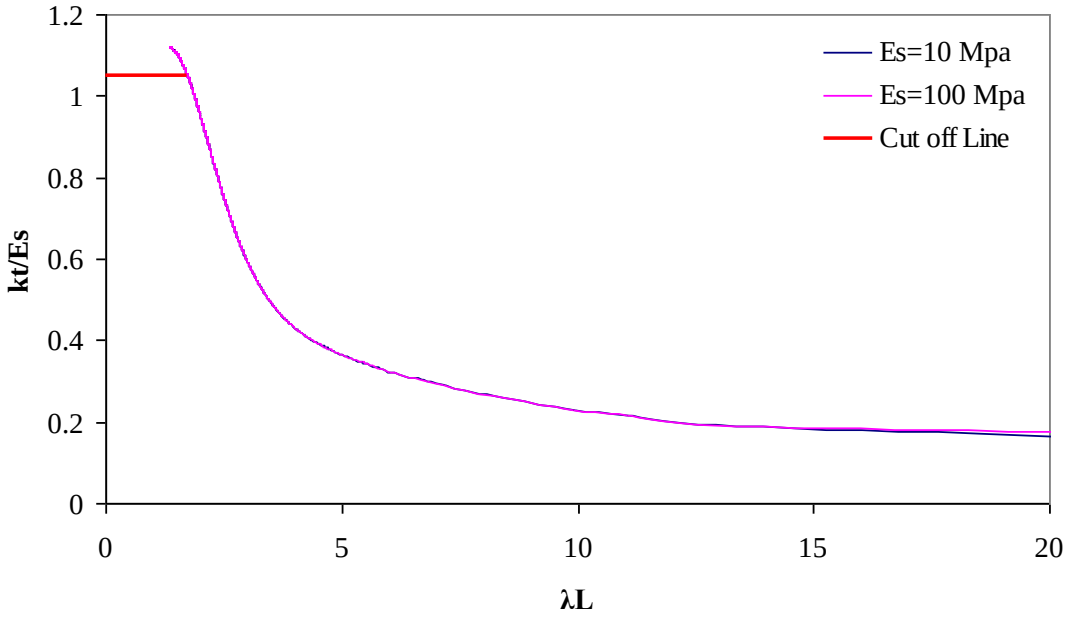

Figure 4-4:The k_t stiffness-λL curve for a beam with the diameter of 0.1 m and the length of 2.15 m buried in the homogenous elastic soil (ν_s=0.3) with the burial depth of 0.9 m.

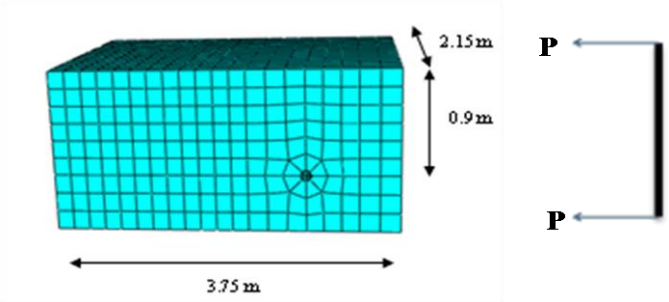

Figure 4-5: The numerical model of the beam and soil to calculate K_t stiffness.

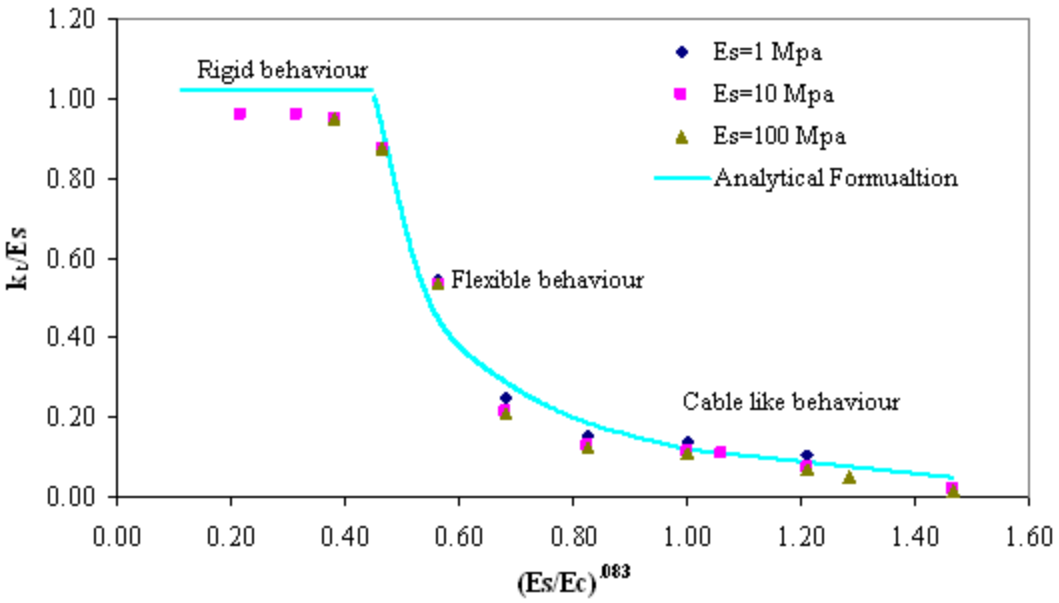

Figure 4-6: k_t stiffness comparison between the analytical prediction and numerical simulation for the beam with the burial depth of 0.9 m and different flexural rigidity.

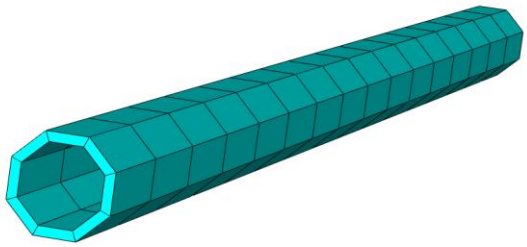

Figure 4-7: Mesh configuration of hollow section used to model the equivalent cable

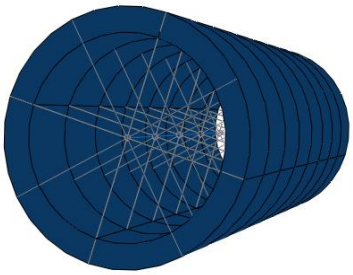

Figure 4-8: Beam core constraint applied to hollow section to form "equivalent cable"

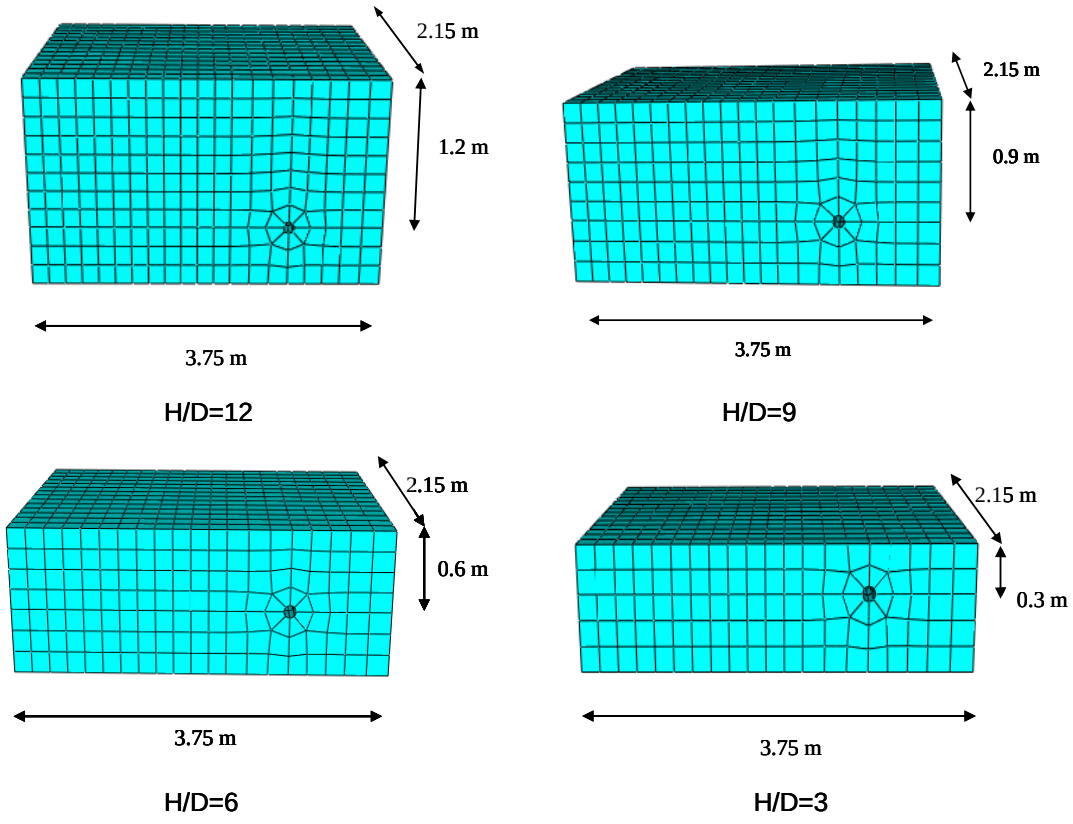

Figure 4-9: Mesh configurations used to model cable-soil interaction for different burial depths

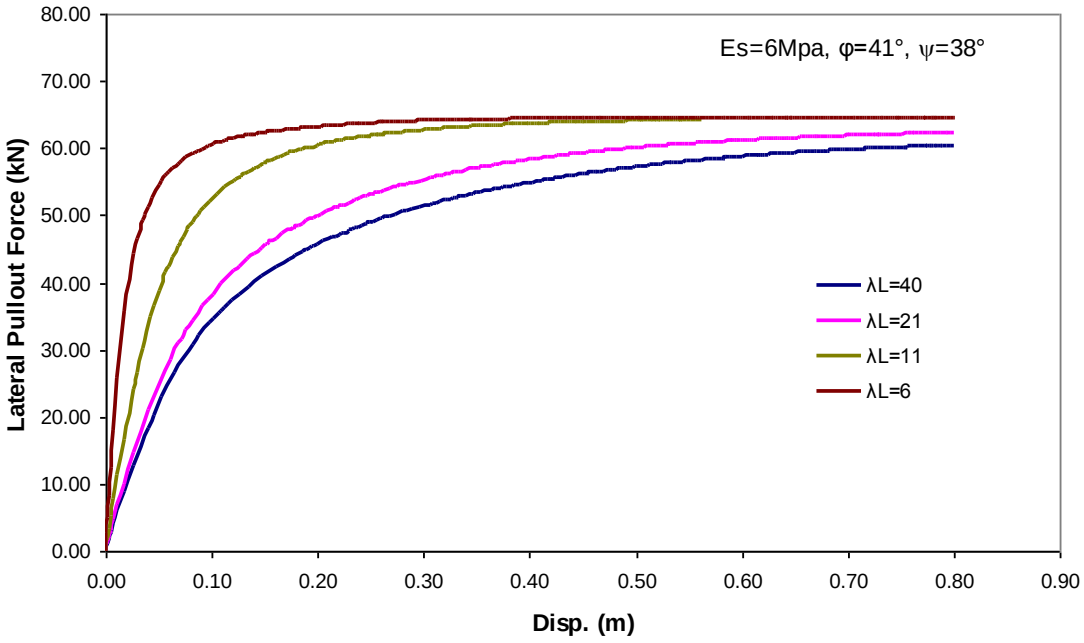

Figure 4-10: Load-deformation curve for the buried cable with different λL. (Mohr-Coulomb Model, *Es*=6 MPa, φ=41°, ψ=38 °)

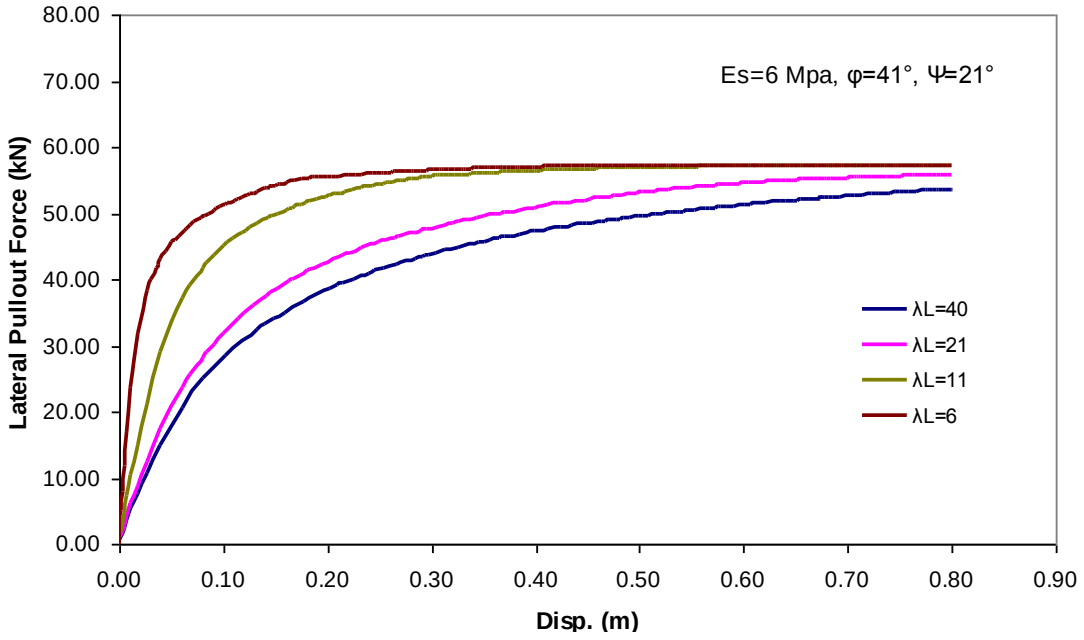

Figure 4-11: Load-deformation curve for the buried cable with different λL . (Mohr-Coulomb Model ,*Es*=6 MPa, φ=41°, ψ=21 °)

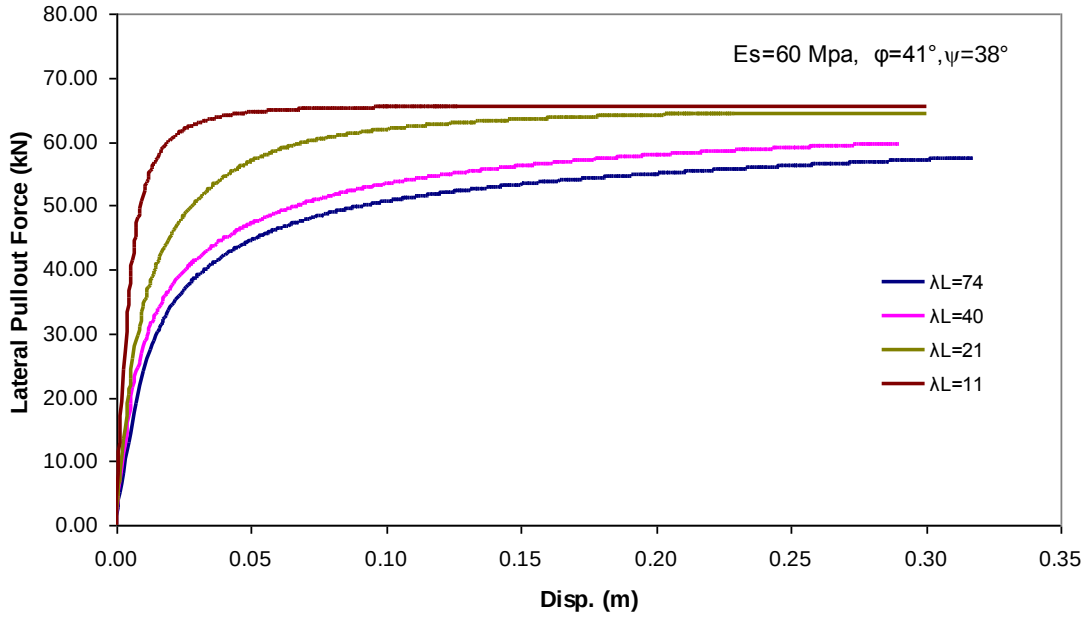

Figure 4-12: Load-deformation curve for the buried cable with different λL. (Mohr-Coulomb Model ,Es=60 MPa, φ=41°, ψ=38 °)

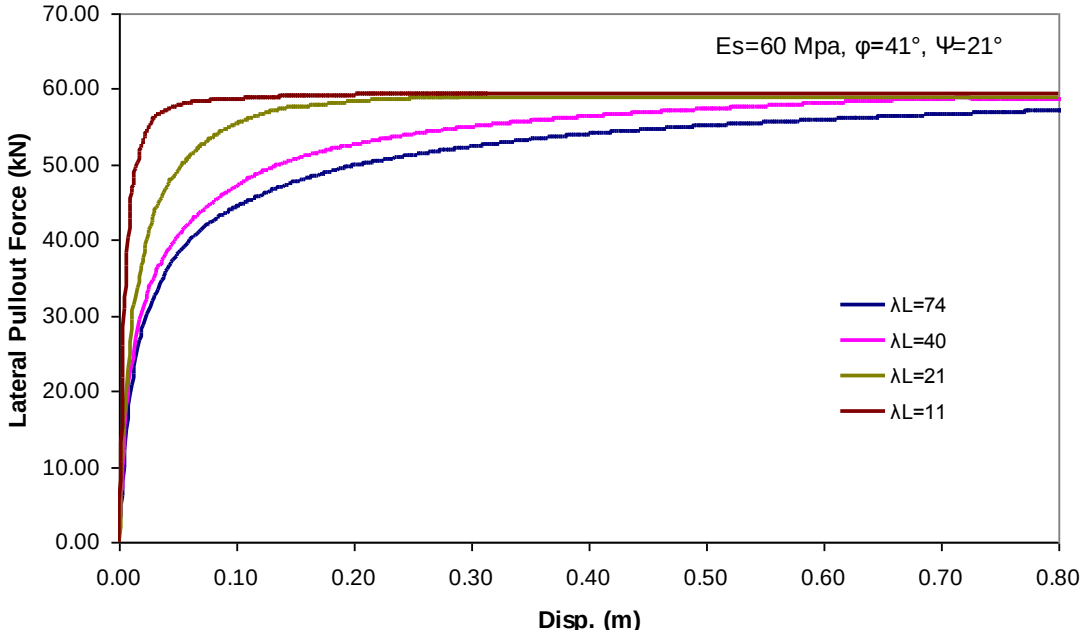

Figure 4-13: Load-deformation curve for the buried cable with different λL. (Mohr-Coulomb Model ,Es=60 MPa, φ=41°, ψ=21 °)

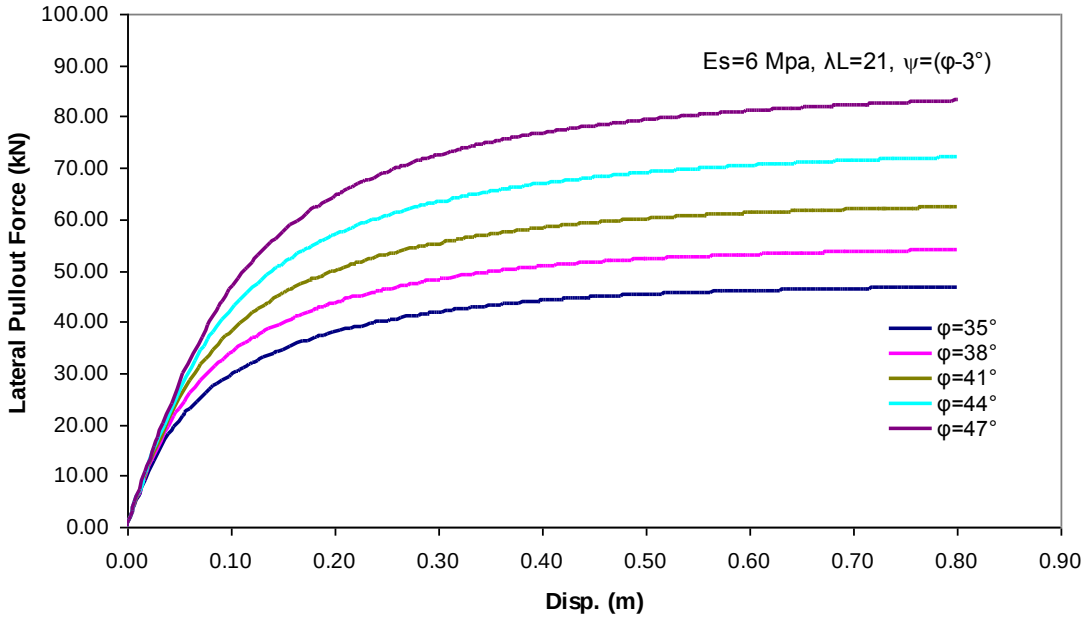

Figure 4-14: Load-deformation curves for the cable with the burial depth of (0.9 m) with different φ parameter and associated flow rule(Mohr-Coulomb Model)

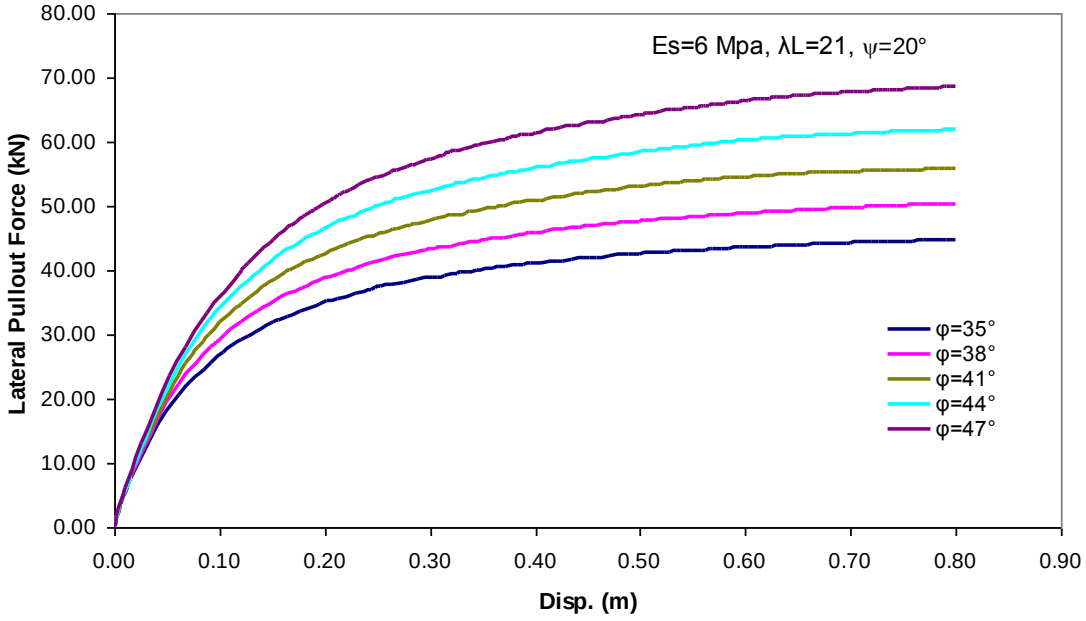

Figure 4-15: Load-deformation curves for the cable with the burial depth of (0.9 m) with different φ parameter and non-associated flow rule ψ=20°(Mohr-Coulomb Model)

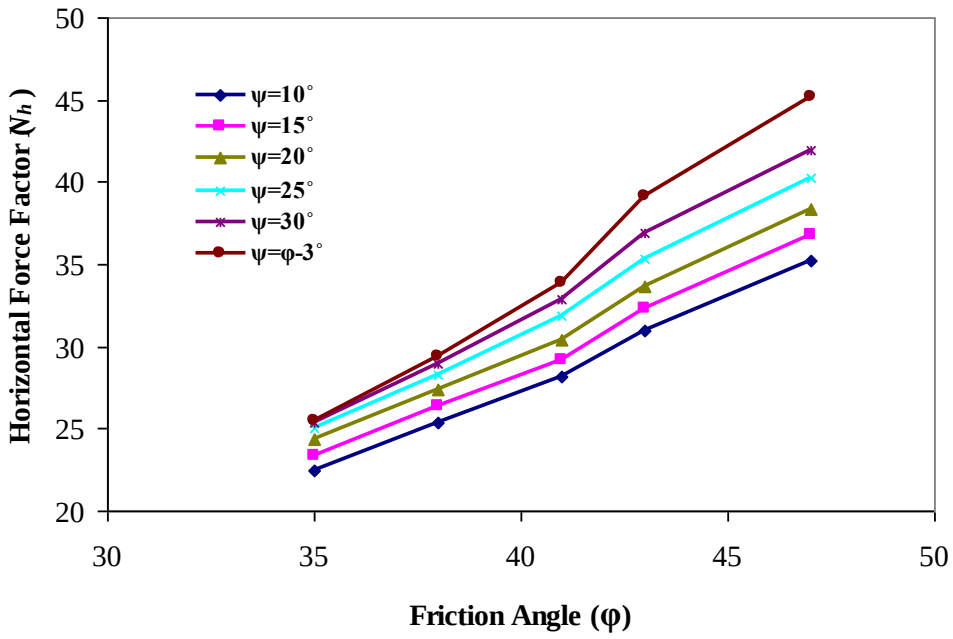

Figure 4-16: Variation of horizontal force factor (N_h) with friction angle for cable with burial depth of 0.9 (m), Mohr-Coulomb Model, *Es*=6 MPa, and $\lambda L=21$.

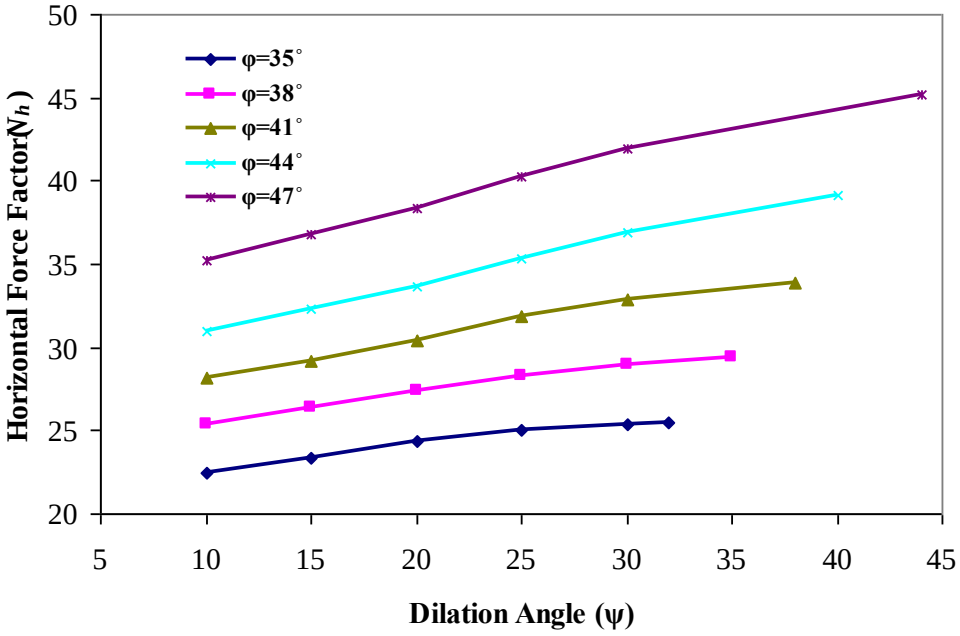

Figure 4-17: Variation of horizontal force factor (N_h) with dilation angle for cable with burial depth of 0.9 (m) , Mohr-Coulomb Model, *Es*=6 MPa, $\lambda L=21$.

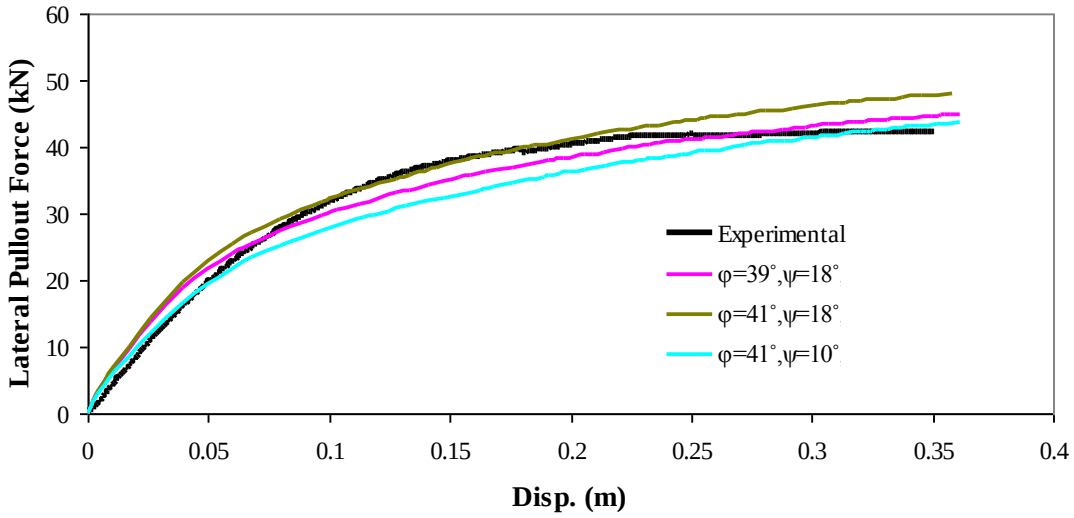

Figure 4-18: Calibration of numerical simulation with test results of experimental studies of *H*/*D*=9, *Es*=10 MPa, *λL=37*.

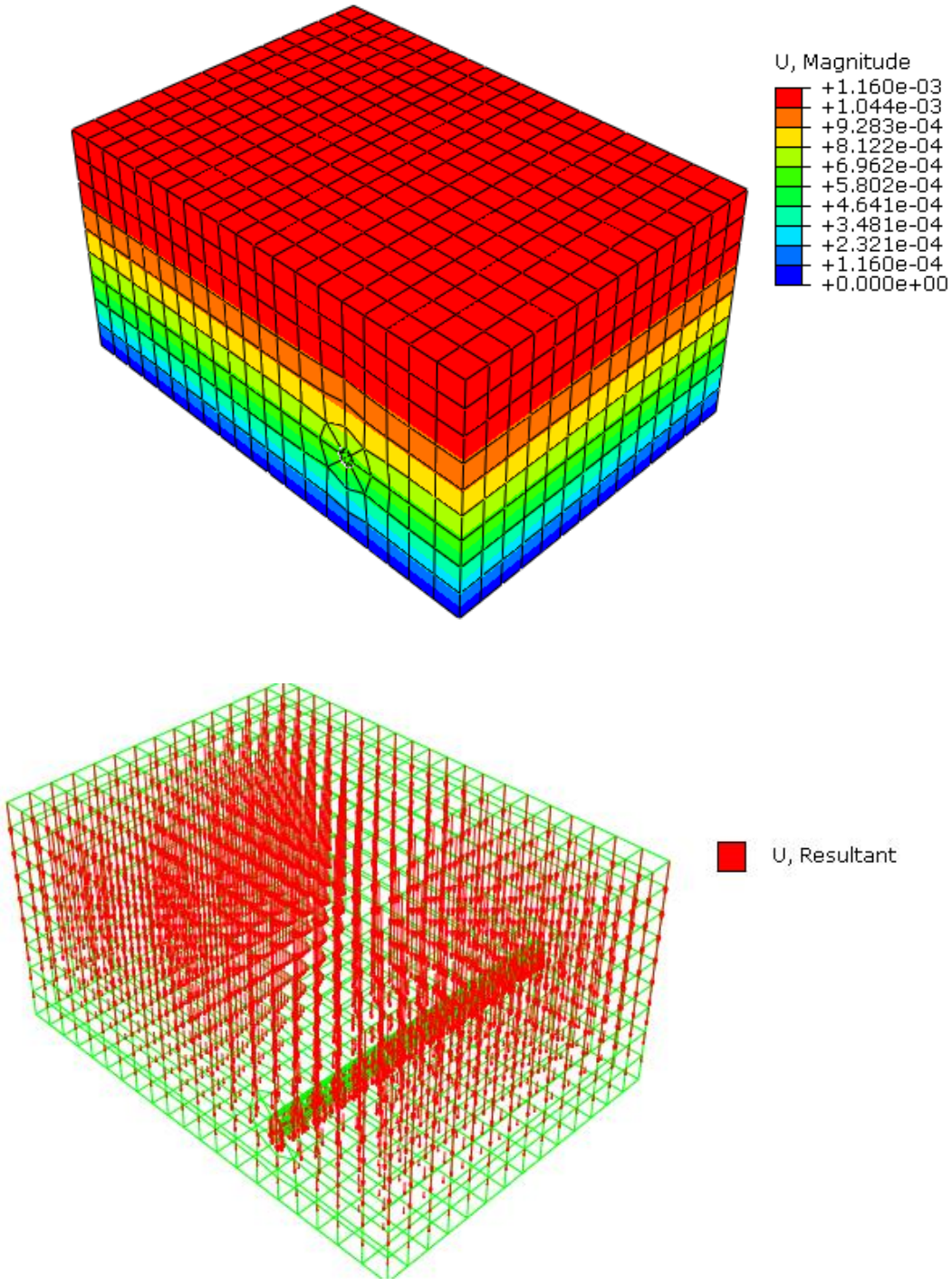

a) Displacement contours after geostatic analysis

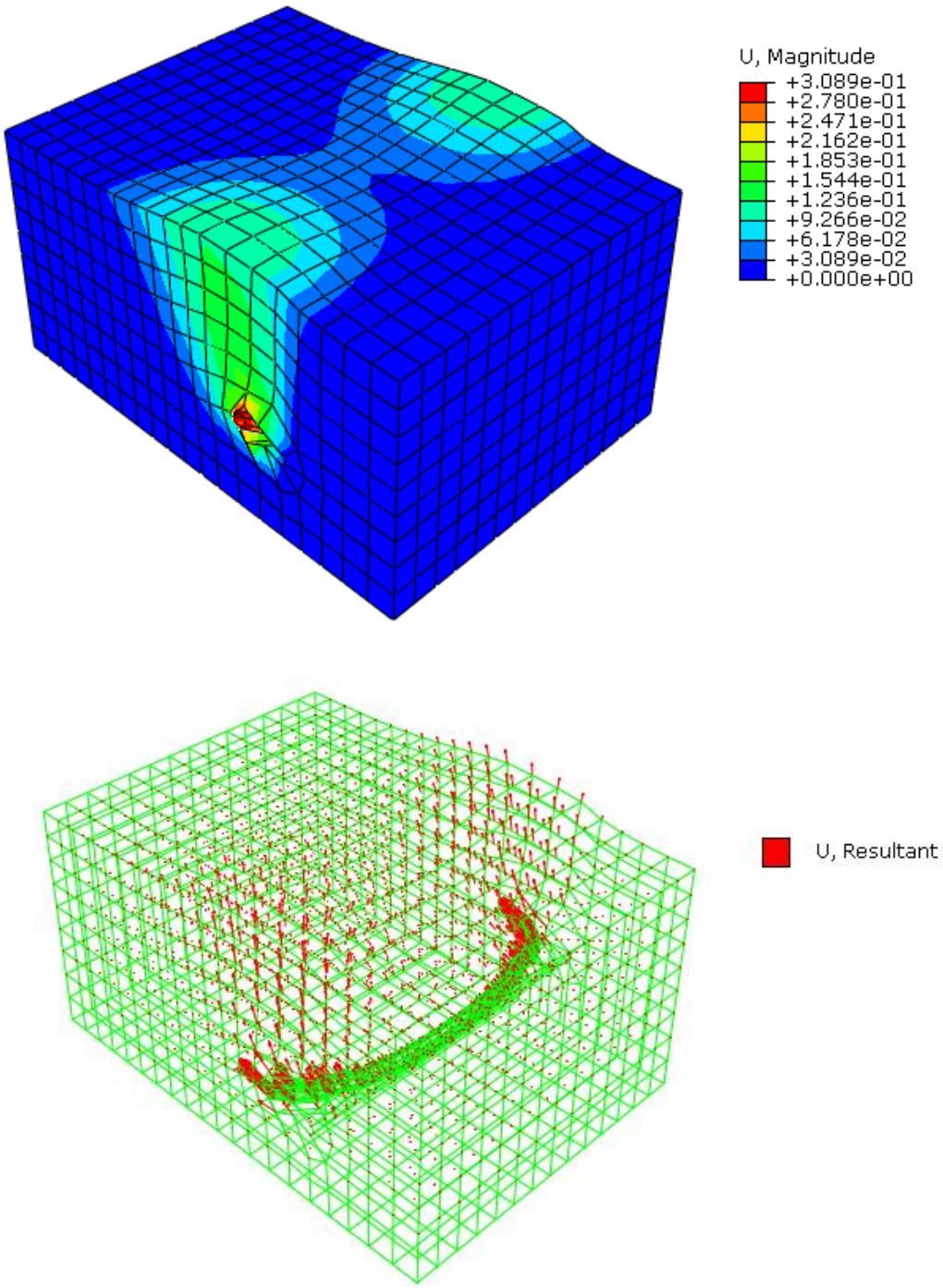

b) Displacement contours after 30 cm pulling of the cable

Figure 4-19: Displacement contours a) after geostatic analysis and b) after 30 cm pulling of the cable with burial depth ratio of H/D=9, E_s=10 MPa, λL=37.

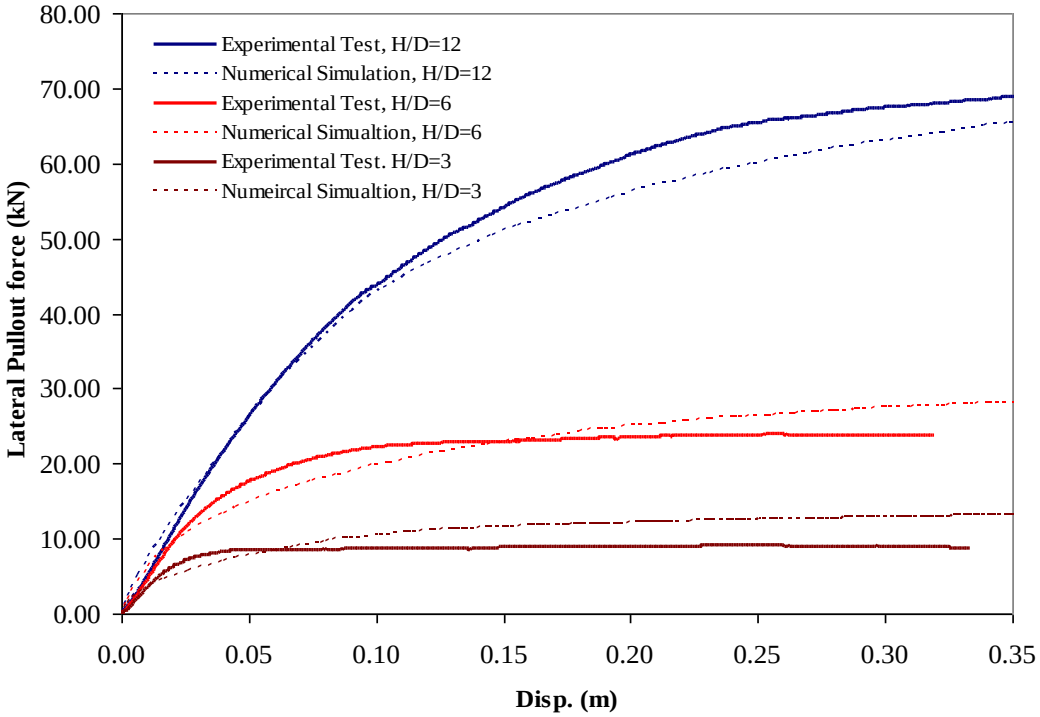

Figure 4-20: Validation of numerical simulation with test results of experimental studies of *H*/*D*=3, 6, 12, , and φ=39°, ψ=18 °.

Table 4-1 Mohr Coulomb parameters

General		Plasticity	
ρ	1900 (kg/m^3)	φ	33° to 47°
Elasticity		ψ	5° to φ-3°
Es	Variable	Meridional eccentricity	0.1
υs	0.3	Deviatoric eccentricity	$e = (3-\sin\varphi)/(3+\sin\varphi)$

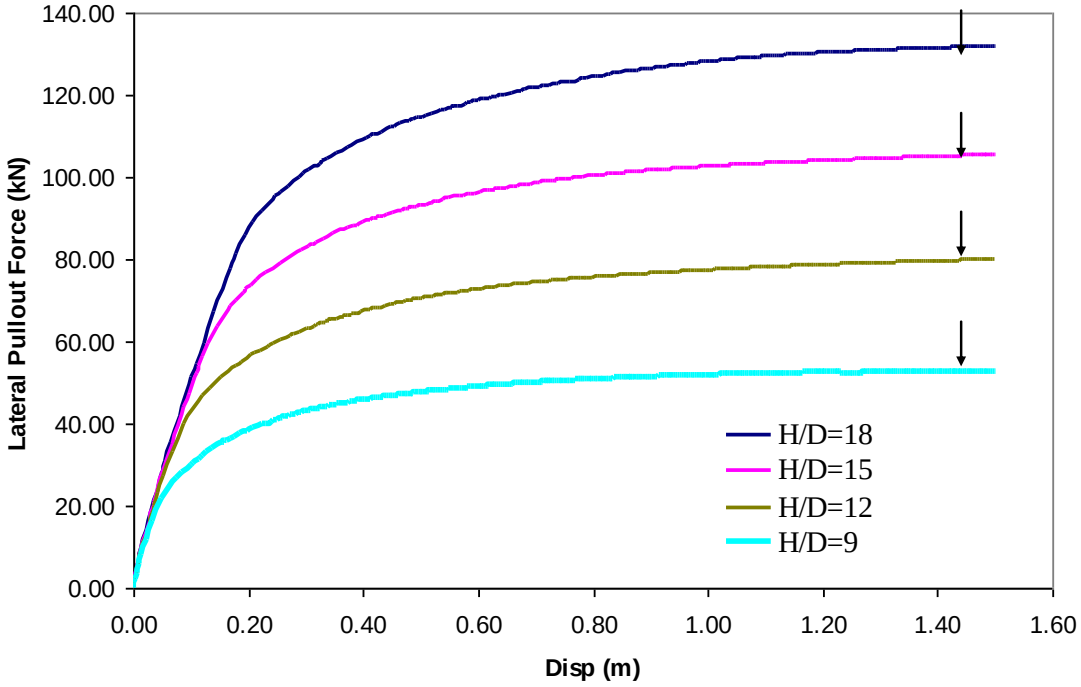

Figure 4-21: Load-deformation curve for a cable with the different burial depth, φ=39°, ψ=18°, E_s=10 *MPa*, λL=37.

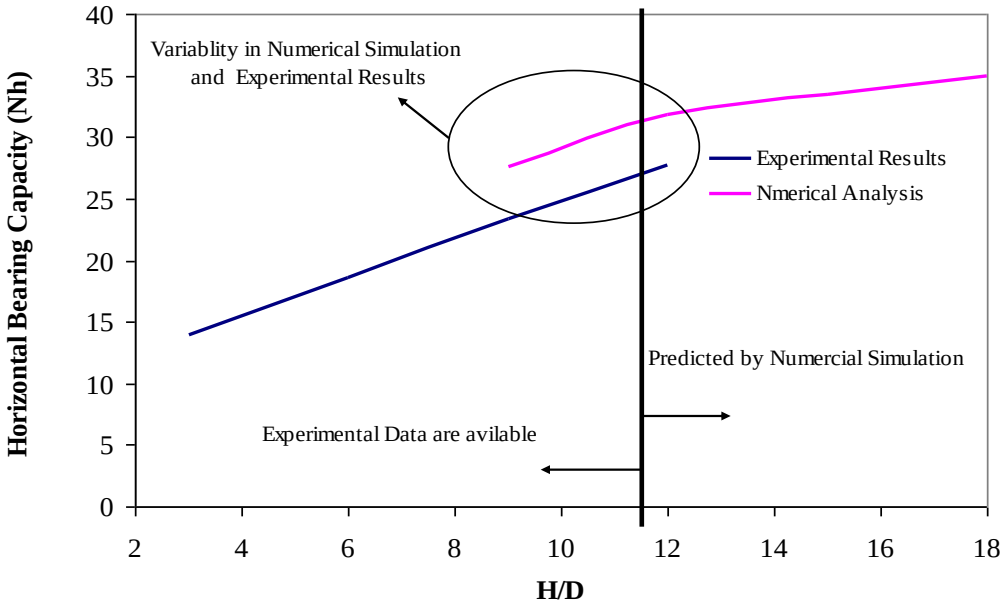

Figure 4-22:Variation of horizontal force factor as a function of the burial depth, numerical simulation and experimental studies.

Table 4-2: Drucker-Prager model parameters

General		Plasticity	
ρ	1900 (kg/m^3)	β (deg)	35° to 50°
Elasticity		ψ (deg)	5° to β°
Es	Variable	Flow Potential eccentricity	0.1
υs	0.3	K	1

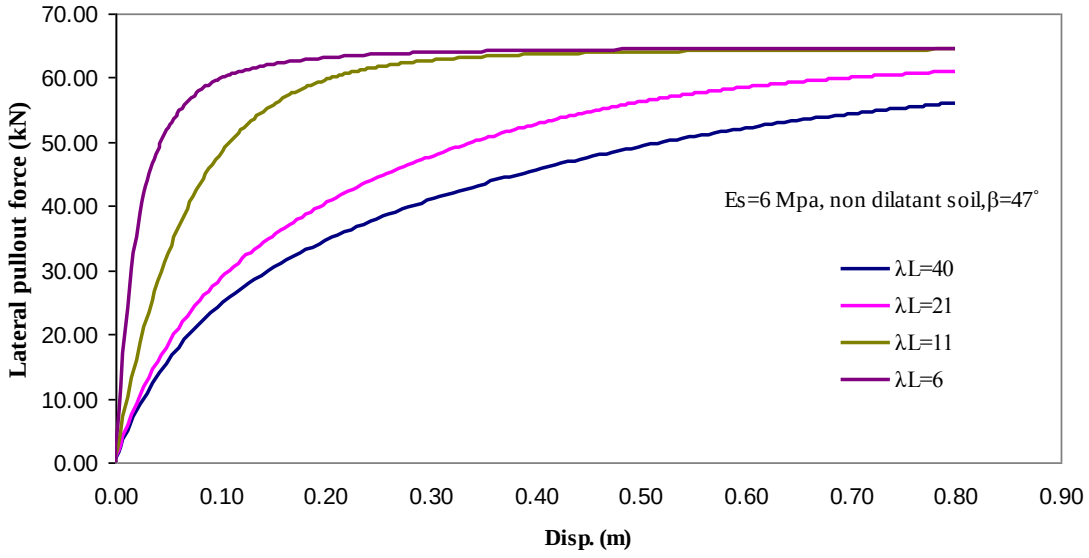

Figure 4-23: Load-deformation curve for the buried cable with different λL. (Drucker-Prager Model, Es=6 MPa, β=47°, and non-dilatant soil)

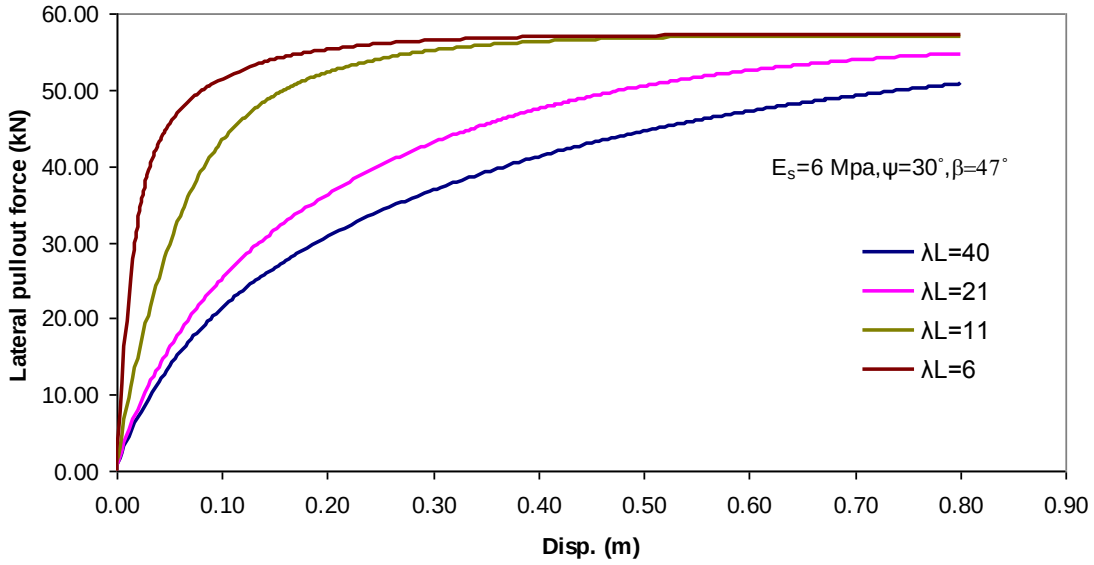

Figure 4-24: Load-deformation curve for the buried cable with different λL. (Drucker-Prager Model ,*Es*=6 MPa, β=47°, and dilatant soil (ψ=30°))

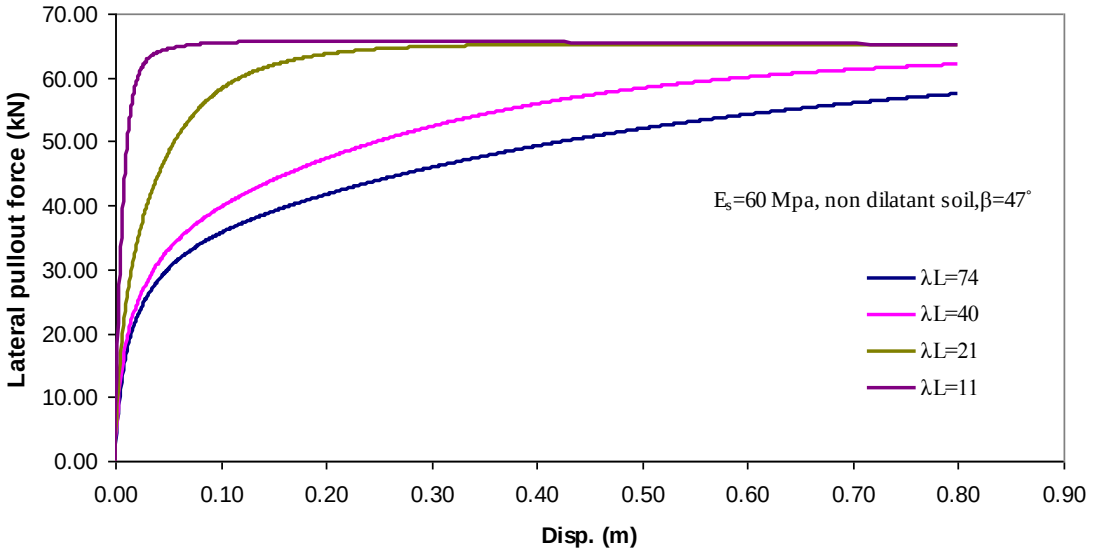

Figure 4-25: Load-deformation curve for the buried cable with different λL. (Drucker-Prager Model, *Es*=60 MPa, β=47°, and non-dilatant soil)

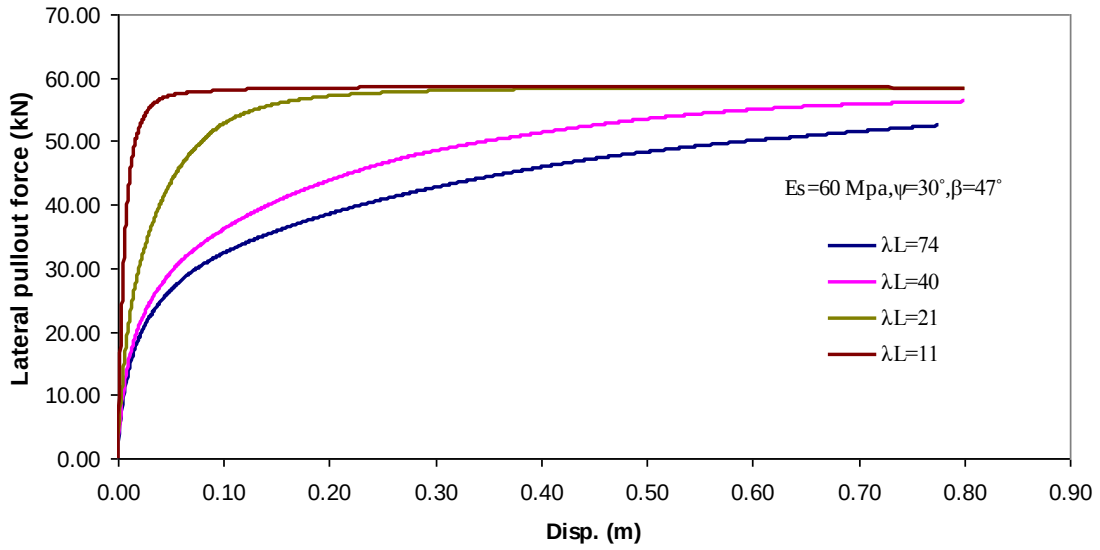

Figure 4-26: Load-deformation curve for the buried cable with different λL. (Drucker-Prager Model, Es=60 MPa, β=47°, and dilatant soil(ψ=30°))

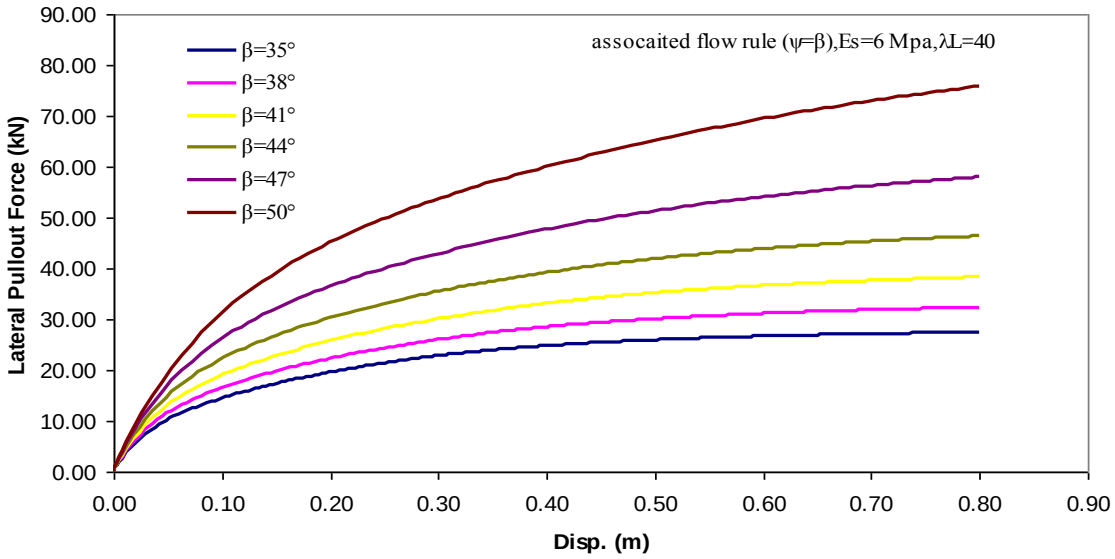

Figure 4-27: Load-deformation curve for the buried cable for different friction angle (β) (Drucker-Prager Model, Es=6 MPa, non-dilatant soil)

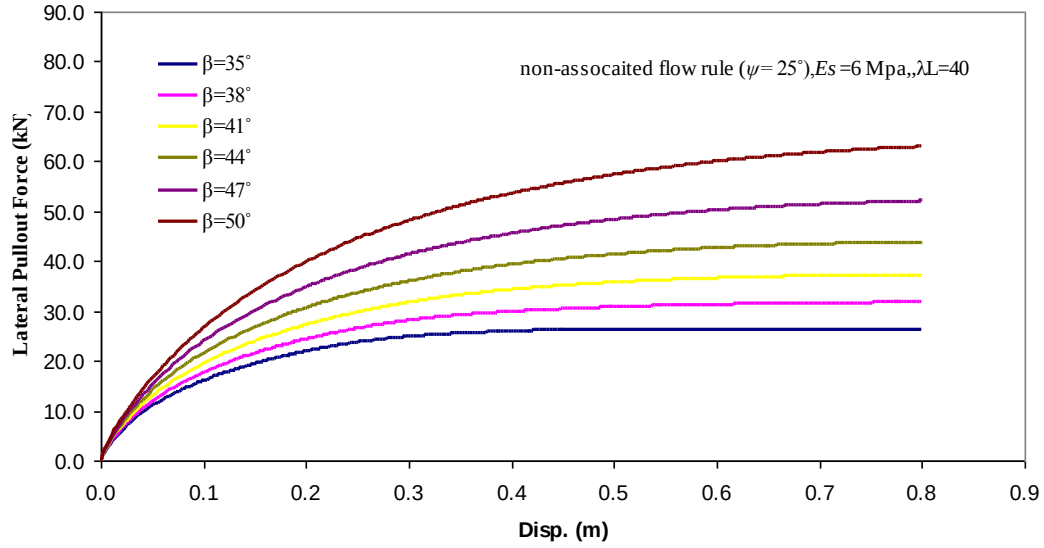

Figure 4-28: Load-deformation curve for the buried cable for different friction angle (β) (Drucker-Prager Model, *Es*=6 MPa, dilatant soil (*ψ*=25°))

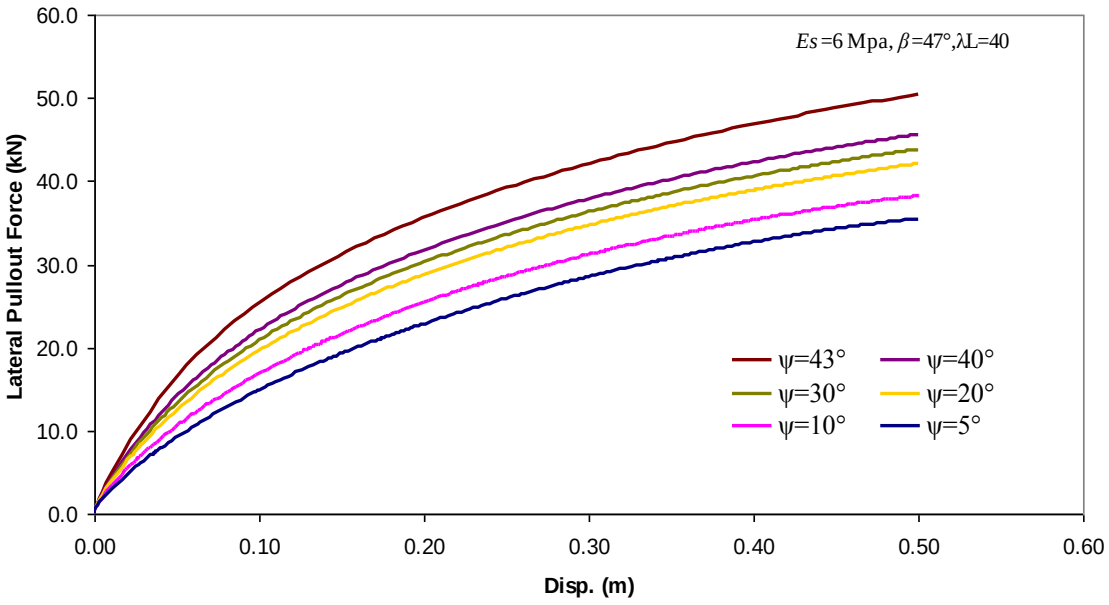

Figure 4-29: Load-deformation curve for the buried cable for different dilation angle (ψ) (Drucker-Prager Model, *Es*=6 MPa, *β*=47°)

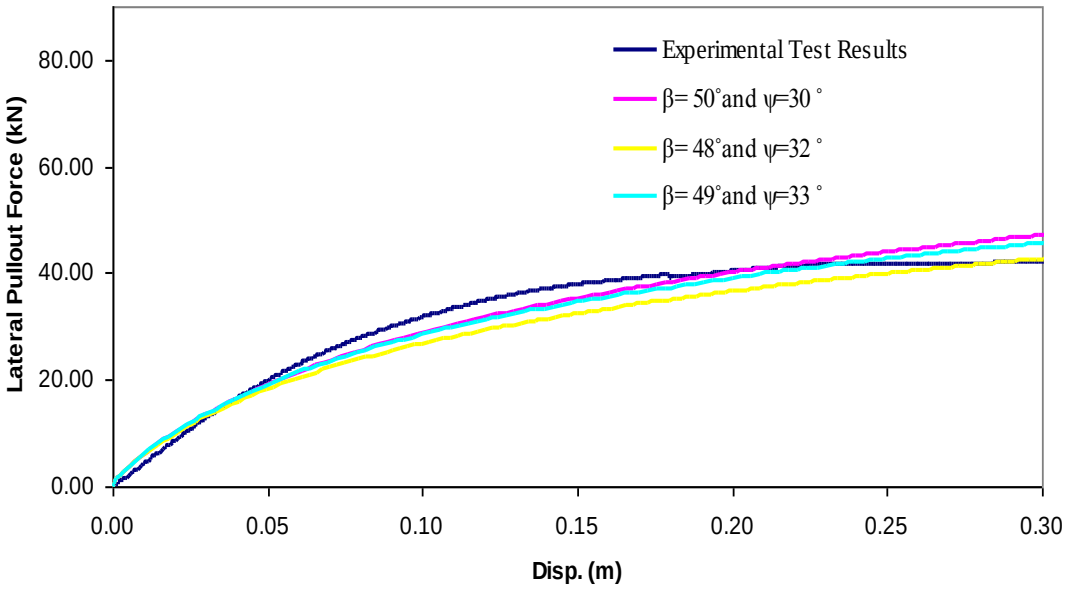

Figure 4-30: Calibration of numerical simulation with test results of experimental studies of *H*/*D*=9, *Es*=10 MPa, $\lambda L=37$.

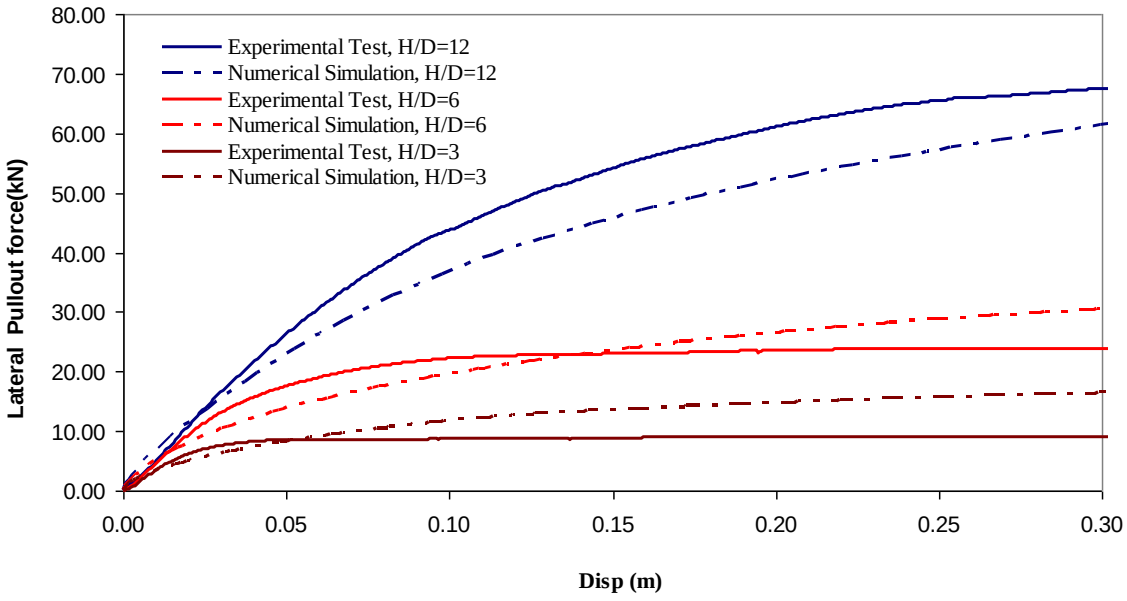

Figure 4-31: Validation of numerical simulation with test results of experimental studies of *H*/*D*=3, 6, and 12, *Es*=10 MPa, $\lambda L=37$.

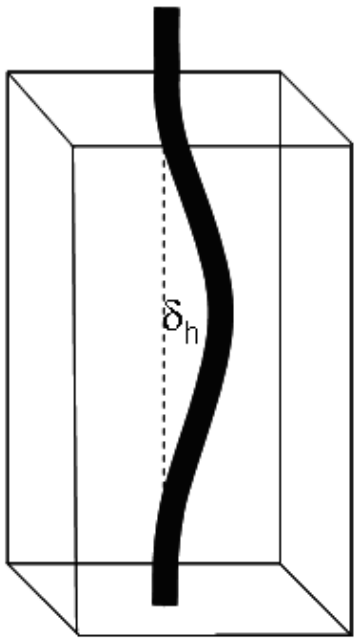

Figure 4-32: Horizontal offset in the buried cable with out-of-straightness

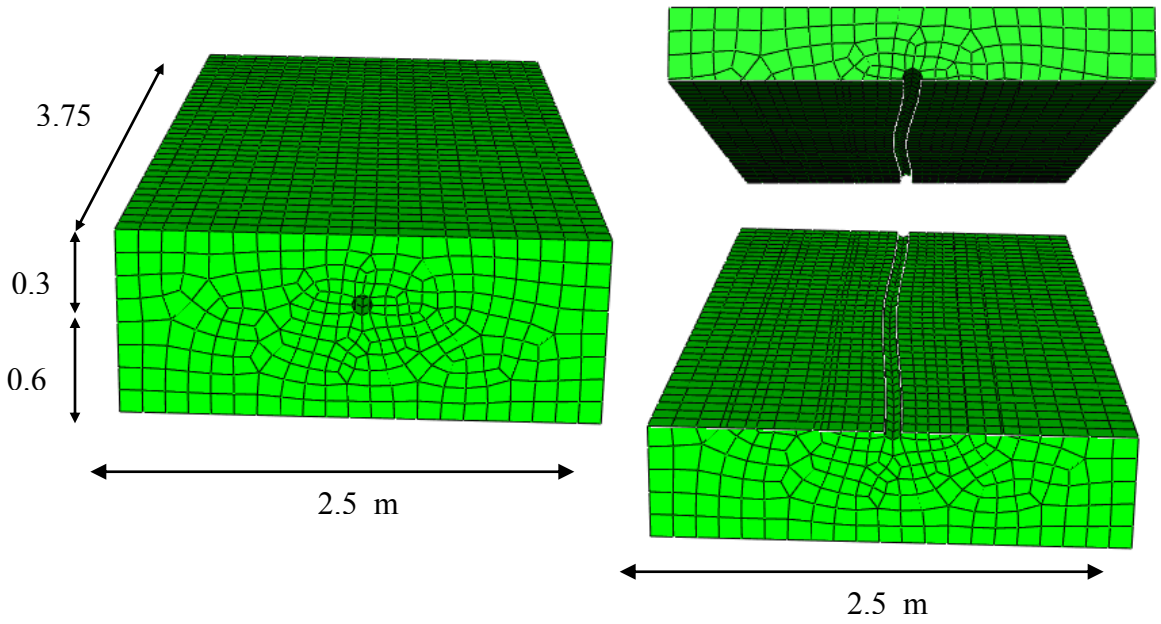

Figure 4-33: The mesh configuration of the soil for the cable with burial depth of 30 cm with the maximum horizontal offset of δ_h=5 cm.

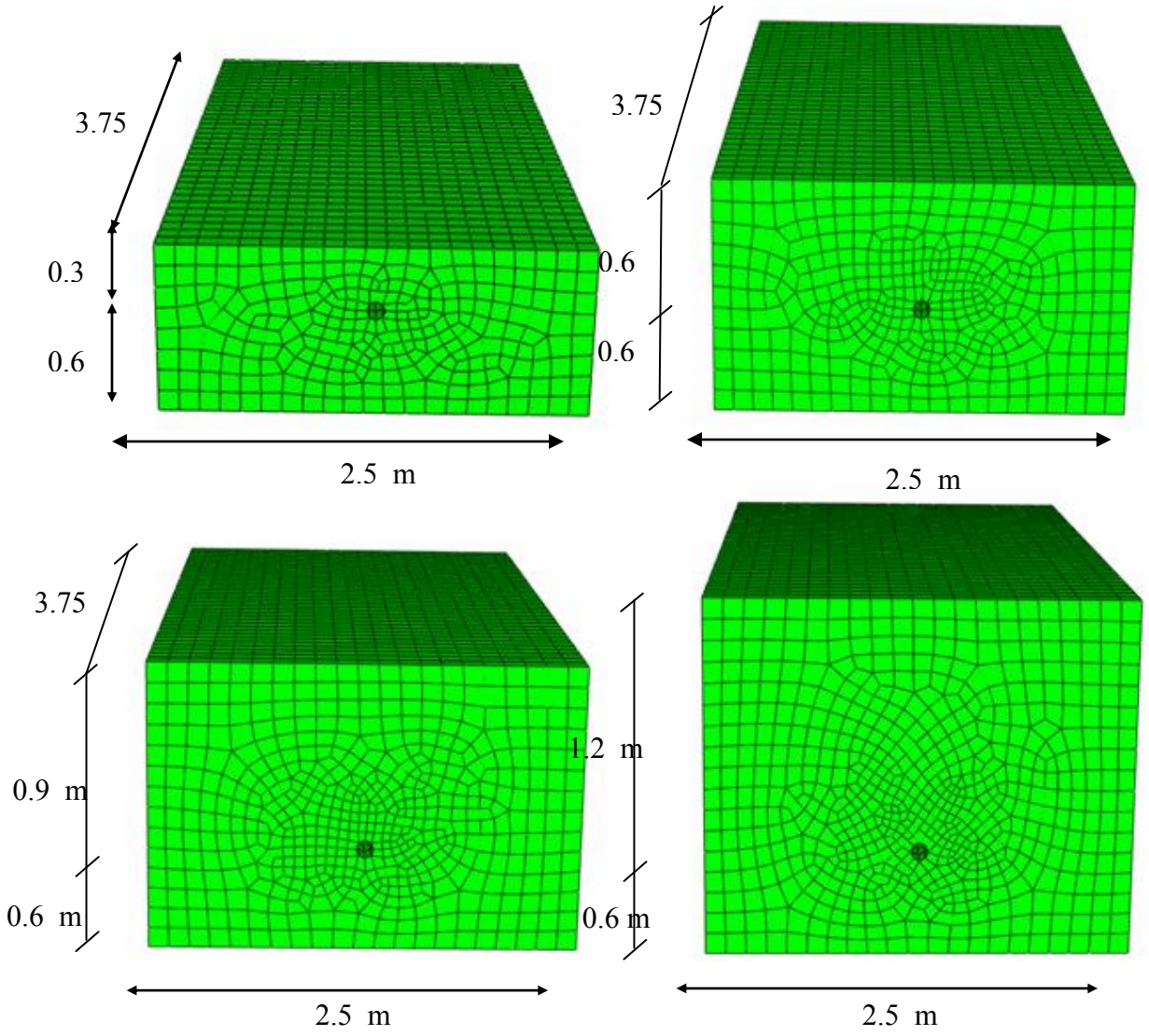

Figure 4-34: Mesh configuration for buried cables with out-of-straightness for burial depth of 30, 60, 90, and 120 cm.

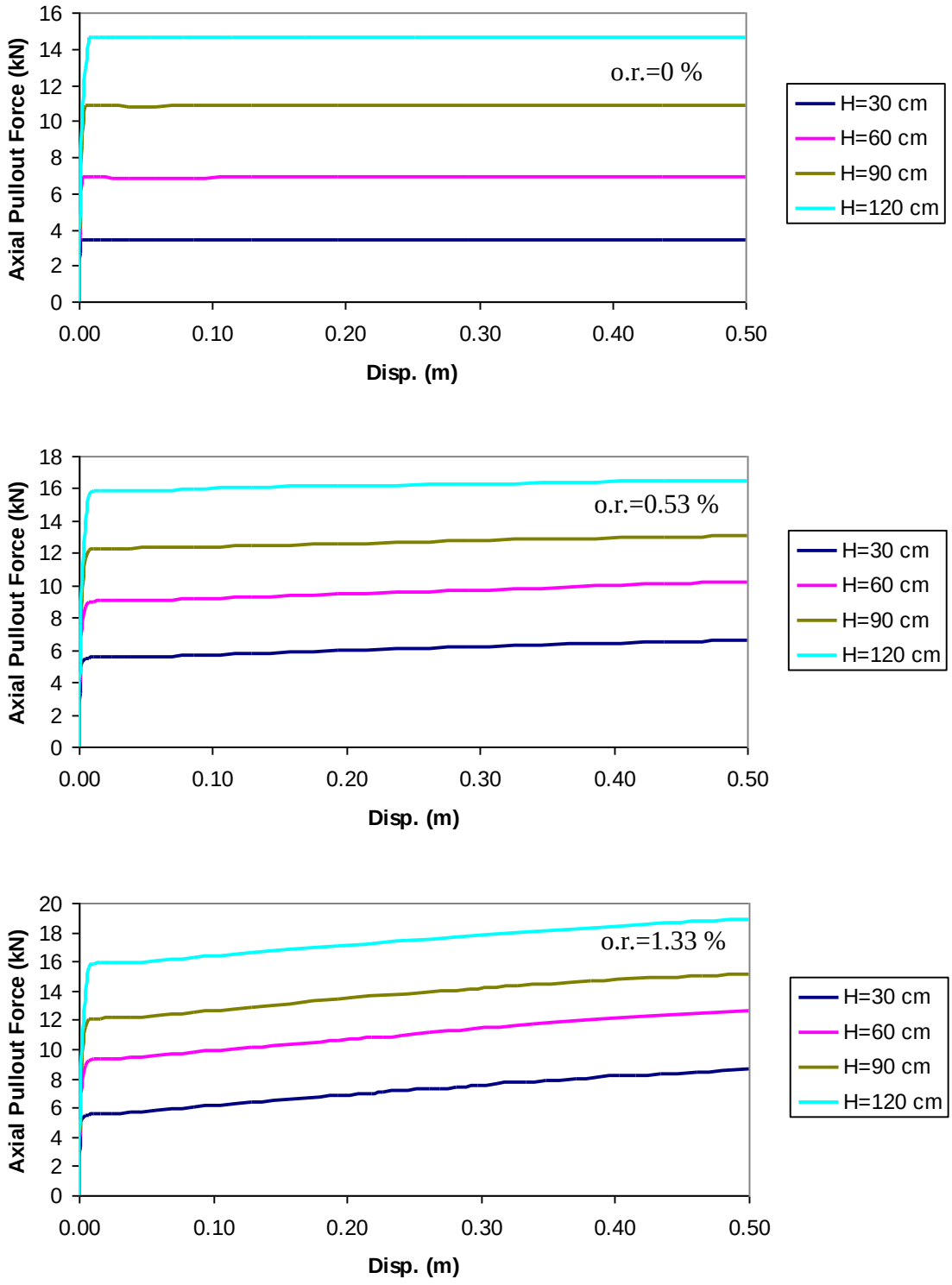

Figure 4-35: The effect of out-of-straightness on the longitudinal response of the cable with different burial depths (*H*=30, 60, 90, and 120 cm), *f*=0.7, *Es*=10 MPa, λ=4.7/m.

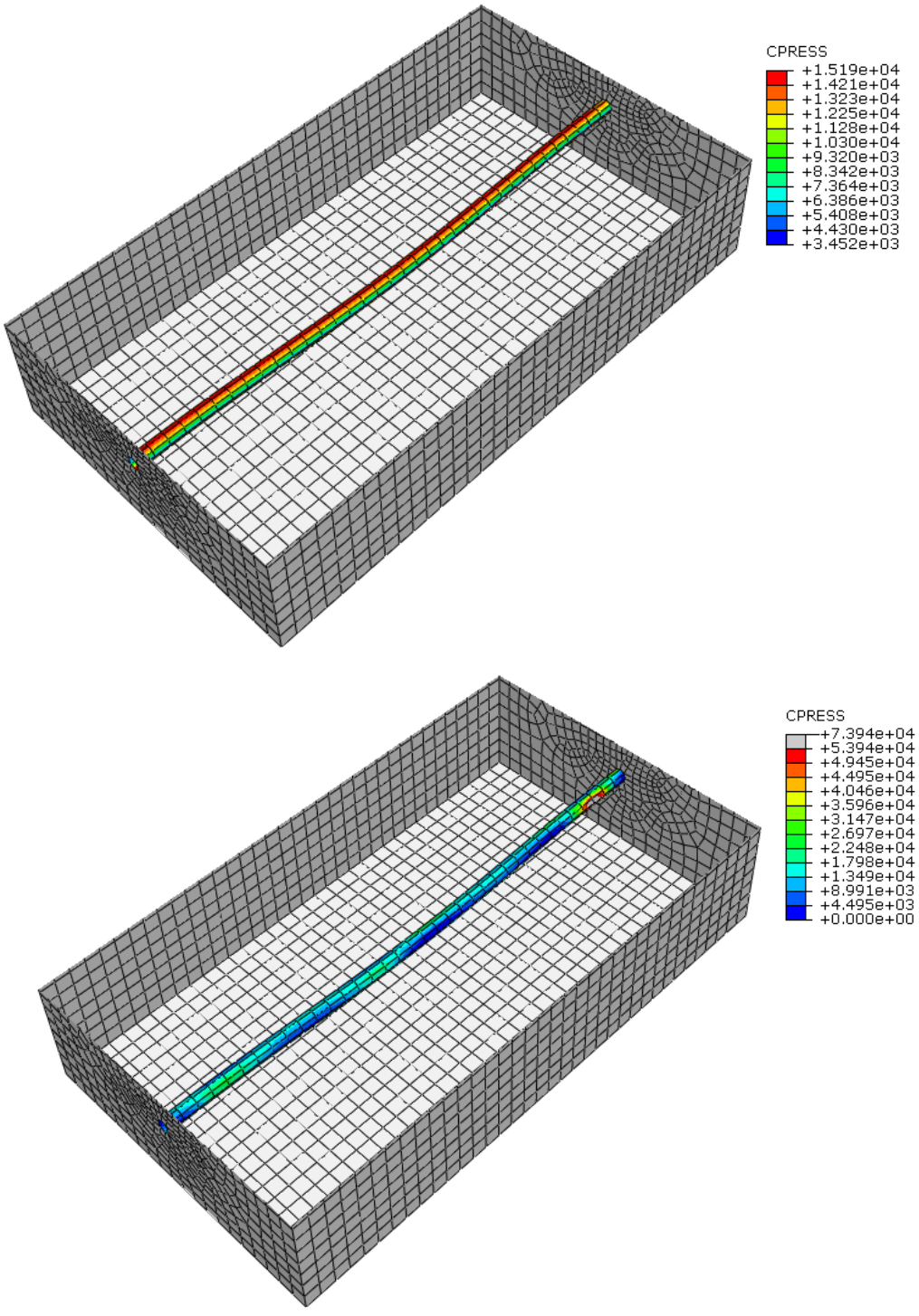

Figure 4-36: Normal contact stresses at the soil/cable interface after geostatic analysis and after 30 cm pulling out the cable with the burial depth of 90 cm, f=0.7, Es=10 MPa, λ=4.7/m.

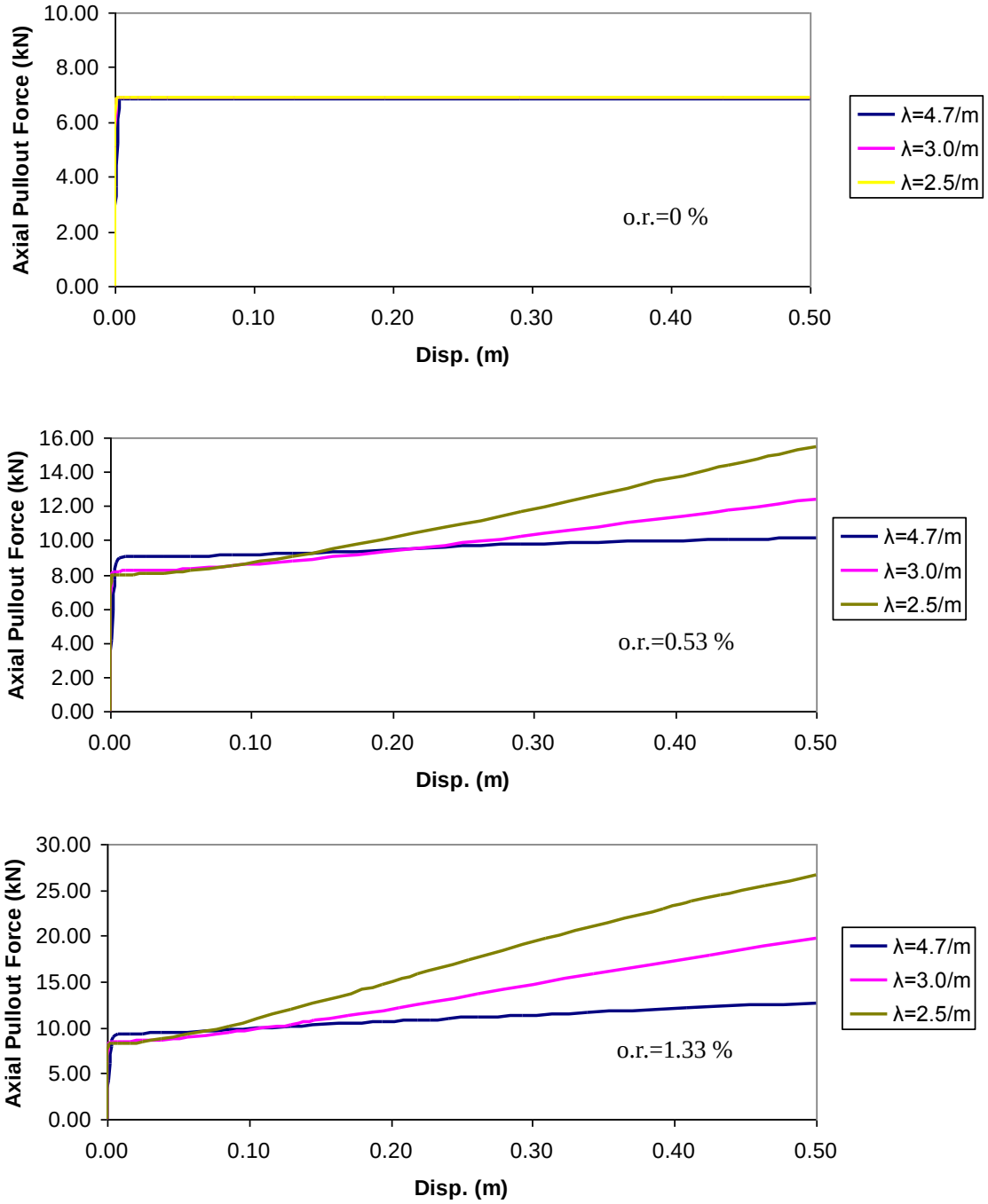

Figure 4-37: The effect of the cable flexibility (λ parameter) on the longitudinal response of the buried cable with different offset ratio (δ/L=0, δ/L=0.53 %, and δ/L=1.33%). (*Es*=10 MPa, *f*=0.7 φ=38˚, and ψ=18˚)

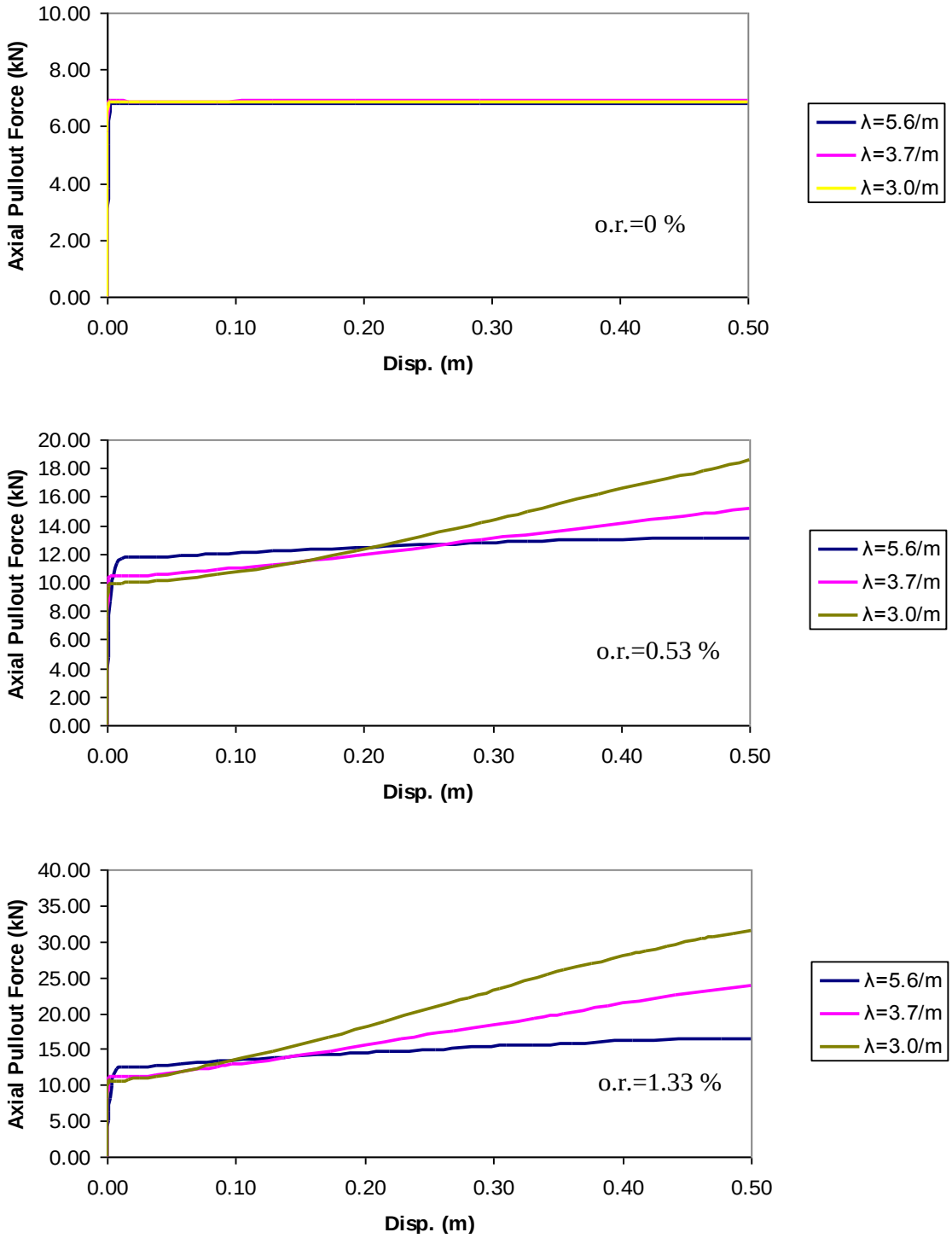

Figure 4-38: The effect of the cable flexibility (λ parameter) on the longitudinal response of the buried cable with different offset ratio (δ/L=0, δ/L=0.53 %, and δ/L=1.33%).(*Es*=20 MPa, *f*=0.7,*φ*=38˚, and *ψ*=18˚)

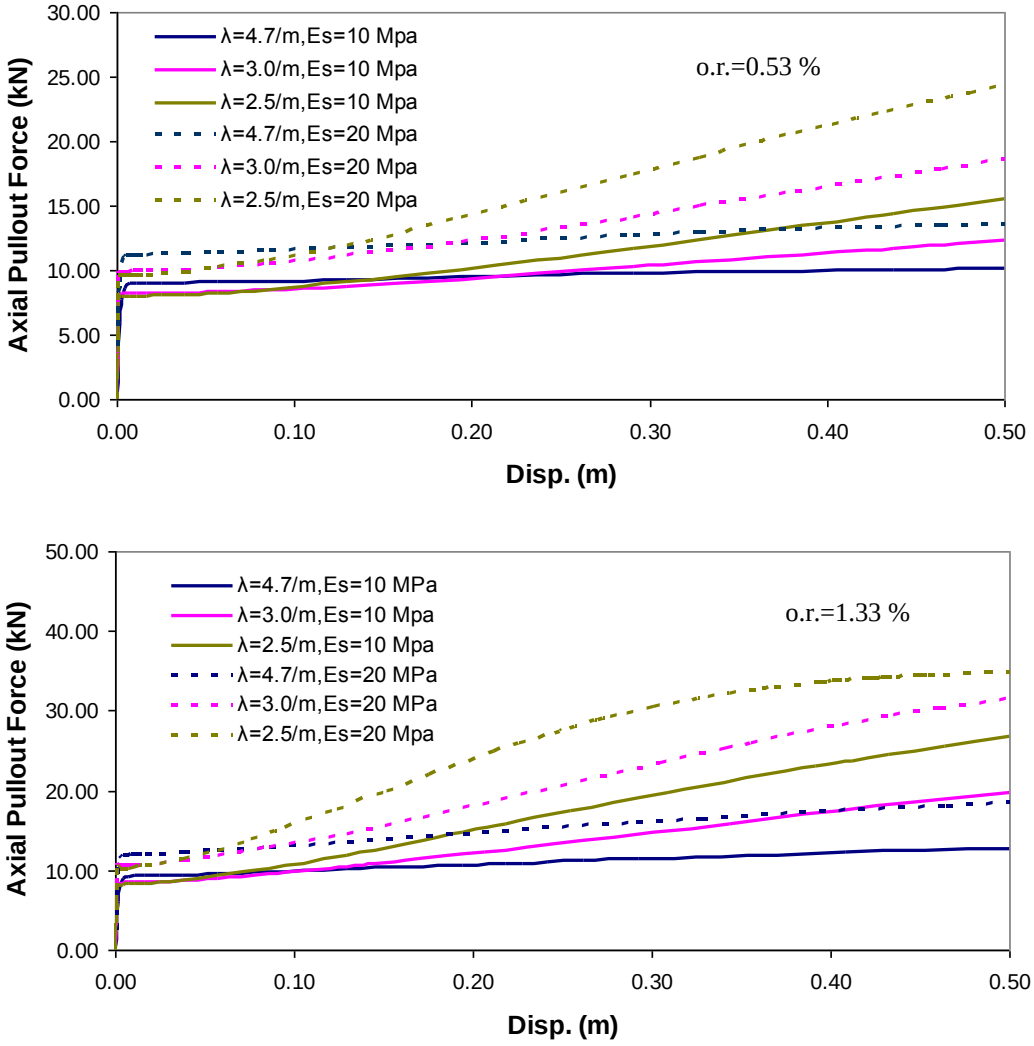

Figure 4-39: The effect of soil elastic modulus on longitudinal soil loads on buried cable with λ=4.7,3.0,2.5/m.

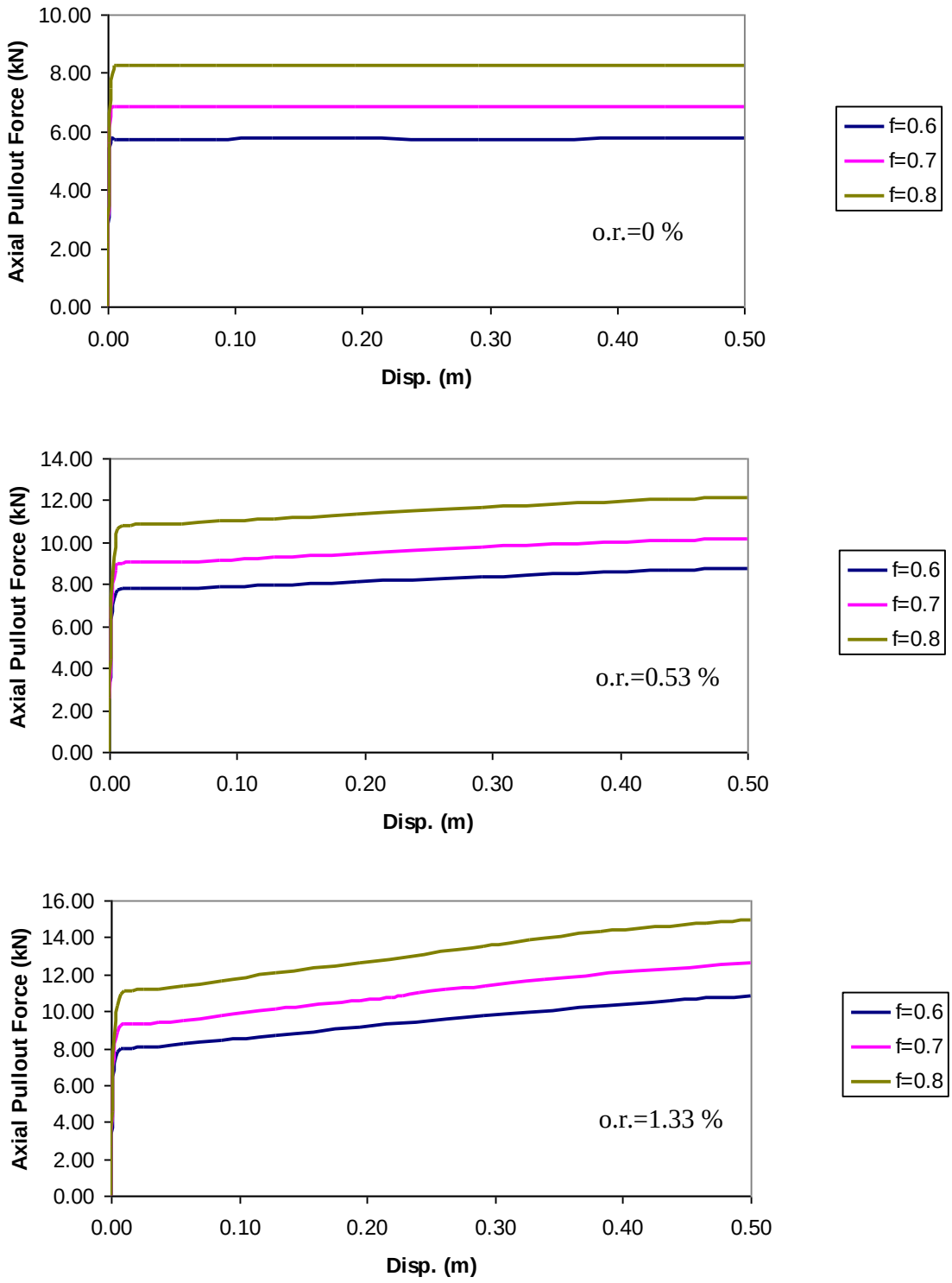

Figure 4-40: The effect of the cable/soil interface friction angle on the longitudinal response of the cable with offset ratio of (δ/L=0, δ/L=0.53 %, and δ/L=1.33%).

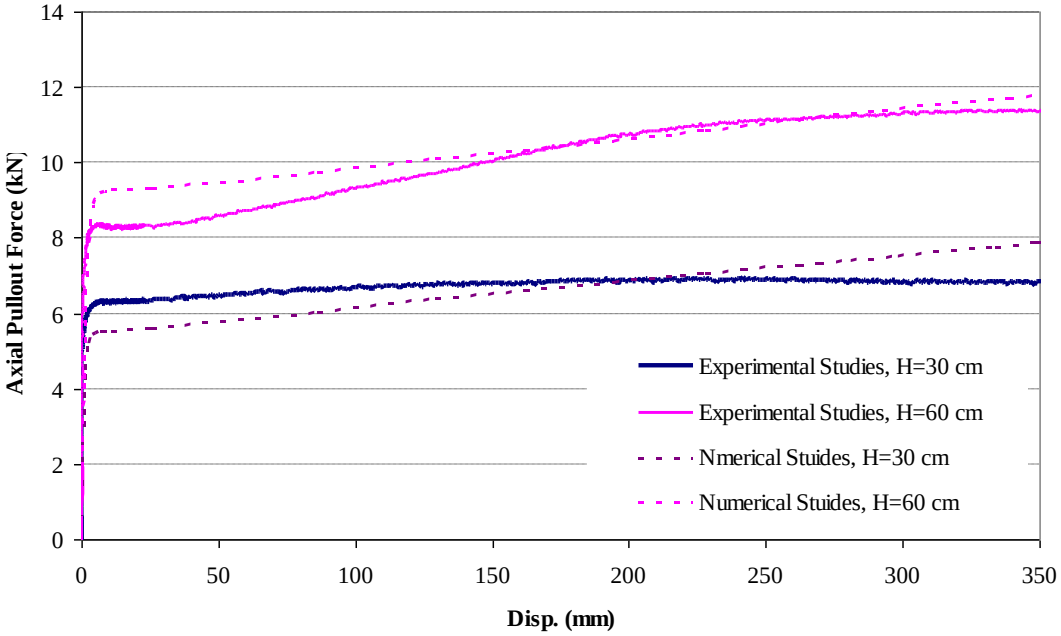

Figure 4-41: Results of experiential tests in comparison with results of numerical simulation for the offset ratio of 1.33 %, f=0.7, Es=10 MPa, φ=38°, ψ=18°,and λ=4.7 /m and burial depth of 30 and 60 cm.

Chapter 5: Application of Results

5.1 Introduction

Observed damages to buried lifeline systems in the past can be attributed either to the permanent ground deformation (PGD) or transient ground deformation (TGD). TGD refers to the ground deformation caused during the seismic wave propagation whereas PGD refers to the permanent ground movement caused by surface faulting or secondary effects causing ground failure (landslide or liquefaction induced lateral spreading). PGD affects lifeline system in the localized geographical area with higher rates of damage; however, TGD affects the lifeline system over a broad area with lower rates of damage (Eguchi (1982)). The buried power transmission cables like other buried lifeline can be damaged by both PGD and TGD. This section only focuses on the approach and the necessary tools to obtain the response of the buried power transmission cables subjected to PGD. Generally, the response of buried lifeline to any arbitrary PGD is measured by decomposing the ground deformation into longitudinal and transverse components, and then combining the response computed for each component. The longitudinal component of ground movement is parallel to the orientation of the buried lifeline whereas the transverse component of ground movement is perpendicular to the orientation of the buried lifeline. The response of buried power transmission cable subjected to any arbitrary PGD can be measured by the similar procedure established for other lifelines.

It is well recognized that liquefaction-induced PGD, particularly lateral spreading, causes significant damage to buried lifelines (Hamada and O'Rourke 1992). For instance, Figure 5-1 depicts the power transmission cable buried in the non-liquefiable soil with mild slope underlain by a saturated liquefiable soil with shallow water table. As the underlying deposit becomes liquefied the lateral spreading occurs and the upper layer moves down the slope toward a steep free face as an intact block. However, the underground power transmission

cables may not comply with the movement of the soil block, and the relative movement of the buried cable and ground strains the underground cable. The induced strain in the buried cable can be described as a function of the magnitude amount of ground deformation, the width, and the pattern of the permanent ground deformation (O'Rourke and Nordberg 1992). It is worthwhile to review some of the approach to determine the magnitude of PGD, spatial extent of the ground deformation and the shape of ground deformation due to liquefaction induced lateral spreading.

The magnitude of PGD due to liquefaction induced lateral spreading is the subject of the ongoing research. Finite element models (Elgamal 2000), simplified analytical models (Newmark 1965), and empirical models have been proposed for predicting the magnitude of PGD. Empirical models provide a simple and reliable approach to predict the magnitude of PGD. Hamada et al (1986) propose an empirical formula to calculate the horizontal ground displacement based on the failure observed in 1964 Niigata and 1983 Nihonkai-Chubu earthquake. The magnitude of ground displacement (D_H) was expressed as a function of the thickness of the liquefiable layer (H_{liq}) and the ground slope (θ) as

$$D_H = 0.75\sqrt{H_{liq}}\sqrt[3]{\theta} \qquad \text{Eqn. 5-1}$$

Other empirical models such as Bardet et al (2002), Bartlett and Youd's MLR model (1992) and Youd and Perkins' LRL model (1987), are widely used in the prediction of the magnitude of PGD, more detailed of these models can be found in Kramer (1996).

The pattern of ground deformation (i.e. the distribution of PGD along the lifeline axis) is another important parameter to consider. O'Rourke and Liu (1995) discussed different idealized PGD pattern for the analysis of the buried pipeline to the longitudinal PGD. Based on the previous study by Flores-Berrones and O'Rourke (1992), they studied the response of buried pipelines to five idealized patterns shown in Figure 5-2. They found that the block pattern yielded the largest strains in the pipeline and they used the block pattern for the determination of circumstances leading to the damage of pipelines. For the analysis of the pipeline subjected to the transverse permanent ground deformation, different researchers

proposed different approximations for the distribution of the PGD along the pipeline axis. O'Rourke (1988) used the beta probability density function whereas Suzuki (1988) used the cosine function to a power *n*. Later Liu and O'Rourke (1997) used the Suzuki (1988) model with *n=2* with the following mathematical equation to assess the behaviour of the pipeline to the transverse PGD.

$$\delta(x) = \delta(1 - \cos(\frac{2\pi x}{w})) \qquad \text{Eqn. 5-2}$$

Figure 5-3 shows the comparison between the Suzuki (1989), Liu and O'Rourke (1997), and O'Rourke (1988).

The spatial extent of PGD zones (i.e. the length of lateral spread zone) was shown to be the most important parameters influencing the response of the buried pipeline to transverse and longitudinal PGD (O'Rourke and Nordberg 1992). The spatial extent of PGD must be calculated based on the expected plan area of liquefaction which depends on the geotechnical and topographical conditions of the area. Unfortunately, the information on the spatial extent of PGD is scarce and the current empirical data shows extensive variations. For instance, Suzuki and Masuda (1991) by using data from 1983 Nihonkai and 1964 Niigata earthquake presented the magnitude and the spatial extent of the PGD. They observed that widths (L) were distributed in the range of 80 m to 600 m with the lateral displacement (δ) typically less than 2 m with the average ground strain (δ/L) $.002<\delta/L<.03$. Because of these variations, the expected length and width of a lateral spread zone should be measured depending on the area that liquefied.

With the background knowledge regarding to ground deformation parameters (magnitude, pattern, and spatial distribution), a thorough study is performed to investigate the response of the underground cable to the permanent ground deformation. This investigation consists of two parts: the first part addresses the response of the underground cable to the longitudinal PGD, and the second part addresses the response of the underground cable to the transverse PGD. As mentioned previously, buried cables have different characteristics from other

pipeline situation that they must be specifically addressed such as its out-of-straightness and bending flexibility. Most of the analyses in this section are performed in a format which is applicable to the cable with different mechanical properties with emphasis on the type of the cable used in the experimental study.

5.2 The Response of Buried Cable Subjected to Earthquake-Induced Longitudinal Permanent Ground Deformation

The objective of this section is to define the approach to quantitatively calculate the cable response due to the longitudinal PGD. Since the buried cable would typically have out-of-straightness during cable installation, the main focus of this study is how to account for the cable out-of-straightness in the prediction of longitudinal soil loads on the cable. In order to achieve this goal, a bench mark problem as created in Chapter 4 for finite element analysis was used to develop the procedure to calculate the longitudinal soil loads on the buried cable. This procedure is then expanded to investigate the influence of parameters such as the amount of ground deformation, the width of ground deformation, the cable offset ratio, and the cable shape on the response of the real underground cable. Finally, a flowchart illustrating the procedure is presented to estimate the maximum axial force and axial strain in cables with out-of-straightness subjected to the longitudinal PGD.

As demonstrated during the numerical simulation of the axial pullout tests, the longitudinal load-deformation curve consists of two distinct regions. These two regions are separated by the yield point. The yield point definition is selected herein since the load-deformation curve of the axial pullout testing has a similar behavior to the result of tension testing of the steel. The yield point is defined when the soil loads on the buried cable are completely mobilized, which occurs at small relative cable/soil displacement. The amount of yield force and the corresponding yield displacement depend on the cable/thermal backfill material interface friction (f), the burial depth ratio (H/D), density, and normal stress distribution on the cable.

Hoeg (1968) found that the normal stresses on the buried cable depend on compressibility ratio (C) and the flexibility (F) as:

$$F = \frac{E_s(1-\nu_s^2)R^3}{E_c I_c(1+\nu_s)} \qquad \text{Eqn. 5-3}$$

$$C = \frac{E_s(1-\nu_s^2)R}{E_c t_c(1+\nu_s)(1-2\nu_s)} \qquad \text{Eqn. 5-4}$$

The compressibility (C) and flexibility (F) factors are a function of E_s , E_c (the soil and equivalent cable modulus of elasticity), ν_s , ν_c ,(the soil and equivalent cable Poisson's ratio), and R is the cable radius. The yield point as shown in Chapter 4 can be related to commonly used approach (ASCE 1984) for the determination of the longitudinal soil loads on the buried pipeline which is

$$F_{axial} = \gamma' H(\frac{1+k}{2})\tan(\delta)(\pi DL) \qquad \text{Eqn. 5-5}$$

The above formula assumes that longitudinal soil load is completely mobilized throughout the length (L) and the coefficient of lateral earth pressure (k) determines average stress distribution on the pipeline.

The second part of the load-deformation curve is the hardening region. Hardening is defined as increases in the amount of load after yielding achieved. The post yield stiffness of the hardening region depends on all the factors contributing to the yield point and it also depends on the offset ratio (*o.r.*), as illustrated in Figure 5-4. Figure 5-5 shows typical idealized normal stress distribution for two buried cables, one at rest and the other subjected to the longitudinal movement (δ_L). As cable moves the normal stresses on the cable increases, thus the longitudinal soil force acting on the cable increases.

When the cable is straight, it can be assumed that the longitudinal soil load can be presented by the elasto-plastic or complete plastic behaviour as the commonly used approach in

practice for other pipelines (ASCE 1984). In order to calculate the additional soil loads on the cable due to out-of-straightness, the variation in normal forces on the buried cable should be first calculated. This can be accomplished by defining the coefficient of subgrade reaction in the horizontal transverse direction. Vesic (1961) presented the coefficient of subgrade reaction (k_v) for the case of the vertically loaded beam on the surface of the elastic foundation based on the continuum elastic analysis. The coefficient of subgrade (k_v) was expressed as a function of the relative beam stiffness to the soil stiffness as

$$k_v = \frac{0.65E_s}{(1-\nu_s^2)}\sqrt[12]{\frac{E_s D^4}{E_b I_b}} \qquad \text{Eqn. 5-6}$$

The coefficient of subgrade reaction can be extended to the case of the beam on the elastic half space but subjected to the lateral loading. This is accomplished by knowing that the ratio of the horizontal static stiffness to the vertical stiffness of the disk foundation on the homogenous half-space is

$$\frac{k_H}{k_V} = \frac{2(1-\nu_s)}{2-\nu_s} \qquad \text{Eqn. 5-7}$$

Therefore, the coefficient of subgrade reaction for the foundation subjected to the lateral loading can be obtained as

$$k_H = \frac{1.3E_s}{(1+\nu_s)(2-\nu_s)}\sqrt[12]{\frac{E_s D^4}{E_b I_b}} \qquad \text{Eqn. 5-8}$$

The presented coefficient of subgrade reactions in the vertical and horizontal directions accounts for surface foundation. For the foundation with the burial depth *H,* the coefficient of subgrade reaction can be approximated by using the cone model theory as established by Meek and Wolf (1994). The cone model theory is based on the one-dimensional theory of wave propagation. The soil underneath a foundation is replaced by an opening cone. The opening of the cone is calculated so that it provides the same static stiffness as the exact analytical result of the foundation on the elastic half space. The parameter Z_0 controls the

opening of the cone. For the surface foundation resting on the elastic half space with the shear modulus of G and Poisson's ratio (ν), the static stiffness and corresponding Z_0 for vertical or translation motions can be obtained as

Vertical Motion: $$K_V = \frac{4Gr_0}{1-\nu_s} \text{ and } \quad \frac{Z_0}{r_0} = \frac{\pi}{4}(1-\nu)$$ Eqn. 5-9

Translational Motion: $$K_H = \frac{8Gr_0}{2-\nu_s} \text{ and } \quad \frac{Z_0}{r_0} = \frac{\pi}{8}(2-\nu)$$ Eqn. 5-10

For the case of the foundation with burial depth of H, the following superposition approach was attempted. First, the static stiffness of the foundation in the full elastic space was obtained. Second, the stresses at the distance H is calculated based on the cone model concept as depicted in Figure 5-6-b. With the knowledge that the stresses on the surface of the buried foundation must be zero, an imaginary foundation was created so that it cancels the stresses resulting from the foundation in the full elastic space as depicted in Figure 5-6-c. With this superposition, the static stiffness of the foundation with burial depth of H can be obtained as:

$$k = 2k_H\left(\frac{1}{1+\frac{1}{1+\frac{16}{\pi(2-\nu)}H/r_0}}\right)$$ Eqn. 5-11

As indicated in the above expression, the translational static stiffness equals to $2k_H$ for the very deep beam and equals to k_H for the surface beam. Once the static stiffness of the foundation with the burial depth H was estimated, the coefficient of subgrade reaction (k_H) for the horizontal lateral direction can be calculated as:

$$k_H = \frac{2.6E_s}{(2-\nu_s)(1+\nu_s)}\sqrt[12]{\frac{E_s D^4}{E_b I_b}}\left(1+\frac{1}{1+\frac{1}{\frac{16}{\pi(2-\nu_s)}H/r_o}}\right)$$ Eqn. 5-12

In order to verify the validity of the estimation of the coefficient of subgrade reaction (k_H) in the horizontal lateral direction, the problem of the buried cable subjected to two concentrated loads as shown in Figure 5-7 is selected. For the sake of comparison, the properties (such as the cable length and cable diameter) of this problem are selected to resemble the lateral pullout test configuration. The force-deformation relationship for the small movement of the cable's end (the elastic case) is calculated by two approaches. In the first approach, the problem was solved by the finite element analysis and the ratios of the force to the corresponding displacement ($k_t=P/\Delta$) were measured for the soil with elastic modulus (E_s). In the other approach, the response of the buried cable was calculated by using the soil spring with the proposed coefficient of subgrade reaction (k_H). The ratio of the force to its corresponding displacement (k_t) can be found as (Timoshenko 1960)

$$k_t = \frac{\sin \lambda L + \sinh \lambda L}{\cos \lambda L + \cosh \lambda L} . \frac{k_H}{2\lambda} \qquad \text{Eqn. 5-13}$$

where $\lambda = \sqrt[4]{\frac{k_H}{4E_b I_b}}$

Figure 5-8 illustrates the variation of the ratio of k_t stiffness nomralized to the soil elastic modulus as a function $(Es/Ec)^{.089}$. Herein, (E_c) and (E_b) are the cable elastic modulus. Also, the results of the finite element analysis were included in Figure 5-8 to compare the results of both cases. As can be seen, a good agreement between the F.E. analysis results and the analytical results with the coefficient of subgrade reaction (k_H) is achieved when $(Es/Ec)^{.089} > 0.45$. For instance, this condition requires that $Ec<7.9\times10^{10}$ for the soil with elastic modulus of $E_s=10^7$ which the tested buried cable characteristics satisfies this condition.

5.2.1 Prediction of the Amount of Lateral Soil Loads during Cable Longitudinal Movement

As observed during the experimental studies and demonstrated by numerical simulation, the cable's offset creates an increase in the normal stresses and consequently increases the axial pullout force. In order to gain more insight and to predict the effect of cable's offset on the amount of soil loads on the cable, analytical formulation with the help of the coefficient of subgrade were provided. The benchmark of this study is the results of numerical simulation of the axial pullout test which were conducted for different burial depths and offset ratios. As mentioned previously in the F.E. analysis of axial pullout tests, the cable shape is assumed to have a maximum offset in the middle and approaches to zero offset at the margins with the shape of

$$s(x) = \begin{cases} s\cos^2(\frac{\pi x}{L}) & -L/2 \le x \le L/2 \\ 0 & otherwise \end{cases} \qquad \text{Eqn. 5-14}$$

in which s is the cable offset and L is the cable length. The cable with this shape is modeled by a beam element with longitudinal and horizontal transverse soil springs. The problem is to understand how much the axial pullout force increases as the cable moves longitudinally by (δ_L). Figure 5-9 shows the initial and subsequent cable configuration after the longitudinal movement (δ_L). This figure shows that the cable longitudinal movement causes cable deformation and mobilization of the horizontal transverse soil spring.

In order to calculate the amount of force mobilizations in the horizontal transverse soil springs, a straight cable resting on the horizontal transverse soil springs is assumed to be subjected to the differential displacement of $S(x) - S(x - \delta_L)$ for every longitudinal cable movement (δ_L). In this way, the problem of the axial movement of the cable is replaced by the problem of the cable subjected to the lateral soil movement as shown in Figure 5-10.

To establish the geometry of a cable subjected to the longitudinal movement, an infinitesimal element of length *dx* located at distance x from the centerline is considered. The basic differential equation of the elastic curve can be obtained as

$$EI\frac{d^4z}{dx^4} = q(x) \qquad \text{Eqn. 5-15}$$

in which $q(x)$ is $k_H(s(x) - s(x-\delta_L) - z(x))$.

The complete solutions of the infinite, semi-infinite, and finite beam on elastic foundation with different patterns of loading are presented in Timoshenko (1960) and Hetenyi (1946). The deflection of the infinite beam subjected to the concentrated load was derived by Timoshenko (1960) as

$$z(x) = \frac{p}{8\lambda^3 EI}e^{-\lambda x}(\cos(\lambda x) + \sin(\lambda x)) \qquad \text{Eqn. 5-16}$$

where λ is

$$\lambda = \sqrt[4]{\frac{k_H}{4EI}} \qquad \text{Eqn. 5-17}$$

It is worth mentioning that the solution of the beam with finite length can be considered as infinitely long if $(\lambda L > 5)$, which normally buried cable falls into this category. This solution for a concentrated load can be expanded by using the principle of superposition to an arbitrary loading ($q(x)$). Figure 5-11 shows an infinite beam on the elastic foundation subjected to the arbitrary loading *q*(*x)* limited to portion of the beam with length *L*.

The deflection at point *A*, positioned *x* from centerline, produced by an element of *qdy*, can be obtained by substituting *qdy* for *P*.

$$z(y) = \frac{q(y)dy}{8\lambda^3 EI}e^{-\lambda y}(\cos(\lambda y) + \sin(\lambda y)) \qquad \text{Eqn. 5-18}$$

Therefore, the deflection at point A due to the distributed load over length L can be calculated as

$$z(x_A) = \int_0^{L/2-x_A} q(x_A + y)e^{-\lambda y}(\cos\lambda y + \sin\lambda y)dy + \int_0^{L/2+x_A} q(x_A - y)e^{-\lambda y}(\cos\lambda y + \sin\lambda y)dy \quad \text{Eqn. 5-19}$$

in which x_A is the location of point A. By knowing the cable deformation at any point, the change in the axial pullout force as a function of longitudinal displacement (δ_L) due to increase in the horizontal transverse force can be calculated as

$$\Delta F_L = \int_{-L/2}^{L/2} f.k_H.|s(x) - s(x-\delta_L) - z(x)|dx \quad \text{Eqn. 5-20}$$

in which, f is the interface friction coefficient between the thermal backfill material and the cable. It should be noted that ΔF_L calculated by this method must be added to the mobilized longitudinal friction force (F_0L).

The procedure to obtain ΔF_L is implemented in Mathcad (ver. 14.0) software. The increase in the axial pullout force is calculated for different burial depth ratios and different offset ratios as a function of the longitudinal cable displacement. In order to investigate the accuracy of this formulation, the comparison is made between the numerical F.E. analysis results and currently developed analytical formulation for burial depth ratios of H/D=10.0 and H/D=6.7, and offset ratios of $o.r.$=0.53 % and $o.r.$=1.33 % as shown in Figure 5-12. The comparison results show that the current analytical solutions slightly overestimate the axial pullout force for large longitudinal displacement (δ_L). This overestimation is caused by: firstly, the coefficient of horizontal lateral subgrade reaction (k_H) is developed for linear media around the buried cable. The media immediately around the cable can behaves nonlinearly particularly for a large offset ratio as shown in Figure 5-12-b. Secondly, the soil spring is a rough representation of the soil behavior around the buried cable. However, the analysis performed by the coefficient of subgrade reaction (k_H) generally gives a reasonable estimation of the axial pullout force.

5.2.2 Estimation of the Additional Axial Soil Loads on the Cable with Out-of-Straightness

The purpose of this section is to understand the amount of increase in the longitudinal soil loads for a longer underground cable subjected to longitudinal PGD. The experimental test and finite element analysis were limited to the certain cable length (3.75 m), and it is almost impractical to use those methods to investigate the effect of out-of-straightness on the axial force in the long cables due to its analysis cost (time or monetary). On the other hand, the analysis with coefficient of the horizontal lateral soil subgrade provides a fast analysis alternative with reasonable approximation in prediction of the axial soil loads on the cable with out-of-straightness. It also gives this opportunity to perform parametric study to investigate the effect of variables such as cable lengths, cable shape and the offset ratio on the response of underground cables subjected to longitudinal PGD.

5.2.2.1 Methodology and Results of Analysis

A simple analytical procedure was developed to calculate the additional increase in the axial pullout force for the small scale buried cable (L=3.75 m) with out-of-straightness. The same analytical procedure is used to predict the longitudinal soil loads for a long scale cable. The assumptions in the analytical procedure are: 1) the soil behaviour in the horizontal lateral direction is idealized by the soil spring with coefficient of subgrade reaction (k_H), 2) the flexural behaviour of the cable is assumed to be linear, 3) the cable is assumed to be axially rigid for the time being, the axially elastic and inelastic cable are discussed later, and 4) the amount of the offset value is assumed to be small.

The cable layout shape is among the most difficult parameters to determine since the small bending flexibility of the cable causes the cable to form an arbitrary shape during laying operation. For the simplicity of this investigation, the buried cable laying shape is assumed to have a sine function whose amplitude is the amount of the offset and the distance between

peaks is L as shown in Figure 5-4. It is evident that the cable shape as a sinusoidal function never happens in reality; however, its features such as its periodic shape make the investigation easier. Even with a simplified shape, still significant complexity exists. Many combinations of sinusoidal shapes can be assumed for the buried cable. For instance in the length L_t of the longitudinal ground movement, the cable can have a different number of the peaks depending on the length L. Another issue is the assumption on the boundary of the ground movement, i.e., the ground movement regions can coincide with peak, zero crossing, or somewhere between those points for the cable with sinusoidal shape. With this information, a preliminary investigation was performed to figure out the conditions in which the maximum longitudinal soil load on the cable with sinusoidal shape occurs and use those conditions for the next phase of study.

5.2.2.1.1 Additional increase in the longitudinal soil loads on the axially rigid cable

The bending flexibility of the cable and the cable manufacturing requirement dictate the distance between the offset peaks (L). For instance, one can expect a larger L for the steel pipeline than for the cable used in the power transmission lines since the bending stiffness of the steel pipeline is higher than that of the cable. Based on the experience with the power transmission cable, the minimum length (L) can be limited to 3 m, and the length of ground movement (L_t) varies from 9 m to 243 m. The parameter n is defined as the ratio of L_t to $2L$ to find the number of the peaks in the length L_t. Furthermore, as discussed before, the boundary of ground movement can coincide with zero offset or maximum offset, or anywhere between those points. For this problem, the two limiting cases are only considered. The schematic description of this problem is shown in Figure 5-13. As shown in this figure, the cable has a sinusoidal shape which its periodic shape is controlled by parameter L and its amplitude is controlled by δ_L.

In order to understand the additional increase in the axial soil restraint (ΔF_L), the problem of a buried cable with length L_t pulling out from a block of soil mass or a buried cable subjected to a block of soil movement with length L_t is evaluated. Figure 5-14 shows cable shapes

meeting the above criteria. In this figure, the region of the soil mass movement with the width (L_t) moves by δ_L. Those figures are different from each other with respects to: 1) the boundary conditions and 2) the number of the positive and negative peaks in the region (L_t). Figure 5-14-a shows a soil mass which its starting and ending parts coincide with the maximum cable offset while Figure 5-14 -b shows a soil mass whose starting and ending parts coincide with the zero offset. The same difference is created in Figure 5-14 -c and Figure 5-14 -d. The difference between the first two figures (*a* and *b*) and the second two figures (*c* and *d*) are the number of the positive and negative peaks in the region, *a* and *b* have even numbers of the positive and negative peaks while *c* and *d* have uneven numbers of the positive and negative peaks. Figure 5-14-e and Figure 5-14-f are different from Figure 5-14 -d and Figure 5-14-b in which the starting point of the soil mass coincides with zero offset and the ending part coincides with maximum offset.

Analyses are performed for each type of the cable layouts (*a* to *f*) as depicted in Figure 5-15 to investigate the effect of cable's shape on the longitudinal soil loads on the cable. Figure 5-15-*a* shows an increase in the axial force (ΔF_{axial}) as a function of the longitudinal movement of the soil mass (δ_L) for the buried cable with n=3, L=8 m, and *o.r.*=0.63%. Figure 5-15-b shows the same information but for the buried cable with n=5, L=8 m, and *o.r.*=0.63%. Results of the analysis show that the patterns *b* and *c* result in the maximum axial soil loads on the cable. Inspection of those patterns shows that the starting and ending points of the soil mass in both patterns coincide with the zero offset while in other patterns they do not coincide with zero offset. The reason that those patterns leads to such an increase in the axial force can be understood by referring to Figure 5-16. Two limiting cases are depicted in this figure in which the soil mass boundaries coincide with the zero offset (Figure 5-16-*a*) and the soil mass boundaries coincide with the maximum offset (Figure 5-16-b). By examining the relative movement of the cable and its original position, as shown as dotted lines, it can be observed that more soil loads subjects the cable when the soil mass region coincides with zero offset since the sinusoidal function has a greater rate of change at zero crossing. The second observation is related to the situation when uneven numbers of positive and negative peaks are located in the region of the soil mass movement (L_t). This situation

leads to a larger soil loads on the cable in compare to the situation where even numbers of positive and negative numbers exist in the region of soil mass movement.

In summary, in order to achieve a maximum axial soil load on the cable, 1) the region of the soil mass movement should be bounded by the zero offset at both ends, and 2) the length of the region of soil movement (L_t) should be an odd multiplier ($2n$-1) of L. With the understanding of which shape leads to a larger longitudinal soil loads on the cable, a thorough parametric study is performed to investigate other influential parameters, including offset ratios (*o.r.*), L, and L_t.

To investigate the effect of the width of ground movement on the axial soil loads on the cable, four widths are selected as L_t=9, 27, 81, and 243 (m). For each width, cables with different sinusoidal shape can be assumed. However, only those shapes creating maximum axial loads are considered. For instance, Figure 5-17 shows a region of the ground movement with length L_t and three cables (L_t / L =1, 3, 9) with offset value (Δ).

Figure 5-18 shows the variation of an additional increase in the axial soil loads on a cable with the maximum offset value (Δ) of 5 cm and the minimum distance between peaks (L=3 m) as a function of the block of soil movement. Since the horizontal lateral subgrade coefficient is developed for a linear behavior of the soil the result of this analysis can be linearly interpolated to the cable with different offset value. By inspecting each graph, the largest increases in the axial soil loads are when the L_t/L ratio has the largest value. Also comparisons between the maximum value of the developed axial soil loads on the cable for different widths of the soil movement (L_t) show that the length (L) is an influencing parameter. As the length L decreases the axial soil loads on the cable increases. The width of the soil movement (L_t) is not important parameter in this problem since the cable has a small bending stiffness, and most of the relative cable/soil deformation is located at the margin of the ground deformation zone. To elucidate this condition, consider an infinite beam on the elastic foundation subjected to the uniform ground deformation (u_g) with the length of L_t as depicted in Figure 5-19. A very flexible beam deforms to u_g in the region of (L_t -2L'). However, the beam does not conform to the ground deformation at margins (L'). The same

analogy can be made when the cable is subjected to non-uniform ground deformation. Therefore, the length of the ground deformation region is not important parameter in the very flexible beam. Based on the result of analysis, it can be concluded that 1) an increase in the soil movement (δ_L) increases the axial soil loads on the cable, 2) a decrease in the distance of the cable offset peaks (L) increases the axial soil loads on the cable, and 3) the cable length (L_t) does not have much effect on the axial soil loads on the cable.

5.2.2.1.2 Additional increase in the longitudinal soil loads on the axially elastic cable

In the previous analysis, the uniform amount of ground deformation (δ_L) is assumed throughout the region of the ground movement (L_t). However, the axial deformation of the cable reduces the relative movement of the cable and surrounding ground; thus, it affects the amount of the soil loads on the cable. It can be easily shown that if the cable and the surrounding ground move together, no soil loads apply on the cable. The good approximation for the distribution of the ground movement can be a quadratic function with the maximum value at one end ($-L_t/2$) and zero at the other end ($L_t/2$) as expressed by the following reduction function

$$\mathrm{Re}(x) = \left(\frac{x}{L_t} - \frac{1}{2}\right)^2 \qquad \text{Eqn. 5-21}$$

The reduction function $Re(x)$ can be interpreted as a displacement profile of the buried cable with the shaft friction (F_0) subjected to the concentrated load at one ends causing the maximum unit axial displacement. Figure 5-20 shows the cable with sinusoidal shape subjected to the mass of the ground movement with the length L_t. The amount of the ground movement is (δ_L) at one ends and it approaches to zero with the reduction function $Re(x)$.

The same plots as illustrated in Figure 5-21 are prepared for this situation when the ground movement is not uniformly distributed along the width L_t due to the cable axial deformation. The widths of soil movement region are selected as L_t=9, 27, 81, and 243 (m).The amount of the offset is selected as 5 cm and the minimum value of the distance between the offset peak

is selected as 3 m. Comparing the results of the Figure 5-18 and Figure 5-21 shows that in the latter case the amount of increase in the axial soil loads on the cable is almost 50% less than the axially rigid cable.

5.2.2.1.3 Additional increase in the longitudinal soil loads on the axially inelastic cable

In the interpretation of *Re*(x) function, it is mentioned that *Re*(x) is an elastic axial deformation of the cable with the shaft friction of F_0 subjected to the concentrated load causing the unit displacement. However, the cable can yield, depending on the amount of the yield strength (T_y) and ground deformation (u_g), and behaves inelasticity. In order to investigate the effect of the inelastic axial deformation of the cable, bilinear behaviour, as depicted in Figure 5-23, is considered for the axial behaviour of the cable. By setting the coordinate at the center of the L_t region, the following expressions can be obtained for the inelastic axial deformation of the cable.

$$\mathrm{Re}(x)=\frac{1}{\frac{1}{\beta}(\frac{L_t}{L_y}-1)^2+2(\frac{L_t}{L_y}-1)+1}\left[\frac{1}{\beta}(\frac{x}{L_y}-\frac{L}{2L_Y}+1)^2-2(\frac{x}{L_y}-\frac{L}{2L_y}+1)+1\right] \quad x<L/2\text{-}L_y \qquad \text{Eqn. 5-22}$$

$$\mathrm{Re}(x)=\frac{1}{\frac{1}{\beta}(\frac{L_t}{L_y}-1)^2+2(\frac{L_t}{L_y}-1)+1}\left[(\frac{x}{L_y}-\frac{L}{2L_y})^2\right] \quad x>L/2\text{-}L_y \qquad \text{Eqn. 5-23}$$

in which β is the hardening slope of the axial-force deformation, L_t is total length of the cable or the region of the ground deformation, and $L_y = T_y / F_0$. Figure 5-22 shows the axial deformation of the cable for two ratios of $L_t/L_y=2$ and 8/7.Analyses are attempted to compare the results of increase on the longitudinal soil loads on the cable for different L_t/L_y. Figure 5-24 shows the proposed reduction function for the cable with different $L_t/L_y=4,\ 2,$ and *1* and the table showing the corresponding axial soil load increase for L_t =9 m, L_t /L =3, β=0.1, Δ=5

cm, and δ_L=0.5 m. Results show that the L_t/L_y ,and consequently the yielding of the cable, is not a determining factor in the calculation of the amount of the increase in the additional longitudinal soil loads on the cable due to out-of-straightness. It should be noted that the results are for the case when *Es*=10 *Mpa* and λ=4.5 /m. The results are definitely varied for other cases as it will be described in the following section.

5.2.3 Other Parametric Studies

The previous results are obtained for the parameter λ=4.5 /m. The λ parameter describes the relative stiffness of the cable to the surrounding medium. In this section, the effect of this parameter on the amount of the axial soil load increase (ΔF_{axial}) due to longitudinal ground movement is investigated. In order to narrow down the parametric study, the following assumptions based on the previous study are used:

The shape of the cable is assumed to be sinusoidal with L=3 m and δ=5 cm. The ratio of L_t / L_y=*2.*The parameter λ varies from 1.5 to 4.0 /m to cover different cable and soil stiffness.

Figure 5-25 shows the results of analysis for the buried cable subjected to the block of soil movement with length L_t=9 and 27 m for different λ parameters. It can be seen that by increasing the λ parameter the effect of the L_t on the ΔF_{axial} decreases since large value of λ parameter corresponds to very flexible bending cable. Furthermore, the analysis shows that the largest increase in the ΔFaxial occurs for the cable with small λ. All in all, the purpose of these graphs is to demonstrate the importance of λ parameter in the increase in the axial soil loads on the cable, and the analysis should be performed for specific case of cable-soil to obtain the increase in the axial force due to longitudinal permanent ground movement. The following sections will be discussed the steps necessary to obtain the response of the buried cable subjected to longitudinal PGD.

5.2.4 Implementation of the Result of Analysis in Practice

In this section, a methodology to assess the performance of the buried cables subjected to the longitudinal permanent ground deformation is presented. The permanent ground deformation is normally characterized by three parameters: the length of ground deformation, the magnitude of ground deformation, and finally the shape or pattern of the ground movement. Figure 5-26 shows the cable subjected to the block pattern of the ground movement with width L_t and amount of ground deformation (u_g).

The soil behaviour surrounding the cable is modeled by a plastic spring with the amplitude of F_0. The axial behaviour of the cable is presented by a bilinear model as shown in Figure 5-23 with the yield strength (T_y) and stiffness hardening (βEA). For the time being, it is assumed that the cable has no out-of-straightness. Depending on the amount of ground deformation and the length of ground deformation, a compliant and non-compliant cable can be identified (O'Rourke (1995)). The non-complaint cable happens when the amount of ground deformation is large and the width of ground deformation is small. In this case, the cable deformation is less than the subjected ground deformation. On the other hand, the complaint cable happens when the amount of ground deformation is small and the width of ground deformation is large. In this case, the cable deformation at some part of ground deformation region is equal to ground deformation. The critical length (L_{crit}) distinguishing the boundary between complaint and non-complaint behaviour can be formulated as a function of cable axial stiffness (EA), cable axial hardening (β), the longitudinal soil-cable interaction behaviour (F_0), and the ratio of yield axial force to F_0 ($L_y=2T_y/F_0$). For the case of non-yielding cable, the critical length can be calculated as

$$L_{crit} = 2\left(\frac{AEu_g}{F_0}\right)^{1/2} \qquad \text{Eqn. 5-24}$$

Depending on the length of the ground deformation (L_t) compared to (L_{crit}) , the maximum axial force in the cable can be calculated and then compared with the cable yield strength (T_y).

$$T_{\max} = (F_0 . L_t)/2 \qquad L_t < L_{crit} \qquad \text{Eqn. 5-25}$$

$$T_{\max} = (F_0 . L_{crit})/2 \qquad L_t > L_{crit} \qquad \text{Eqn. 5-26}$$

The combination of the length (L_t) and the amount of ground deformation (u_g) cause yielding in the cable. For the situation when $T_{\max}$ is greater than T_y, the yielding in the cable occurs and new critical ground deformation length should be calculated. By referring to Figure 5-27, the new critical ground deformation for yielding cable can be expressed as a

$$L_{crit} = L_y + (\beta(4AEu_g / F_0 - L_y^2))^{1/2} \qquad \text{Eqn. 5-27}$$

Where $L_y = 2T_y / F_0$

By knowing the new critical ground deformation length, the maximum axial strain can be obtained as

$$\varepsilon_{\max} = \varepsilon_y + \frac{F_0(L - L_y)}{2\beta AE} \qquad L_t < L_{crit} \qquad \text{Eqn. 5-28}$$

$$\varepsilon_{\max} = \varepsilon_y + \frac{F_0(L_{crit} - L_y)}{2\beta AE} \qquad L_t > L_{crit} \qquad \text{Eqn. 5-29}$$

Figure 5-28 outlines the procedure to obtain the axial stain in the underground cable due to the longitudinal permanent ground deformation. As shown in Figure 5-28, at first step the yield ground deformation (L_y) and an elastic critical ground deformation $L_{crit} = 2(AEu_g / F_0)^{1/2}$ should be obtained. By comparing the minimum of L_t and L_{crit} to L_y, the possible yielding in the cable can be investigated. The reason for obtaining the minimum of those values is that the maximum possible axial force (T_{max}) in the cable is a function of L_{crit}. By following the procedure outlined in Figure 5-28, the axial strain for a straight cable

can be derived. At the final stage, the effect of out-of-straightness can be added as an additional force (ΔF_{axial}) to the maximum axial force resulting from a straight cable analysis. The following procedure describes in details the approach to calculate ΔF_{axial}

1) determine the cable properties (E_b, D) and burial depth ratio (H/D)

2) determine the soil properties (E_s, ν_s)

3) calculate coefficient of subgrade reaction (k_H)

4) determine the soil/cable interaction behaviour (F_0) as table Table 5-1

5) calculate parameter λ

6) define a shape for the cable ($s(x)$), as a guideline the results of preliminary analysis on the cable with sinusoidal shape can be used.

7) determine the length L_1. This length is defined as the distance between zero tensile forces to the maximum tensile force as shown in Figure 5-27. It is worth mentioning that $L_1 \leq 0.5L_{crit}$.

8) determine L_y and the ratio of L_1/L_y to define $Re(x)$ function.

9) using proposed analytical formulation to measure the increase in the axial soil loads (ΔF_{axail}) for the relative cable /ground deformation (u) at the maximum tensile force ($u \leq 0.5u_g$)

10) finally, the calculated increase in the axial force ($\Delta \varepsilon_{axial}$) should be added to calculated ε_{max} for the axial stain in the straight cable as shown in Figure 5-28.

Clearly this additional force (ΔF_{axail}) increases axial tension in the cable and it possibly changes the critical length calculation. At this stage, the new interface friction factor (F_0) is proposed by assuming first the additional axial force is uniformly distributed on the length L_1

and then adding this value to the initial value of interface friction force and recalculating the new critical length as depicted in Figure 5-28.

5.2.5 Summary of the Response of Buried Cables to Longitudinal PGD

The methodology is presented to calculate the buried power transmission cable response subjected to the longitudinal block pattern of PGD. In this methodology, the maximum axial force should be first calculated for the straight cable and then the additional force due to out-of-straightness is added. Several parametric studies are performed to investigate the effect of the cable length, cable offset ratio, cable shape, and λ parameter on the additional axial soil loads on the cable due to out-of-straightness. It is found that λ parameter and offset ratio are the most important parameters in measuring an additional increase in the axial soil loads on the cable. The effect of width of ground deformation (L_t) on the additional increase in axial force depends on λ parameter. It is found that for the large value of λ parameter, which the power transmission cable is in this category; L_t is not a significant parameter.

5.3 The Response of Buried Cable Subjected to Earthquake-Induced Transverse Permanent Ground Deformation

5.3.1 Representation of Soil Spring Behaviour in the Transverse Direction

In the analyzing the cable with out-of-straightness to the longitudinal PGD, an approach was discussed to obtain the horizontal transverse soil spring. Since that study was conducted for the cable with small out-of-straightness, the linear assumption for the soil spring was valid. However, the assumption of the linear soil is unjustifiable when the soil subjected to large deformation due to large movement of the buried cable. This section presents an approach to obtain the horizontal lateral soil spring for the soil and cable with different mechanical properties. The method consists of following two steps: 1) the response of the buried cable

(i.e. the load-deformation curve) is measured by either numerical simulations or experimental testing; 2) the nonlinear spring model is obtained by calibrating the response of the buried cable to that of numerical simulation or experimental testing. In order to accomplish this goal, a numerical model was developed in ABAQUS 6-7.1. The soil and the cable behaviour are represented by macro element models. Macro element models provide the least expensive yet most efficient analysis method that it is widely used in engineering practices.

ABAQUS standard provides pipe soil interaction (PSI) element to model the interaction between the pipe and its surrounding soil. The PSI elements are formulated for the two-dimension (PSI24, PSI26) and three-dimension (PSI34, PSI36) problems. One edge of PSI elements is attached to the interacting structure, such as the pipe, and the other edge is connected to the far-field, such as the ground surface. Figure 5-29 shows the two-dimensional PSI24 element with four nodes.

PSI elements only have a displacement degree of freedom. The relative displacement (Δu) between the far-field (U_f) and the interacting structure (U_s) causes strains in the element according to its defined behaviour. The behaviour is expressed by the force per unit length in three independent directions (longitudinal, transverse horizontal and horizontal vertical). The spring behaviour can be either linear or nonlinear as depicted in Figure 5-29. The advantage of PSI element over other conventional spring models is that the same behaviour can be used for a uniform and non-uniform mesh. For this analysis, the buried cable-soil interaction behaviour is modeled with PSI34 element. The PSI element is defined so that one edge of the element shares nodes with the buried cable, and the other nodes on the other edge represent a fix surface. The type of behaviour for the spring model in the longitudinal and lateral direction will be discussed in the next section.

5.3.1.1 Soil-Cable Modelling

The behaviour of the soil spring model in the horizontal transverse can be represented by rectangular hyperbolic model or bilinear model. The rectangular hyperbolic model was first

introduced by Kondner (1963) and it was used later by Audibert and Nyman (1977) and by Trautmann and O'Rourke (1983) to represent the soil behaviour in the horizontal transverse direction. Elasto-plastic model can be used conveniently in the commercial software with reasonable accuracy. This model is defined by two-unknown parameter, the yield force and corresponding yield displacement.

5.3.1.1.1 Longitudinal behavior of the PSI element

A detailed study on the behaviour of the longitudinal soil spring is presented in the response analysis of the buried cable subjected to the longitudinal PGD. By revisiting the load-deformation curve of the axial pullout test, three distinct regions can be identified as depicted in Figure 5-30. As mentioned previously, the hardening part of load-deformation curve occurs at large displacement. The buried cable subjected to only horizontal lateral PGD activates the small part of load-deformation curve since it undergoes a small longitudinal movement. Thus, the hardening part of this graph can be ignored. The elasto-plastic model as shown in Figure 5-30 is the reasonable selection to model the longitudinal behaviour of the PSI element. The darker curve shows the typical load-displacement curve as observed in the experimental studies, and the lighter curve shows the conservative idealization of the longitudinal soil behaviour in the form of the elastically-perfectly plastic.

Its behaviour (yield force and yield displacement) can be easily obtained from the mean response of buried cables in the experimental axial pullout test. Since the displacement at the pulling head and the tailing end are equal the spring behaviour can be obtained by calculating the axial force per unit length. The results of this idealization are tabulated in the Table 5-1 for different burial depths.

5.3.1.1.2 Modeling of the cable

One of the inexpensive approaches, with regard to analysis time ,to obtain the overall response of the buried cables is to model the buried cable with a beam element. ABAQUS

offers a wide range of the three-dimensional beam elements with the linear (*B31*), quadric (*B32*), and cubic (*B33*) interpolation functions. Furthermore, ABAQUS provides an alternative formulation for beams undergoing large deformation that they have significant axial rigidity such as a flexing long pipe or cable. The geometrically nonlinear analyses of this type of the problem are better solved by using hybrid elements (*B31H*, *B32H*, *B33H*). The material nonlinearity of the beam cross section can be considered by using a general beam section behaviour, i.e., the beam section's response to axial, shear, bending, and torsion is described by defining axial force (N), bending moment (M_{11}, M_{22}), shear (V), and torsion (T) as a function of axial strain (ε_{11}), curvature (k_{11},k_{22}), shear deformation(γ), and twist (Φ) respectively.

$$N = N(\varepsilon_{11}),\ M_{11} = M(k_{11}),\ T = T(\phi),\ \text{and}\ V = V(\gamma)$$

When the section's behaviour is defined in this way, no interactions between these nonlinear behaviours are assumed. Therefore, this assumption is only valid if the section response behaviour can be uncoupled. Since the axial behaviour of the buried cable is dominant the section behaviour of the buried cable can be approximated by this method of modeling, uncoupling the axial and bending behaviours.

5.3.1.1.3 Cable axial behaviour characterization

The result of the standard compression test on the buried cable is used to define its axial behaviour model (N-$\boldsymbol{\varepsilon}$). The load-displacement curve as described in the experimental section can be modeled by the bi-linear curve, with the yield resistance of 160 N and stiffness hardening of 2%. In the case that experimental study is not available the simple strength of material concept can be used to find the axial behavior of the cable. Given that the copper core with elastic modulus of (E_{co}) and yield strength of (Fy_{co}), and aluminum shield with elastic modulus of (E_{al}) and yield strength of (Fy_{al}), are the only parts participating in the compression resistance of the buried cable. The behavior of the buried cable can be approximated by the tri-linear behavior curve with the yield strength and the yield strain as:

$$F_u = F_{al}A_{al} + F_{co}A_{co} \quad \varepsilon_u = \frac{E_{al}A_{al} + E_{co}A_{co}}{A_{al} + A_{co}}$$ Eqn. 5-30

$$F_y = F_{al}A_{al} + F_{al}A_{co}E_{co}/E_{al} \quad \varepsilon_y = \frac{Fal}{E_{al}}$$ Eqn. 5-31

5.3.1.1.4 Cable flexural behaviour characterization

The flexural behavior of the cable is not important issue for modeling this type of the cable since the axial behavior of the cable plays more important role in the overall response of the cable. However, the flexural behavior characterization is required for the numerical simulation. The load-displacement curve of three-point-bending testing, as described in the experimental part, was used to approximate the flexural behavior of the buried cable. A simply supported beam with the span of 78 cm was created in the ABAQUS, and nonlinear static analysis was performed by applying a monotonically increasing displacement at the cable midpoint. The flexural behavior (M-φ) of the cable is back-calculated by seeking the best match between the midpoint displacement obtained from numerical simulation and the one obtained from experimental studies (3.1.2.3). The results of this match, as shown in Figure 5-32, led to the quad-linear relationship curve for the moment-curvature (M_{11}-k_{11}) as depicted in Figure 5-33.

5.3.1.2 Method of Analysis and Calibration of Results

The results of the lateral pullout tests were summarized as a load-displacement curve for the cable with different burial depths. Numerical models with the same characteristics of the experimental testing were created separately for the cable with different burial depths to achieve the same load-displacement curve. The cable modeled as a beam element (B31H type) with the length of 2.15 (m), and the nonlinear type PSI element was used to define the interaction model. The behavior in the longitudinal direction was obtained as discussed in the previous section, and the behavior in the horizontal transverse direction was defined as an

elasto-plastic behavior. The unknown parameters, i.e., yield strength and corresponding yield displacement, of the horizontal transverse behavior of the soil spring were obtained with calibration of the numerical simulation with the experimental studies so that the best possible match between load-displacement curves from experimental studies and those from numerical simulations can be achieved. Since each load-displacement curve approaches an asymptote value, referring to the experimental lateral pullout tests, the yield strength can be readily obtained, and the yield displacement remains the only unknown.

The loading on the buried cable is caused by a displacement applying to the cable's ends. The geometric nonlinearity was included in the analysis to consider the effect of the finite displacement. The geometric model of the buried cable with the loading mechanism and the boundary condition is depicted in Figure 5-34**.**

The load-displacement curves of this analysis are depicted in Figure 5-35 for different burial depths. Each figure shows the results of experimental lateral pullout tests and the results of numerical calibration for different yield displacements to find the best match. Table 5-2 summarizes the calibration results for the soil spring model in the horizontal transverse direction.

5.3.2 Analyzing the Buried Cable Subjected to the Horizontal Transverse Permanent Ground Deformation

5.3.2.1 Introduction

The response of buried pipeline subjected to the transverse PGD was studied previously by O'Rourke (1988), Suzuki et al (1988), Kobayashi et al (1989), and Liu and O'Rourke (1996). Brief discussions of their assumptions and results are presented herein. O'Rourke (1988) studied the response of X-60 grade steel pipe (with diameter of 24 inch and wall thickness of 3/8 inch) to the PGD. The PGD pattern was assumed to have a beta probability distribution function with the width (W) and the amount of ground deformation (δ). The maximum tensile and compression strains were calculated for three widths (W=10, 30, and 50 m) as a function

of the maximum soil displacement. He concluded that the width of PGD has a greater influence on the tensile strains. Suzuki et al (1988) studied the response of X-50 grade steel pipe (with diameter of 24 inch and the wall thickness of ½ inch) to the transverse PGD. Several PGD patterns were assumed as a cosine function to the power of $n \geq 1$. Their physical model is very similar to that of T. O'Rourke (1988); however, Suzuki model assumed a longer pipe so that the axial force formed in the pipe due to PGD can be transferred to the ground. They analyzed the pipe for different ground deformation widths (W=10, 30, and 50 m) and different ground displacements ($\delta <$ 2m). They observed that the ground deformation with width of around 30 m created the maximum tensile strain in the pipe.

Liu and M. O'Rourke (1996) studied the response of X-52 grade steel pipe (with diameter of 24 inch and the wall thickness of 3/8 inch). They used the nonlinear soil springs and Ramberg-Osgood stress-strain relationship for the pipe material. The pattern of ground deformation was assumed to be cosine function to the power of 2. They analyzed the response of the pipe to three different widths of ground deformation (W=10, 20, and 50 m) and ground movements with different intensity. Based on their analysis, they concluded that the width of PGD, followed by the transverse soil spring resistance, pipe diameter, steel grade, wall thickness, PGD pattern, anchor length, and the longitudinal soil spring resistance are the most influential parameters affecting the response of the buried cable. Furthermore, the closed-form analytical formulations were developed to estimate the maximum tensile strain in the buried pipeline.

5.3.2.2 Description of Numerical Model

The primary objective of this section is to gain an understanding on the parameters that influence the response of the buried cable, and elucidate some features of the response which are limited to the buried cable. The cable performance is expected to be influenced by, 1) cable mechanical properties, 2) the soil/cable interaction behavior, and 3) the transverse PGD deformation parameters. This study focuses mainly on the effects of the ground deformation parameters; namely the amount of the PGD and width of PGD zones (W and D). In order to

accomplish this goal, two cables with the burial depth ratios of 6 and 10 were selected for the analysis. The cable structure has the same mechanical properties as the one used in the experimental lateral pullout tests, which were also used to calibrate the behavior of the transverse soil springs. The analyses were performed by the finite element program ABAQUS 6.7-1. The PSI element was used to model the interaction behavior between the cable and the soil. The behavior of PSI element in the longitudinal and transverse directions was obtained as the bilinear behavior as calibrated with experimental tests. The nonlinear general beam section was used to define the moment-curvature (M-φ) and the axial-deformation (N-ε) relationship of the buried cable. The cable was modeled as a continuous long beam with the mentioned mechanical properties. The length of the cable was long enough to reduce the effect of boundary conditions. In each analysis, strains at the ends of the cable were checked to confirm that the strains were small enough. This makes sure that the location of anchor points was not influencing the analysis results. The ground deformation was applied to the other end of the PSI element to simulate transverse PGD. The pattern of ground deformation as proposed by Suzuki (1988) with n=2 was selected. By keeping the pattern of the ground deformation constant and by increasing the amount of the ground deformation monotonically, the responses of the buried cable were conducted for different ground displacements. The analysis considers both the material and geometric nonlinearities in the buried cable.

5.3.2.3 Results of Numerical Analysis

5.3.2.3.1 Cable deformation

The first observation is related to how the buried cable is deformed when it is subjected to the ground with increasing levels of movement. Figure 5-36 shows that the buried cable matches to the pattern of ground movement up to the certain level, after that the buried cable does not match to the ground movement pattern anymore and eventually the maximum deformation in the cable reaches to a certain plateau deformation (D_{pl}). For instance, Figure 5-37 shows the maximum cable deformation as a function of the ground movement. As can

be seen, the cable approaches to plateau deformation (2 m) after the ground moves about 3.8 m. For small amount of the ground deformation, the cable does not resist to any lateral movement since the cable has a small bending rigidity. Thus, any resistance to the lateral movement is attained by developing the tension force in the cable. In this phase, no relative movement between the cable and ground is observed until the cable starts resisting to the lateral movement. Thereafter, the relative movement of the cable and the ground causes the activation of the lateral soil spring resistance. Since the behavior of the soil springs is an elasto-plastic type, spring force can be yielded when the relative movement of the cable and ground deformation exceeds the yield displacement of the soil spring. There is a point that the most of the lateral soil springs in the region of the width of ground deformation (W) are yielded, and this is the time that the cable reaches to its plateau deformation. As cable deforms, the axial stains are developed due to cable stretching and curvature until the cable reaches to its plateau deformation. This observation was also captured by Liu and O'Rourke (1996) for the buried pipeline.

5.3.2.3.2 Cable axial strain

The response of the buried cable is defined as the developed axial force, axial strain, bending moment and corresponding curvature due to the PGD. Figure 5-38 shows the cable deformation with the burial depth of 60 and 100 cm when subjected to PGD with the width of 10 and 20 m. Figure 5-39 shows the relative deformation of the cable and the ground movement. In those figures, the cables subjected to the PGD with the width of 20 m are analyzed to the maximum ground deformation of 8 m whereas the cables subjected to the PGD with the width of 10 m are analyzed to the maximum ground deformation of 3 m since cables subjected to the wider PGD requires more ground deformation to show any resistance to the ground movement. The positive and negative relative movements occur to balance out the normal forces acting on the buried cable. The positive portion of the graph indicates that the soil pushes the cable whereas the negative portion of the graph indicates that the cable pushes the soil. In order to locate the distance at which the positive and negative relative soil

movement occurs, the distance from centerline is normalized with respect to the width of ground deformation ($2x/W$). Inspecting those graphs show that the changing occurs at distance ratios of *0.5-0.6*. Understanding this location helps to analytically formulate the problem which will be discussed later.

Figure 5-40 shows the axial force and bending moment profiles in the cable with the burial depth of H=60 cm subjected to PGD with the width of 10 m and 20 m, and maximum ground deformation of 3 m. As can be seen, the maximum axial force occurs close to the center of the PGD zones and its value decreases as it approaches to margins. After a certain ground deformation (D_y), the axial force profile in the cable remains constant although ground deformation increases. Since axial behavior of the cable is assumed to have a bilinear behavior with a small stiffness hardening the axial force profile in the cable starts roughly from yield force (T_y).

Figure 5-41 shows the axial strain in the cable with burial depth of H=60 and H=100 subjected to PGD with the width of 10 m and 20 m. As can be seen, the maximum axial strain does not occur at the center of PGD zones. It roughly happens at $2x/w$=0.5-0.6 depending on the width of PGD and burial depth and decreases toward margins. Inspecting the curvature profile, it can be seen that the curvature at point around $2x/W$=0.5-0.6 is zero indicating that this point is an inflection point. This point (2x/w=0.5-0.6) has interesting features: it is an inflection point, the maximum strain occurs at this point, and it is a point that a change in the positive and negative relative displacement happens there.

Tracking the cable deformation profile during PGD with increasing amount of ground deformation shows that the cable deformation matches the ground movement up to certain deformation. Comparison between the cable lengthening due to this deformation and the cable original length can be used to determine the amount of axial deformation. The axial deformation can be simply expressed as

$$\Delta S = \int_0^{L_0} \sqrt{1+(\frac{dy}{dx})^2}\, dx - L_0 \qquad \text{Eqn. 5-32}$$

By using the first and second terms of Maclaurin series for the square root and substituting the assumed shape of the ground deformation, the axial deformation can be obtained as

$$\Delta S = \frac{1}{2}\left(\frac{dy}{dx}\right)^2 = \frac{\pi^2 D^2}{8W} \qquad \text{Eqn. 5-33}$$

Inspecting this equation shows that the cable lengthening is inversely proportional to the width of ground deformation (W). This indicates that wider PGD creates less axial stain than narrower PGD. However, this expression is valid provided that the cable does not reach to its plateau deformation and the cable does not yield. As mentioned earlier, the cable reached to its plateau ground deformation does not match the ground deformation; thus, the axial deformation is not proportional to the power two of ground deformation (D^2). On the other hand, since the axial force profile of the cable remains more or less constant after the cable yields the axial strains due to axial lengthening is concentrated in the small regions of the plastic link. As can be seen, the plastic links are more or less limited to the half the width of PGD; thus, the narrower PGD causes more axial strain ($\Delta S/2W$). For instance, as shown in Figure 5-41, the axial strain of the cable with burial depth of 100 cm subjected to the PGD with the width of 10 m creates greater axial strain than PGD with the width of 20 m. However, the axial strain for the cable with burial depth of H=60 cm shows a larger axial strain for wider PGD. Since the shallow cable subjected to narrower PGD reaches to its plateau deformation at smaller ground deformation; thus, the above equation does not hold. For instance, the axial strain of the cable with burial depth of 100 cm is greater than the axial strain of the cable with burial depth of 60 for the same width of PGD. In order to quantitatively compare the axial strain in the buried cable, the following condition should be considered: 1) if the axial behavior in the cable reaches to its yield behavior and 2) if the cable transverse deformation reaches to its plateau deformation. It is obvious that those considerations depend on the ground deformation parameters (W and D), the axial characteristics of the cable (yield strength and strain), and cable-soil interaction model in the longitudinal and transverse directions.

5.3.2.4 Description of Analytical Approach

As observed in the numerical analysis of the buried cable, two critical ground deformation and cable deformations can be defined that influence the buried cable response. The ground deformation level outsets the axial yielding in the buried cable (D_y), and the maximum transverse deformation of the cable (D_{pl}). In order to establish the analytical approach to determine those deformations, previous analytical procedures by M. O'Rourke (1989, 1997) were reviewed. Their analytical approach was specifically presented for the steel pipeline with elastic behavior. The analytical approaches presented herein are for the cable with nonlinear behavior, and are based on the results of numerical simulation as conducted in the previous section

5.3.2.4.1 Yield ground deformation (D_y)

As the buried cable subjected to the transverse ground deformation, the axial force is developed. The forces acted on the infinitesimal piece of the cable are shown in Figure 5-42. In this figure, T is the axial force, θ is the slope of tangent line to the cable deformation, F_L is the longitudinal soil restraint and F_T is the transverse soil restraint. The equilibrium in the longitudinal direction can be written as

$$(T+dT)\cos(d\theta)-T-F_L ds=0 \text{ or } \quad dT-F_L ds=0 \qquad \text{Eqn. 5-34}$$

The results of numerical analysis show that the yielding outsets in the center of PGD. Furthermore, the yielding occurs when the ground deformation is still small. Thus, the cable transverse deformation can be assumed to match the ground deformation, and the maximum axial deformation of the cable can be written as

$$u_{\max}=\frac{\pi^2 D^2}{8W} \qquad \text{Eqn. 5-35}$$

Since the longitudinal behavior of soil spring is a bilinear behavior as the distance increases from the center of ground deformation zone the linear behavior can be expected while near to the center of ground deformation zone plastic behavior can be assumed. Let's assume beyond distance x_t from the center of the ground movement zone the longitudinal soil spring is linear. Therefore, the axial force and corresponding axial displacement can be written as

$$T(x)=\begin{cases} T_{\max}-f_L x & \mathrm{x} < \mathrm{x_T} \\ T_1 e^{-k_g(x-x_T)} & \text{otherwise} \end{cases} \qquad \text{Eqn. 5-36}$$

and

$$u(x)=\begin{cases} u_{\max}-\varepsilon_y x+0.5k_g^2\delta_{yl}x^2 & \mathrm{x} < \mathrm{x_T} \\ \delta_{yl}e^{-k_g(x-x_T)} & \text{Otherwise} \end{cases} \qquad \text{Eqn. 5-37}$$

in which

$$x_T=(\frac{T_{\max}}{F_L}-\frac{1}{k_g}),\quad T_1=\frac{F_L}{k_g},\quad k_g=\sqrt{\frac{F_L}{\delta_{yL}AE}},\quad u_{\max}=\varepsilon_y x_T+(1-0.5k_g^2x_T^2)\delta_{yL}$$

ε_y is the axial yield strain of the cable with axial rigidity (EA). δ_{yL} is the yield displacement of the longitudinal soil restraint with the maximum value F_L. Figure 5-43 shows a good agreement of the developed analytical formula for the axial deformation with those obtained from numerical simulations for the cable with the burial depth of 60 cm subjected to PGD with the width of 10 m. With the knowledge obtained from numerical simulation that the axial yielding occurs at small ground deformation, the amount of the ground deformation creating the axial yielding in the buried cable can be obtained by

$$\frac{\pi^2 D_y^2}{8W}=u_{\max}\rightarrow D_y=\sqrt{\frac{8W}{\pi^2}u_{\max}} \qquad \text{Eqn. 5-38}$$

Figure 5-44 shows the axial force in the cable at a center of PGD region as a function of the amount of ground deformation as obtained from numerical simulation. The aim of this figure is to obtain the amount of ground deformation causing yielding in the cable (D_y), and

compare it to the one proposed by analytical formulation. As shown in Figure 5-44**,** analytical procedure predicts D_y considerably well.

5.3.2.4.2 Plateau cable deformation (D_{pl})

An increase in the amount of ground deformation ($D>D_y$) leads to the accumulation of axial strain in the cable in the plastic region . After certain ground deformation, as demonstrated by numerical simulation, the cable does not conform to the ground deformation and it eventually yields to its maximum deformation (D_{pl}). In this section, we try to provide a simple analytical tool to calculate D_{pl}. Plateau ground deformation (D_{pl}) has an important feature in the buried cable response evaluation since the maximum axial strain which can be occurred in the buried cable can be calculated.

The cable transverse deformation reaches to its plateau deformation when the soil-cable interaction elements are yielded. This problem resembles a cable structure with uniform loading as shown in Figure 5-45. The differential equation governing the static of a cable subjected to a uniform loading can be written as

$$\frac{d^2y}{dx^2} = \frac{F_T}{T_0} \qquad \text{Eqn. 5-39}$$

in which $T_0 = T\ cos(\theta)$ is the constant horizontal force component. The solution of to the differential equation provides a quadratic shape. The cable sag (h) can be calculated as

$$h = \frac{F_t W^2}{8T_0} \qquad \text{Eqn. 5-40}$$

The numerical analysis of the buried cable shows that the buried cable deformation zone is not limited to the PGD zone, and it extends beyond the PGD width (W). The relative cable-ground deformation shows that the ground deformation lags behind the cable deformation after distance (x=0.5-0.6(W/2)) from the center of the ground deformation zone, these two

regions are shown as “thrust” and “heave” zones in Figure 5-46. The “thrust and heave” zones are required to happen irrespective of the assumed shape of the ground deformation to balance out the exerted normal forces on the buried cables.

Cable deformation plateau (D_{pl}) can be calculated by using the cable theory. Three steps should be performed: 1) the region of “thrust” and “heave” should be identified. It was observed that those regions are isolated depending on the width of PGD and burial depth, at distance $2x/W$=0.5 -0.6. 2) from the previous formulation, the axial force profile in the cable should be calculated. Since the axial force in the cable is not constant due to the longitudinal soil resistance, the average horizontal force in the regions of “thrust” and “heave” should be calculated. 3) Finally, the amount of sag can be calculated as

$$h = \frac{F_T (2x_1)^2}{8\overline{T}} \qquad \text{Eqn. 5-41}$$

in which $2x_1$ and $\overline{T}$ are the width and the average axial force in “thrust” or “heave” region respectively. For instance, Figure 5-47 illustrates the schematic representation to calculate the (h_1, h_2) value and correspondingly maximum cable ground deformation ($D_{pl}=h_1+h_2$).

Figure 5-48 shows the transverse deformation of the cable profile with burial depth of 60 and 100 cm subjected to PGD with the width of 10 as calculated from numerical simulations. In these numerical analyses, the amount of ground deformation increases until the cable deformation reaches to its plateau. The results of analytical formulation are shown in this figure with the table showing parameters used to calculate plateau deformation (D_{pl}). As can be seen, the analytical formulation results are in a good agreement with the numerical simulation result.

Thrust Zone

Analytical formulations of two levels of deformations (D_y , D_{pl}) can be used in the quick assessment of buried power transmission cable response subjected to transverse PGD. For the amount of the ground deformation ($D<D_y$), the buried cable will operate in the elastic

range. When the amount of the ground deformation approaches ($D=D_y$), the first yield in the buried cable will form. For the amount of the ground deformation ($Dy<D$), the plastic link is developed with maximum strain concentration in the plastic link. The maximum strain in the cable due to transverse PGD scenario occurs when the cable reaches to its plateau deformation. It can be said that for the amount of ground deformation greater than D_{pl} the rate of increase in the axial strain will be decreased until the cable reaches to its plateau deformation.

5.3.3 Summary of the Response of Buried Cable to the Transverse PGD

From the results of experimental study, the soil-cable interaction spring model in the horizontal transverse direction is developed for the cable with burial depth of 30, 60, 90, and 120. The methodology is introduced to determine the soil-cable interaction behaviour for the cable and backfill with different characteristics.

The response of the buried cable to transverse PGD scenario is evaluated. The result of numerical simulation shows that, in the order of importance, the amount of ground deformation, width, and burial depths are the most significant parameters affecting the response of the buried cable.

Investigation shows that the buried cable subjected to transverse PGD are subjected to both bending strains and axial strains. However, the axial strain due to stretching are more pronounced.

Based on the observation from numerical simulation, two levels of deformations are introduced for the buried cable; namely: D_y the amount of ground deformation causing yielding in the cable and D_{pl} the maximum possible deformation of the cable. Figure 5-49 provides the flowchart to approximately obtain the response of buried cable subjected to transverse PGD. The calculated response can be used to determine whether further detailed analysis is required.

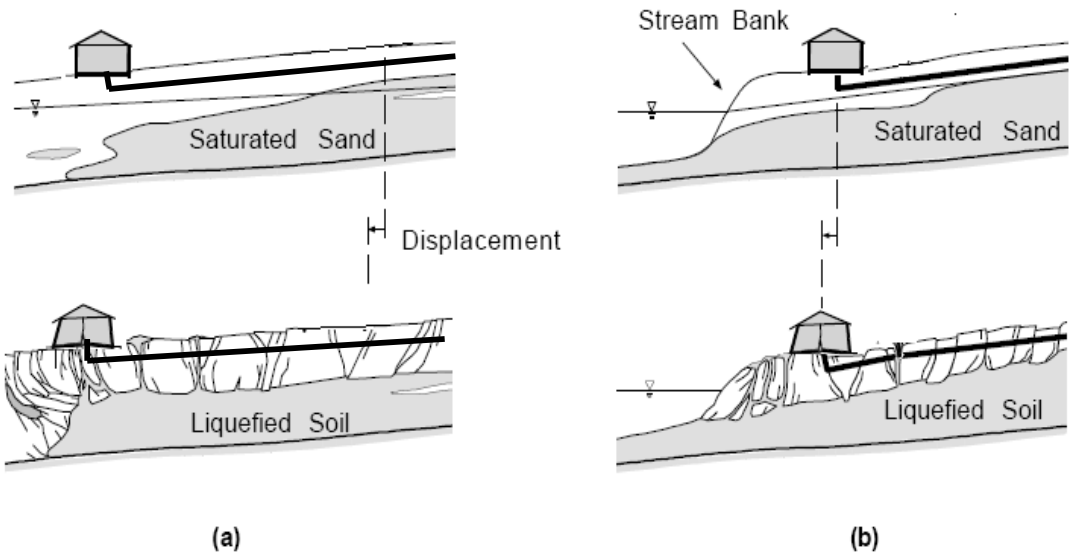

Figure 5-1:Longitudinal soil restraint on the buried cable due to liquefaction induced ground movement with a) gently sloping ground and b) a free face, adapted from Raunch(1997).

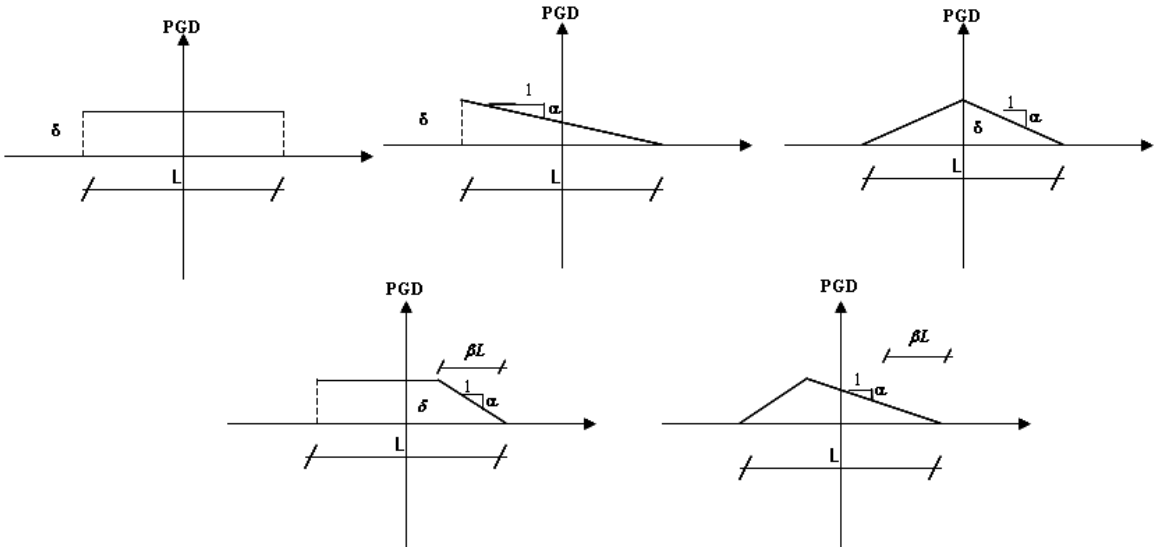

Figure 5-2: Idealized pattern of longitudinal PGD, after O'Rourke (1995)

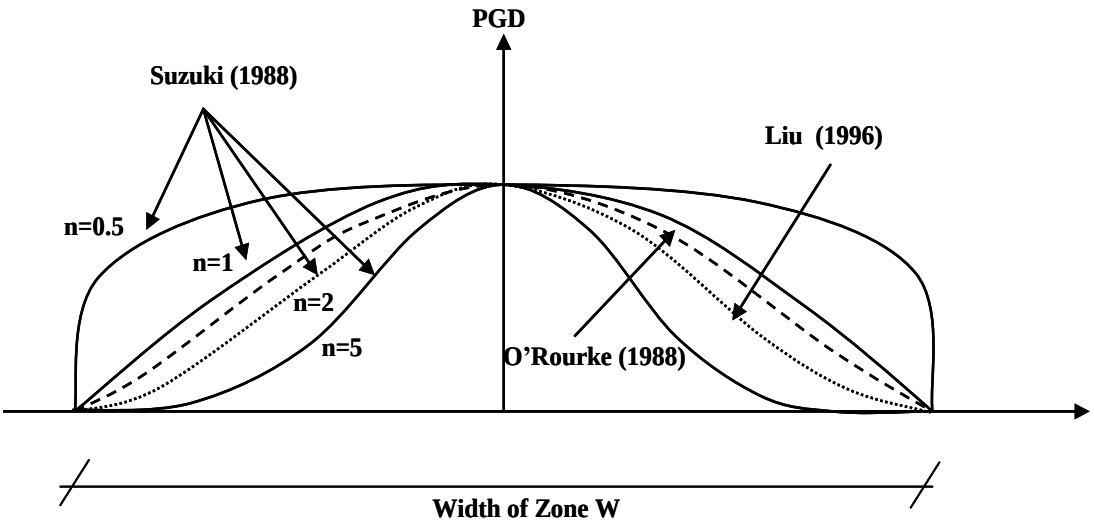

Figure 5-3: Idealized pattern of transverse PGD, after Liu and O'Rourke (1996).

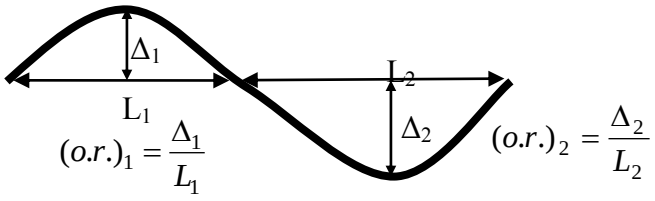

Figure 5-4: Definition of the offset ratio

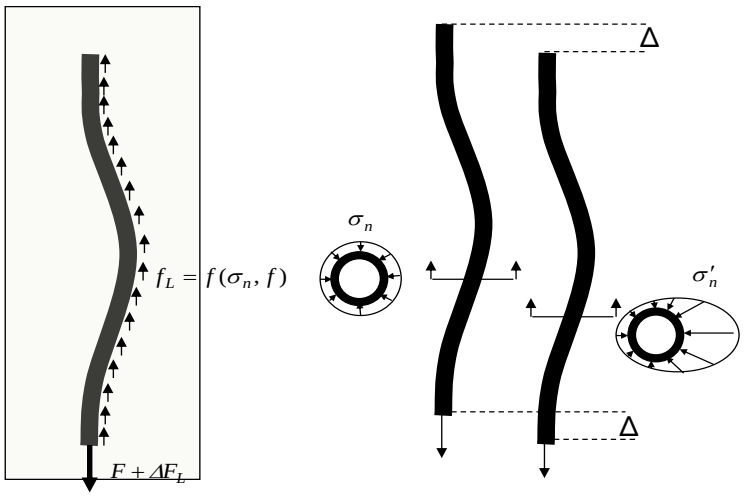

Figure 5-5: Schematic representation of the axial pullout force increase in the cable with out-of-straightness.

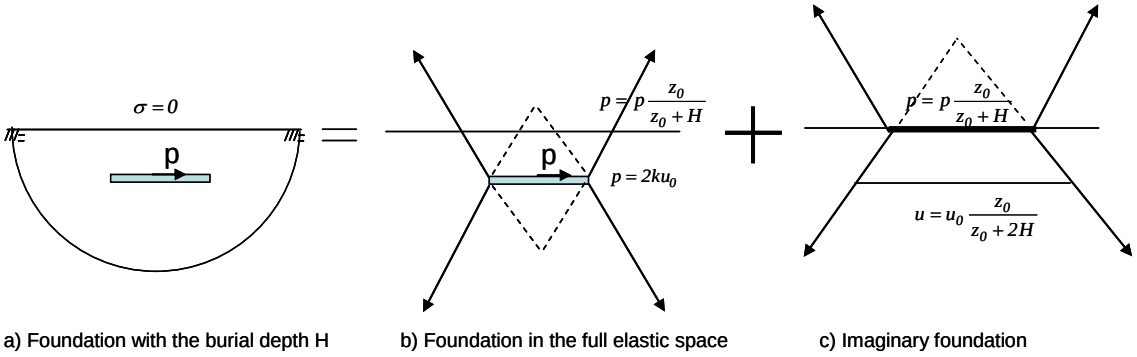

Figure 5-6: Cone model method to calculate the static stiffness of the foundation with burial depth *H*

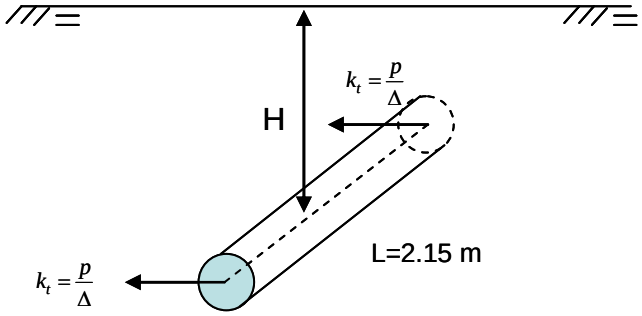

Figure 5-7: Horizontal Cable subjected to the two concentrated load at ends

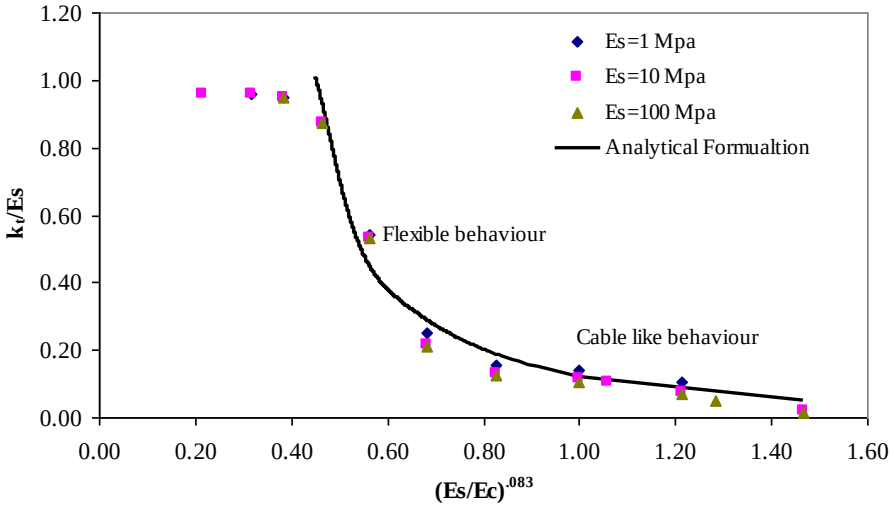

Figure 5-8: K_t stiffness comparison between the analytical prediction and numerical simulation for the cable with length of 2.15 m and burial depth of 0.9 m.

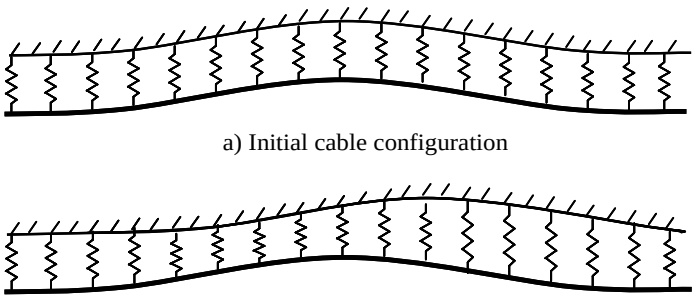

a) Initial cable configuration

b) Cable configuration after δ_L longitudinal movement

Figure 5-9: Buried cable subjected to the longitudinal movement, showing the activation of the horizontal transverse soil springs

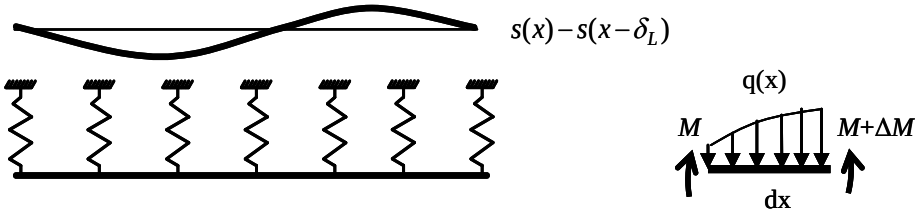

Figure 5-10: Simplified model for the cable with out-of-straightness subjected to the longitudinal movement

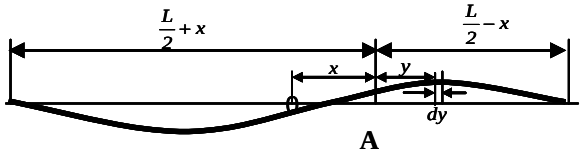

Figure 5-11: Beam on the elastic foundation subjected to an arbitrary loading q(x).

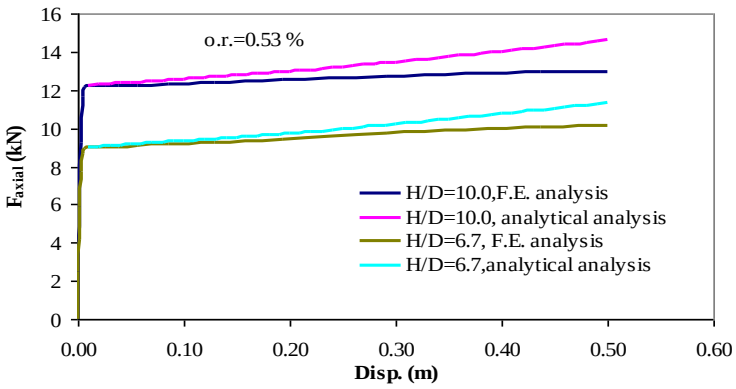

a) axial pullout force in the cable for the offset ratio 0.53%

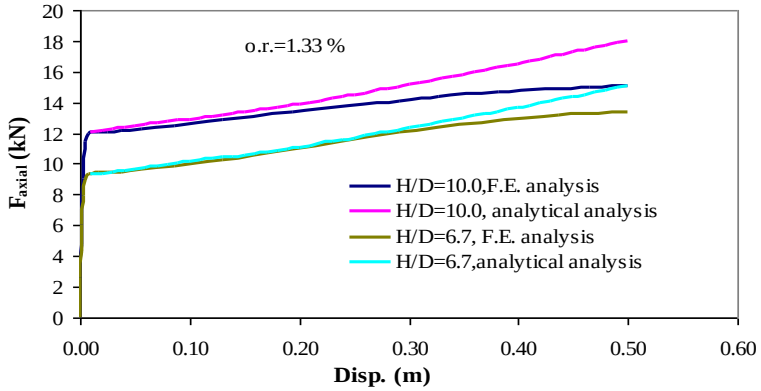

b) axial pullout force in the cable for the offset ratio 1.53%

Figure 5-12: Comparison between results of finite element analysis and developed analytical formulation in prediction the axial force in the cable, *Es*=10 Mpa, λ=4.7 /m.

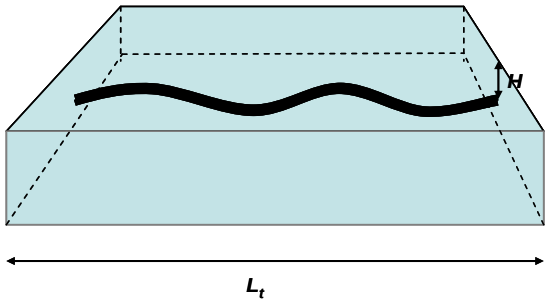

Figure 5-13: The cable with burial depth ratio (H/D) subjected to the soil mass movement with the length L_t

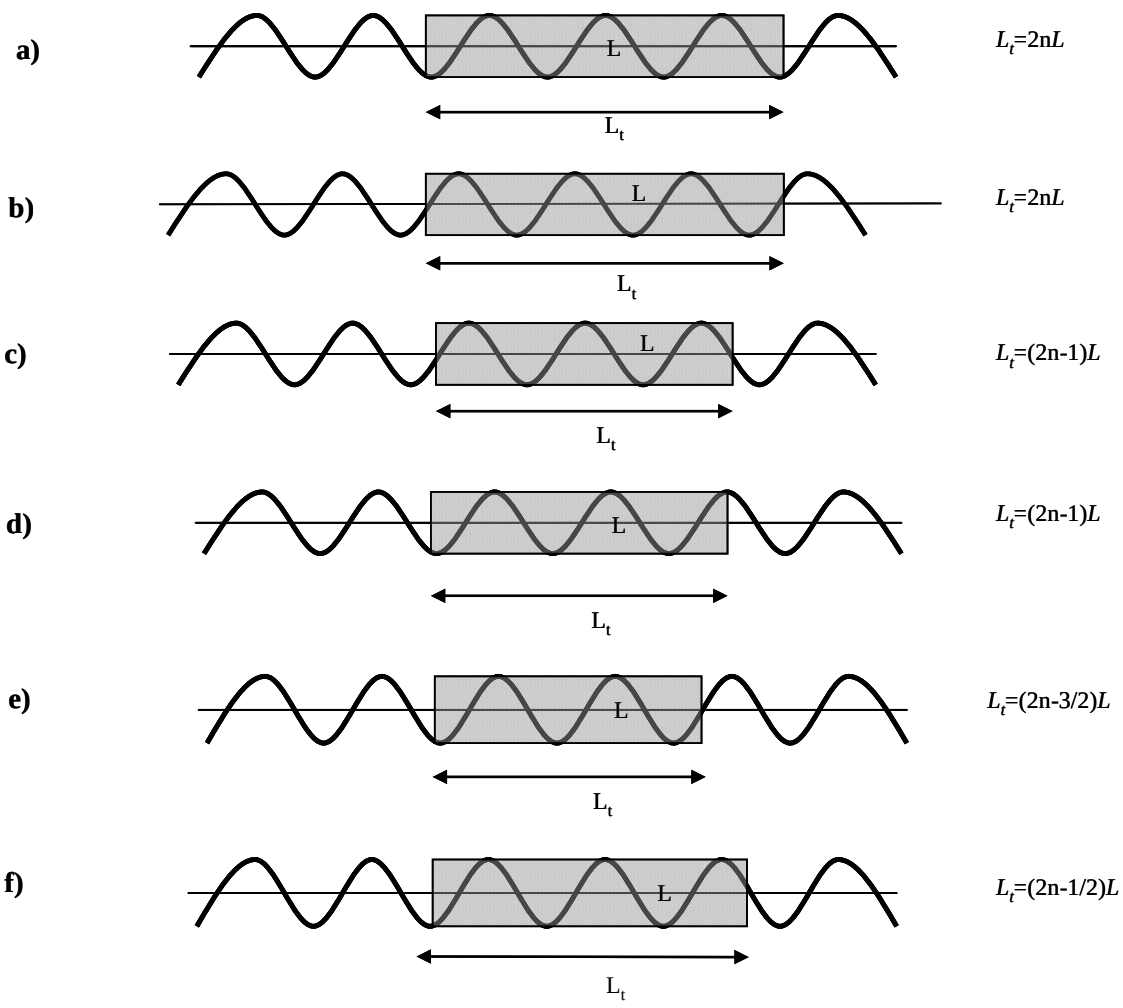

Figure 5-14: Different laying patterns of the buried cable subjected to the movement of the soil mass with length L_t, in this figure L_t is drawn for n=3.

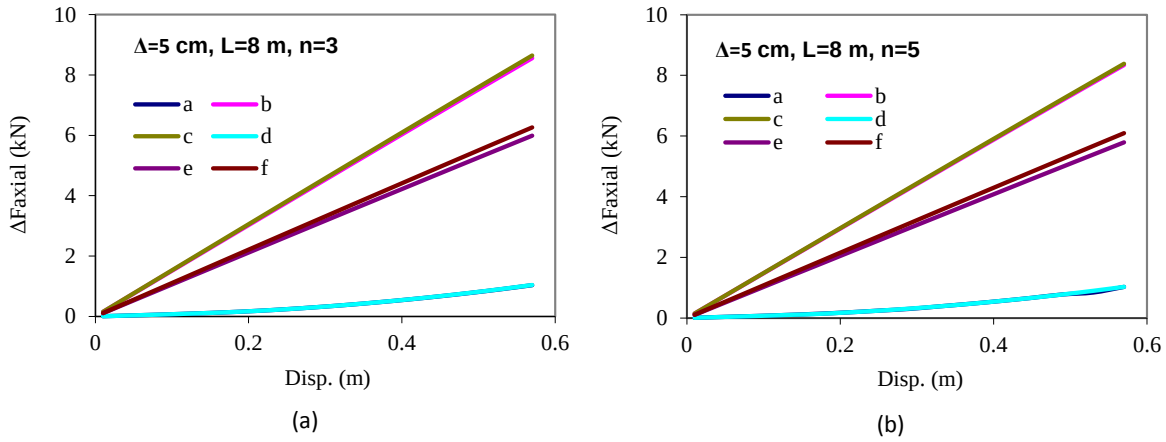

Figure 5-15: Prediction of an increase in the axial force (ΔF_{axial}) in the buried cable with different laying patterns as shown in Figure 5-14, a) results for n=3, L=8 m, b) results for n=5 , L=8 m

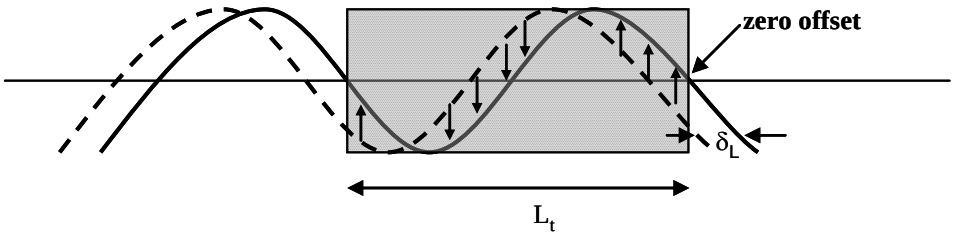

a) The region of the soil mass movement coincides with the zero offset

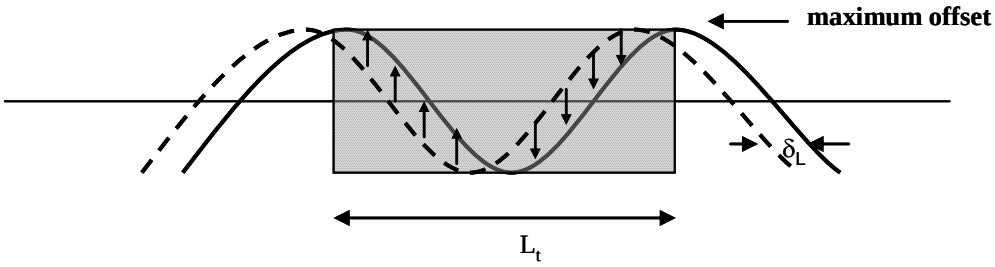

b) The region of the soil mass movement coincides with the maximum offset

Figure 5-16: Schematic of the buried cable when the boundary of the soil movement coincides with zero offset (a) or coincides with maximum offset (b).

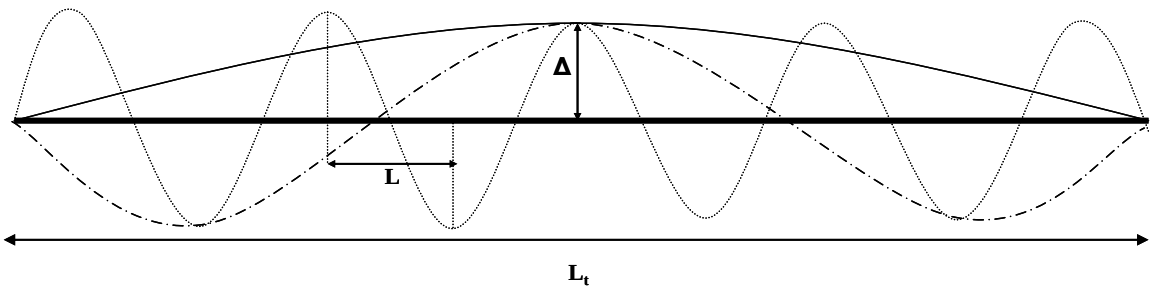

Figure 5-17: Schematic representation of three cables with the maximum offset *Δ and* L_t/L=1, 3, and 9 subjected to the mass of the soil movement with the width L_t.

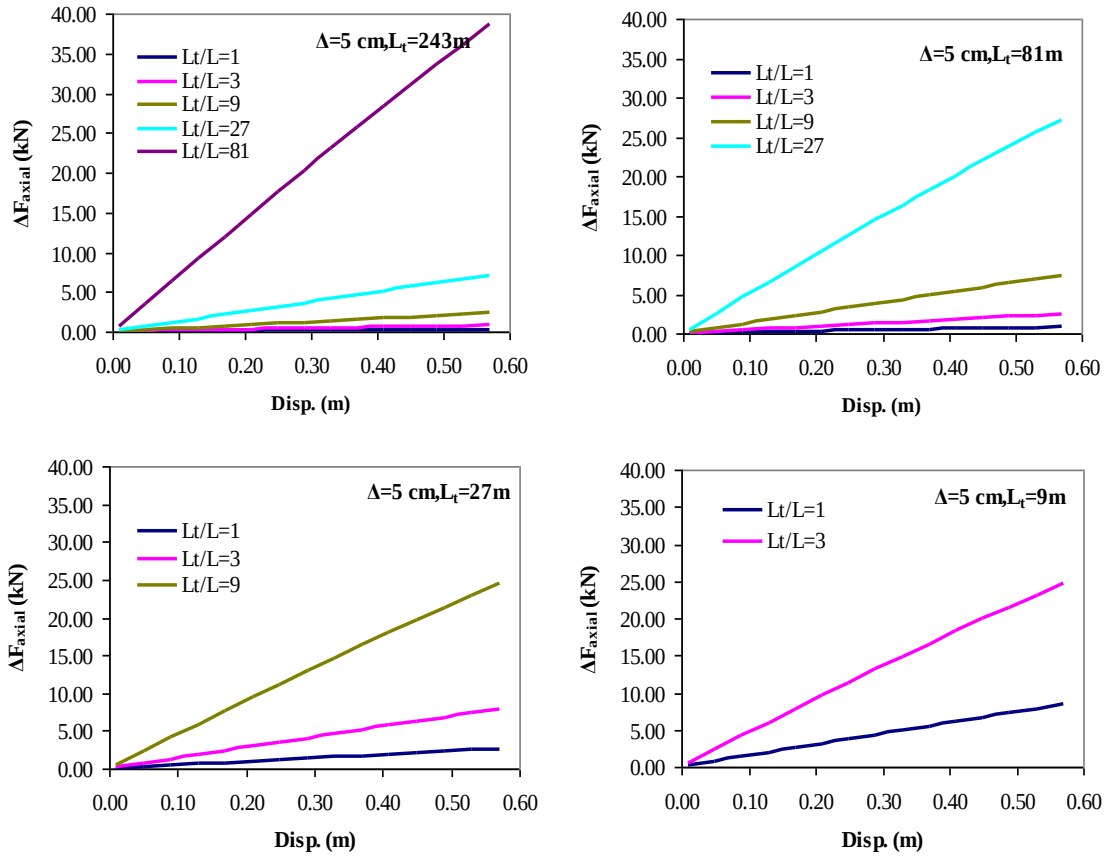

Figure 5-18: The effect of L_t/L ratio on the increase in the axial force in the cable

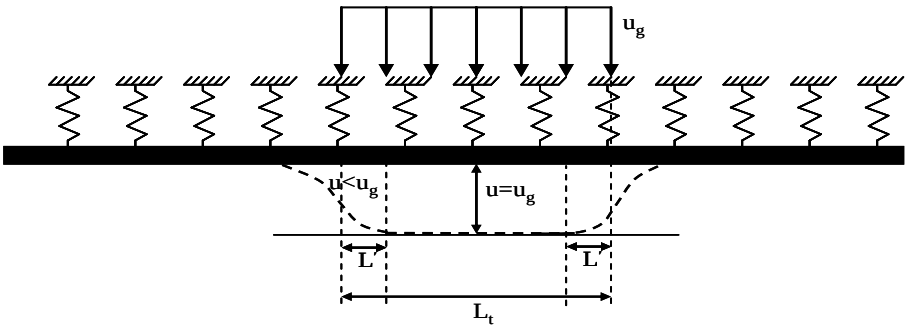

Figure 5-19: A very flexible Beam on elastic foundation subjected to the uniform ground deformation

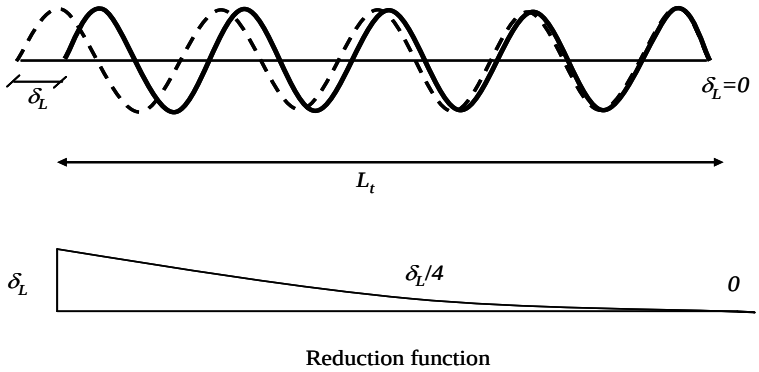

Figure 5-20: Elastic cable subjected to the mass of the ground movement with non-uniform distribution of the ground movement

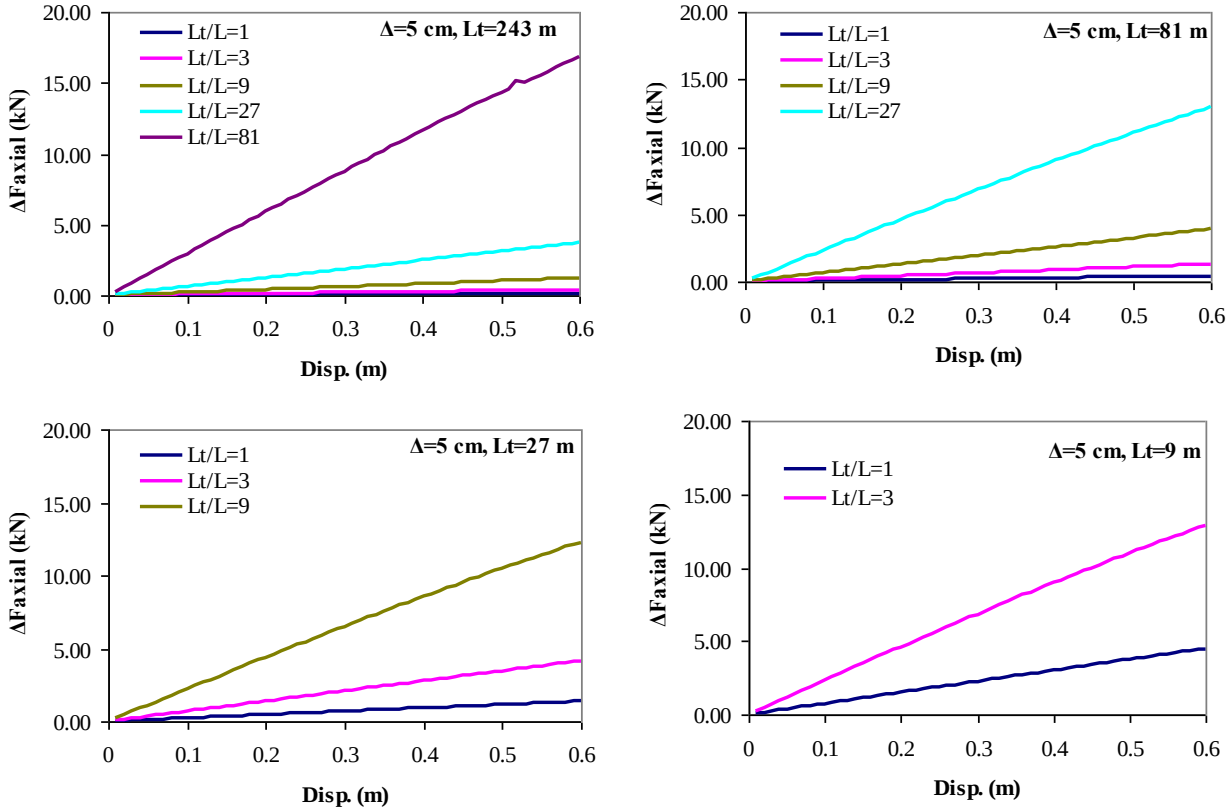

Figure 5-21: The effect of L_t/L ratio on the increase in the axial force in the cable, non-uniform ground displacement

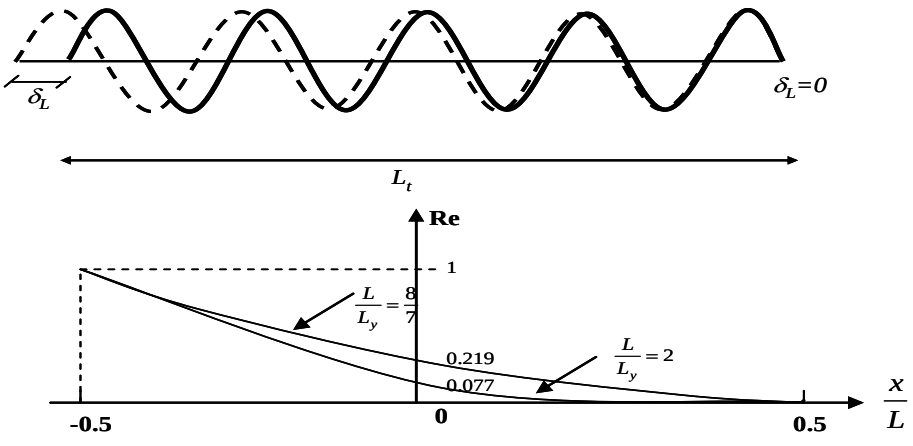

Figure 5-22: Inelastic cable subjected to the mass of the ground movement with non-uniform distribution of the ground movement.

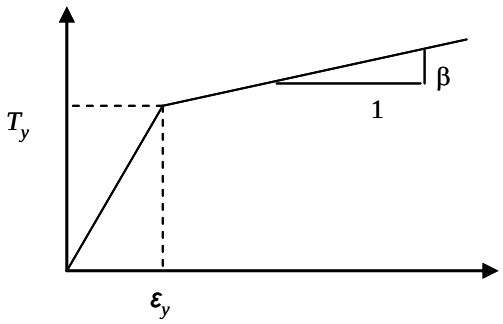

Figure 5-23: Bilinear representation of the axial behavior of the cable

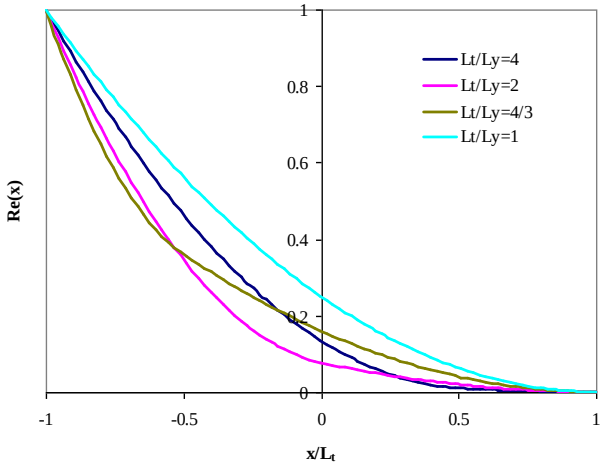

	ΔF_{axial} (0.5 m)
***Lt/Ly*=1**	**11.318**
***Lt/Lt*=4/3**	**11.417**
***Lt/Ly*=2**	**11.356**
***Lt/Ly*=4**	**11.332**

Figure 5-24: Prediction of increase in the axial force in the cable for Lt/Ly=1, 4/3, 2, and 4 for 0.5 m of the ground movement.

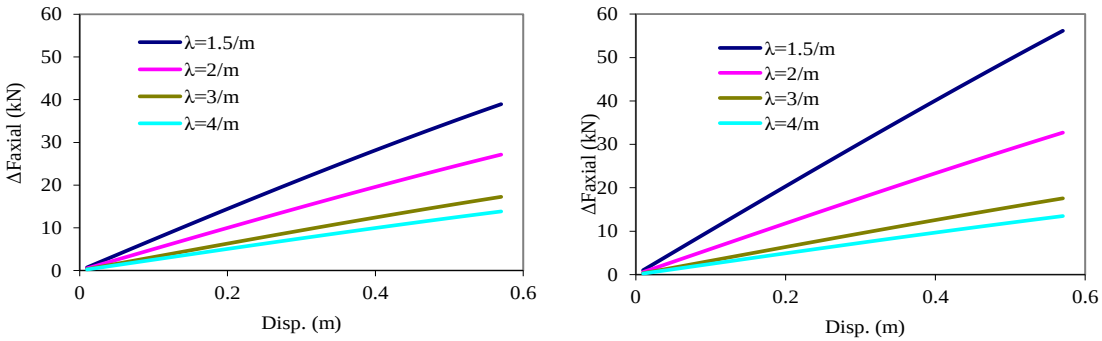

a) L_t=9 m, Es=10 Mpa

b) L_t=27 m, Es=10 Mpa

Figure 5-25: Prediction of an increase in the axial force (ΔF_{axial}) in the buried cable for λ=1.5,2,3, and 4/m a) L_t=9m and b) L_t=27m

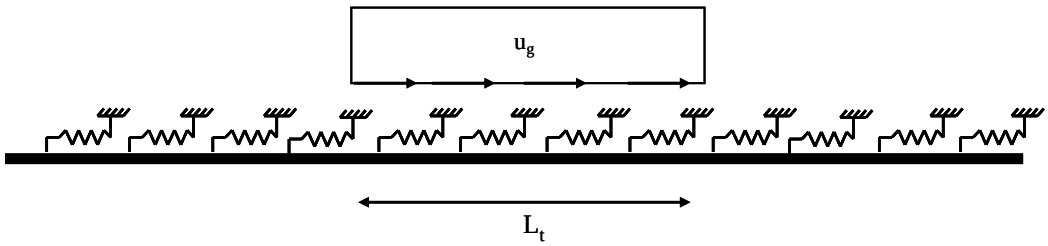

Figure 5-26 : The buried cable subjected to the longitudinal block pattern of the soil movement

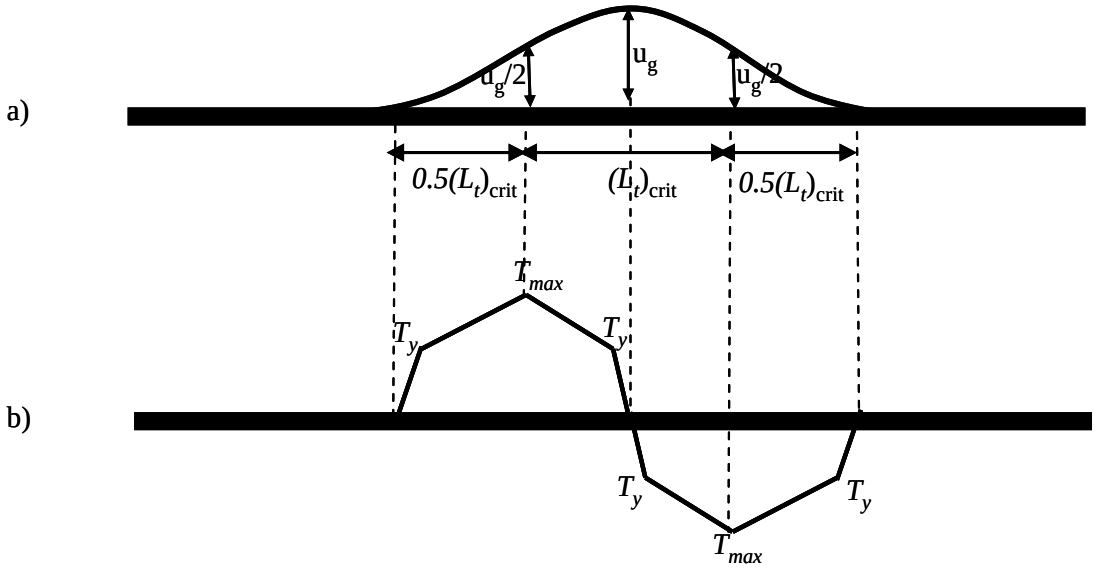

Figure 5-27: Cable deformation and axial force for the critical length of ground deformation: a) cable deformation; b) axial force

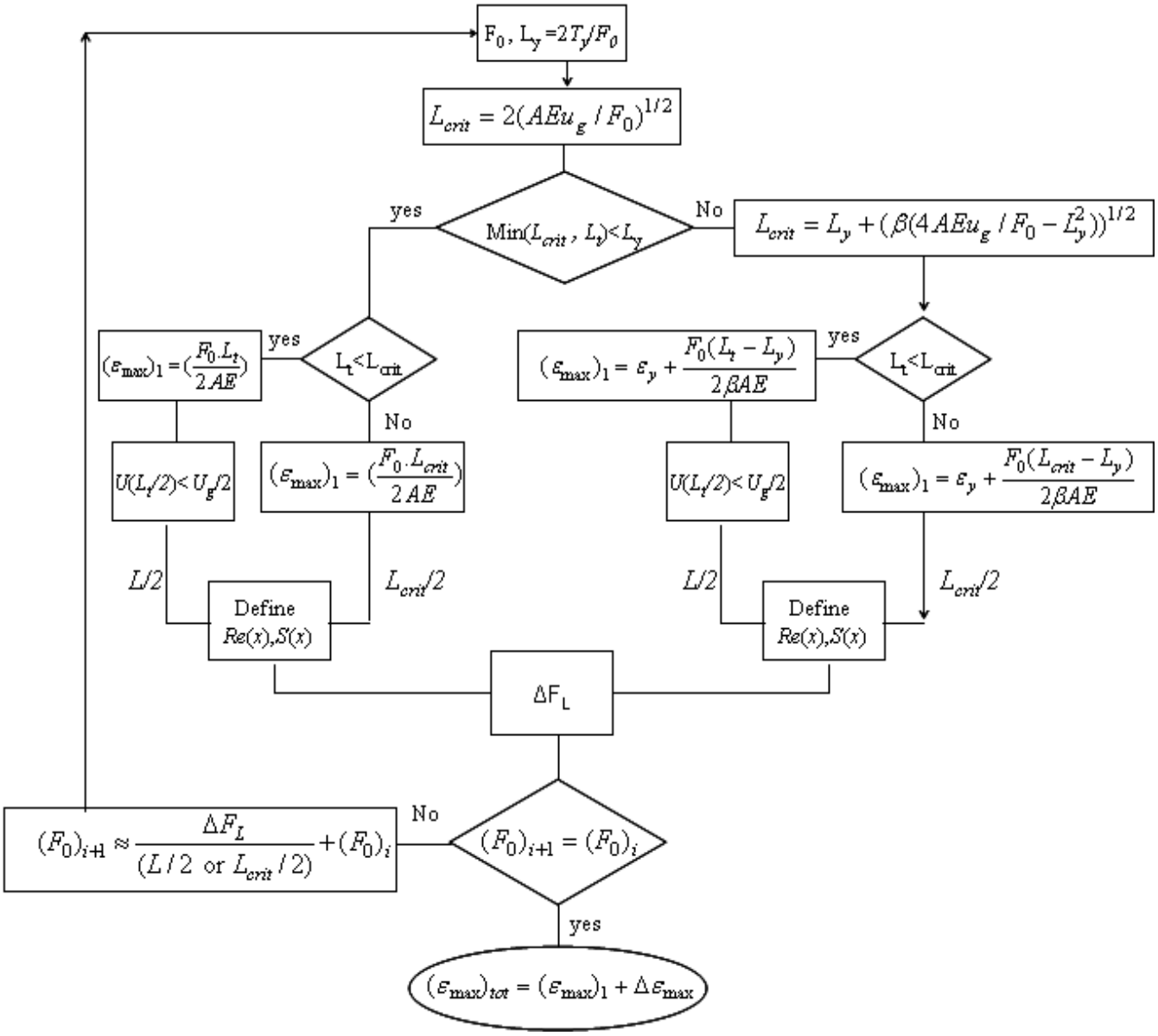

Figure 5-28: Procedure to calculate the total axial strain subjected to the longitudinal permanent ground deformation.

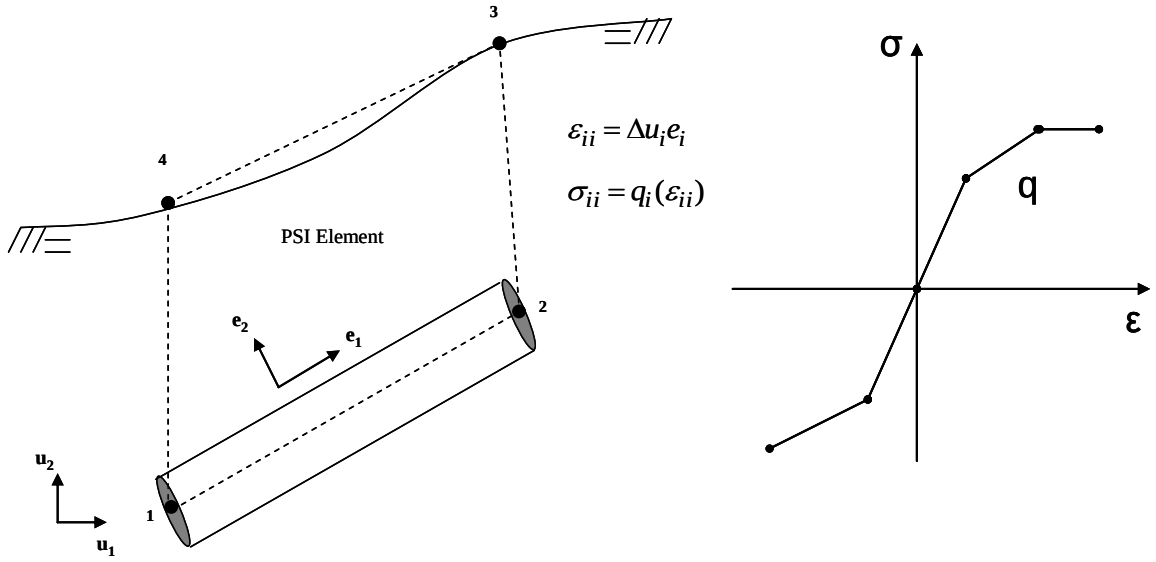

Figure 5-29: Four nodded PSI elements to model the soil-cable interface behavior.

Table 5-1: Summary table of the bilinear representation of the longitudinal behaviour of soil springs for different burial depths.

D (mm)	*H* (m)	H/D	*F*/*L* (kN/m)	δ*y* (mm)
89	30	3.3	1.6	3
89	60	6.7	2.2	3
89	100	11.1	2.8	3
89	120	13.3	3.5	3

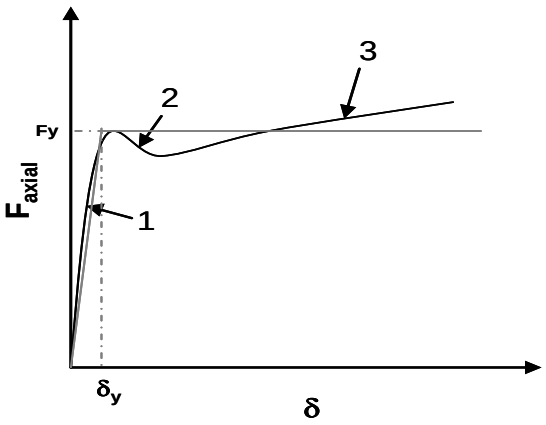

Figure 5-30: Typical load-deformation curve and corresponding elasto-plastic behavior of longitudinal soil springs.

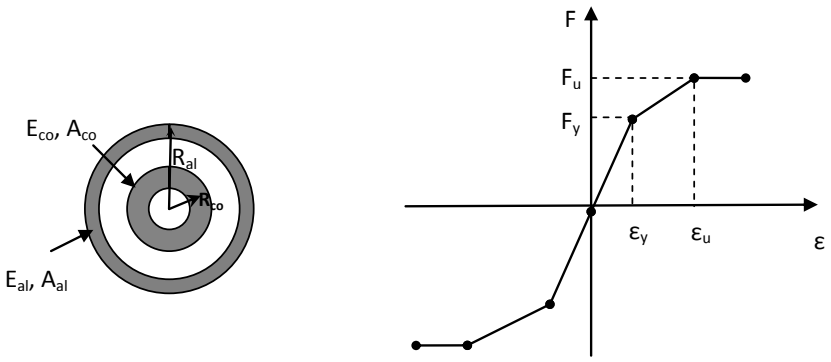

Figure 5-31: Representation of the axial behaviour of the buried power transmission cable.

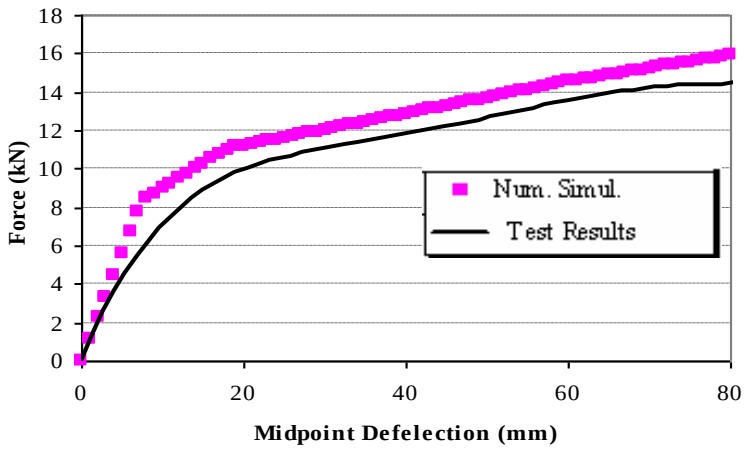

Figure 5-32: Results of experimental three-point-bending test and calibrated numerical simulation with the moment curvature as depicted in Figure 5-33.

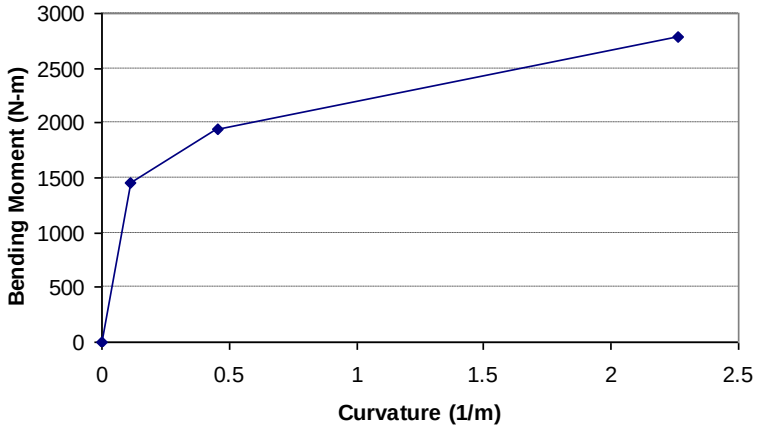

Figure 5-33: The proposed moment-curvature for the buried cable

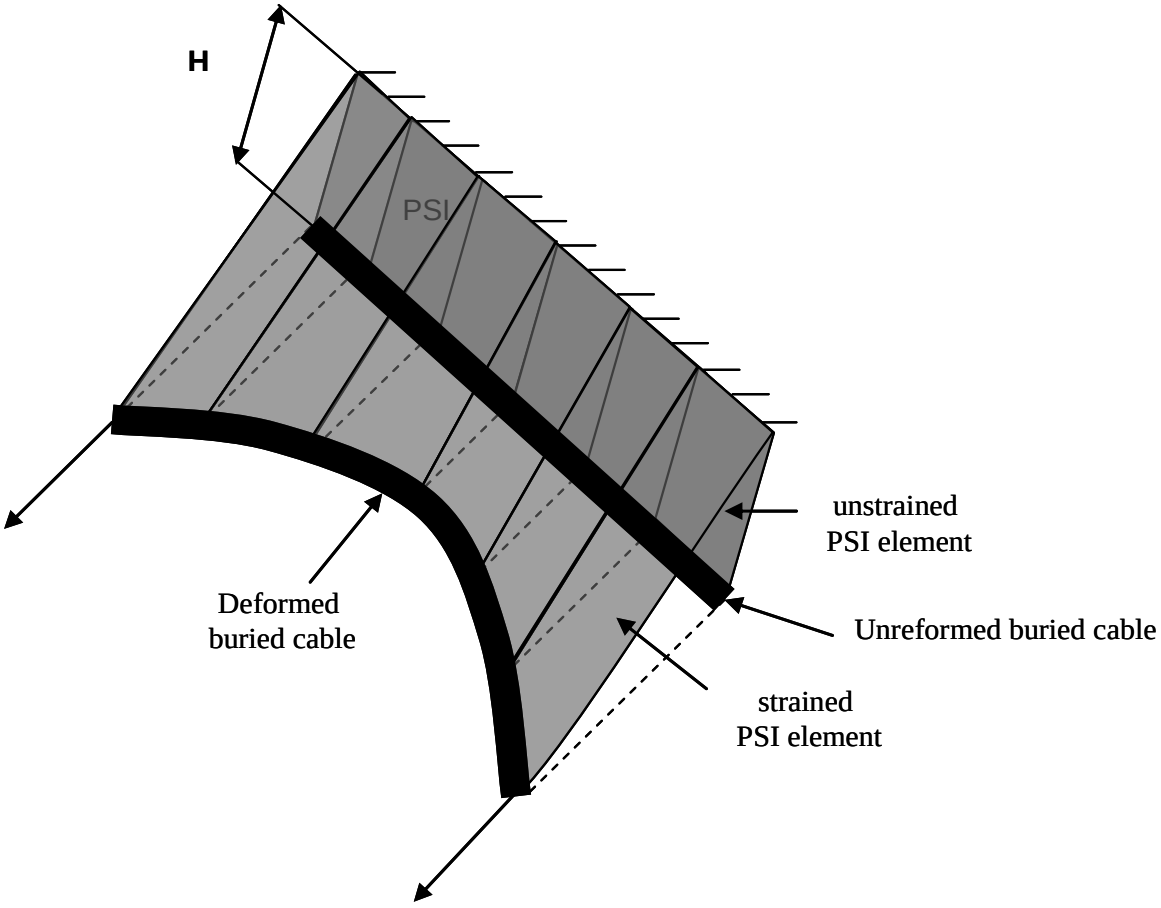

Figure 5-34: Buried cable, modeled in ABAQUS, subjected to the end displacement

Table 5-2: Summary table of the bilinear representation of the horizontal transverse behavior of soil springs for different burial depths.

D (mm)	*H* (mm)	H/D	Nq	δ*y*(mm)	δy/H
100	300	3.0	14.2	10	.033
100	600	6.0	18.4	20	.033
100	900	9.0	21.5	30	.033
100	1200	12.0	26.8	35	.029

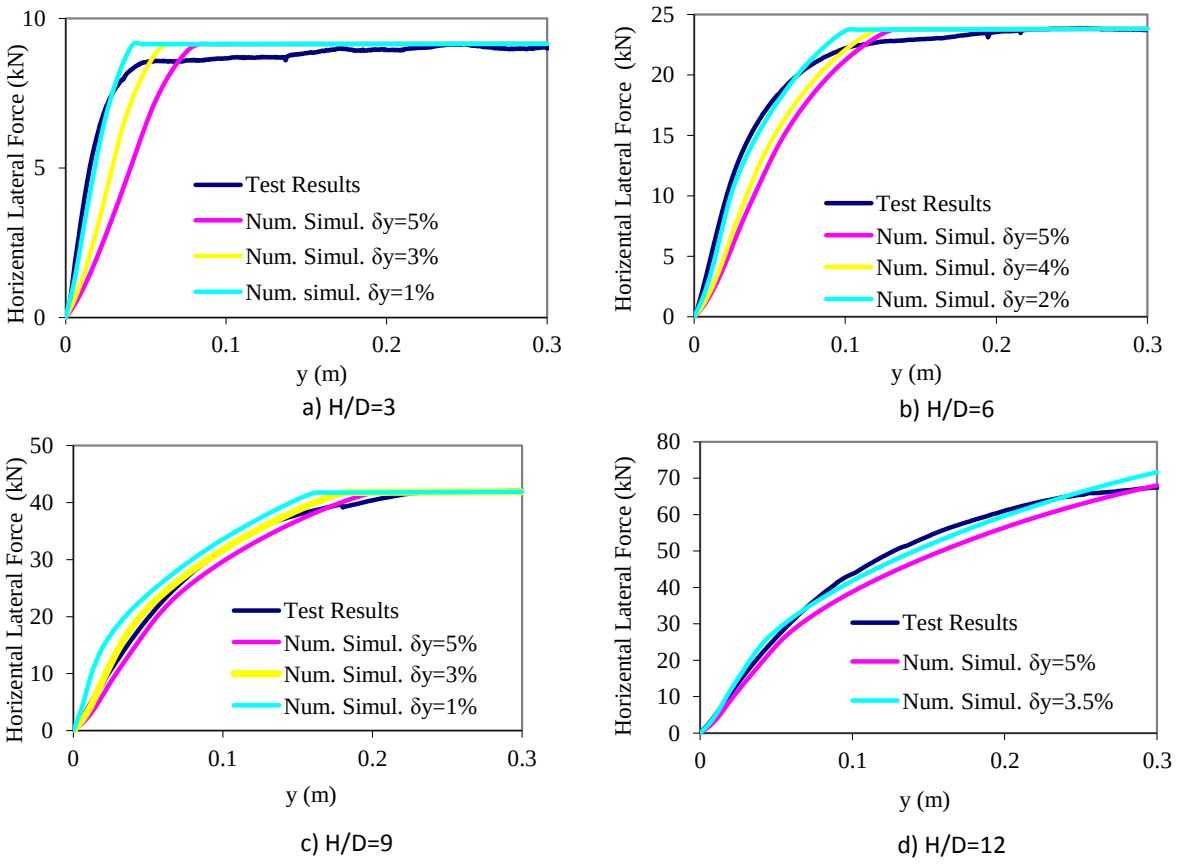

Figure 5-35: Results of calibration of the horizontal spring model with experimental testing for cable with different buried depth ratio (H/D=3,6,9, and 12)

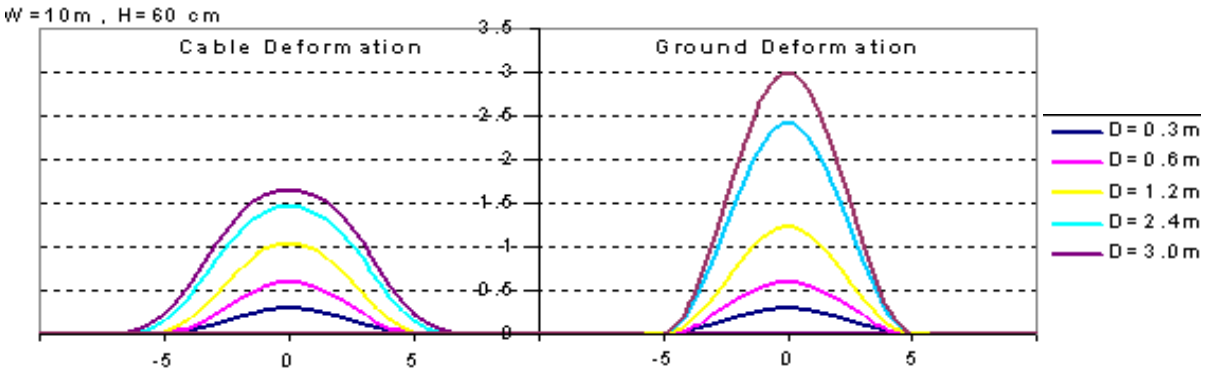

Figure 5-36: The cable deformation profile with the burial depth of H=60 cm, subjected to the permanent ground deformation of W=10 m and different amount of ground deformation (D=0.3, 0.6, 1.2, 2.4, and 3.0 m).

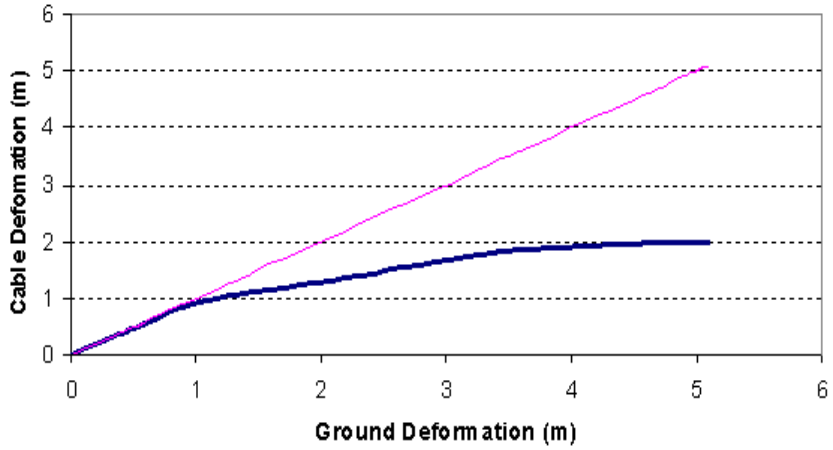

Figure 5-37: Maximum cable deformation as a function of the ground deformation for the cable with buried depth of H=60 cm, W=10 m.

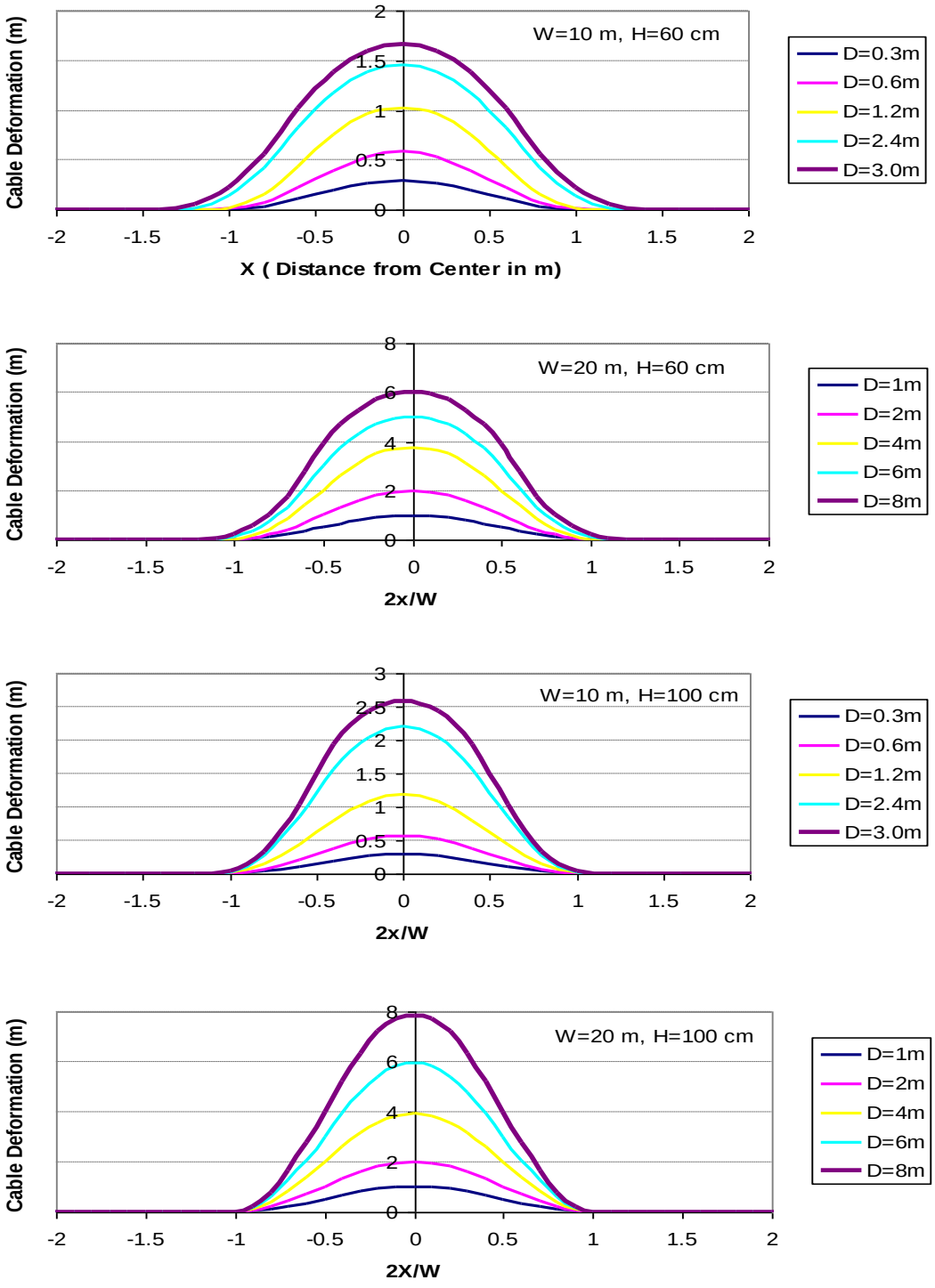

Figure 5-38: The deformation of the cable with burial depth of 60 and 100 cm subjected to PGD with the width of 10 and 20 m

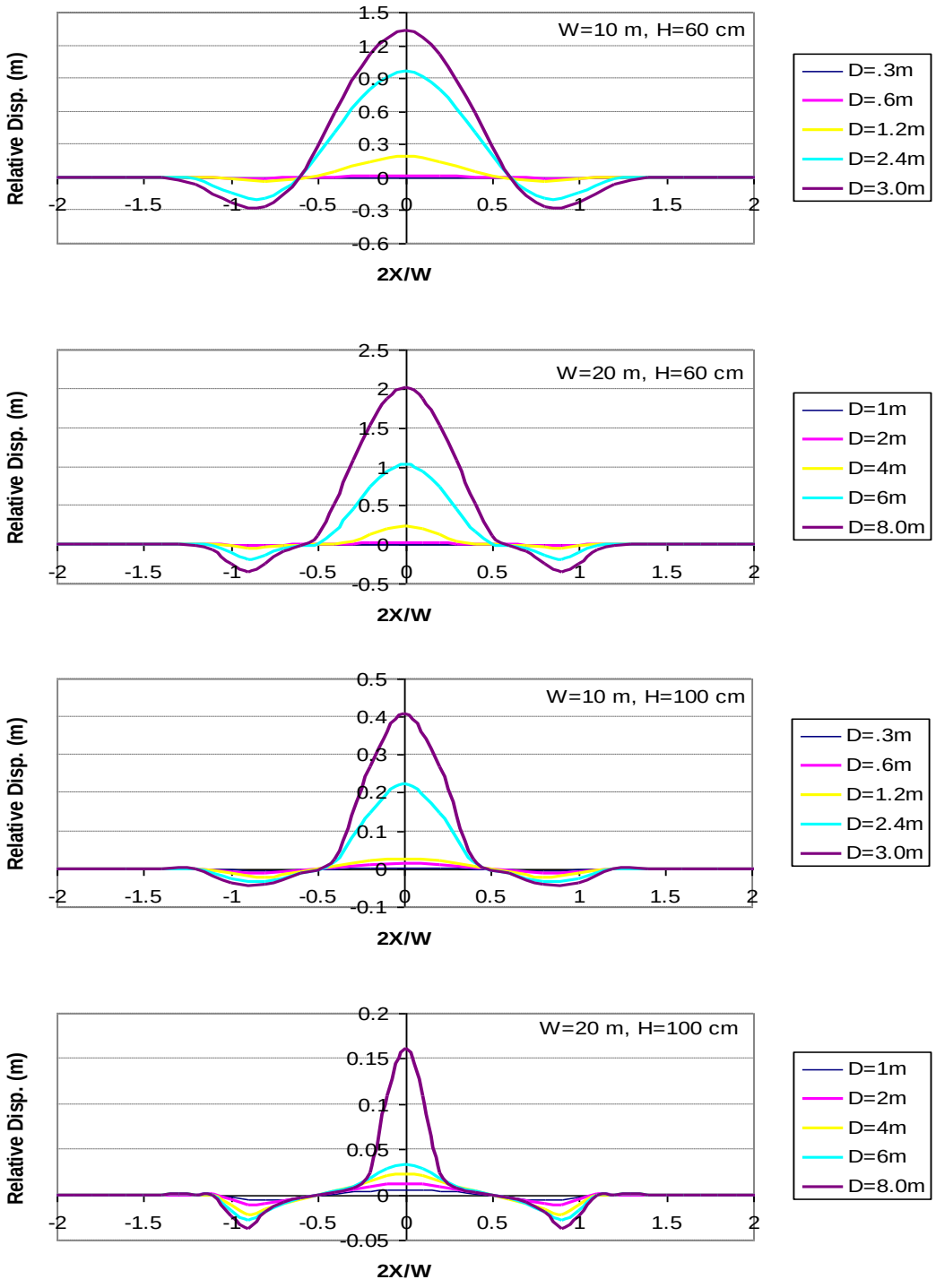

Figure 5-39: The relative movement of the cable and the ground deformation for *H*=60 cm and *H*=100 cm.

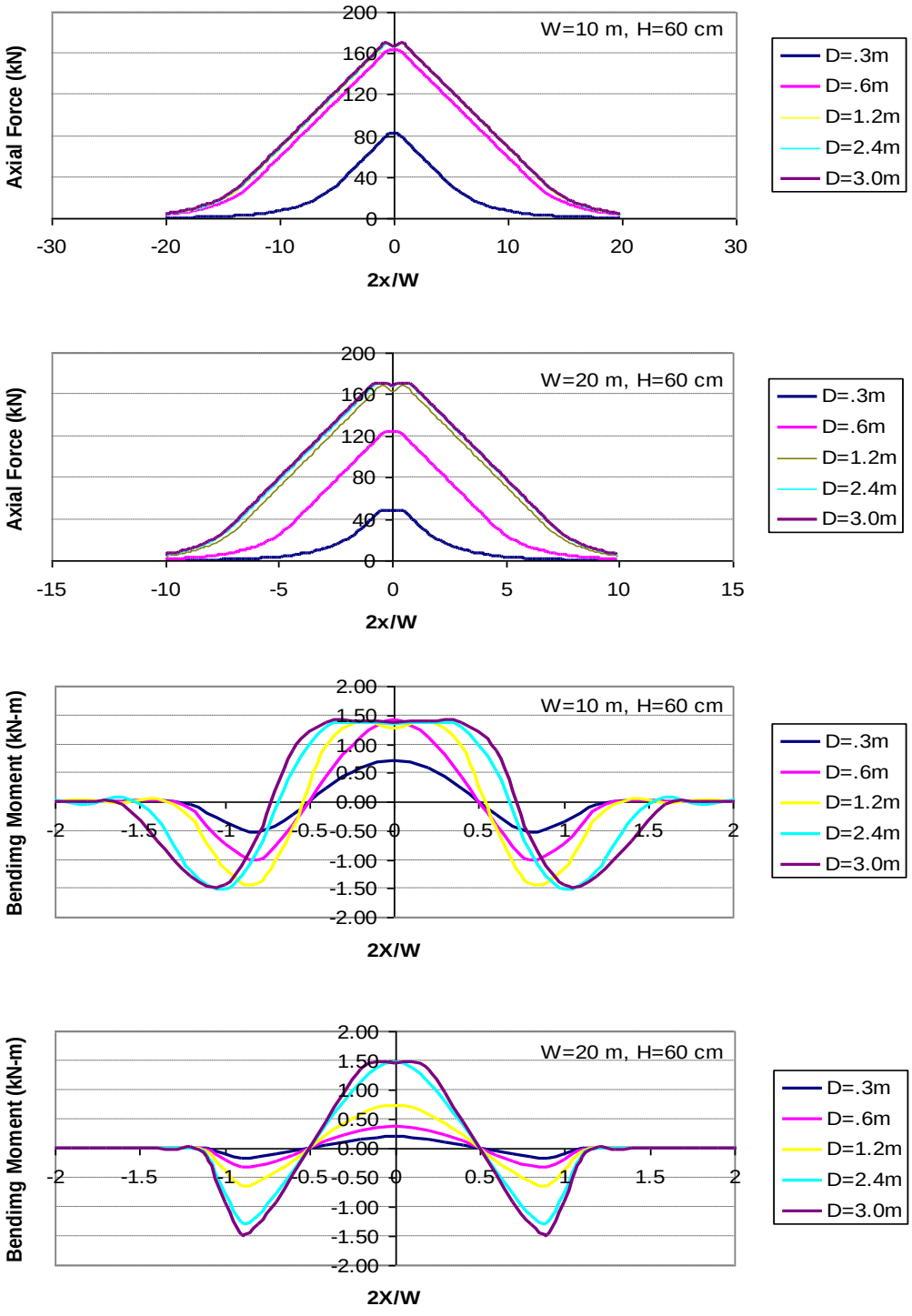

Figure 5-40: Axial force and bending moment profile in the cable with the buried of depth of *H*=60 cm subjected to PGD with the width of 10 and 20 m.

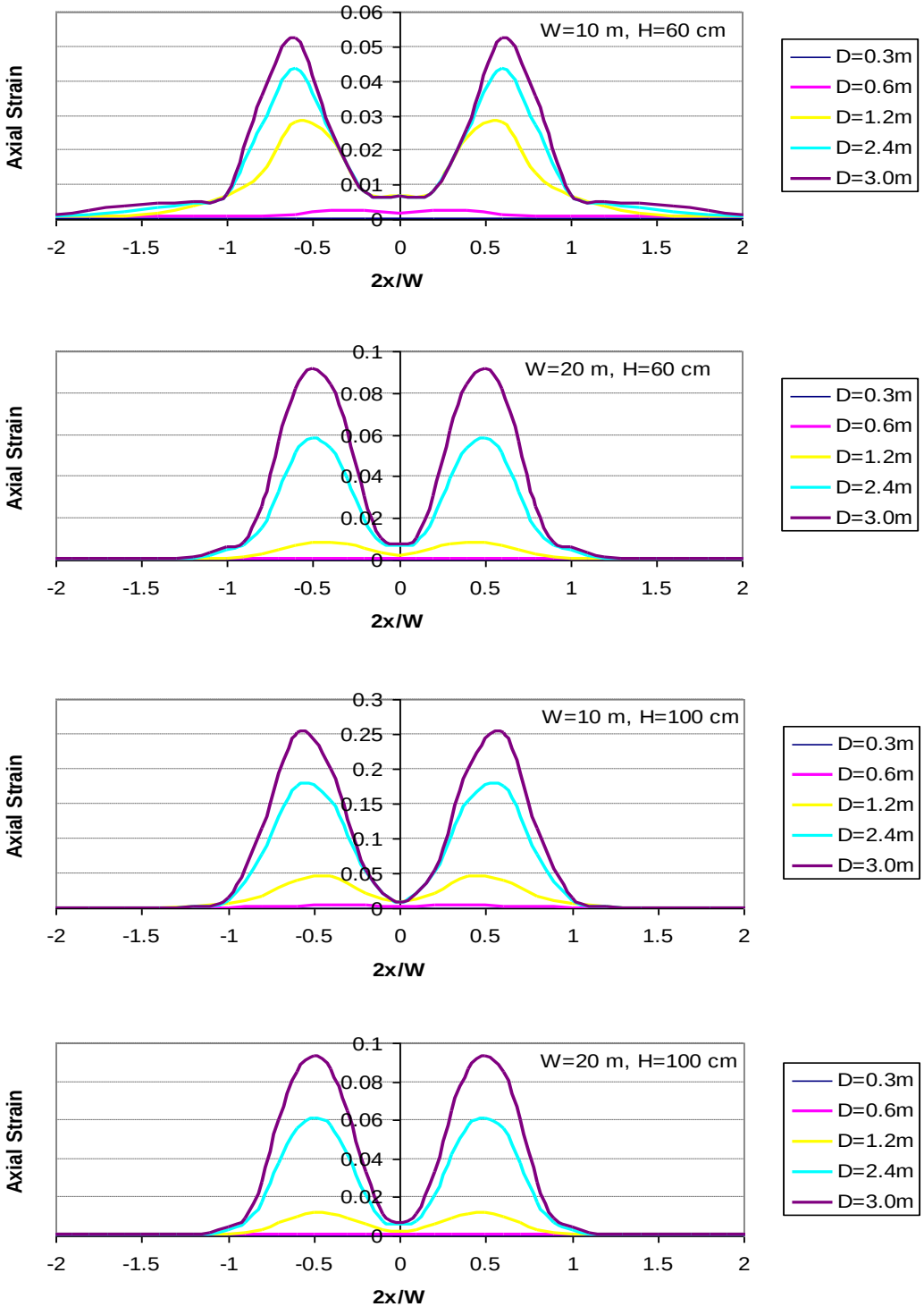

Figure 5-41: Axial strain in the cable for burial depths of 60 and 100 (cm) subjected to PGD with the width of 10 and 20 (m) and different ground deformation

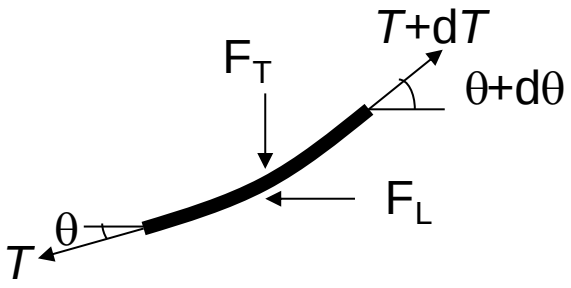

Figure 5-42: Forces acted on the infinitesimal piece of the cable

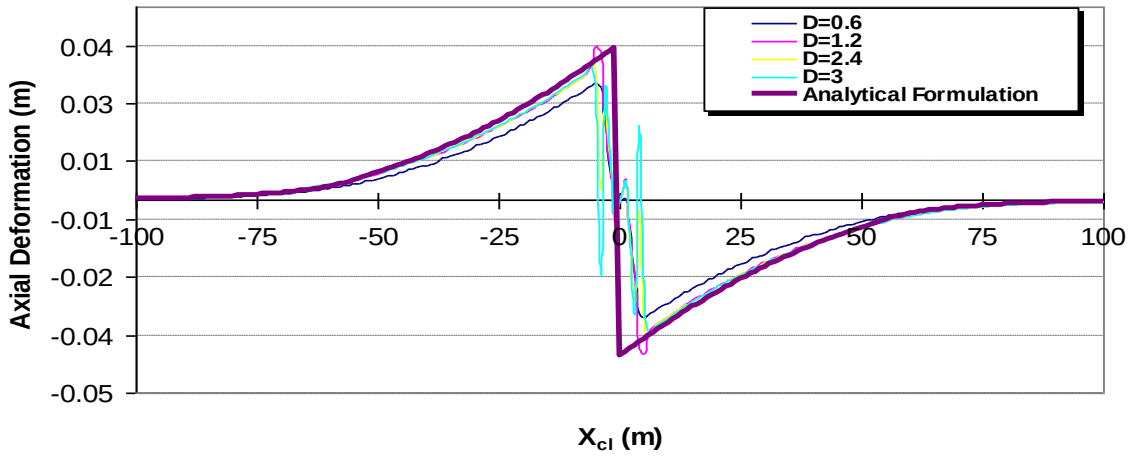

Figure 5-43: Verification of the proposed formula with the numerical simulation to predict the axial deformation development in the cable with the burial depth of 60 cm and subjected to PGD with width of 10 m.

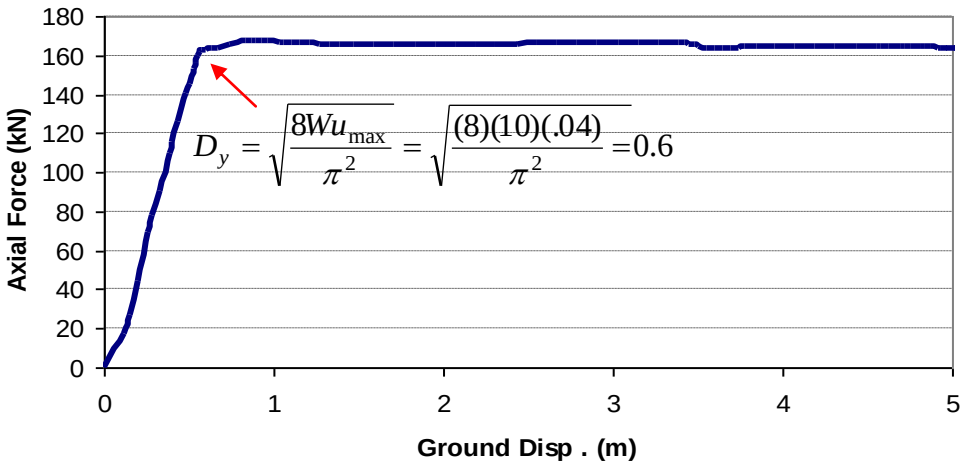

Figure 5-44: Prediction of the amount of the ground deformation causing the axial yielding in the cable with burial depth of 60 cm subjected to PGD with the width of 10 m.

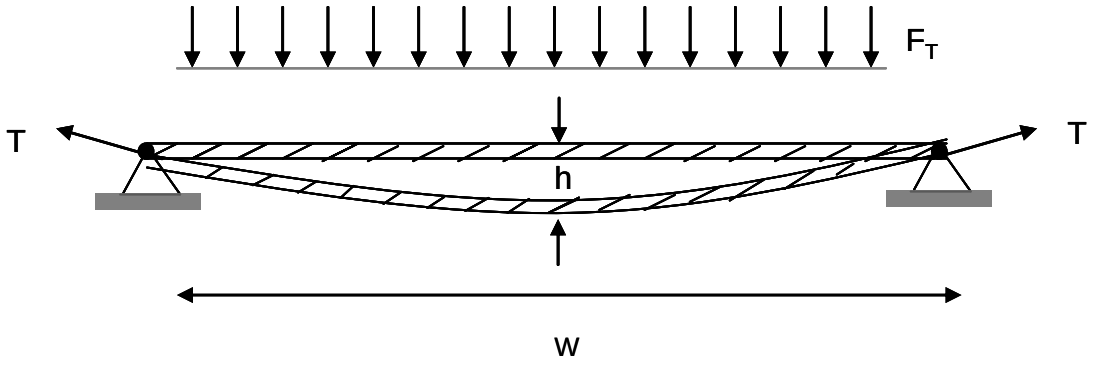

Figure 5-45: Cable structure loaded by the vertically uniform load (F_T).

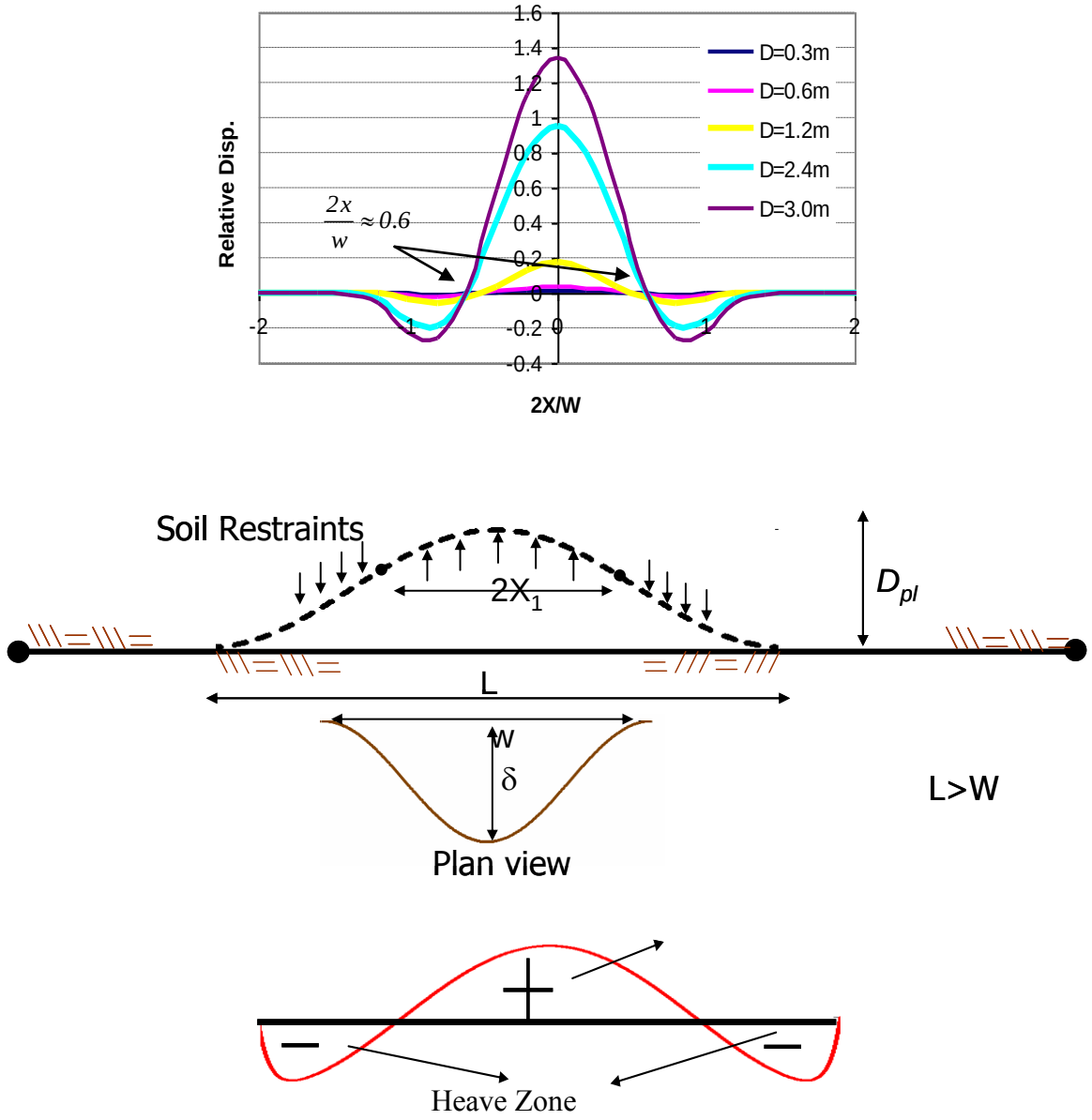

Figure 5-46: The relative deformation of the ground and the buried cables and the formation of the "thrust" and "heave"

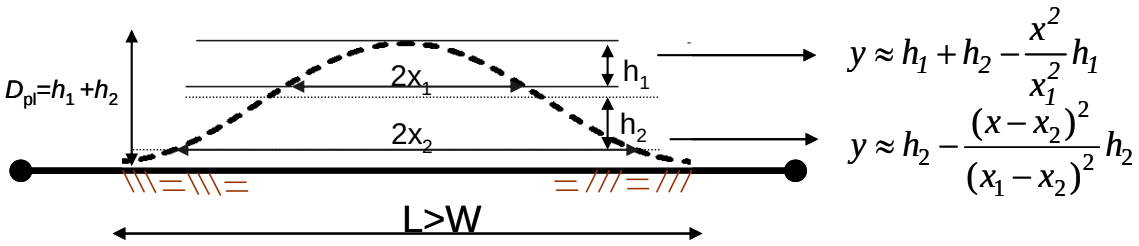

Figure 5-47: Analytical formula representation of the plateau deformation

	H=60,h_1	H=60,h_2	H=100,h_1	H=100,h_2
T (kN)	150	140	150	140
Ft (kN/m^2)	22.1	22.1	47.2	47.2
L (m)	6	7	6	7
h_1 or h_2	0.66	1.26	1.4	2.69
$\delta=h_1+h_2$		1.92		4.11

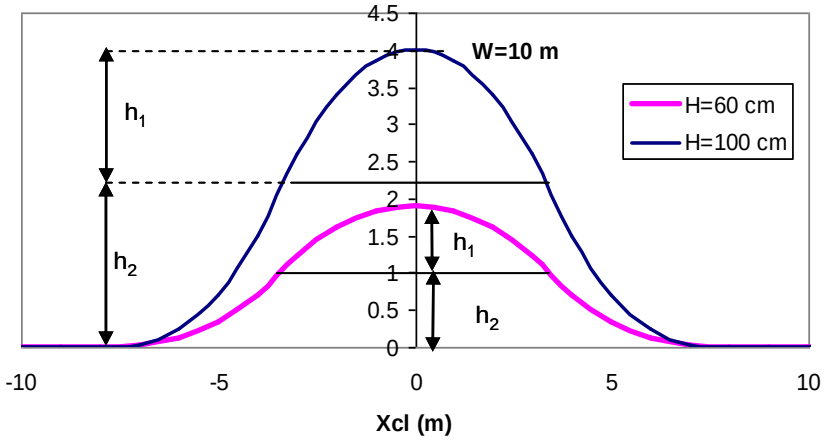

Figure 5-48: Verification of the predicted D_{pl} for the case of cable with burial depth of 60 and 100 cm subjected to PGD with the width of 10 m.

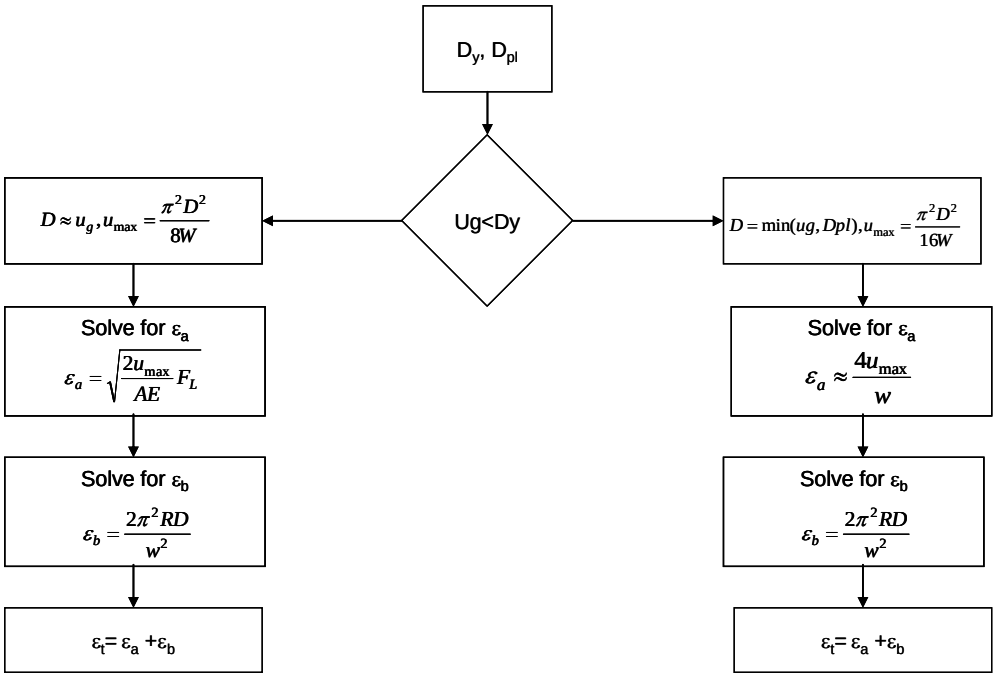

Figure 5-49: Procedure for calculation the axial strain in the buried power transmission cables subjected to the transverse ground movement

D*:** maximum cable deformation, u_g**:** maximum ground deformation, ε_a**:** maximum axial strain due to axial force, ε_b: maximum axial strain due to bending, ***R: the radius of the cable, F_L: the longitudinal soil restraint, ***W***: the width of ground deformation.

* ε_a is approximated based on the assumption of the perfectly plastic behavior of the longitudinal soil restraint

** ε_a is approximated based on the assumption that the maximum axial strain occurs at $x=\pm W/4$ and the length of plastic link is $W/2$ as observed by numerical simulations as depicted in Figure 5-41.

Chapter 6: Summary and Conclusions

This dissertation presented a study on the response of the underground power transmission cable subjected to the earthquake-induced PGD. The motivation behind this research was to provide the analysis methodology for utility owners to obtain the response of buried cable subjected to PGD. Since the knowledge regarding the cable-soil interaction was new, a three-phase study was conducted.

In the first phase, large full-scale experimental studies were conducted to characterize the cable-soil interaction behaviour. The testing facility included 1) a 2.5 m height, 2.5 m width, and 3.75 m length soil chamber, 2) two 418 kN actuators for pulling out the cable ends in the displacement controlled manner with the rate of 3.6 cm/hr, and 3) load cells and string potentiometers to measure the pullout loads and displacement at the cable ends. By the assumption that every PGD can be decomposed into two components of a longitudinal and a transverse ground movement, a series of axial pullout tests, simulating the longitudinal soil loads on the cable, and lateral pullout tests, simulating the horizontal transverse soil loads on the cable, were conducted. The results of those experimental studies were expressed as a load-deformation curve for different burial depths. The results of experimental studies were compared to those of the previous studies and guidelines that specifically obtained for other pipeline systems,in terms of load-deformation curve and the maximum soil loads on the buried lifeline. In this phase, the following key conclusions were made:

- The experimental tests provided new information on the cable-soil interaction behaviour in the longitudinal and horizontal transverse directions. The comparison between test results and the current guideline (ASCE 1984) shows that the current guideline underestimates the soil loads on the cable.

- The response of the cable in the axial pullout tests shows that load-deformation curve consists of: 1) the almost linear region up to the peak load, 2) the strength degradation region, and 3) the hardening region. The first and second regions are a typical

response of every buried pipeline in a dense material. However, the cable with out-of-straightness activates additional longitudinal frictional force along the buried cable due to an increase in the normal stress on the buried cable. Consequently, the hardening region of the load-deformation has created. The effect of out-of-straightness on the longitudinal soil loads on the cable is a new feature and it has been addressed in the current guidelines (ASCE 1984 , PRCI , and ALA).

- The response of the buried cable in the lateral pullout tests shows that the load-deformation curve follows the rectangular hyperbola. The horizontal force factor (N_h) measured for the cable with different burial depth during lateral pullout tests indicates that the recommended value for N_h by ASCE (1984) guideline underestimates the soil loads on the cable.

In the second phase of this research, 3-D numerical models were developed to simulate the results of the axial and lateral pullout tests. The soil was modelled as a continuum medium and the cable was modelled as an equivalent cylinder in finite element code ABAQUS. In the numerical simulation of lateral pullout tests, numerical models using Mohr-Coulomb material model and Drucker-Prager material model were calibrated and validated with the help of laboratory element testing. Also, parametric studies were performed to study the effect of the following factors on the load-deformation curve: 1) the effect of the cable-soil relative stiffness by introducing λL parameter, 2) the effect of material types (Mohr-Coulomb or Drucker-Prager model) 3) the effect of material model parameters ,i.e., friction angle(ϕ or β) and dilation angle(ψ), and 4) the effect of dilatant and non-dilatant characteristic of soil. A family of load-deformation curves was developed for the cable with different flexibility buried in the soil with different friction angle and dilation angle.

In the numerical simulation of axial pullout tests, numerical model, using Mohr-Coulomb material model, was developed. The effect of out-of-straightness was assessed by introducing the offset ratio (δ/L). Numerical models with different offset ratios, burial depths, interface cable/soil friction angles, and cable/soil relative stiffness were investigated. Studies show that the cable/soil relative stiffness and the amount of offset ratios are the most significant

variables. A family of load-deformation curves was created for the cable with different offset ratio and cable/soil relative stiffness.

In the third phase of this study, the response of the buried cable subjected to the PGD was assessed. This phase of research consists of two sections,1) a buried cable subjected to the longitudinal PGD and 2)a buried cable subjected to the horizontal transverse PGD. For the cable subjected to the longitudinal PGD, the following studies were performed:

- Based on the experimental testing and numerical simulations, a longitudinal nonlinear spring model was developed. The nonlinear soil spring model was presented as an elasto-plastic behaviour in which the yield force and yield displacement were calibrated to the experimental axial pullout tests.

- The procedure, which was tested against the numerical simulation models, was defined to account for the effect of the out-of-straightness on the longitudinal soil loads on the buried cable by developing 1) a horizontal transverse coefficient of subgrade reaction, and 2) an analytical expression to calculate the additional increase in the longitudinal soil loads on the buried cable.

- The response of the straight cable to the longitudinal PGD with the block pattern of ground movement was formulated analytically. The cable axial behaviour was represented by a bilinear behaviour. In this formulation, the ground deformation was characterized by the width and amount of ground deformation, and the length of ground deformation zone (L_y) causing a yield in the cable was determined.

- The response of the non-straight cable subjected to the longitudinal PGD with the block pattern of ground movement was formulated analytically. Also, the influence of the layout shape by assuming a sinusoidal shape was investigated. The main parameters of this study were offset ratio, the corresponding length in which offset occurs, the length of ground deformation zone, and the boundary condition. The study showed that in the case of the cable with small bending flexibility, the offset ratio is

the most important parameter and the length of ground deformation zone is the least significant parameter to consider.

- Parametric studies were performed to identify the effect of different parameters such as offset ratio, the cable/soil relative stiffness (λ) and the width and the amount of ground deformation on the longitudinal soil loads on the cable. The research showed that the offset ratio and the cable/soil relative stiffness ratio play an important parameter in estimating the additional longitudinal soil loads on the non-straight cable.

For the cable subjected to the horizontal transverse PGD, the following studies were performed:

- Based on the experimental studies and numerical simulations the nonlinear horizontal transverse soil springs with elasto-plastic behaviour were developed for the cable with different burial depths.

- Parametric studies were performed to investigate the effect of the ground deformation parameter on the response of buried cables. Analytical formula, tested with numerical simulation, was developed to obtain the response of the buried cable. The analytical formula can reasonably predict the ground deformation creating a yielding in the cable (D_y) and the maximum cable deformation (D_{pl}).

- An approximate procedure to obtain the response of buried cable subjected to the PGD event was formulated as a flowchart. This flowchart can be used as an approximate method to determine whether further detailed analysis is required.

6.1 Recommendation for Future Research

- A number of experimental studies, as axial pullout tests, are recommended for the next step of this research to characterize the effect of out-of-straightness on the

longitudinal soil loads on the pipeline with different relative soil/pipeline stiffness. In this study, a pipeline with pre-defined shape is buried in the controlled full-scale experimental environment to investigate the effect of different parameters including offset ratios, burial depths and soil/pipeline relative stiffness ratio. The results of the experimental studies can be compared with the results of numerical simulation model, developed in this thesis to study those factors.

- As mentioned in Chapter 3, the current experimental lateral pullout tests assumed the cable is buried in the environment full of thermal backfill material. However, the cable is buried in the thermal backfill material surrounded by native soils. Therefore, a number of experimental studies, as lateral pullout tests, are suggested to investigate the effect of native soils on the horizontal transverse soil loads on the buried cable. It should be mentioned the results of lateral pullout tests in this research provide a conservative result since thermal backfill material normally have a higher friction angle than the native material.

- In this thesis, a longitudinal and horizontal transverse soil loads on the buried cable were examined separately, and the results can be combined for any oblique relative soil/cable deformation. In order to study this assumption, a series of experimental and numerical simulations are suggested for the next phase of this research. In the future study, a cable with different oblique angles buried in different burial depths should be tested.

- The numerical simulation in this study considered the Mohr-Coulomb and Drucker-Prager material model. However, those material models consider the failure in the soil as a shear and neglected the fact that soil material can be failed in the compression. A set of triaxial testing on the thermal backfill material is required to define a mean effective yield stress (P_b) variation with the volumetric plastic strain to calibrate the CAP plasticity model as describe in Appendix B. This plasticity models are required for the numerical simulation of the behaviour of the cable in the larger burial depth with the chance of punching failure.

- In this research as mentioned in Chapter 5, for the sake of simplicity, it is assumed that the non-straight cable only have a sinusoidal shape with the amplitude (δ) and offset ratio δ/L subjected to block pattern of ground movement, and find the shape creating the largest increase in the soil loads on the cable. For the next phase of this study, it is recommended that the effects of offset ratio for the cable with different laying shape and different cable/soil stiffness ratio are investigated.

- It is recommended for the next phase of this study to define performance criteria which can be strain levels corresponding to the safe operational level, repairable damage level, and failure level. By defining those service levels, the fragility curves can be developed for assessing the seismic vulnerability of buried transmission lines which helps the utility owners to estimate the associated risk and to allocate resources for the seismic mitigation of the buried power transmission cables.

- To better understand the longitudinal soil loads on the cables is to perform field tests. The benefit of the field tests is to take advantage of the natural cable laying shape to characterize the effect of out-of-straightness. A pulling-out mechanism should be designed to employ displacement at cable ends and corresponding load-deformation curve should be obtained. The results of the field tests can be compared to the procedures outlined in the thesis to calculate longitudinal soil loads on the cable.

- Studies showed that the reliable estimation of normal stresses on the cable during ground movement leads to a better prediction of longitudinal soil loads on the cable. For the next part of this study, the experimental research program is recommended to monitor the normal stresses on the cable at several locations during longitudinal ground movements to finally estimate the longitudinal soil loads on the cable.

References

ALA. 2001. Guidelines for the design of buried steel pipe. American Lifeline Alliance, Available from http://www.americanlifelinesalliance.org/Products_new3.htm (cited July 2007).

Anderson C. Wijewickreme D., Ventura C.E. (2005), Full-Scale Laboratory Testing of Soil-Pipe Intereaction in Branched Polyethylene Pipelines, Experimental Techniques, 29(2), 33-37.

ASCE. 1984. Guidelines for the seismic design of oil and gas pipeline systems. Committee on Gas and Liquid Fuel Lifelines, Technical Council on Lifeline Earthquake Engineering, ASCE, New York.

Audibert, J. M. E. and Nyman K.J., (1977), Soil Restraint against horizontal motion of pipes, Journal of the Geotechnical Engineering Division, ASCE, 103(GT10), 1119-1142.

Bardet, J.P. , Tobita, T., Mace, N., and Hu, J. (2002), Regional Modeling of Liquefaction-induced Ground Deformation, Earthquake Spectra, 18,1,19-46.

Bartlett, S.F. , and Youd T.L. (1992), Empirical analysis of horizontal ground displacement generated by liquefaction-induced lateral spread, Technical paper NCEER-92-0021, SUNY.

Biot M.A. ,(1937), Bending of Infinite Beam on an Elastic Foundation, Journal of Applied Mechanics, Transactions American Society of Mechanical Engineers, 59, A1-A7.

Bolton, M.D. (1986), The shear strength and dilatancy of sands, Geotechnique, 36,1,65-78.

Chen W.F. (1982), Plasticity in reinforced concrete, MacGraw-Hill Book company

Chen W.F. , Mizuno E. (1990) , Development in Geotechnical Engineering 53, Nonlinear Analysis in Soil Mechanics, Theory and Implementation, Elsevier, NY,

Craig R.E., (1987), Soil Mechanics, Van Nostrand Reinhold (international), Fourth Edition.

Das, B.M. , Introduction to Soil Mechanics, (1979), First Edition, The Iowa State University Press/Ames

Eguchi, R.T. (1982), Earthquake Performance of water supply components during 1971 San Fernando Earthquake, Technical Report 1396-2a, Wiggins JH Company, Redondo Beach, CA.

Elgamal A.W. and Zhaohui Y., (2000), Numerical Modeling of Liquefaction-Induced Lateral Spreading, 12th World Conference of Earthquake Engineering, Auckland, New Zealand.

Guo P.J. and Stolle D.F.E. (2005) Lateral pipe-soil interaction in sand with reference to scale effect, Journal of Geotechnical and Geoenvironmental Engineering, 131,3, 338-349.

Hamada, M. ,Yasuda, S. , Isoyama, R. , and Emoto, K. (1986), Study on Liquefaction induced Permanent Ground Displacement, Report for the Association for the Development of earthquake prediction.

Hamada, M. and O'Rourke T.D. (1992), Case studies of Liquefaction and Lifeline Performance during Past Earthquake, Technical Paper NCEER-92-0001, SUNY.

Hansen J. (1961), The Ultimate Resistance of Rigid Piles against Transversal Forces, Bulletin, No. 12, Danish Geotechnical Institute, Copenhagen, Denmark.

Hetenyi M., (1946) Beams on Elastic Foundation: Theory with Applications in the Fields of Civil and Mechanical Engineering,

Hibbit, (2007) , ABAQUS theory manual, Ver. 6.4., Dassault Systemes.

Hoeg (1968), Stress against Underground Structural Cylinder, Soil Mechanics and Foundation Division, Proceeding of the American Society of Civil Engineers, 98, SM4, 833-858.

Honeggar, D.G., and Nyman, D.J. (2004), Guideline for the seismic design and assessment of natural gas and liquid hydrocarbon facilities, Pipeline Research Council International, Inc. , Arlington, Va. Catalogue No. L51927.

Hurley, S. and Phillips, R. (1999), Large scale modelling of pipeline/soil interaction under lateral loading-Final report. *Contract report for Mineral Management Service, U.S. Department of the Interior, C-CORE Publication 99-C25*.

Hurley, S. and Phillips, R. (1999), Large scale modelling of pipeline/soil interaction under lateral loading-Final report. *Contract report for Mineral Management Service, U.S. Department of the Interior, C-CORE Publication 99-C25*.

Jacky J., (1944), The coefficient of earth pressure at rest, Journal for Society of Hungarian Architects and Engineers, 78, 22, 355-358.

Karimian H., (2006), Response of Buried Steel Pipelines subjected to Longitudinal and Transverse Ground Movement , Ph.D. Thesis, University of British Columbia

Kobayashi, T. , Nakane, H. , Suzuki, N. , Ishrkawa, M. (1989), Parametric study on flexibility of buried pipeline subject to large ground displacement, proceeding of the second US-Japan workshop on liquefaction, large ground deformation and their effect on lifelines, Buffalo, New York, Technical Report NCEER-89-0032, Multidisciplinary center for Earthquake Engineering Research, Buffalo, New York, 348-362.

Kramer S.L., Geotechnical Earthquake Engineering, (1996) Prentice-Hall International Series in Civil Engineering and Engineering Mechanics.

Lamb, T.W., and Whiteman, R. (1969), Soil mechanics in engineering practice, Chichester/ New York, John Wiley & Sons.

Liu X. and O'Rourke M. , Behaviour of Continuous Pipeline Subject to Transverse PGD, (1997), Earthquake Engineering and Structural Dynamics, 26, 989-1003.

Meek, J.W., Wolf, J.P. (1994), Cone Models for Embedded Foundation, Journal of Geotechnical Engineering, ASCE, 120,1,60-80.

Menetrey, Ph., and Willam K.J. (1995), Triaxial Failure Criterion for Concrete and its Generalization, ACI Structural Journal, 92, 311-318.

Newmark, N., 1965, Effects of Earthquakes on Dams and Embankments, Geotechnique, 15,2, 139-160.

Northcutt L. N., Effect of particle fabric on the one-dimensional compression response of Fraser river sand, M. Sc. Thesis, University of British Columbia.

O'Rourke M.J. and Nordberg (1992), Longitudinal Permanent Ground Deformation Effects on Buried Continuous pipelines, Technical Paper NCEER-92-0014, SUNY.

O'Rourke M.J., Liu X., and Flores-Berrones R., (1995), Steel Pipe Wrinkling due to longitudinal Permanent Ground Deformation, Journal of Transportation Engineering, 121,5, 443-451

O'Rourke, T.D. and Hamada, M. (1992), Case Studies of Liquefaction and Lifeline Performance during Past earthquake, Technical Paper NCEER-92-0002, SUNY.

Ovesen, N.K. (1964), Anchor Slab, Calculation Methods and Model Tests, Bulletin, No. 16, The Danish Geotechnical Institute, Copenhagen, Denmark.

Pais A. and Kausel E., (1988), Approximate Formula for Dynamic Stiffness of Rigid Foundation, Soil Dynamics and Earthquake Engineering, 7, 213-227.

Popescu R. , Nobahar A. (2003) , 3D Finite Element Analysis of Pipe/Soil Interaction,- Effects of Groundwater-Final Report, Prepared by C-CORE, Report R-02-029-076.

Popescu R. , Nobahar A. (2003) , 3D Finite Element Analysis of Pipe/Soil Interaction,- Effects of Groundwater-Final Report, Prepared by C-CORE, Report R-02-029-076.

Popescu R. , Phillips R. , Konuk I. , Guo P., and Nobahar A. (2002) , Pipe-soil interaction: large scale tests and numerical modelling, Proceeding of the international conference on physical modelling in Geotechnics/ICPMG '02/ST.John'S / Newfoundland Canada.

Popescu R., Phillips R., Konuk I. (1999) , Physical and numerical analysis of pipe-soil interaction, Proceeding 52nd Canadian Geotechnical Conference, Regina, 437-444.

Popescu, R. Guo, P. and Nobahar, A. (2001), 3D finite element analysis of pipe/soil interaction, Final report for Geological Survey of Canada, Chevron Corp. and Petro Canada, and the Minerals Management Service, C-CORE Contract report 01-C8, Cited by Popescu R. , Nobahar A. (2003).

Rauch, Alan F., (1997), An Empirical Method for Predicting Surface Displacements due to Liquefaction-Induced Lateral Spreading in Earthquakes, Ph.D. Thesis, Virginal Tech University.

Rowe P.W. (1962), The Stress-Dilatancy realtion for static equilibrium of an assembly of particle in contact, Proceeding of the Royal Society, 269A,500-527.

Rowe P.w. (1969), The relationship between the shear strength of sands in triaxail compression, plane strain and direct shear, Geotechnique, 19,1,75-86.

Rowe, P.W., (1962), The stress-dilatancy relation for static equilibrium of an assembly of particle in contact, Proceeding of Royal Society of London, 269,1339, 500-527.

Selvadurai A.P.S. (1979), Elastic Analysis of Soil-Foundation Interaction, Development in Geotechnical Engineering, Vol. 17, Elsevier Scientific Publishing Company.

Suzuki N., Arata O. , Suzuki I., (1988), Subject to liquefaction-induced permanent ground displacement, Proceeding 1st Japan-U.S. Workshop on liquefaction, large ground deformation and their effects on lifeline facilities, 152-162.

Suzuki, N. and Masuda, N., (1991), Idealization of Permanent Ground Movement and Strain Estimation of Buried Pipes, Proceedings of the Third Japan-US Workshop on Earthquake

Resistance Design of Lifeline Facilities and Countermeasures for soil Liquefaction, San Francisco California, NCEER, Report Number 91-0001, Multidisciplinary center for Earthquake Engineering Research, Buffalo, New York, 455-469.

Timoshenko S. , Strength of Materials, Part II, (1960), Advanced Theory and Properties, Third Edition, D. Van Nostrand Company INC, NEWYORK.

Trautmann, C.H., and O'Rourke, T.D. (1985). Lateral force–displacement response of buried pipes. Journal of Geotechnical Engineering, 111(9), 1077–1093.

Vesic´, B.A., (1961) Bending of Beams Resting on Isotropic Elastic Solid, Journal of the Engineering Mechanics Division, Proceeding of the American Society of Civil Engineers, 87,EM2, 35-53.

Weerasekara L., Wijewickreme D., (2008), Mobilization of soil loads on buried, polyethylene natural gas pipeline subject to relative axial displacement, Canadian Geotechnical Journal, 45, 9, 1237-1249.

Wijewickreme, D., Karimian, H., and Honegger, D. (2009) "Response of Buried Steel Pipelines Subject to Relative Axial Soil Movement, Canadian Geotechnical Journal, 46, 7, 732-752.

Youd, T.L., and Perkins D.M., (1987), Mapping of Liquefaction Severity Index, Journal of Geotechnical Engineering, ASCE, 113, 11, 1374-1392.

Appendix A: Test Results

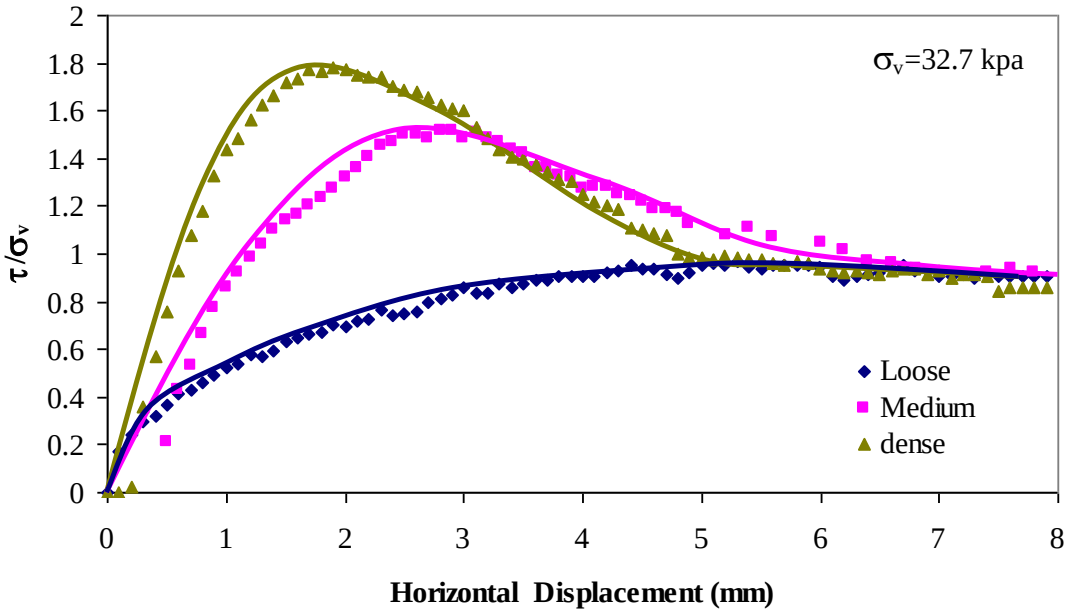

Figure A- 1: Variation of normalized shear stress with shear displacement in direct shear test at normal stress of 32.7 kPa

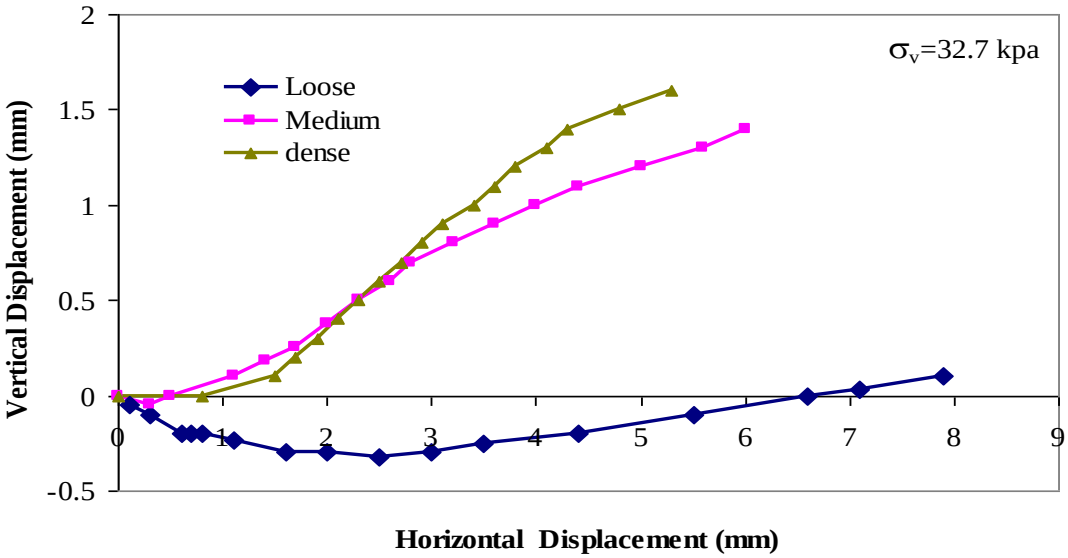

Figure A- 2: Variation of vertical displacement with horizontal shear displacement in direct shear test at normal stress of 32.7 kPa

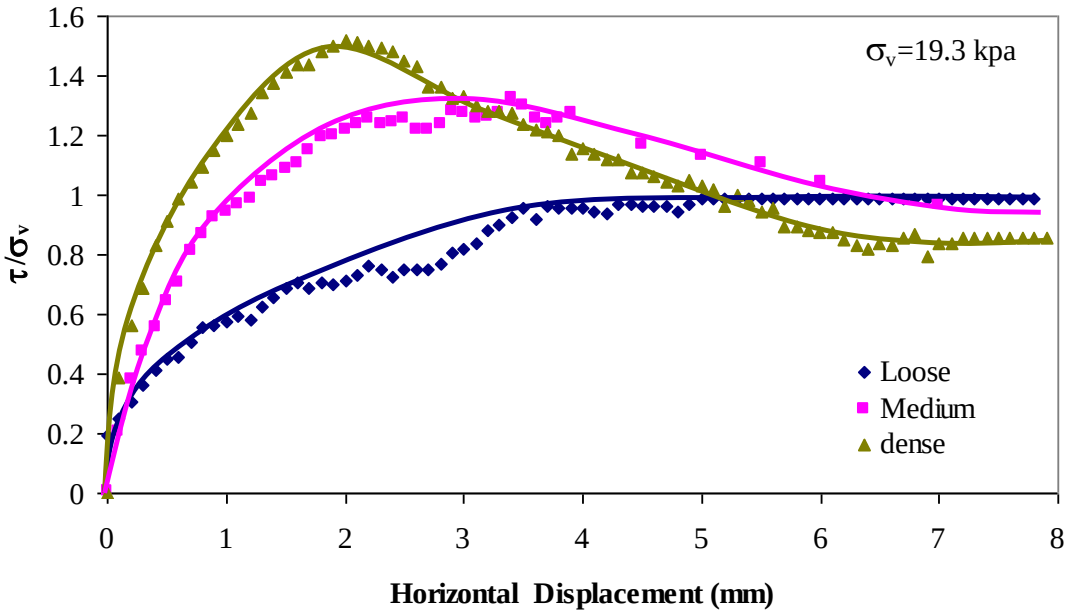

Figure A- 3: Variation of normalized shear stress with shear displacement in direct shear test at normal stress of 19.3 kPa

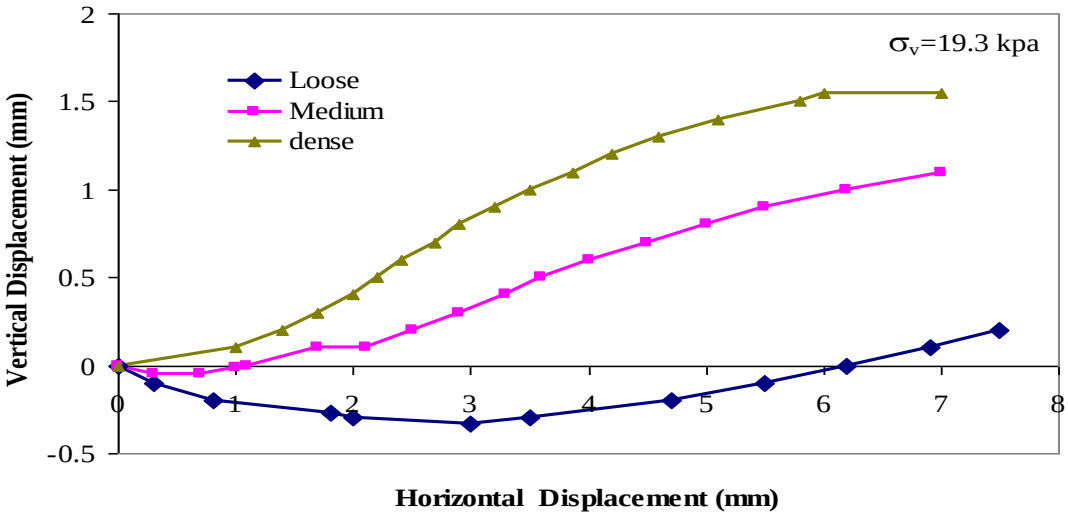

Figure A- 4: Variation of vertical displacement with horizontal shear displacement in direct shear test at normal stress of 19.3 kPa

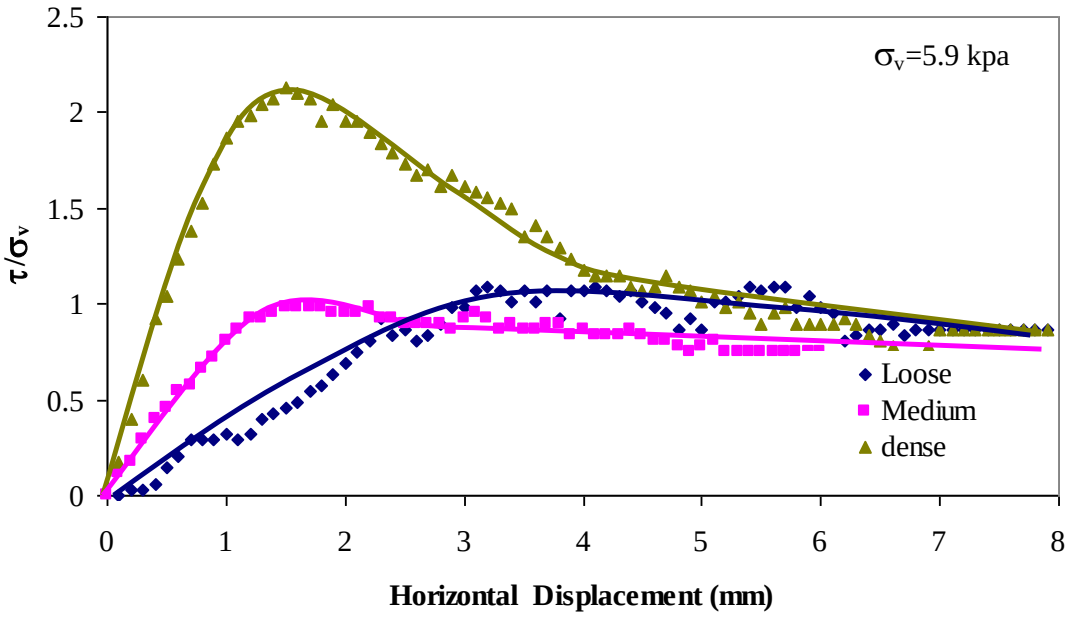

Figure A- 5: Variation of normalized shear stress with shear displacement in direct shear test at normal stress of 5.9 kPa

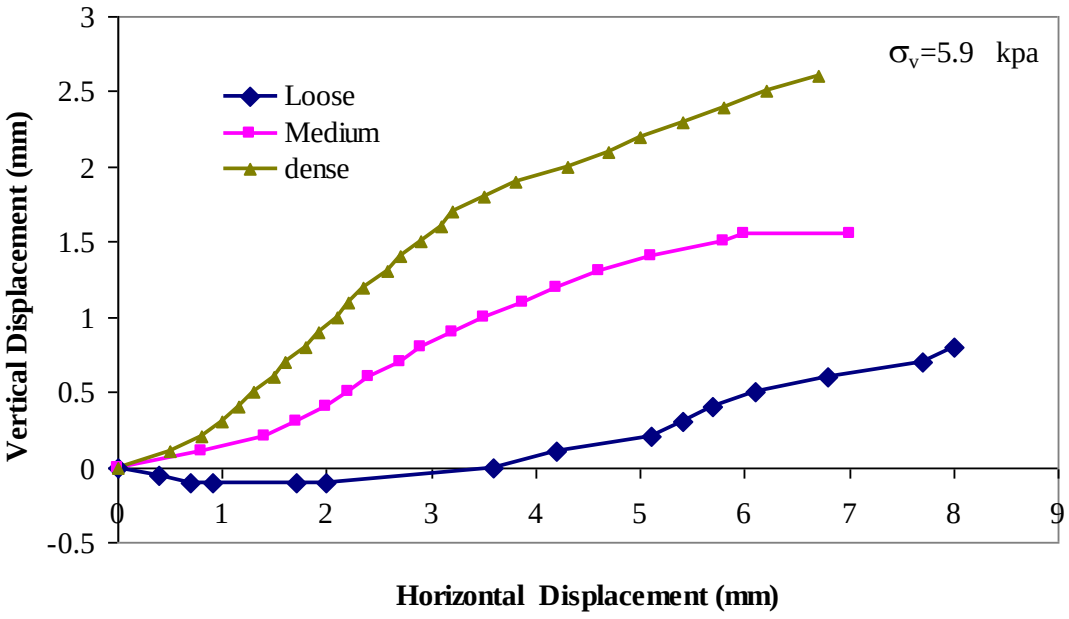

Figure A- 6: Variation of vertical displacement with horizontal shear displacement in direct shear test at normal stress of 5.9 kPa

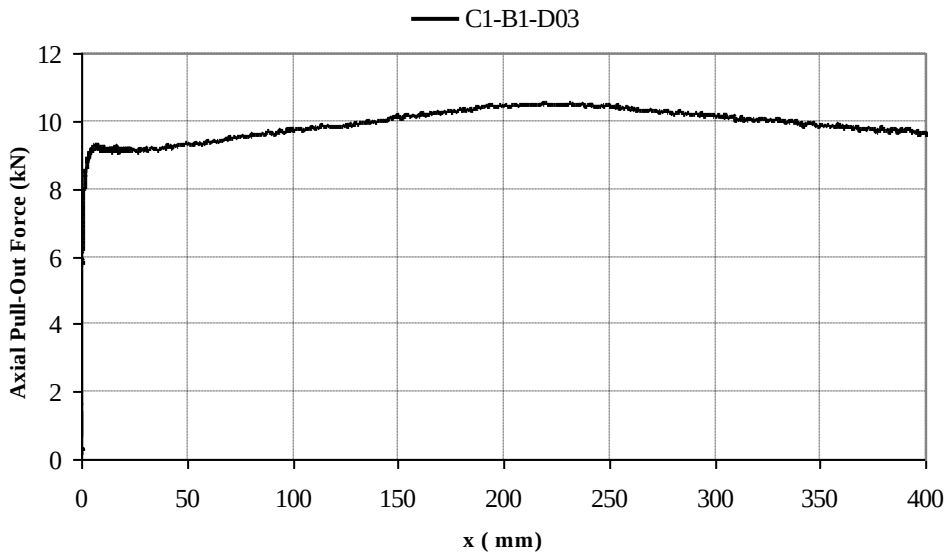

Figure A- 7: Response of the buried cables in axial pullout test, Test C1-B1-D03

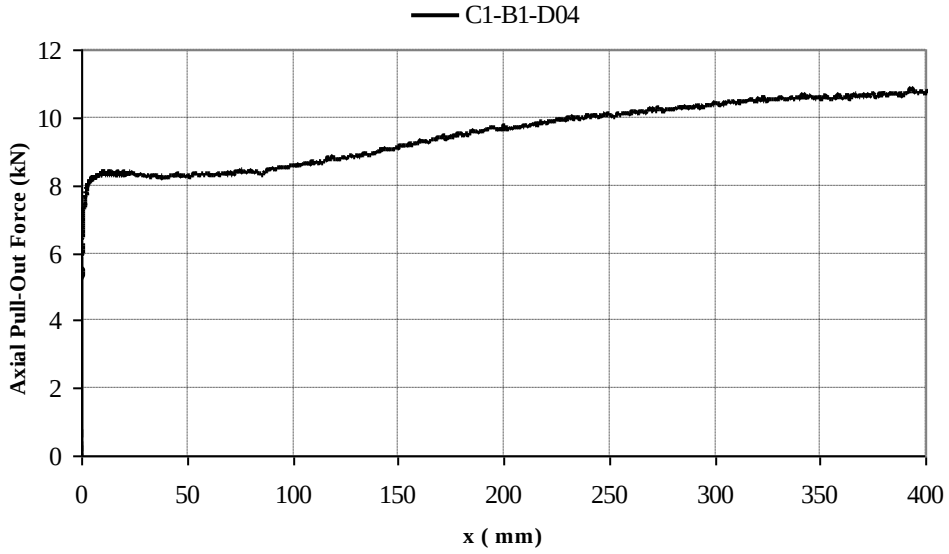

Figure A- 8: Response of the buried cables in axial pullout test, Test C1-B1-D04

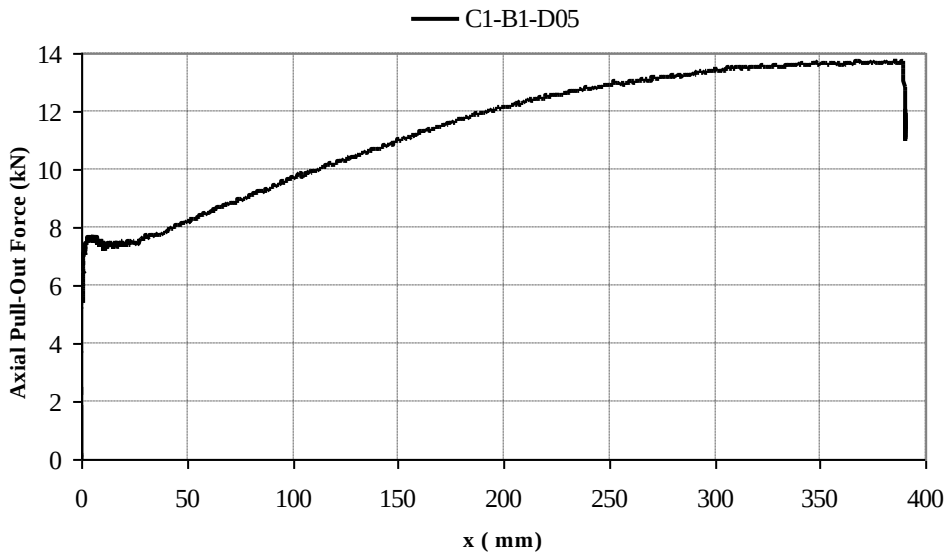

Figure A- 9: Response of buried cables in axial pullout test, Test C1-B1-D05

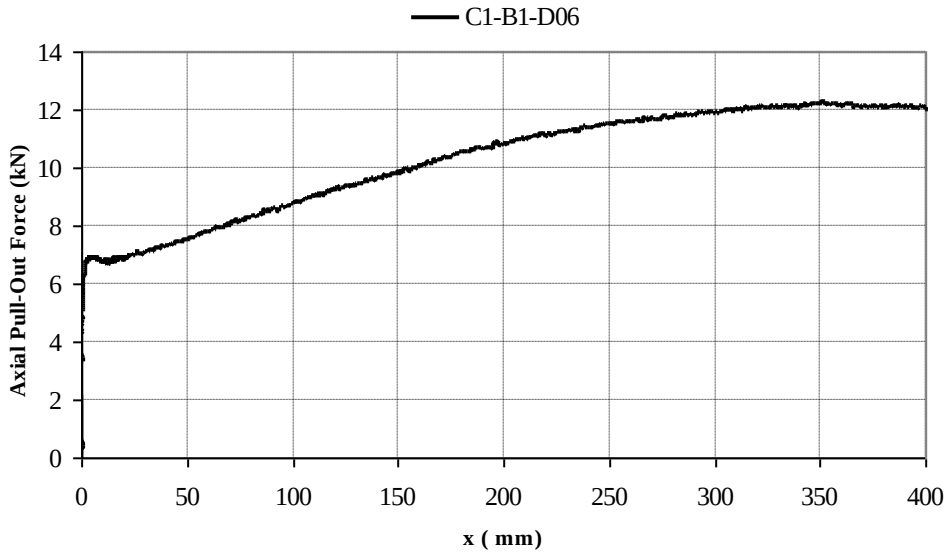

Figure A- 10: Response of buried cables in axial pullout test, Test C1-B1-D06

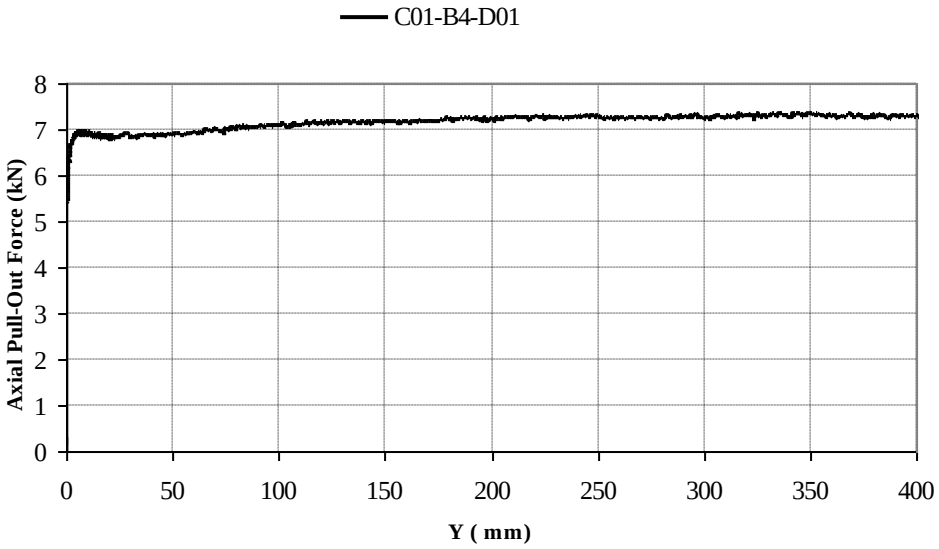

Figure A- 11: Response of buried cables in axial pullout test, Test C1-B4-D01

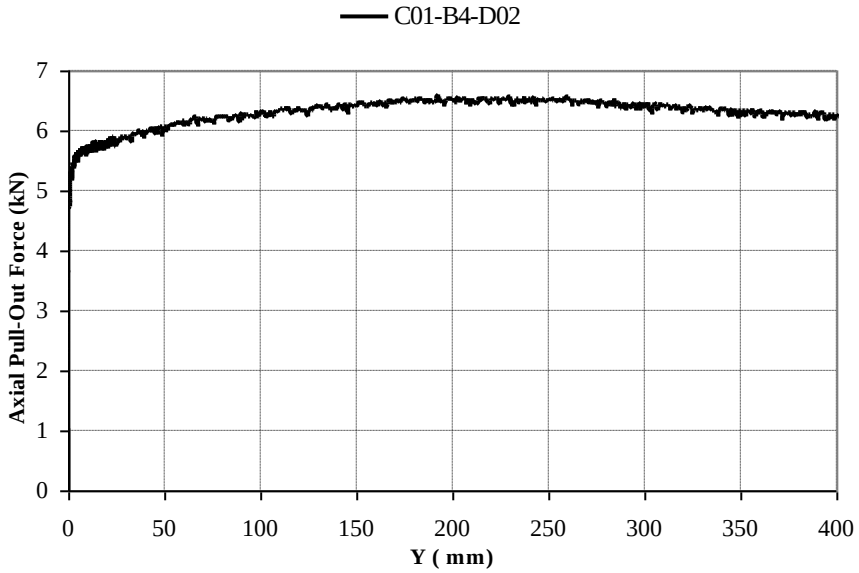

Figure A- 12: Response of buried cables in axial pullout test, Test C1-B4-D02

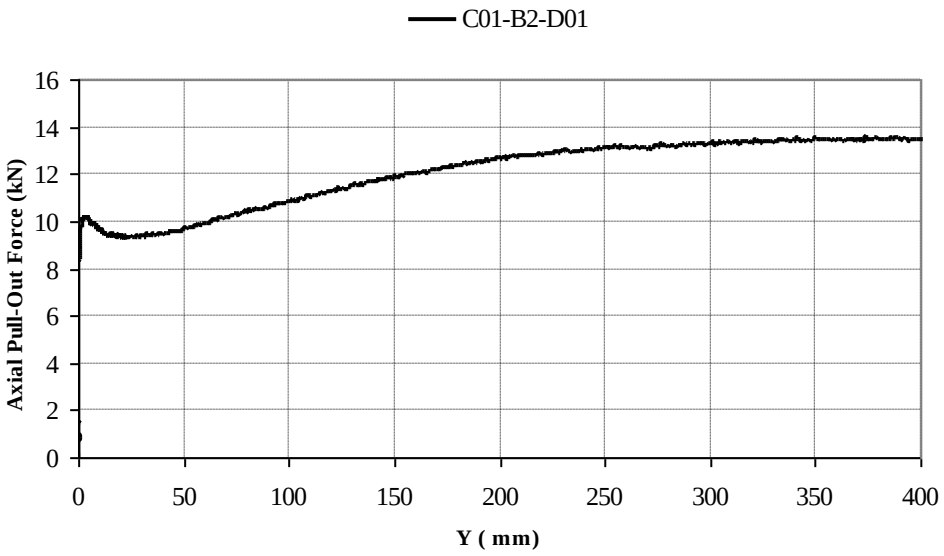

Figure A- 13: Response of buried cables in axial pullout test, Test C1-B2-D01

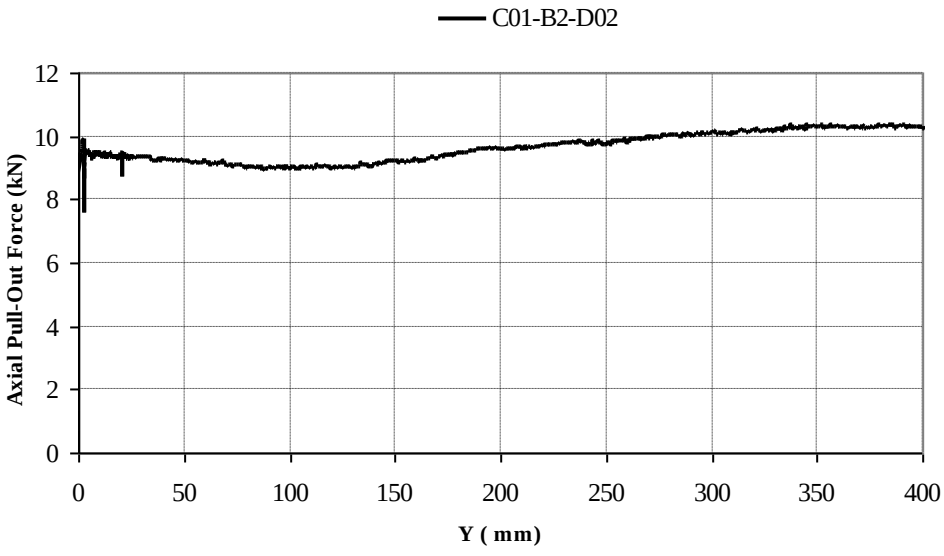

Figure A- 14: Response of buried cables in axial pullout test, Test C1-B2-D02

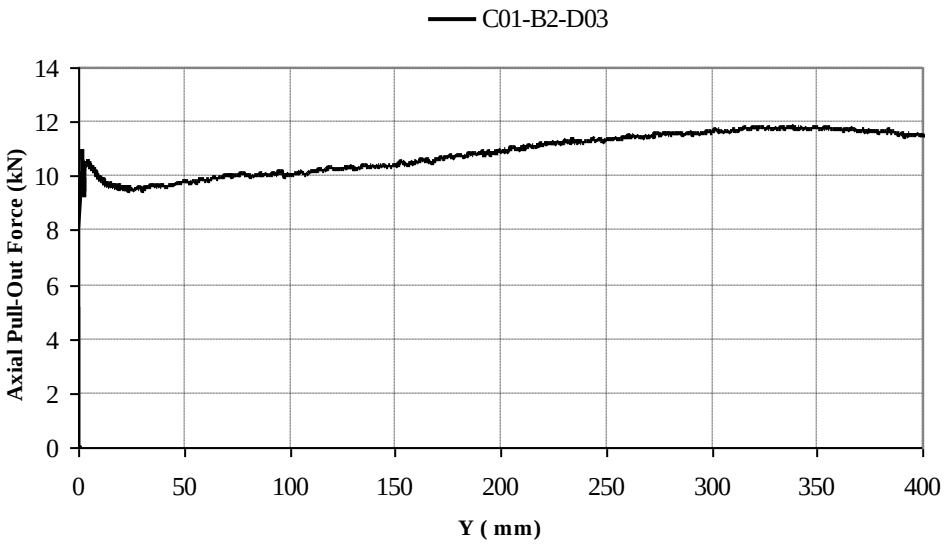

Figure A- 15: Response of buried cables in axial pullout test, Test C1-B2-D03

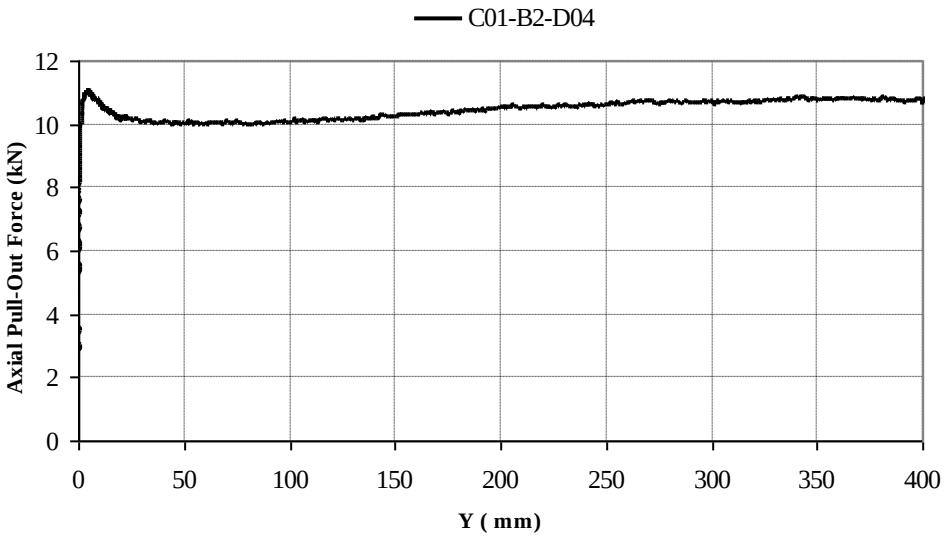

Figure A- 16: Response of buried cables in axial pullout test, Test C1-B2-D04

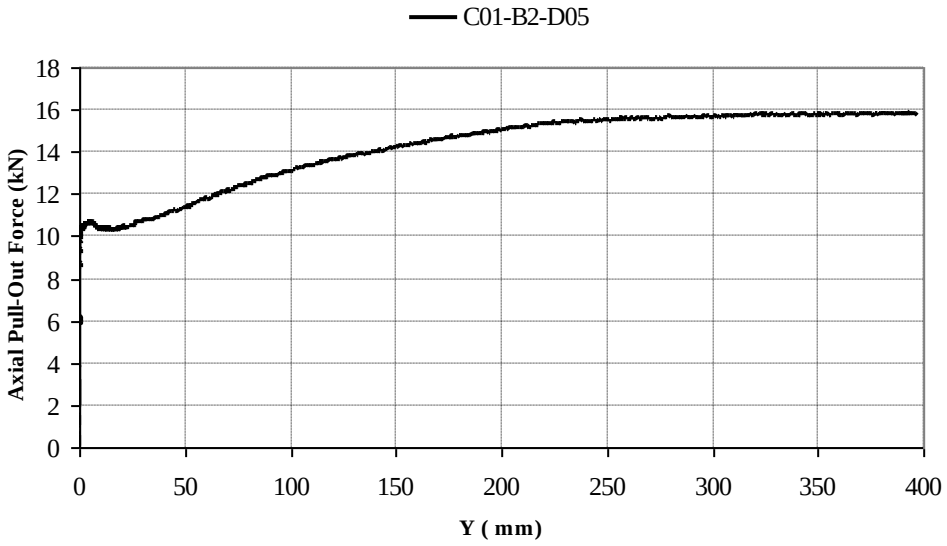

Figure A- 17: Response of buried cables in axial pullout test, Test C1-B2-D05

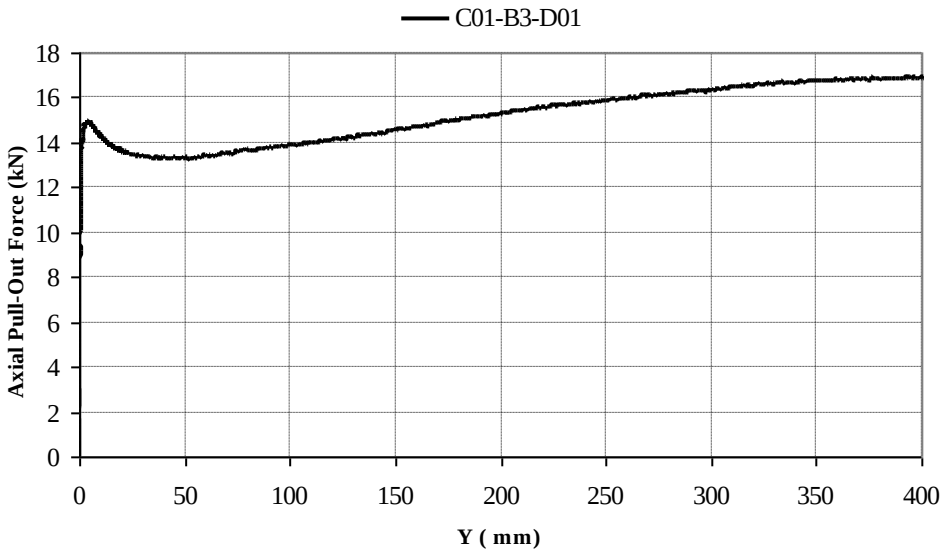

Figure A- 18: Response of buried cables in axial pullout test, Test C1-B3-D01

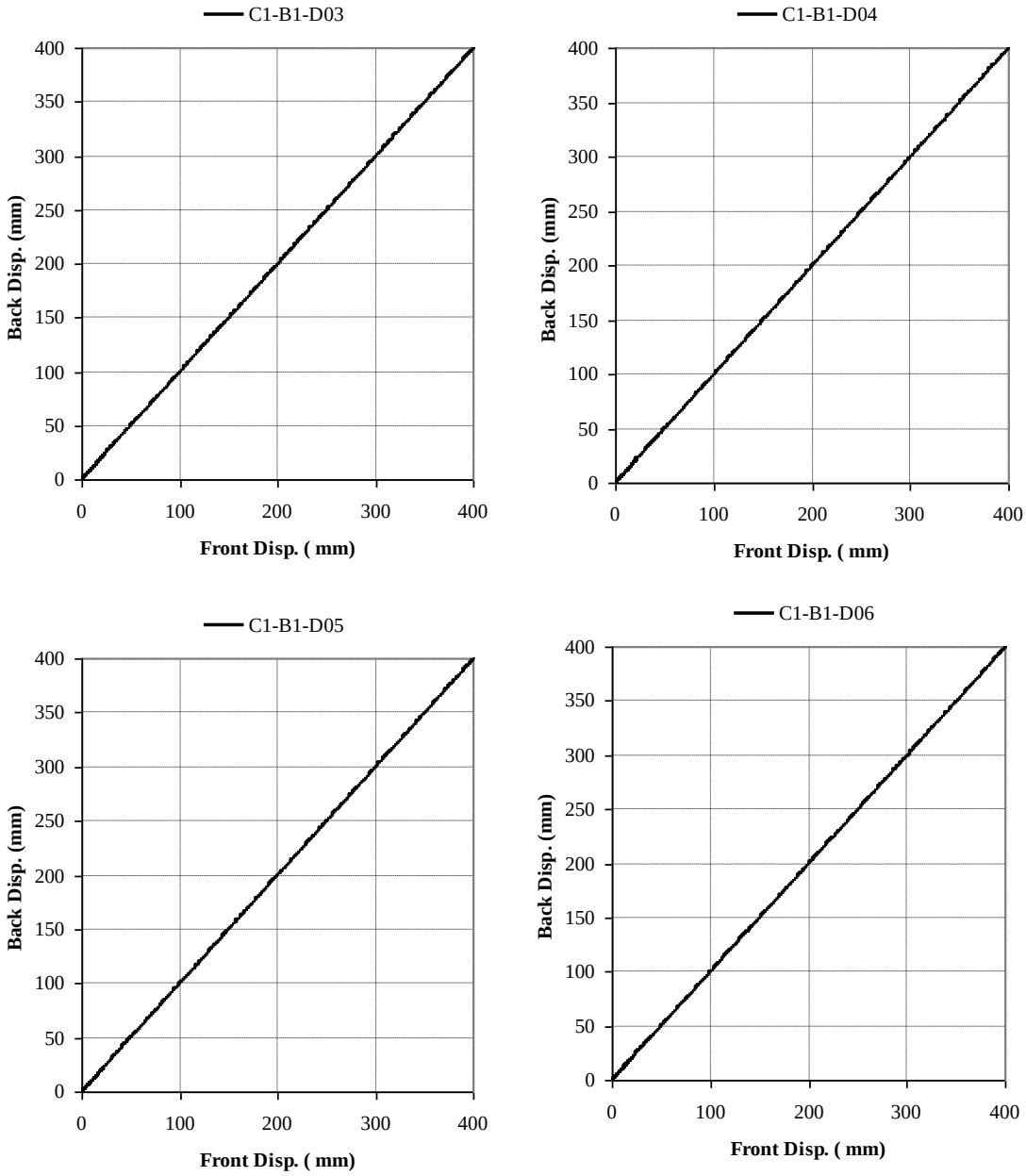

Figure A- 19: Displacement of the leading and tailing ends of buried cable with burial depth of 60 cm

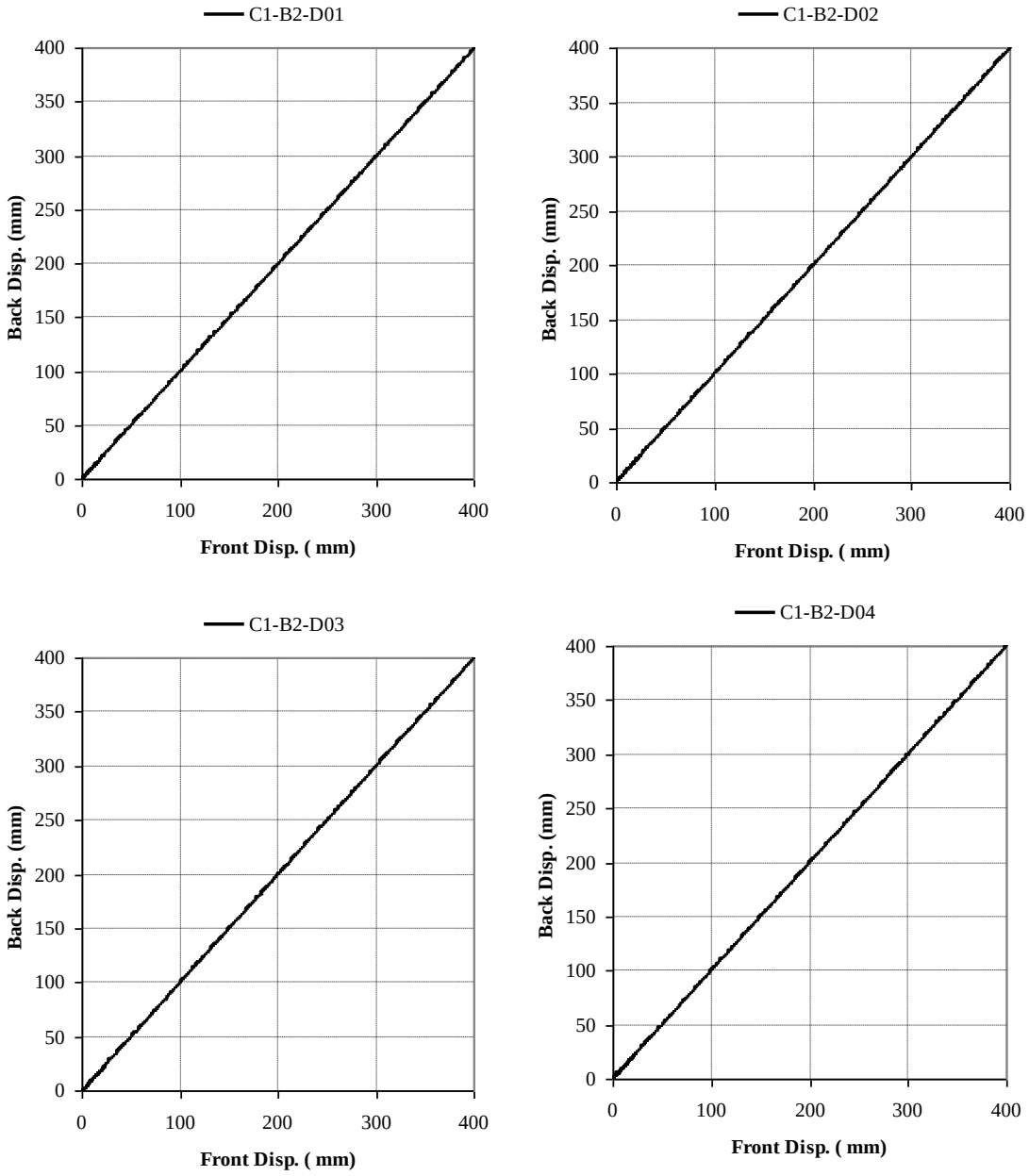

Figure A- 20: Displacement of the leading and tailing ends of buried cable with burial depth of 100 cm

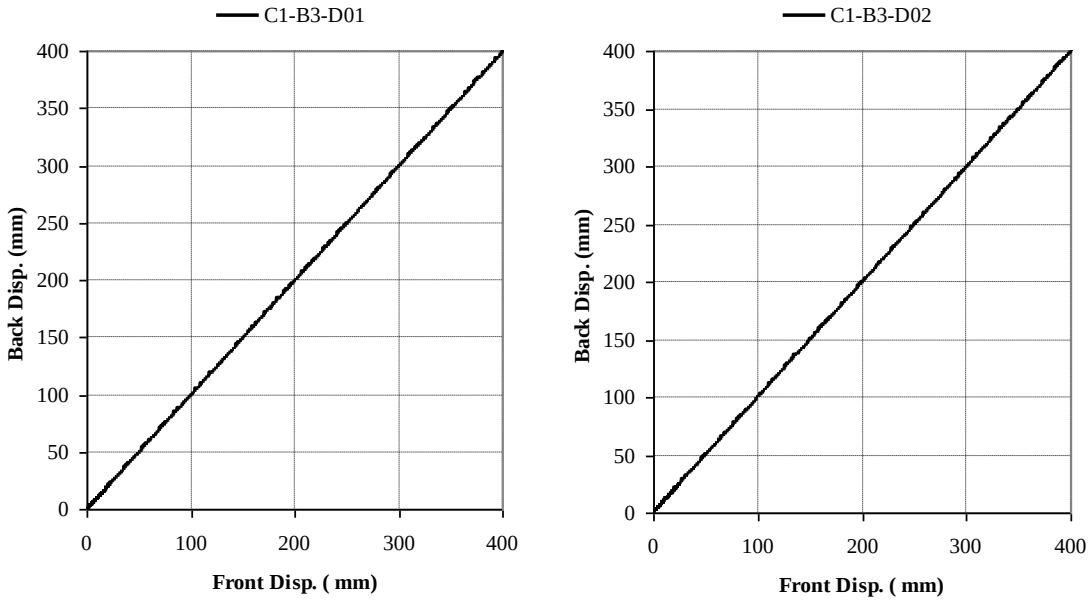

Figure A- 21: Displacement of the leading and tailing ends of buried cable with burial depth of 120 cm

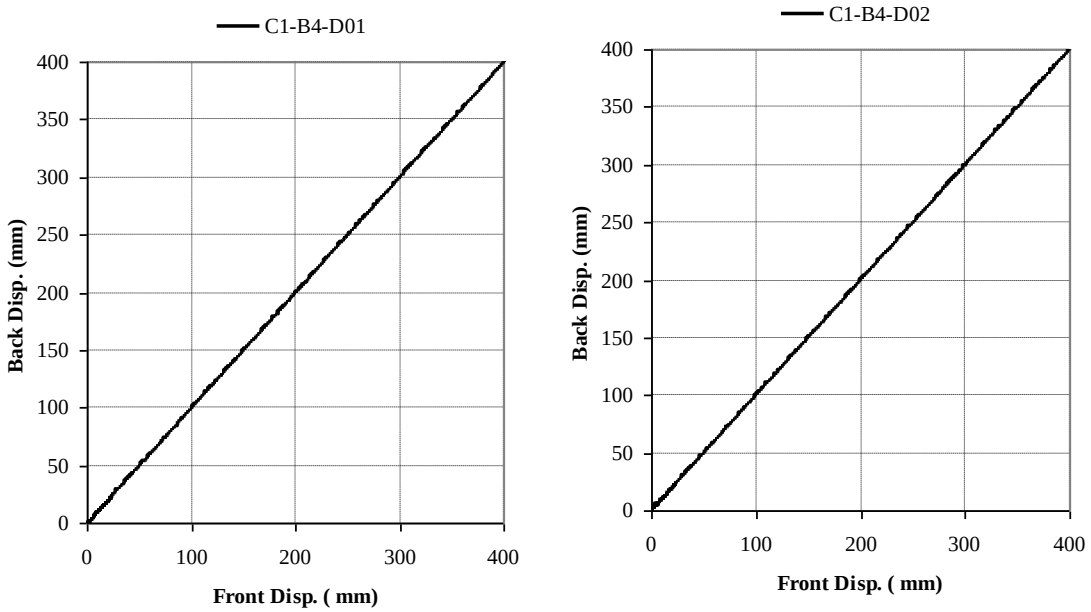

Figure A- 22: Displacement of the leading and tailing ends of buried cable with burial depth of 30 cm

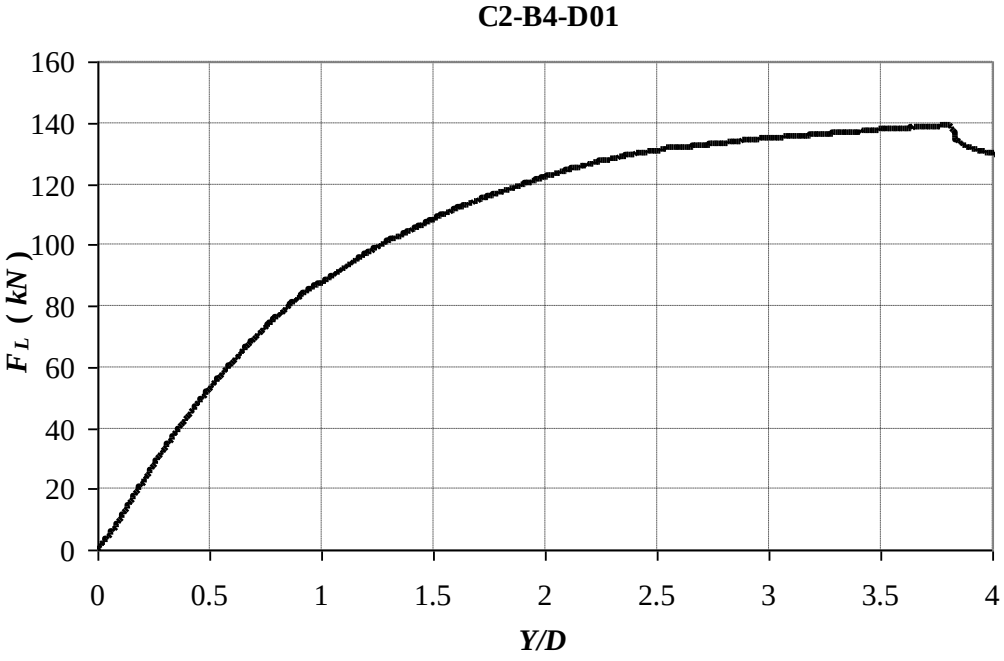

Figure A- 23: Response of buried cables in Lateral Pullout test, Test C2-B4-D01

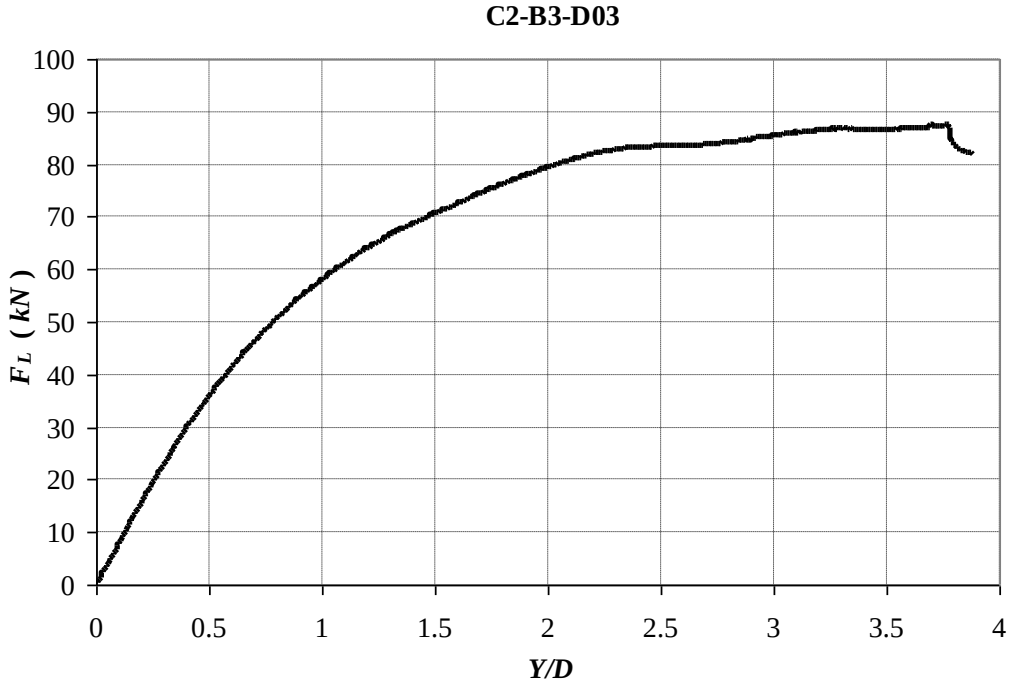

Figure A- 24: Response of buried cables in Lateral Pullout test, Test C2-B3-D03

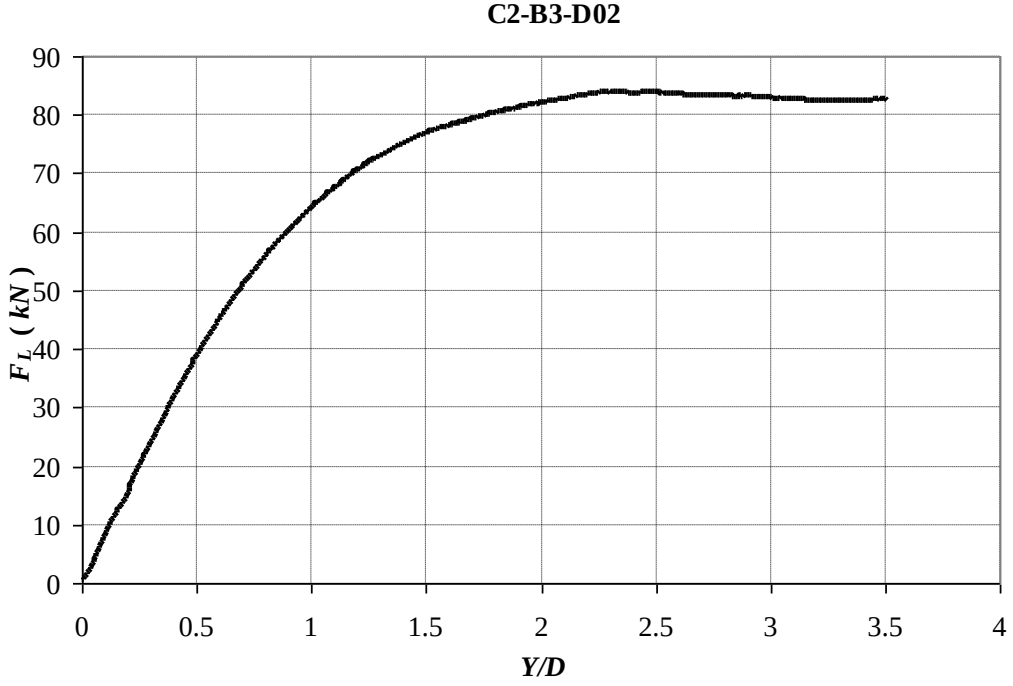

Figure A- 25: Response of buried cables in Lateral Pullout test, Test C2-B3-D02

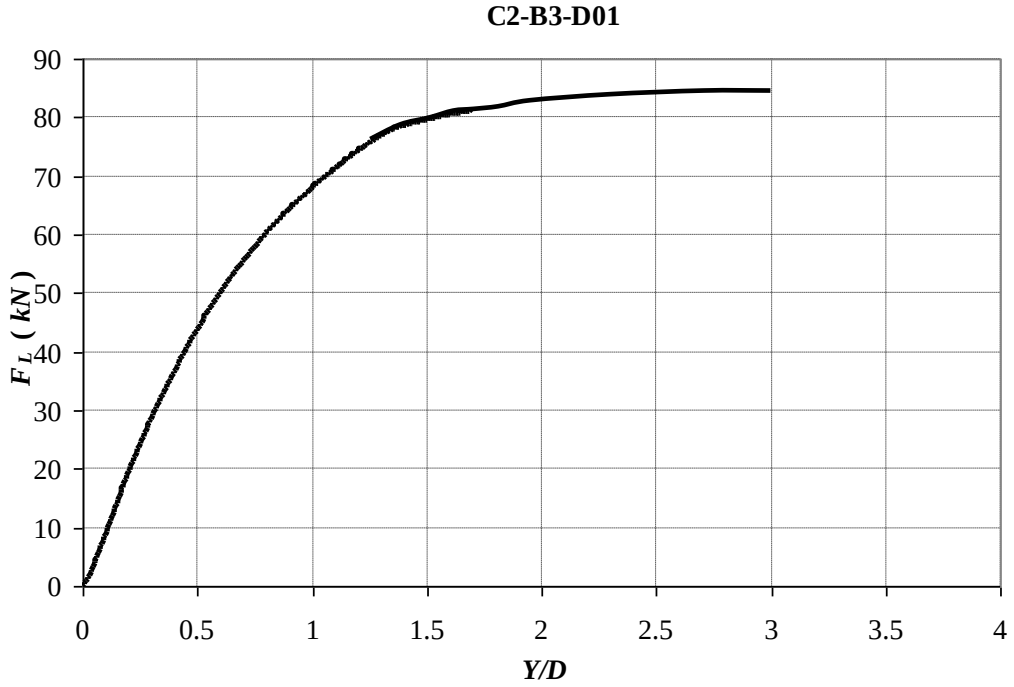

Figure A- 26: Response of buried cables in Lateral Pullout test, Test C2-B3-D01

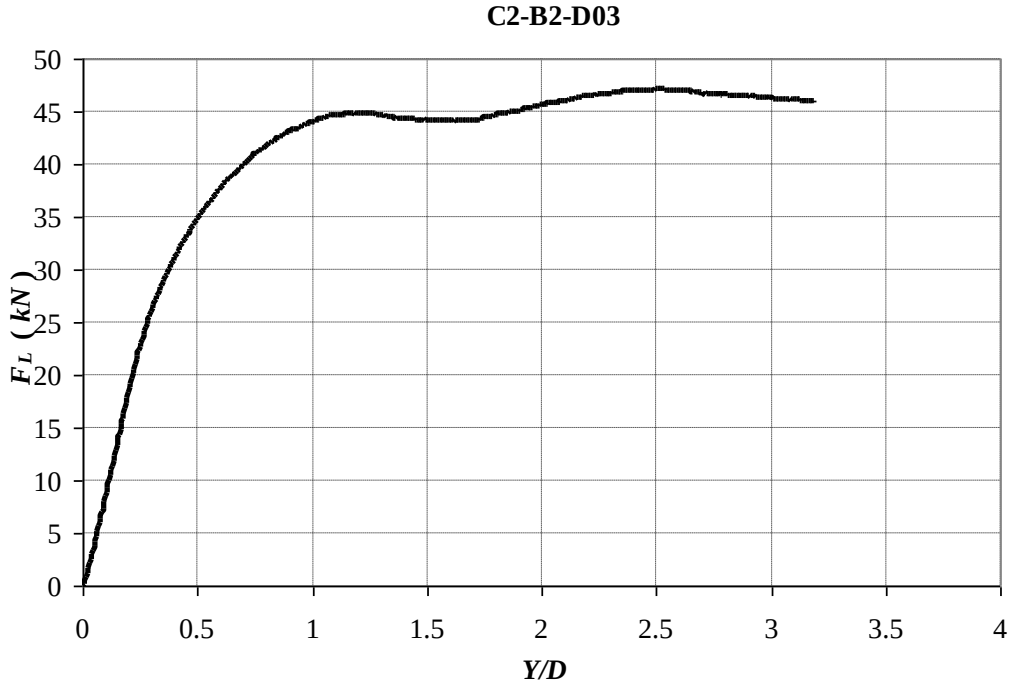

Figure A- 27: Response of buried cables in Lateral Pullout test, Test C2-B2-D03

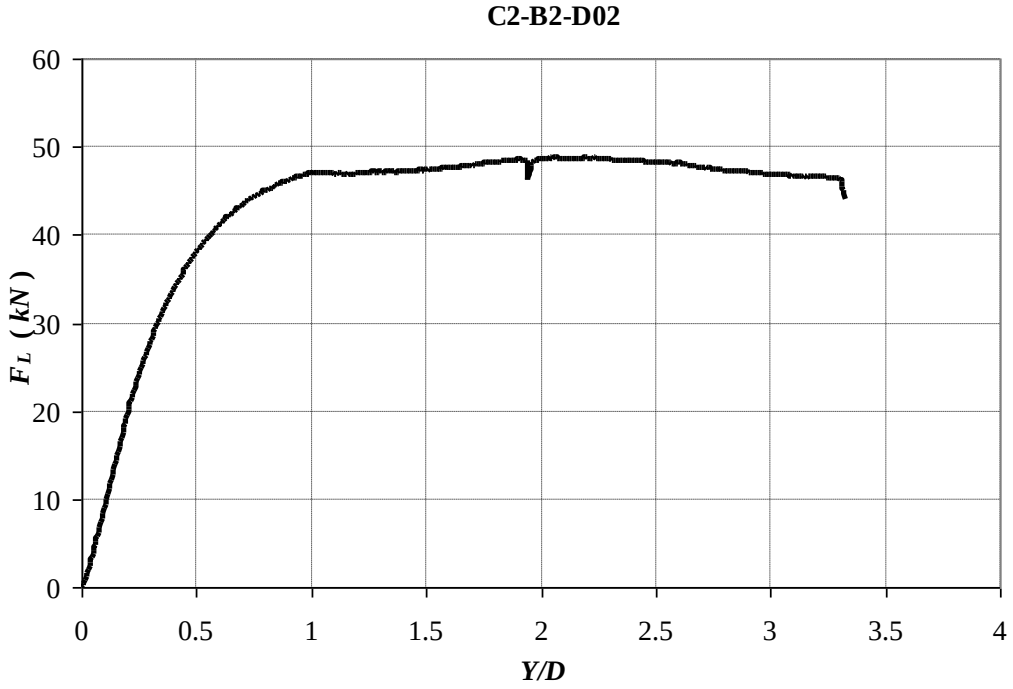

Figure A- 28: Response of buried cables in Lateral Pullout test, Test C2-B2-D02

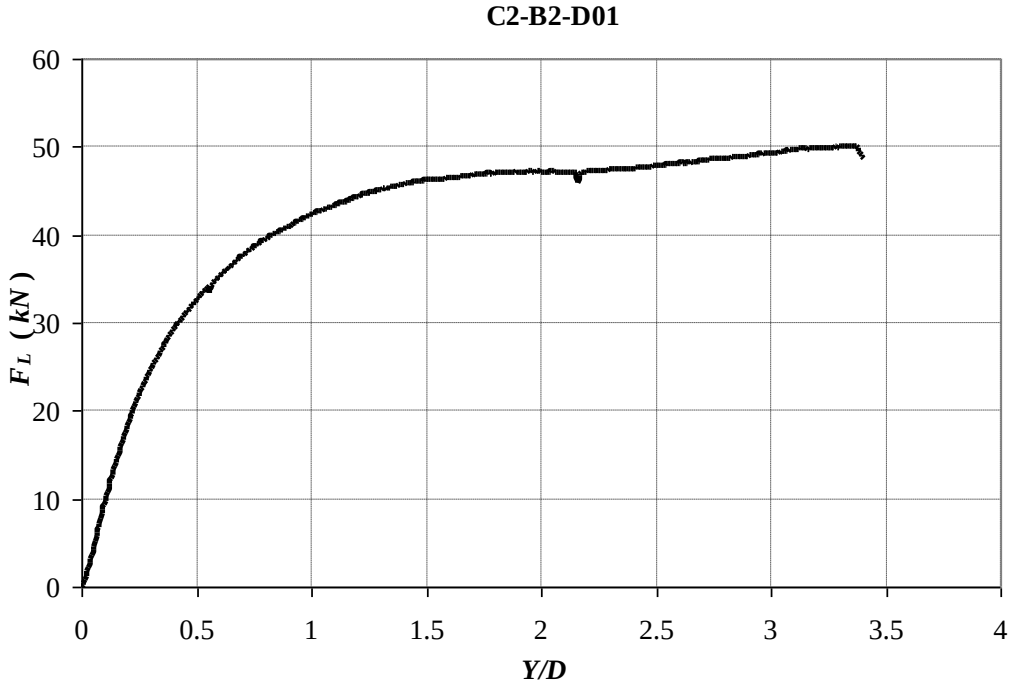

Figure A- 29: Response of buried cables in Lateral Pullout test, Test C2-B2-D01

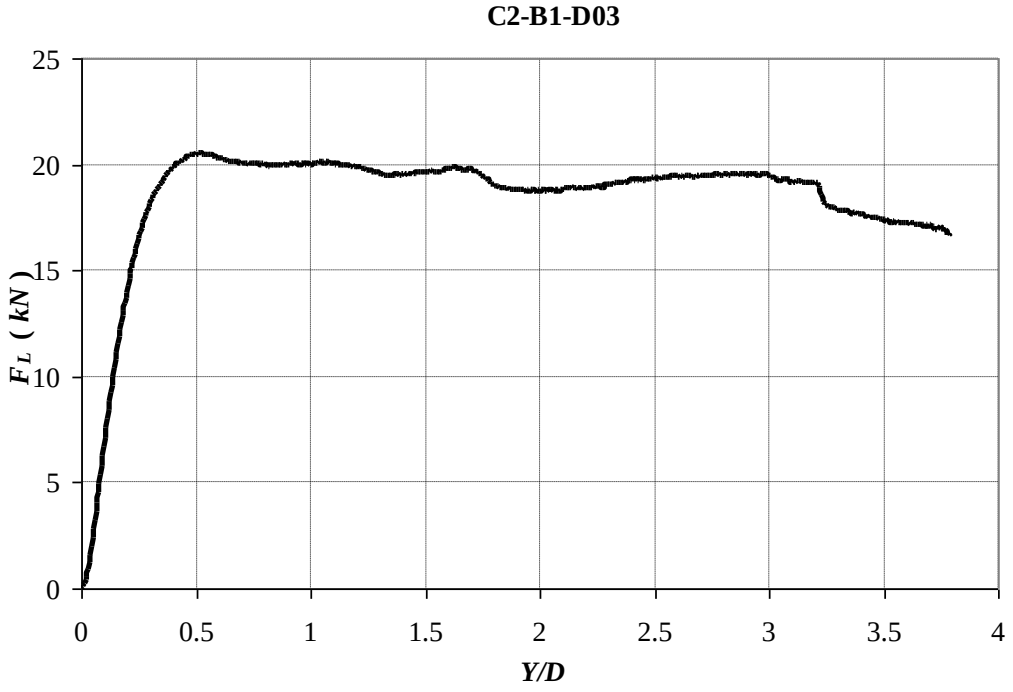

Figure A- 30: Response of buried cables in Lateral Pullout test, Test C2-B1-D03

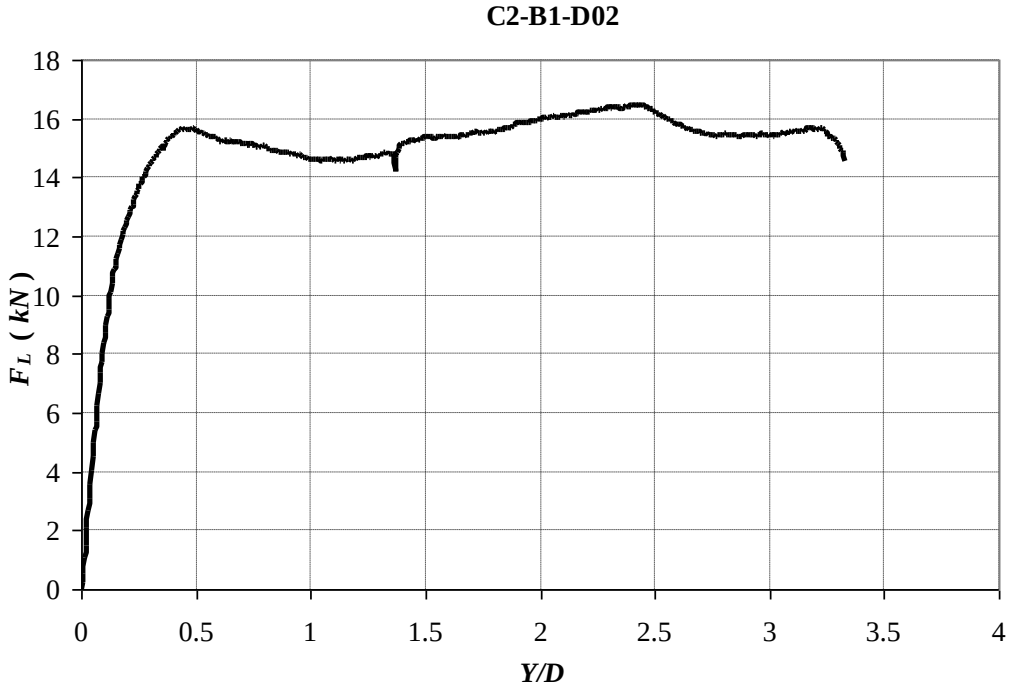

Figure A- 31: Response of buried cables in Lateral Pullout test, Test C2-B1-D02

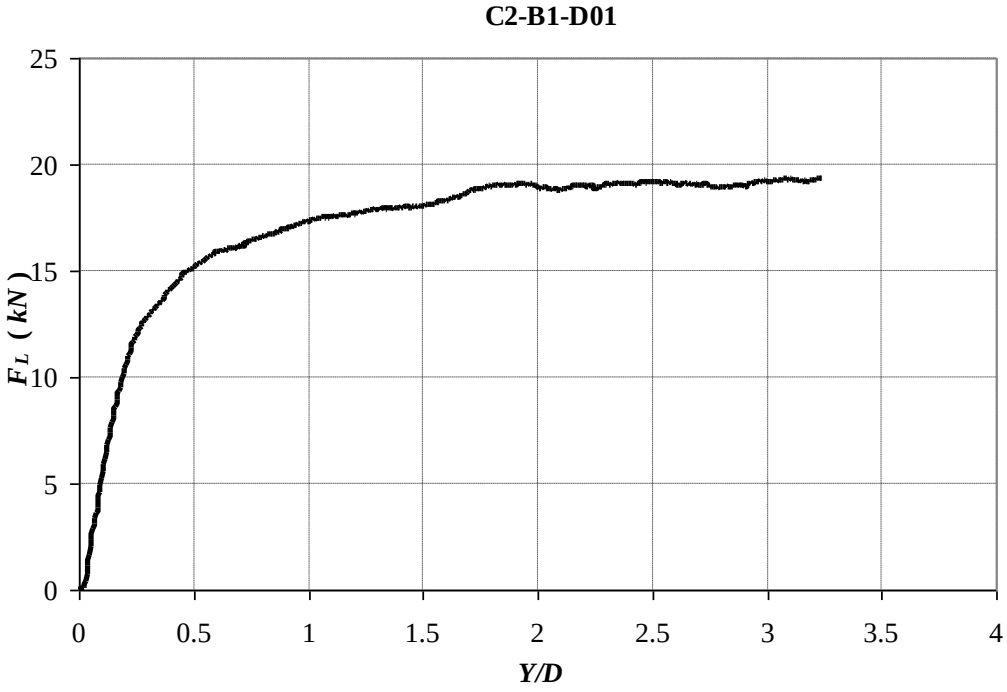

Figure A- 32: Response of buried cables in Lateral Pullout test, Test C2-B1-D01

Appendix B: Finite Element Description

B.1. Element Selection

A wide variety of three dimensional solid continuum elements are available in ABAQUS. Each element has a certain characteristics that must be selected according to a particular application. The three-dimensional elements in ABAQUS are classified by first-or second-order elements; tetrahedral/triangular prism (wedge)/hexahedral (brick) elements; full or reduced integration; regular/hybrid/incompatible mode formulations. The quadratic hexahedra with reduced integration (C3D20R) are a good selection to model the soil continuum. This element provides higher accuracy than its counterpart the element with linear interpolation function. However, the element performs poorer when subjected to sever distortion. The reduced integration of this element results in a more accurate results than its equivalent full integration element. Since the reduced integration element is susceptible to hourglassing, program provides an option to control hourglassing in this element. Unlike the tetrahedral elements the brick element is less stiff and a very fine meshing is not required. Furthermore, brick element has a better convergence rate than triangle element. However, brick element is sensitive to its initial element shape and it performs better when it is almost rectangular. Figure B- 1 shows the node ordering of the C3D20 element with 20 nodes and C3D8 element with 8 nodes.

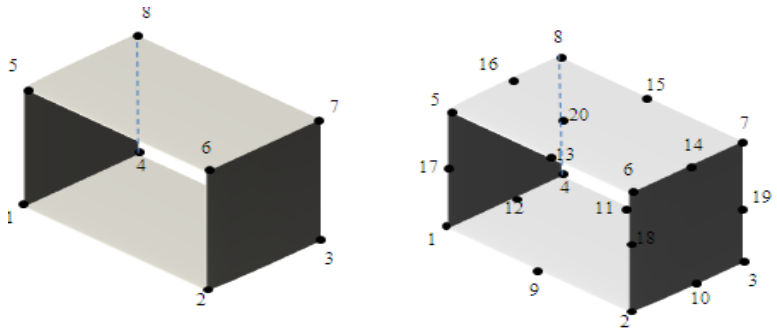

Figure B- 1: Node ordering of C3D20 and C3D8 elements

B.2. Material Selection

Before discussing the material models, it is worthwhile introducing some basic definitions, which are repeatedly will be mentioned during the following sections. Most of the failure criteria are formulated based on the stress invariants which are independent of the choice of coordinate systems. The invariant of the state of the stress tensor σ_{ij} can be expressed by forming the characteristics equation.

$$\sigma^3 - I_1\sigma^2 + I_2\sigma - I_3 = 0 \qquad \text{Eqn. B- 1}$$

where I_1, I_2, and I_3 are the invariant of the stress tensor σ_{ij}. The term I_1 is mostly used in the material formulation that their strength is dependent on the hydrostatic pressure. The stress tensor σ_{ij} is also expressed as a summation of the hydrostatic stress and deviatoric stress (S_{ij}). The hydrostatic pressure deviatoric stress can be imagined as stresses causing volumetric changes and shape change respectively.

$$\sigma_{ij} = S_{ij} + \frac{1}{3} I_1 \delta_{ij} \qquad \text{Eqn. B- 2}$$

The invariant of the deviatoric stress tensor also can be obtained by forming the characteristics equation.

$$S^3 - J_1 S^2 + J_2 S - J_3 = 0 \qquad \text{Eqn. B- 3}$$

where J_1, J_2, and J3 are the invariant of the deviatoric stress tensor S_{ij}. I_1 and J_2 are used to define octahedral stresses which are very important in the theory of plasticity. Octahedral stresses are stresses acting on the octahedral plane having equal angles with each of the principle stresses. Shear stress on this plane is octahedral shear stress (τ_{oct}) ,

normal stress on this plane is octahedral normal stress (σ_{oct}), and the direction of the octahedral shear is defined by the similarity angle (θ). Their relation with I_1, J_2 and J_3 can be expressed by the following relation:

$$\sigma_{oct} = \frac{1}{3} I_1 \qquad \text{Eqn. B- 4}$$

$$\tau_{oct} = \sqrt{\frac{2}{3} J_2} \qquad \text{Eqn. B- 5}$$

$$\cos(3\theta) = \frac{3\sqrt{3}}{2} \frac{J_3}{J_2^{3/2}} \qquad \text{Eqn. B- 6}$$

A geometric interpolation of stress invariants can be better presented with reference to Figure B- 2.If vector *op* represents the state of stress in the principle-stress space, *on* vector corresponds to the octahedral normal stress (σ_{oct}) and *np* vector corresponds to octahedral shear stress (τ_{oct}). Since the decomposition of the state of stress in the octahedral plane always corresponds to the shear part of the state of stress the octahedral plane is therefore called the deviatoric plane. A geometric interpolation of the similarity angle (θ) can be best understood in the deviatoric plane by projecting the principle axes onto this plane. The similarity angle is interpreted as the angle measured from the positive principle axis to deviatoric stress vector *np*.

The stress state space is bounded by the three dimensional failure surfaces. The shape of any failure surface can be described by two plane shape, commonly referred as the meridian and cross section plane. The meridian plane is formed by intersecting the failure surface with the plane consisting of the normal to deviatoric plane (hydrostatic axis) with constant similarity angle (θ). Therefore different such plane can be found ranging from $\theta=0$ to 60. The plane corresponding to $\theta=0$ is called the tensile meridian plane and the plane corresponding to $\theta=60$ is called the compressive meridian plane. In addition, the plane corresponds to $\theta=30$ is often called the shear meridian. On the other hand the cross

section plane is formed by intersecting the failure surface with the deviatoric plane. For more description, the reader is referred to Chen (1982).

B.2.1. Mohr-Coulomb Plasticity

The Mohr-Coulomb failure criterion is one of the oldest failure criterion even older than Tresca and Von-Mises failure criteria. It is widely used in geotechnical problems since the strengthening of the soil due to the hydrostatic pressure is considered in the model.

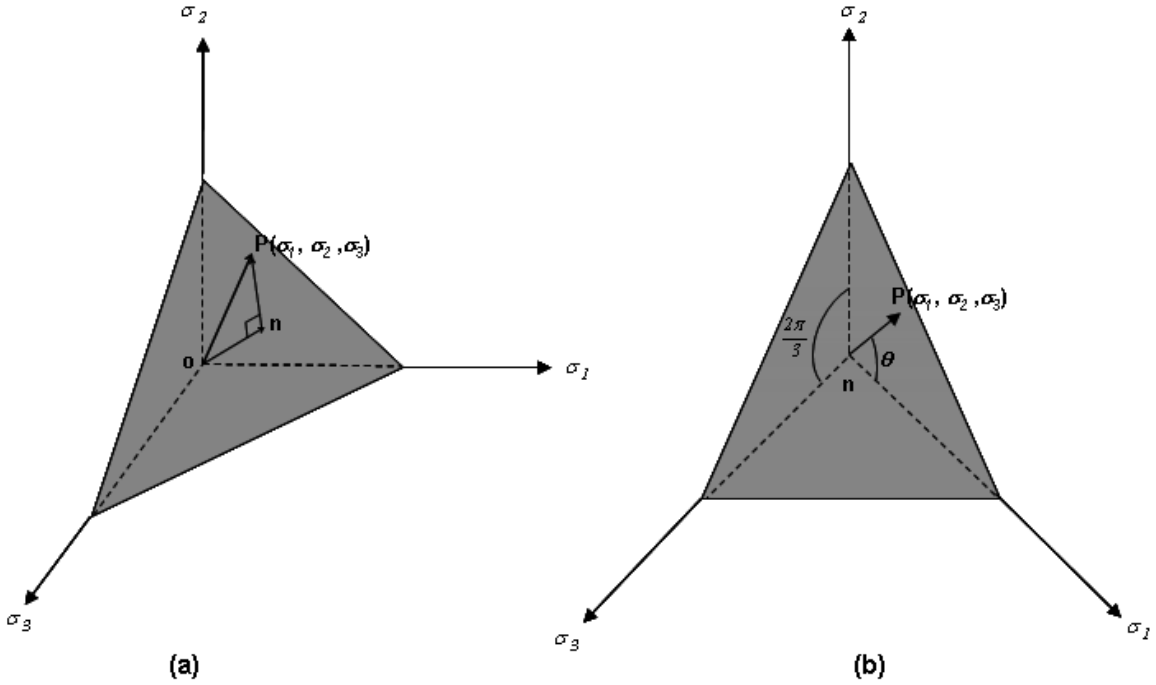

Figure B- 2: (a) Decomposition of the state of stress, (b) Deviatoric plane

The classic Mohr-Coulomb assumes a straight line relating the shear stress to the normal stress.

$$|\tau| = C + \sigma \tan(\phi) \qquad \text{Eqn. B- 7}$$

Where C and ϕ denotes the cohesion and the internal friction angle respectively. It assumes that failure occurs when the largest Mohr's circle is just tangent to the Mohr-Coulomb envelop failure criterion. Therefore, the effect of the intermediate stress is ignored. If the maximum principal and minimum principle stresses happen in the (1) and (3) directions respectively ($\sigma_1 \succ \sigma_2 \succ \sigma_3$). The Mohr-Coulomb failure can be rearranged as the following equation.

$$\frac{1}{2}(\sigma_1 - \sigma_3) + \frac{1}{2}(\sigma_1 + \sigma_3)\sin(\phi) + c\cos(\phi) = 0 \qquad \text{Eqn. B- 8}$$

Substituting the principle stresses with their corresponding stress invariant (I_1, J_2, θ) the Mohr-Coulomb leads to the stress invariant form of the Coulomb criterion.

$$F = \frac{1}{3} I_1 \sin(\phi) + \sqrt{J_2}\,\sin(\theta + \frac{\pi}{3}) + \sqrt{\frac{J_2}{3}}\cos(\theta + \frac{\pi}{3})\sin(\phi) - c\cos(\phi) = 0 \qquad \text{Eqn. B- 9}$$

ABAQUS uses the same formulation for the Mohr-Coulomb failure criterion. For the simplicity, it introduces notation p, q, and R_{mc} which is defined as

$$R_{mc}(\theta,\phi) = \frac{1}{\sqrt{3}\cos(\phi)}\sin(\theta + \frac{\pi}{3}) + \frac{1}{3}\cos(\theta + \frac{\pi}{3})\tan(\phi)\ ,\ p = \frac{I_1}{3}\text{, and } q = \sqrt{3J_2} \qquad \text{Eqn. B- 10}$$

The Mohr-Coulomb criterion can be written as

$$F = R_{mc}(\theta,\phi)q - p\tan(\phi) - c = 0 \qquad \text{Eqn. B- 11}$$

Mohr Coulomb yield surface is the irregular hexagonal shape. Figure B- 3 represents the shape of the Mohr-Coulomb yield surface in meridional and deviatoric planes. Mohr-Coulomb plasticity is only available in ABAQUS/Standard.

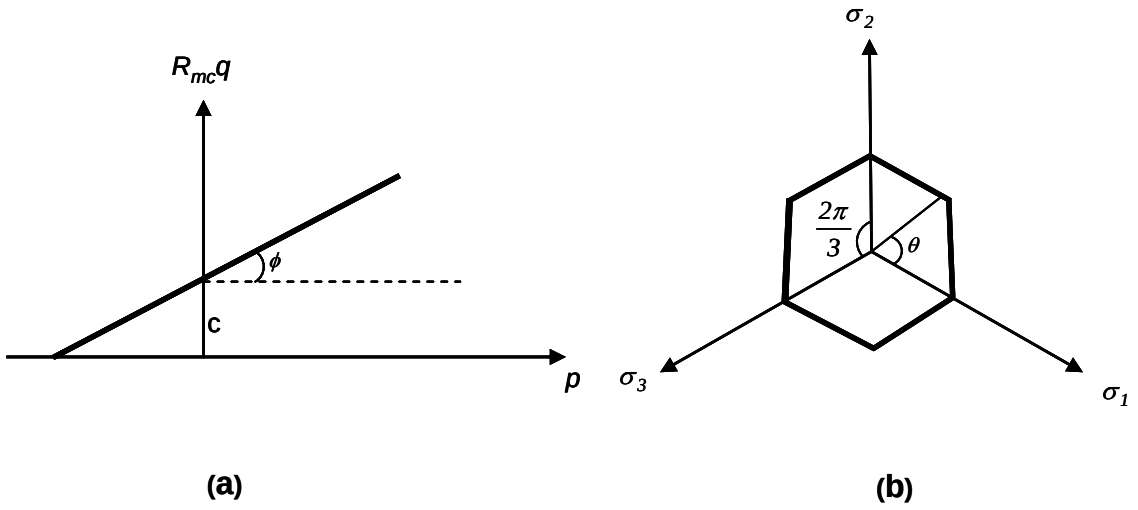

Figure B- 3: Presentation of Mohr-Coulomb yield surface in (a) meridional plane and (b) deviatoric plane (adapted from ABAQUS)`

B.2.2. Drucker-Prager Plasticity

Von Misses yield criterion has a smooth yield surface; however, it is pressure-independent model which is mainly developed for metal plasticity. On the other hand Mohr coulomb yield criterion is pressure-dependent model, however, the hexagonal yield surface causes the numerical difficulties at its corner. Druker-Prager model can be regarded as a model that has a smooth yield surface like Von-Misses model and is suitable for pressure-dependent martial like soil and concrete (Chen (1990)). The Drucker-Prager yield surface assumes the following equation

$$F = \alpha I_1 + \sqrt{J_2} - k = 0 \qquad \text{Eqn. B- 12}$$

where α and k are Drucker-Prager constants that they control the size of the surface. Drucker-Prager yield surface can be reduced to Von-Misses yield criterion or J_2 plasticity by neglecting the pressure-dependent term (I_1) or assuming α as zero. Furthermore,

Drucker-Prager model can approximate Mohr-Coulomb failure surface by adjusting Drucker-Prager constants (α and k) to Mohr-Coulomb constant parameters (C and ϕ).

ABAQUS Drucker-Prager model can have three different forms in the meridional plane: a linear, hyperbolic, or exponent form. Linear form of Drucker-Prager model depends on the third invariant of the deviatoric stress (J_3). The linear yield surface of Drucker-Prager model can be defined by first introducing two auxiliary parameters (r and t) which is defined as:

$$r = (\frac{27}{2} J_3)^{1/3} \qquad \text{Eqn. B- 13}$$

$$t = \frac{q}{2}(1 + \frac{1}{k} - (1 - \frac{1}{k})(\frac{r}{q})^3) \qquad \text{Eqn. B- 14}$$

where k is the constant that correlates the yield surface to the third deviatoric stress invariant. In order to ensure the convexity, k value assumes the range $0.778 \le k \le 1.0$. The upper bound of k corresponds to a condition that the yield surface is independent of third deviatoric stress invariant, i.e., a classical Drucker-Prager model with a circular shape in the deviatoric plane. Figure B- 4 shows the effect of the k parameter on the shape of the yield surface in the deviatoric plane.

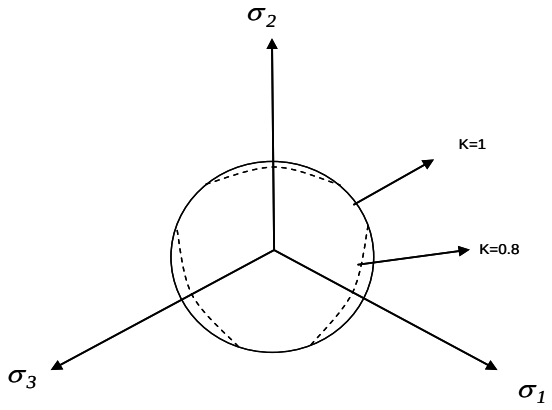

Figure B- 4: Drucker-Prager model in the deviatoric planes for different k value (adapted from ABAQUS)

The linear Drucker-Prager criterion assumes a linear dependence between t and p as follows:

$$F = t - p\tan(\beta) - d = 0 \qquad \text{Eqn. B- 15}$$

where β and d are the soil's friction angle and cohesion in the p-t plane as shown in Figure B- 5.

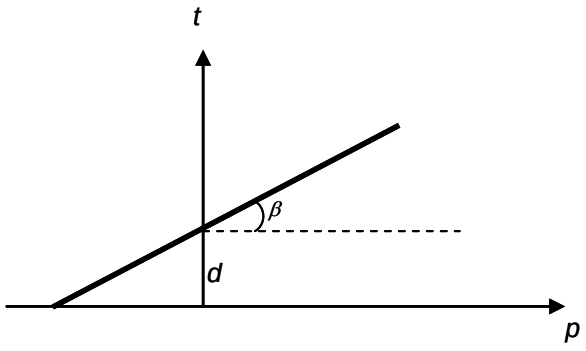

Figure B- 5: Linear Drucker-Prager model (adopted from ABAQUS)

B.2.3. Drucker-Prager Plasticity Model With Cap(CAP Model)

ABAQUS offers Drucker-Prager model with cap which is called CAP plasticity model hereafter. CAP yield surface has a linear Drucker-Prager form (F_s) in the t-p plane which is bounded by the elliptical cap function (F_c). A smooth transition function (F_t) between those surfaces is provided to facilitate the numerical implementation. CAP plasticity model provides the inelastic volume decrease due to compaction and inelastic volume increase due to dilation depending on where the material yields on the failure surface. Figure B- 6 illustrate the shape of the CAP plasticity in *t-p* plane. The trace of the CAP model in the deviatoric plane is the same shape as Drucker-Prager model as depicted in Figure B- 4. The linear part of the CAP model, which is the Drucker-Prager shear failure surface, is written as

$$F_s = t - p\tan\beta - d = 0$$ Eqn. B- 16

The cap yield surface is written as

$$F_c = \sqrt{(p - p_a)^2 + (\frac{Rt}{1 + \alpha - \frac{\alpha}{\cos\beta}})^2} - R(d + P_a \tan\beta) = 0$$ Eqn. B- 17

Where parameter R (between .0001 and 1000.0) controls the shape of the cap and parameter α (between .01 and .05) defines the smooth transition between the shear failure surface and cap yield surface. P_a is the evolution parameter expressed as a function of P_b.

$$p_a = \frac{p_b - Rd}{1 + R\tan\beta}$$ Eqn. B- 18

Pb is a hydrostatic compression yield stress that it is used to obtain its evolution as a function of the volumetric plastic strain (ε_{vol}^{pl}). The transition yield surface is written as

$$F_t = \sqrt{(p - p_a)^2 + (t - (1 - \frac{\alpha}{\cos\beta})(d + P_a \tan\beta))^2} - \alpha(d + P_a \tan\beta) = 0$$ Eqn. B- 19

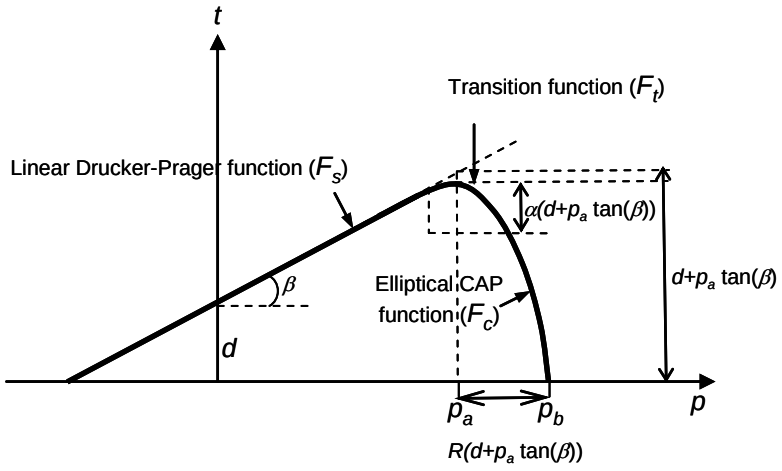

Figure B- 6: CAP plasticity model as adapted from ABAQUS

In sum, friction angle (β) and cohesion (d) is needed to define the Drucker-Prager shear failure surface, cap eccentricity parameter (R) and P_b is required to define the CAP failure surface, and the parameter (α) is needed to define the transition surface. The Drucker-Prager model is available in both ABAQUS/Standard and ABAQUS/Explicit.

B.3. Flow Rule and Hardening Rule

When the state of the stress reaches to the yield surface the plastic strain (ε^p) will be developed. For the sake of mathematical simplicity, a flow rule is introduced which related the plastic strain increments ($d\varepsilon^p$) to the current state of stress. The flow rule can be easily established by defining a plastic potential function G in the form:

$$d\varepsilon^p = \lambda \frac{\partial G}{\partial \sigma} \qquad \text{Eqn. B- 20}$$

The plastic potential function can take a form of a yield surface which is called an associated flow rule or it can take a completely different form which is named as a non-associated flow rule. During a plastic flow the yield surface can be modified. The hardening rule dictates how the yield surface is changed. The most basic types of hardening rule are isotropic hardening and kinematic hardening. In the isotropic hardening rule, the yield surface is assumed to expand uniformly as plastic straining occurs. However, in the kinematic hardening rule, the yield surface translates. Figure B-7 illustrates the isotropic hardening rule in two dimensions besides the equivalent one dimensional isotropic hardening material. Figure B- 8 shows the kinematic hardening rule in two dimensions besides the one dimensional kinematic hardening.

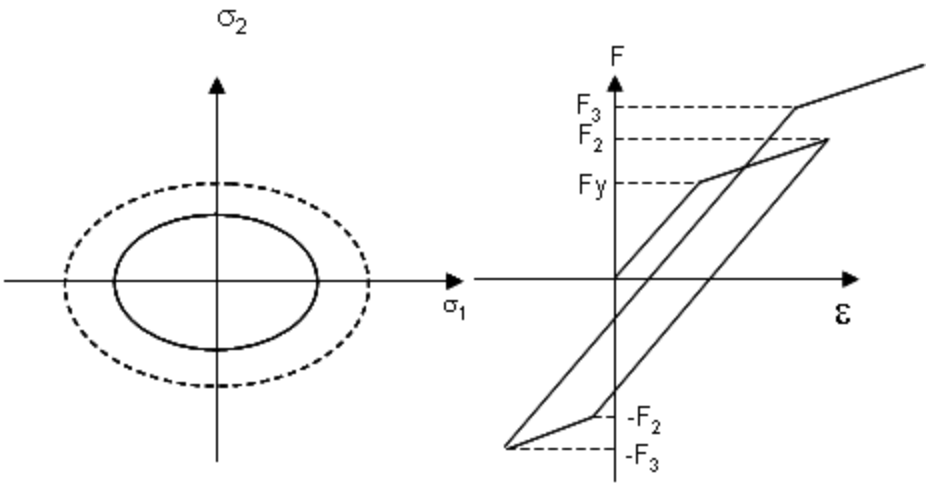

Figure B- 7: Isotropic hardening in the two dimension stress plane and one dimension stress-strain behaviour

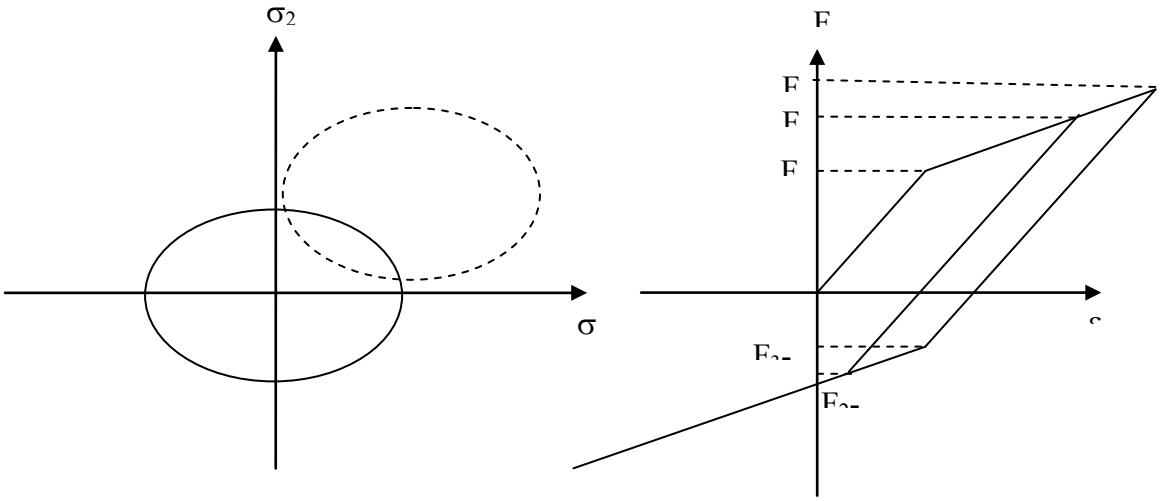

Figure B- 8: Kinematic hardening in the two dimension stress plane and one dimension stress-strain behavior

B.3.1. Plastic Flow in ABAQUS Mohr-Coulomb Yield Criterion

ABAQUS adopted the plastic potential function (G) as proposed by Menetrey and Willam (1995).

$$G = \sqrt{(\varepsilon C_0 \tan(\psi))^2 + (R_{mw}(\theta, e)q)^2} - p\tan(\psi) \qquad \text{Eqn. B- 21}$$

Where R_{mw} is defined as a function of the similarity angle (θ) ,deviatoric eccentricity (e), ,friction angle (ϕ), and R_{mc}.

$$R_{mw}(\theta, e) = \frac{4(1-e^2)\cos^2\theta + (2e-1)^2}{2(1-e^2)\cos\theta + (2e-1)\sqrt{4(1-e^2)\cos^2\theta + 5e^2 - 4e}} R_{mc}(\frac{\pi}{3}, \phi) \qquad \text{Eqn. B- 22}$$

Menetrey potential function has a hyperbolic shape in the meridional plane. At high confining pressure the potential function forms a straight line and at low hydrostatic pressure it curves. The rate at which the hyperbolic function approaches to the straight line controls by the parameter ε which is called meridional eccentricity. When ε is close to zero the flow potential in the meridional stress tends to form a straight line as shown in Figure B- 9.

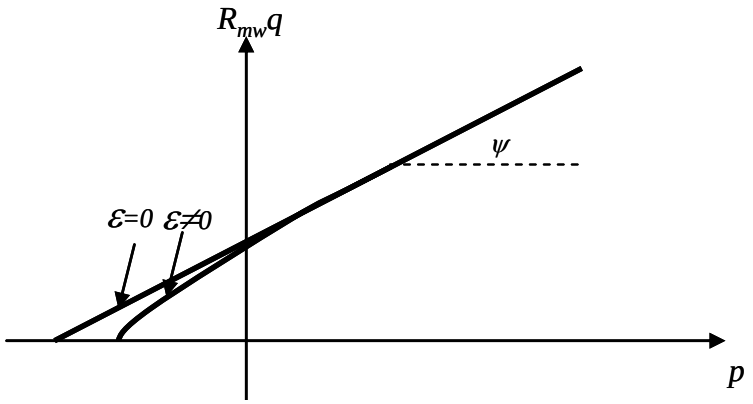

Figure B- 9: The effect of the ε on the shape of the Menetrey potential function in the meridional plane

Menetrey potential function has a smooth elliptic function in the deviatoric stress plane. Its shape in controlled by the deviatoric eccentricity (e) that describes the "out-of-roundness". The condition of convexity and smoothness requires that $0.5<e<1$. The upper bound value of $e=1$ corresponds to Von-Mises yield surface. As mentioned before, ABAQUS assumes two separate yield function and potential function for Mohr-Coulomb plasticity which means the non-associated flow rule. Eccentricity parameter (e) can be found as a function of friction angle (ϕ) so that the yield surface and the potential flow function matches each other for a specific similarity angle. For instance, if the user wants that the meridional compression and meridional tension of Mohr-Coulomb failure criterion matches those for Drucker-Prager failure criterion the following relationship between (e) and (ϕ) is necessary.

$$e = \frac{3-\sin\phi}{3+\sin\phi} \qquad \text{Eqn. B- 23}$$

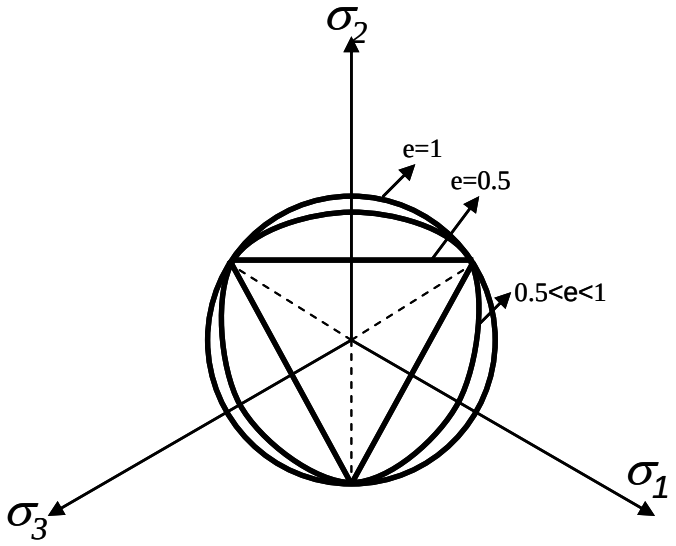

Figure B- 10: The effect of the deviatoric eccentricity(e) on the plastic potential function in the deviatoric plane

B.3.2. Plastic Flow in ABAQUS Drucker-Prager Yield Criterion

Plastic flow (G) for linear ABAQUS Drucker-Prager model is defined in *p*-*t* plane as:

$$G = t - p\tan(\psi) \qquad \text{Eqn. B- 24}$$

where ψ represents a dilation angle. As shown previously in Figure B- 5, the Drucker-Prager failure criterion is a straight line forming an angle β with the hydrostatic pressure (p) axis. Flow potential function also assumes a linear form in the *t*-*p* plane but with an angle ψ with respect to hydrostatic pressure as illustrates in the Figure B- 11. Furthermore, the shape of flow potential function in the deviatoric plane is the same as the shape of the yield surface. That means that the plastic strain rate is normal to the yield surface in the deviatoric plane while in general is not perpendicular to the yield surface except for the case of associated flow rule as shown in Figure B- 11-a.

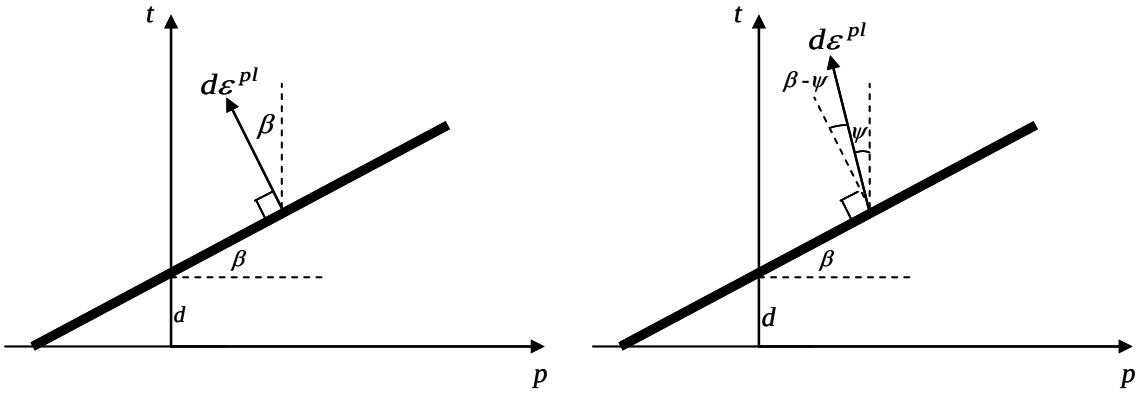

a) associate flow rule **b) non-associate flow rule**

Figure B- 11: Associated and Non-associated flow rule for linear Drucker-Prager Model

B.3.3. Plastic Flow in ABAQUS CAP Plasticity Model

Plastic potential function for CAP plasticity model is formed by two separate functions: one on a cap surface and the other on a shear and transition surface. The potential function on a cap surface is the same form of the yield surface, implying associated flow rule on a cap part as expressed by G_c potential function.

$$G_c = \sqrt{(p - p_a)^2 + \left(\frac{Rt}{1 + \alpha - \frac{\alpha}{\cos\beta}}\right)^2} \qquad \text{Eqn. B- 25}$$

The potential function on the shear and transition region is expressed by G_s function as expressed by the following equation.

$$G_s = \sqrt{((p - p_a)\tan\beta)^2 + \left(\frac{t}{1 + \alpha - \frac{\alpha}{\cos\beta}}\right)^2} \qquad \textbf{Eqn. B- 26}$$

The potential function takes a form different than yield function on those region, implying non-associated flow rule. Those two potential functions create a smooth and continuous surface. Figure B- 12 illustrates the plastic potential surface for CAP plasticity model in *t*-*p* plane.

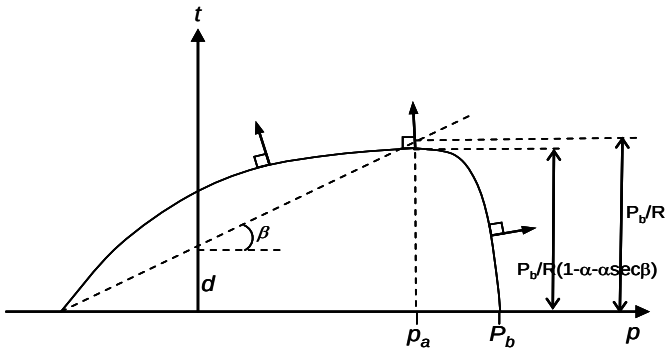

Figure B- 12: Plastic potential function for CAP model, adapted from ABAQUS

B.4. Calibration of Plasticity Models

ABAQUS offers three material model that they are able to reproduce the material behaviour of the granular material. The previous section elaborately discusses the mathematical formulation for Mohr-Coulomb, Drucker-Prager, and CAP plasticity models. The following table is summarized the input parameters for each plasticity model.

B.4.1. Calibration of Mohr-Coulomb Plasticity Model

Mohr-Coulomb plasticity is normally calibrated by using the test results from the element testing using direct shear apparatus. Typical results of the direct shear testing (DST) include mobilized soil shear strength (τ)-horizontal displacement (δ_h) curve at different level of vertical force as shown in Figure B- 13-a for a typical compacted granular material. Corresponding to the horizontal displacement, a friction angle and cohesion can be determined by mapping mobilized shear strength and associated vertical stress into τ-σ plane as shown in Figure B- 13-b for horizontal displacement A and B. This mapping can be performed for each level of horizontal box movement. Consequently, the friction and cohesion curve can be defined as a function of horizontal displacement. Popescu et al (1999) used this method to define a hardening/softening rule for sand model in ABAQUS standard. In order to define the hardening rule in ABAQUS Mohr-Coulomb model, the relationship between plastic strain magnitude and *C* is required. However the DST results give a soil strength parameter as a function of horizontal box displacement. To relate the soil strength parameter to plastic strain magnitude, a numerical simulation of DST are employed to express the dependency of soil shear strength parameter as a function of plastic strain magnitude(γ) which is defined as

$$\gamma = \sqrt{\frac{2}{3}\varepsilon_{ij}^{pl}\varepsilon_{ij}^{pl}} \qquad \text{Eqn. B- 27}$$

Based on the good match between the DST results and numerical simulation, the soil strength parameters are expressed as a function of plastic strain.

Material Model Name	Yield surface parameters	Potential surface parameters	Hardening Parameters
Mohr-Coulomb Model	Friction angle (ϕ), Cohesion (c)	Deviatoric Eccentricity (e) Meridional Eccentricity (ε) Dilation angle (ψ)	$c = f(\bar{\varepsilon}^{pl})$ $\bar{\varepsilon}^{pl} = \int_0^t d\bar{\varepsilon}^{pl}$
Modified Drucker-Prager Model	Friction angle (β), Cohesion (d) K value	K value Dilation angle (ψ)	$d = f(\bar{\varepsilon}^{pl})$ $\bar{\varepsilon}^{pl} = \int_0^t d\bar{\varepsilon}^{pl}$
CAP Plasticity Model	Friction angle (β), Cohesion (d) K value Transition parameter (α) Cap eccentricity parameter (R) Evolution Parameter (P_b)	K value Transition parameter (α) Cap eccentricity parameter (R) Evolution Parameter (P_b)	$P_b = f(\varepsilon_{vol}^{pl})$

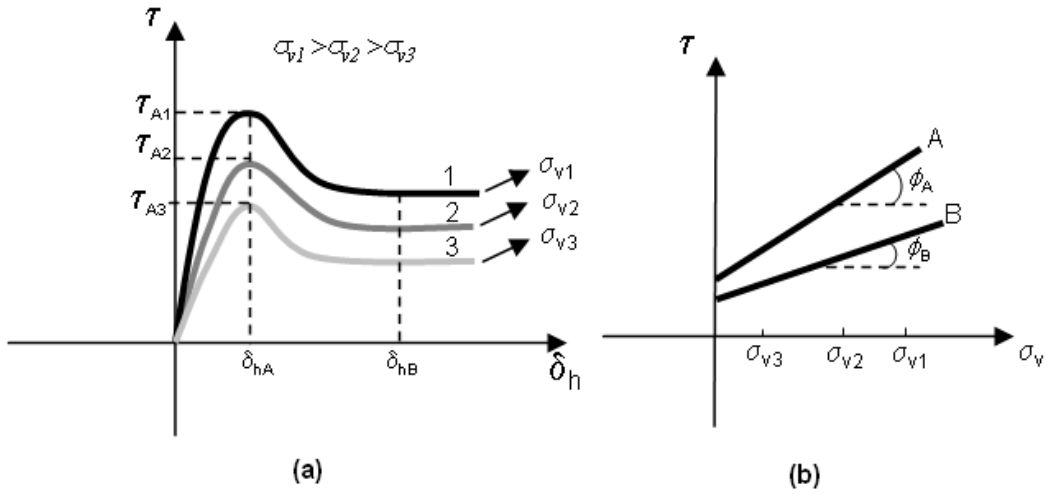

Figure B- 13: (a) Typical direct shear testing results for compacted granular material (b) Mapping mobilized shear strength and corresponding vertical stress to τ-σ plane

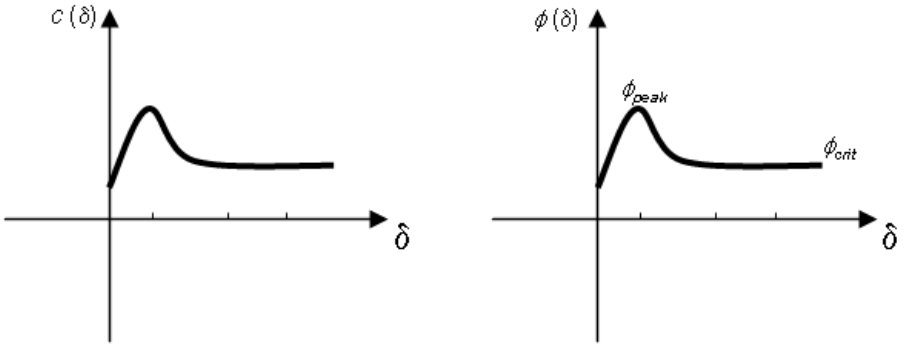

Figure B- 14: Mobilization of soil shear strength as a function of horizontal displacement

Dilation angle can be obtained through Rowe stress- dilatancy theory or Bolton empirical method. Rowe (1962) defined the stress-dilatancy for a biaxial compression of an assembly of particles, such as rods, uniform spheres, and glass marbles. He expressed the relationship among the applied stress ratio (σ_1' / σ_3'), the true inter particle friction angle, the geometry of the particle rearrangement and the rate of change of unit volume relative to the longitudinal strain for a given assembly. The angle of dilation is defined as the rate of plastic volume change to the rate of plastic shear strain change as

$$\sin(\psi) = -\frac{d\dot{\varepsilon}_v}{d\dot{\gamma}}$$ Eqn. B- 28

By minimizing the ratio between the incremental plastic work by principal stresses (σ_1, σ_2) the dilation angle is defined as

$$\sin(\psi) = \frac{\sin\phi - \sin\phi_{cv}}{1 - \sin\phi \sin\phi_{cv}}$$ Eqn. B- 29

where ϕ_{cv} is the critical friction angle or constant volume friction angle and ϕ is a mobilized friction angle.

Bolton (1986) proposed an empirical formulation relating the angle of shearing (ϕ) to dilation angle (ψ) and the friction angle at critical state(ϕ_{crit}), based on the test results of 17 different sands. Those relations are expressed by two different formulas for the case of plane strain and triaxial test as:

Plain strain: $\phi - \phi_{crit} = 0.8\psi = 5I_R$ Eqn. B- 30

Triaxail $\phi - \phi_{crit} = 3I_R$ Eqn. B- 31

where I_R is a relative dilatancy index which is related to the rate of dilation by the following equation.

$$\frac{-d\varepsilon_v}{d\varepsilon_1} = 0.3I_R$$ Eqn. B- 32

By observing that the dilation angle is dependent on the density and confining pressure, he expressed the relative dilatancy index as a function of relative density(D_r) and the mean effective stress as

$$I_R = D_r(10 - \ln p') - 1$$ Eqn. B- 33

B.4.2. Calibration of Drucker-Prager Plasticity Model

Results of DST and triaxail testing can be used to calibrate the ABAQUS Drucker-Prager model. As mentioned before, the main differences between Mohr-Coulomb and Drucker-Prager plasticity models lies on how those models treat the intermediate stress. The Mohr-Coulomb failure criterion is independent of intermediate stress while the Drucker-Prager model depends on it. There are several ways to approximate the Drucker-Prager model by Mohr-Coulomb model. The most commonly approach is to match the Mohr-Coulomb parameters with Drucker-Prager model in the plain strain condition. The matching can be performed by assuming plane strain condition in one direction ($d\varepsilon_1^{pl} = 0$) for Drucker-Prager model. This assumption creates a constraint that expressing the yield criterion based on the two principle stresses. Finally comparing the obtained new Drucker-Prager criterion with Mohr-Coulomb yield criterion leads to a relationship between (d,c,β, and ϕ) as

$$\sin(\phi) = \frac{\tan\beta\sqrt{3(9-\tan^2\psi)}}{9-\tan\beta\tan\psi} \quad \text{and} \quad c\cos\phi = \frac{\sqrt{3(9-\tan^2\psi)}}{9-\tan\beta\tan\psi}d \qquad \text{Eqn. B- 34}$$

As can be seen, the relations between two model parameters are set by knowing the dilation angle. To investigate the effect of dilation angle, two extreme cases , nondilatant flow (ψ=0) and associated flow rule (ψ=β), are examined. The following expressions can be established for nondilatant flow

$$\tan(\beta) = \sqrt{3}\sin\phi \quad \text{and} \quad \frac{d}{c} = \sqrt{3}\cos\phi \qquad \text{Eqn. B- 35}$$

and for associated flow rule

$$\tan(\beta) = \frac{\sqrt{3}\sin\phi}{\sqrt{1+\frac{1}{3}\sin^2\phi}} \quad \text{and} \quad \frac{d}{c} = \frac{\sqrt{3}\cos\phi}{\sqrt{1+\frac{1}{3}\sin^2\phi}} \qquad \text{Eqn. B- 36}$$

These two extreme cases gives almost equal value for Drucker-Prager model (β,d) for the case of low friction angle. However, their discrepancy increases by increasing the friction angle. For instance, the friction angle of 50^o gives Drucker-Prager friction angle of 50.5^0 degrees for associated flow and 53^0 for nondilatant flow.

Another way to approximate Drucker-Prager model with Mohr-Coulomb failure criterion is to match them in triaxail compression and tension. However, this matching method is suitable for a material with a low friction angle ($\phi < 22$).

B.4.3. Calibration of CAP Plasticity Model

The CAP plasticity model requires information about friction angle (β) and cohesion (d) parameters for a Drucker-Prager shear failure surface part as discussed in the previous section. The elliptical cap can be calibrated by hydrostatic compression test to obtain the mean effective yield stress (P_b) variation with the volumetric plastic strain ($pb = pb(\varepsilon_{vol}^{pl})$) as shown in Figure B- 15, this can be used to express hardening/softening law. The transition region requires the parameter R, varies between .0001 and 1000.0, which can n be obtained from triaxial tests at high confining pressure.

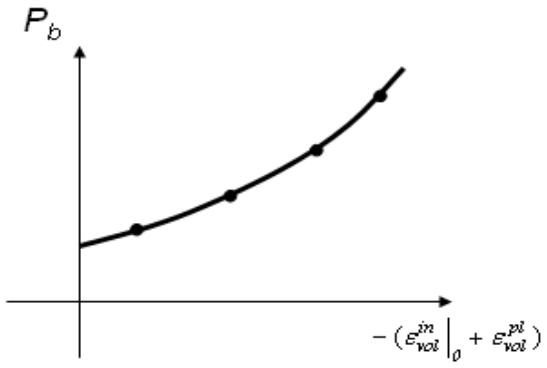

Figure B- 15: Typical results of Hardening/Softening rule for CAP plasticity model calibration

B.5. Contact Modelling

Buried cable and its surrounding soil are interacted with each other by defining the contact simulation model. Three steps are required to define the contact modelling in ABAQUS. The first step involves defining contact surfaces and designating the master surface and slave surfaces, the slave surface is normally attached to deformable bodies. Then, the surfaces that might be interacted are identified as contact pairs. Finally the constitutive model for interacting surfaces is defined. The constitutive model relates the transmitted forces, shear or normal forces, between two interaction surfaces as a function of clearance distance and over-closure.

The mechanical contact property for normal behaviour can be classified as a “hard” or “soft” contact. In “hard” contact the pressure-over closure relationship assumes the behaviour as depicted in Figure B- 16-a. When the two surface are in contact any contact pressure can be transferred between two surfaces and no pressure will be transferred when the two surfaces are separate. The “hard” contact minimizes the penetration of slave surface into the master surface. On the other hand, in “Softened” contact, a constitutive model representing the contact pressure-over closure and clearance relationship is defined as shown in Figure B- 16-b.

ABAQUS uses three different methods to handle the pressure-over closure contact constraint numerically. The direct method strictly enforces the defined pressure-over closure constraint. The penalty method approximates the pressure-over closure constraint, therefore, it is less accurate and it needs less iterations. The augmented Lagrange method uses the same approximation as the penalty method but it performs extra iteration to enhance the accuracy. The appropriate selection of the constraint enforcement method depends on the type of pressure-over closure behaviour, convergence and accuracy issues.

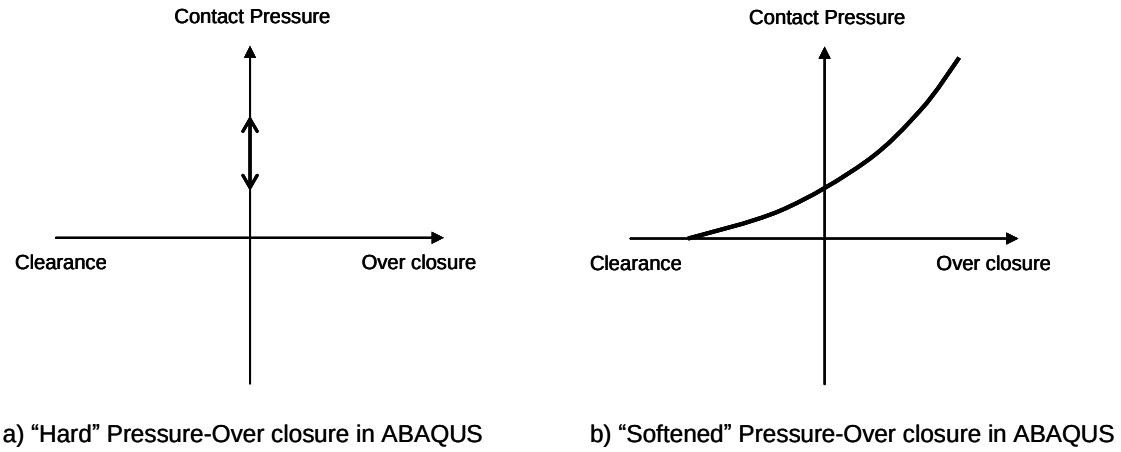

a) "Hard" Pressure-Over closure in ABAQUS b) "Softened" Pressure-Over closure in ABAQUS

Figure B- 16: Pressure-Over closure relationship in ABAQUS

In addition to normal forces, two contacting surfaces also transfer shear forces. The shear forces can be obtained from friction models. Friction model define the mechanical contact property in the tangential direction. The more basic form of friction model is a Coulomb friction model. In this model, two contacting surfaces are sticking together and developing shear stresses up to the certain limits or critical shear stresses (τ_{crit}). At this point the two surfaces are prone to slide relative to one another. The critical shear stresses is defined as a function of contact pressure and coefficient of friction angle (μ) as follows

$$\tau_{crit} = \mu P \qquad \text{Eqn. B- 37}$$

ABAQUS uses the equivalent shear stresses ($\tau_{eq} = \sqrt{\tau_1^2 + \tau_2^2}$) in Coulomb friction models to check slip/stick calculation, where τ_1, τ_2 are the two perpendicular components of shear forces on the contacting surface. The Coulomb friction model forms a region that contacting surfaces can be either in the sticking or slipping region, depending on the value of equivalent shear stresses as shown in Figure B- 17-a. Often some elastic slip deformation can be allowed while in the sticking part before the shear stresses reaches to critical shear stress as shown in Figure B- 17-b.

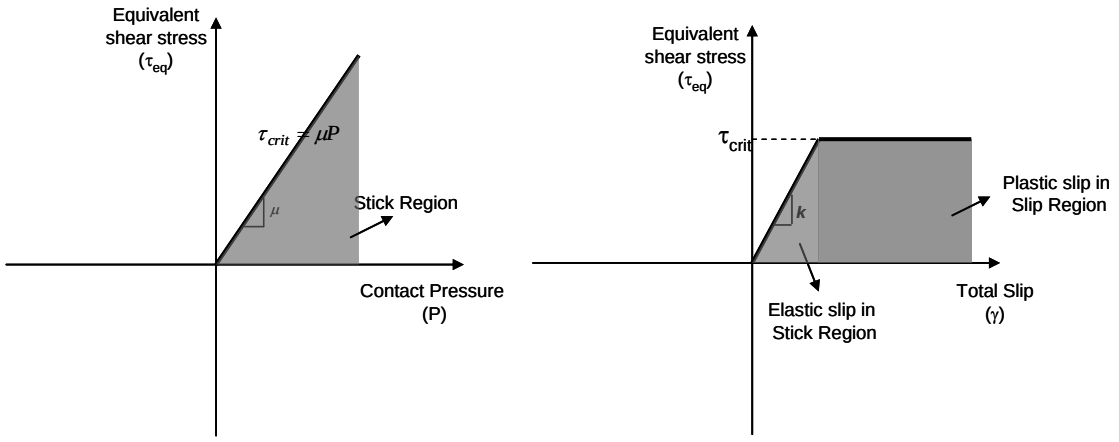

a) Slip and Stick region in classic Coulomb friction model

b) Elastic-Plastic behavior of friction-slip model

Figure B- 17: Basic Coulomb friction model, adapted from ABAQUS

ABAQUS also offers a friction model allowing to define the static and kinetic friction coefficient (μ_s, μ_k). This model assumes that the coefficient of friction angle (μ) reduces exponentially from static friction angle to kinetic friction angle by defining the decay coefficient (d_c) as depicted in the following equation

$$\mu = \mu_k - (\mu_s - \mu_k)e^{-d_c \dot{\gamma}_{eq}} \qquad \text{Eqn. B- 38}$$

Where $\dot{\gamma}_{eq}$ is the equivalent slip rate. Figure B- 18 shows the exponential decay function as implemented in ABAQUS.

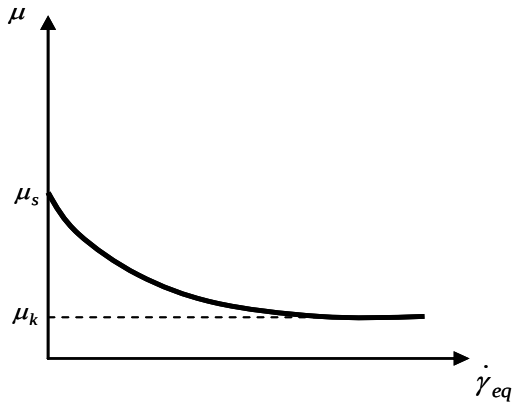

Figure B- 18: Exponential decay friction coefficient function, adapted from ABAQUS

To enforce frictional constraint, ABAQUS uses different schemes depending on the analysis type, implicit or explicit analysis. Since the implicit analysis is utilized throughout this research, only the methods available in implicit will be discussed. The stiffness method (penalty method) and Lagrange multiplier method are the algorithm to enforce the tangential constraint. The penalty method requires the definition of the elastic slip (γ_e) regardless of the selection of the friction model, i.e., the friction model with no elastic slip. Selection of the Small and large value of the elastic slip depends on the accuracy and convergence problem. The large value of the elastic slip means a faster convergence at the expense of accuracy. Problems with small elastic slip, for instance no slipping in the sticking state, are better dealt with Lagrange multiplier method. ABAQUS by default uses the elastic slip as a fraction of the characteristic contact surface length ($\bar{l}_i$) by using the slip tolerance (F_f). The selection of slip tolerance is based on the trade-off between the accuracy and efficiency, the pre default value is .005. As mentioned, for the problems that stick-slip frictional behaviour is necessary and no elastic slip is desirable the Lagrange method is more suitable. However, the Lagrange method is more computationally expensive and it needs more iteration to converge. Other than these cases, the stiffness method works acceptably well in most problems.

B.6. Analysis Procedure

A large class of problems can be solved with ABAQUS. Each problem requires a specific analysis procedure, depending on the nature of the problem. The simulation of the the buried cable soil interaction problem can be analyzed utilizing the static stress analysis or quasi-static analysis. The static analysis in the ABAQUS includes both linear and nonlinear problems. Types of nonlinearity that can be solved are material nonlinearity, geometric nonlinearity, such as large displacement problems, and boundary nonlinearity, such as contact problems. Since the response of buried-cable soil interaction must be assessed up to its ultimate stage some instabilities would occur. Such instabilities might arise from sever distortions of elements in the vicinity of the buried cable. This localized

instability terminates the analyses. For this class of problems, the analysis can be switched to quasi-static analysis or it can still be performed by static analysis with the aid of artificial damping. In unstable elements the local velocity increases and strain energy wants to transfer the neighbouring elements. Introducing the artificial viscous damping force prevents the localized transfer of the strain energy developing in the unstable element. The viscous force (F_v) is defined as $F_v = cM^* v$,where M^* is the artificial mass matrix with a unit density, C is the damping matrix, v is the local velocities., added to the global equilibrium equations. ABAQUS provides an automatic stabilization and issues warning massage if the amount of damping force is large and it may affect the solution in ways that are not desirable.

Alternatively, the nonlinear static problems can be handled by the explicit dynamic analysis in the form of quasi static analysis. The explicit dynamic analysis should be used with caution so that the effect of the inertia effects is minimal. To achieve this aim, the loads must be applied so slowly to avoid any excitation of the finite element model due to the wave propagation. Therefore the quasi-static explicit analysis requires a very small time increment, usually 100 times of the first vibration mode, to minimize the effect of inertia forces. The simulation of buried cable soil interaction is mostly performed by static analyses; however, whenever the convergence is an issue the analysis is switched to explicit quasi static analysis.

B.7. Geostatic Stress Analysis

A geostatic field analysis is the first step of any geotechnical analysis. This step is an important step since the soil behaviour is dependent on the confining stresses. Geostatic stress state in ABAQUS checks whether the initial stress state is in equilibrium with applied loads and boundary conditions. If the equilibrium does not occur, ABAQUS will iterate to obtain an equilibrium stress field that balances the prescribed conditions. In the

beginning of each analysis, gravity loads are applied in this step to the finite element model of buried-cable soil interaction.